Auto-ignition characterisation of synthetic fuels via Rapid Compression Machine

by

Myeji Chrysostom Materego

BSc, MSc.

Submitted in accordance with the requirements for the degree of

Doctor of Philosophy.

The University of Leeds

School of Mechanical Engineering

September 2015

Acknowledgements

The candidate confirms that the work submitted is his own, except where work which has formed part of jointly authored publications has been included. The contribution of the candidate and the other authors to this work has been explicitly indicated below. The candidate confirms that appropriate credit has been given within the thesis where reference has been made to the work of others.

Figure 4.12 in Chapter 4 has appeared in a jointly authored publication:

Agbro E; Materego M; Lawes M; Tomlin AS, (2015), 'Low temperature ignition properties of n-butanol: key uncertainties and constraints', Proceedings of the European Combustion Meeting, P1-37.

I was responsible for providing experimental measurements of ignition delay times for n-butanol. The contribution of the other authors was to carry out computer simulations of ignition delay times using chemical kinetic models.

Section 3.3 in Chapter 3 has appeared in a jointly authored publication:

Bradley, D, Lawes, M and Materego, M. (2015), 'Interpretation of Auto-ignition Delay Times Measured in Different Rapid Compression Machines', *25th International Colloquium on the Dynamics of Explosions and Reactive systems*, Paper 194.

I was responsible for collecting experimental measurements of ignition delay times of iso-octane, and conduct analysis and compare with those collected from other rigs in the Consortium. Other authors have provided technical discussions and guidance on the results produced in the publication.

Acknowledgements

The completion of this work was not possible without the support of many people around my life. If I could, I would have mentioned each one of you.

I would first and foremost like to thank the Lord God Almighty, ‘El-Shaddai’, for giving me health and strength to undertake this PhD study. My supervisors, Dr. Gary Sharpe for having faith in me from day one and went an extra mile for me, you were ready to sacrifice your job over my welfare, I thank you. Prof Derek Bradley for your tireless efforts, discussions and guidance, thank you. Dr. Malcolm Lawes for your guidance and constructive criticism which have always put me on my toes, thank you.

I must thank the Commonwealth Scholarship Commission for funding my studies for the three and a half years of my PhD. The Lab technicians, even though we started at a very difficult time when you were short staffed but you have continually been supportive, I thank you. My colleagues Richard Mumby, Luke Bates, Ben Thorne and Moustafa Shehata, for your great discussions. I learnt a lot from you guys, thank you.

Last but not least, a very special thanks go to my lovely family. My wife Priscilla and my two little princesses Carissa and Abigail, you guys always gave me strength to carry on. Thank you Carissa for your tireless, almost every day question, “Daddy when are you finishing your work?”, Abigail for your natural love and kisses every day and of course Priscilla for your love, support and out of this world delicious food. My parents and my siblings, I thank you for bearing with me as I have not been in contact very often but you always look out for me. I have no words to thank you enough.

ABSTRACT

Availability and sustainability of fuels for road and air transport is essential for economic development and growth of any nation. New alternative fuels provide an opportunity to limit the use of ever declining conventional petroleum oil reserves as well as offsetting CO_2 generation from their use. Liquid fuels have the highest energy density for transportation applications and synthetic liquid fuels, which can be produced from renewable non-food bio feedstock offer an exciting opportunity for partial or even total substitution of remaining fossil fuel supplies. It is therefore of great interest to study the fundamental combustion characteristics of these fuels if they are to be used commercially. This work is aiming at characterising the auto-ignition properties of individual fuel components representative of the chemical families present in the synthetic fuels which in this case are toluene, *iso*-octane, n-heptane, and bio-alcohols; ethanol and *n*-butanol. The auto-ignition characterisation was made by measurements of ignition delay times, τ. The time τ for these fuels and their blends were measured after rapidly compressed to an elevated pressure and temperature using a Rapid Compression Machine (RCM).

RCM provides good platform to study the fuel auto-ignition process without complicated physical effects in engines which are continually changing. However, they are not without problems, practical applications are usually not within the ideal conditions. Different machines have different extent of deviation from ideal conditions, making comparison of results between rigs difficult. In the present study, a dedicated work was conducted to study the difference between the measurements originated from these rigs and were characterised against their deviations from ideal conditions. These cover chemical reaction during the finite compression time, the effects of heat loss during the ignition delay period, the effects of piston displacement (piston bounce), and non-homogeneous auto-ignition. An interesting aspect of the study is that a plot of the measured different delay times at a given temperature, on the separate machines, against the corresponding degrees of reaction during compression, when extrapolated to zero reaction, yield a more accurate delay time for that condition. As the temperature is increased, so also are the oscillatory pressure amplitudes generated at the auto-igniting hot spots. This is in line with other studies of hot spot auto-ignition.

Measurements of ignition delay times of different chemical groups separately and when blended with each other were made. They provided an understanding of how their interaction influences the overall ignition delay times. When blended the change of their τ values do not vary linearly especially when the blended components have large difference in reactivities. Toluene for example, which is commonly known for its long ignition delay times, was made extremely reactive when blended with *n*-butanol. Comparison of addition of bio-alcohols (ethanol and *n*-butanol) on gasoline surrogate fuel (TRF) showed that at lower temperatures, they both increased the ignition delay times of TRF, while at high temperatures they reduced TRF delay times to almost the same value. *n*-butanol started to reduce TRF delay times at lower temperatures compared to ethanol.

Development of auto-ignition blending laws offers an opportunity to enable quick methods for choosing an appropriate blend for a particular application. In this work, a Linear by Mole (LbM) auto-ignition blending law was proposed, it uses the measured ignition delay times of individual components in the blend and varies them linearly with the fractional concentration of each component. This was found to be satisfactory only for blends of chemical families without NTC behaviour such as CH_4/H_2, for fuels with NTC behaviour an empirical based law was generated for the conditions studied.

Overall, this study has broadened our understanding in auto-ignition behaviour of selected individual fuel components and their blends at varying conditions of pressure, temperature and concentration. It has also enabled substantial development of Leeds RCM to achieve fast compression with good piston damping.

Table of Contents

LIST OF FIGURES.

LIST OF TABLES.

CHAPTER 1: INTRODUCTION

1.1 General overview and motivation.

After the industrial sector, the transportation sector is the second main consumer of world energy and has been so for many decades. Up to 26.6% of the world's total energy consumption is in transportation [Energy Information Administration, 2014] and is increasing by an average of 1.1% per annum [Energy Information Administration, 2013]. Transportation is the biggest consumer of liquid fuels, contributing up to 63% of the total growth in the global consumption of liquid fuels [Energy Information Administration, 2013]. Petroleum liquid fuels predominate due to their high energy content on both volumetric and mass basis, with good performance, availability, ease of handling and affordable price, compared with other fuels [Greg et al., 2006]. In addition, there is a highly developed infrastructure for their production, transportation and distribution. For many years, until recently, increasing demand and political instability in the Middle East have stimulated price rises. Increasing supply of fuels within the US will continue to lower prices in the coming years, until their reserves level off in the 2030s [Energy Information Administration, 2014].

The increasing use of conventional petroleum liquid fuels in transport is expected to continue, and is one of the main contributors of greenhouse gases emissions to the atmosphere, amounting for 16% of the total [Energy Information Administration, 2014]. This results in devastating effects, such as global warming, smog formation and acid rain. It also has resulted in the introduction of strict counter measures against combustion products throughout the world, and increasing efforts to achieve higher engine efficiencies, with new cleaner and sustainable fuels. Increasing research in these areas is therefore inevitable.

New, alternative, renewable, liquid fuels should be designed to be efficient, sustainable and clean. One approach commonly used is to mimic conventional petroleum based fuels in their physical and chemical characteristics [Nazim et al., 2008]. New fuels may be used alone or mixed with regular petroleum oil based fuel, thus reducing dependency upon conventional petroleum based fuels. Liquid fuels can be synthesised from syngas in the Fischer-Tropsch (F-T) process. Feed-stocks can be biomass, natural gas, coal or other carbon containing sources. For any new fuel, a clear understanding of the fundamental combustion behaviour and properties under different conditions is necessary before they can be commercially used.

Auto-ignition is one of the key fundamental fuel combustion characteristic which plays a vital role in combustion efficiency. It is a sudden exothermic heat release from the fuel, occurring without an application of external source after a delay time. It critically depends on pressure, temperature and mixture concentration. Even though the generation of new alternative, renewable fuels is a very attractive proposition, the auto-ignition of such fuels under different conditions provides a challenge for the new generation of fuels and engines. The phenomenon of "knock" in SI engines arises from the auto-ignition of the end gas, accompanied with a rapid rise and oscillatory pressures which can be very detrimental to the engine. Compression ratio in SI engines is knock limited, constraining fuel efficiency and reduction of CO_2 emissions. In controlled auto-ignition (CA) engines, the auto-ignition influences the smooth operation and drivability especially under high load. In all these cases, auto-ignition usually arises at hotspots, due to the non-uniformity of temperature and/or composition [Mansfield et al., 2015; Bradley et al., 2015], a process not fully understood. Auto-ignition can also arise in fuel storage and transportation, and a study of such hazards is vital.

Auto-ignition property is characterised using the ignition delay time, τ_i, which is the time lapsed before the onset of main combustion explosion. Measured τ_i values are ideally characterised for a homogeneous mixture, at a given temperature and pressure. It is the parameter that is most featured in the present study. The general nature of τ_i for non-aromatic hydrocarbons is that, it decreases exponentially with increasing temperature, in the higher and lower temperatures ranges, whereas at intermediate temperatures, a negative temperature coefficient (NTC) occurs. Here τ_i increases, or remains constant with increasing temperature [Griffiths et al, 1993; Griffiths et al., 1997; Gersen et al., 2010; Westbrook et al., 1998; Pfahl et al., 1996]. Near and within this region, combustion is usually taking place in two stages. After an initial delay, heat is released in a first stage in a "cool flame", followed by the main heat release. Aromatic hydrocarbons do not exhibit NTC behaviour, nor two stage ignition phenomenon [Mittal et al., 2007; His-Ping et al., 2009]. A very interesting consideration is how the blending of such different fuel components will affect the resulting τ_i of the blend.

1.2 Scope of the work and methodology.

The primary activity has been centred around the measurements and study of τ_i for different liquid fuels and their blends, under different conditions of pressure, temperature and mixture concentration, with τ_i measurements made using a Rapid Compression Machine (RCM). The principal measurements were taken at University of Leeds, with others at the SASOL Advanced Fuel Laboratory at the University of Cape Town. In the course of this research, the author was a participant in the first RCM workshop, which was conducted at the Argonne National Laboratory in Chicago in 2012. Researchers from thirteen different research groups around the world, users of RCMs, met to discuss the challenges associated with the use of these machines and the interpretation of their measurements, with the aim of reaching a universal consensus through their improved understanding of the RCMs. Detailed findings and agreements made in the workshop are subsequently discussed in Chapter 4.

The scope of this work comprises:

- Modification and Improvement of the Leeds RCM to achieve conditions of pressure and temperature relevant to engines.
- Measurements of τ_i values for selected liquid fuels and their blends under various conditions of pressure, temperature and mixture concentration.
- Interpretation of the measured τ_i values, taking into consideration the non-idealities existing in the RCM.
- Development of τ_i blending laws for the fuels studied.

This study ran in parallel with a study of burning velocity of similar liquid fuels and their blends, using the Leeds MK II combustion bomb. The complete combined study of ignition delay times and burning velocity will play an important role in characterizing new fuels and their blends, particularly with regards to the engine knocking phenomena. The nature of end gas auto-ignition in SI engines depends on τ_i values, their spatial distribution, temperature, pressure, composition and burning velocity. Such data are relevant to both spark ignition, SI and controlled auto-ignition (CA) engines.

1.3 Alternative liquid fuels.

Alternative fuels are possible substitutes to conventional fossil fuels. They can be either renewable or non-renewable, depending on the feedstock resources used in their production. The main groups discussed here are the Fischer Tropsch (F-T) synthetic liquid fuels and biofuels. The following two sections overview both groups, covering their history, production and classification.

1.3.1 Fischer-Tropsch (F-T) Synthetic liquid fuels.

Synthetic liquid fuels are alternative fuels obtained from syngas, a combination of hydrogen and carbon-monoxide. Syngas is catalytically processed to produce liquid hydrocarbons fuels, with predetermined characteristics. The classifications of synthetic fuels depend on the feedstock used to make the syngas and the technology used to convert it into liquid fuel. This type of fuel can be considered as renewable, if the feedstock comes from renewable sources such as biomass.

The F-T process is the most common method used for industrial production of synthetic liquid fuels. It is named after its founders, Prof. Franz Fischer and Dr. Hans Tropsch, who developed it in Germany during the World War II to satisfy demand for fuel at the time. It was thereafter further developed into a less expensive process by SASOL in South Africa. The F-T process is preceeded by a gasification process in which synthesis gas (H_2+CO) is produced, usually through gasification. Syngas is then converted into long chain liquid hydrocarbons using a range of catalytic chemical reactions. The whole process can be thought of as catalytic polymerization of carbon monoxide together with reaction by hydrogen to generate the long straight chains of methylene units: $CO + H_2 \xrightarrow{\text{catalyst}} (CH_2)_n + H_2O$. These are further processed and cracked into smaller units, rearranging some of the atoms to obtain liquids with a wide boiling range, ranging through gasoline naphtha, kerosene, and diesel fuel. The overall composition of the liquid fuels depends on the quality of the synthesis gas, process conditions and the catalyst employed. [Greg et al., 2006]

The first South Africa F-T commercial plants used coal for the syngas but currently coal, natural gas, or biomass are used as raw materials. The naming of the process depends on the raw materials, CtL (coal to liquid), BtL (Biomass to liquid) and GtL (Gas to liquid).

F-T synthesis gas is free from sulphur and aromatic compounds, cleaner than the petroleum fuels. However, the lack of aromatics may result in shrinkage of some types of elastomers during operation and promote fuel leakage. This is usually avoided by either finding additives that can reduce the shrinkage, or by the use the fuel produced from synthesis gas and blended with a conventional petroleum [Greg et al., 2006].

Raw materials used for syngas production are widely available, compared to limited petroleum oil reserves. Coal is available worldwide with the biggest reserve in USA, China, Russia and India [World Coal Institute, 2005]. Natural gas is also available almost in every continent of the world with production growth estimated at 1.8% per annum [Energy Information Administration, 2010].

F-T synthetic fuels, are characterised by their main components (alkanes, alkenes and ethers) followed by their blends, ranging from binary to more complex blending. Measurements of τ_i for selected individual components and their blends are reported in Chapter 4.

1.3.2 Bio-fuels.

Biofuels are hydrocarbons produced from organic materials such as plants, animals, and agricultural wastes. They can be liquid, such as ethanol and biodiesel; gaseous such as methane; or solid such as charcoal or wood pellets. As with the F-T fuels, they reduce the reliance on fossil based fuels, with advantages such as sustainability, environmental compatable, and good adaptability. Several technologies are used to convert feed stocks into biofuels. These include fermentation, hydrolysis, transesterifications, hydrocracking, pyrolysis and gasification. Biofuels are classified according to the feedstock or the conversion technology. These are categorised mainly in four "generations". ["Generations of biofuels" (n.d), para. 1-4].

First generation biofuels are made from sugars, starches, oil, and animal fats and are converted into fuel using well established processes. These fuels include biodiesel, bio-alcohols, ethanol, and bio-gases, such as methane, captured from landfill decomposition. The second generation biofuels are made from non-food crops or agricultural waste, especially ligno-cellulosic biomass like switch-grass, willow, or wood chips. The third generation comprises algae or other quickly growing biomass sources. The fourth generation biofuels are made from specially bio-engineered plants or biomass that may have higher energy yields or lower barriers to cellulosic breakdown or grown on non-agricultural land or in water.

The most popular, well researched and widely used liquid biofuel is ethanol [Georgios et al., 2015; Jaeho et al., 2015; Ashraf et al. 2015; Jörg et al., 2015]. Its popularity came particularly from its high octane number (ON). Other fuels that have received research attention include biodiesels [Shahir et al., 2015; Jiang et al., 2014; Ndaba et al., 2015], methanol [Xudong et al., 2013; Chunhua et al., 2015; Vancoillie et al., 2013] and bio-butanol [Ivo et al., 2012; Abdullah et al., 2015; Weiqi et al., 2015]. Table 1.1 compares the characteristics of these biofuels with their oil based counterparts.

Biofuel	Fossil Fuel	Differences
Ethanol	Gasoline	Ethanol has about half the specific thermal energy of gasoline. It generates less CO_2 and particulates than gasoline [Georgios et al., 2015; Jaeho et al., 2015; Ashraf et al. 2015]. Engines must be modified to run on ethanol due to corrosion effects [Jörg et al., 2015]. It is hygroscopic and hence makes transport through the existing infrastructure impossible. It cannot be blended with gasoline in refineries, but at the selling station.
Biodiesel	Diesel	This has only slightly less specific thermal energy than regular low sulphur diesel [Jiang et al., 2014]. It is more corrosive to engine parts than standard diesel [Ndaba et al., 2015]. It generally burns cleaner producing less particulate, CO and HC, but slightly higher NO_x [Shahir et al., 2015].
Methanol	Methane	Methanol has less specific thermal energy than methane. It is liquid and easy to transport, whereas gaseous methane must be compressed for transportation.
Biobutanol	Gasoline	Biobutanol has a similar specific thermal energy to gasoline. Engines do not require modifications. It is less hygroscopic than ethanol, making it easy to transport. It readily mixes with other fuels such as diesel and gasoline without separating. [Szwaja et al., 2010]

Table 1.1. Comparison of properties for common biofuels with oil based fuels and methane.

Comparisons of bio-butanol and ethanol with gasoline show bio-butanol properties are the closest to that of gasoline. Nevertheless, bio-butanol had not been able to replace ethanol as an engine fuel, one reason being its expensive production routes and very poor yields from traditional acetone-butanol-ethanol (ABE) fermentation discussed in [Jones et al., 1986]. Recent methods are more economical, with better yield [Tashiro et al., 2015], making it competitive with ethanol. Measurements of τ_i for the blends of gasoline surrogate with butanol and ethanol are compared in Chapter 4.

1.4 Combustion and auto-ignition.

Combustion mainly occurs in either a propagating flame, driven by molecular transport processes and chemical reactions or as an auto-ignition in a region of near-uniform composition, temperature and pressure, but usually at localised hotspots. An example of both modes is illustrated in SI engines, shown in Fig 1.1, where flame propagation originates at the spark source causing the temperature and pressure to rise in the unburned gas sufficiently to create auto ignition at hot spots. Modes of flame propagation can be further classified, depending on whether the fuel and air are premixed (premixed flame), or separate (diffusion flame). The associated fundamental properties that need to be characterised for the new fuels and its individual components are the auto-ignition delay times and burning velocity.

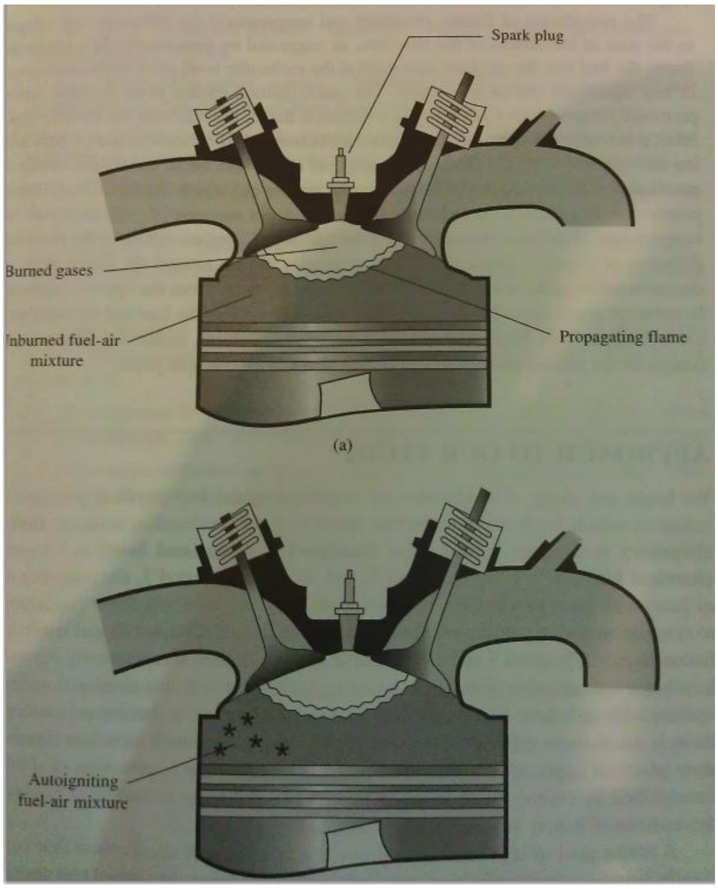

Figure 1.1 (a) Flame and (b) Auto-ignition mode of combustion in a spark ignition engine. [Turns, 2012].

(b)

Combustion and auto-ignition are complex phenomena involving the interactions between different disciplines including thermodynamics, chemical kinetics, fluid dynamics, heat and mass transfer and turbulence. As a result, detailed solutions are difficult to achieve. Nevertheless, the development of new/improved experimental techniques (e.g high speed cameras and 3D laser imaging), advance in research devices such as Shock Tubes and Rapid Compression Machines (discussed in the preceding section), and improved mathematical modelling aided by computers, have greatly advanced understanding of flames and auto-ignition in recent years.

1.5 Ignition delay time measurements.

Experimental measurements of ignition delay time, τ_i, have been used to characterise auto-ignition behaviour. Within τ_i there is another important parameter known as excitation time τ_e, a time during which most of the heat release occurs [Andrew et al., 1989]. While τ_i values are in the range of milliseconds, those of τ_e are in microseconds, making experimental measurements of τ_e very difficult. τ_e is therefore usually calculated using chemical kinetic models.

Measurements of τ_i in engines or turbines would be very complex due to the continually changing conditions and the complex flow fields. Thus, in order to enhance fundamental understanding and interpretation, measurements are conducted under controllable conditions in relatively simple devices. Low pressure constant volume vessels, combustion bombs, and flow reactors have all been used. For the high pressure engine condition the most suitable devices are RCM and Shock Tubes, which are now described.

1.5.1 Shock tubes.

Shock tubes, STs, have been in use for over 115 years. The idea of a ST came primarily from the detection of deflagration-detonation transition in the flame propagation in tubes by the French physicists F. Mallard, H. Le Chatelier, M. Berthelot, and P. Vieille [Fomin N.A., 2010]. STs allow for variations of the pressure and temperature over a wide range by using a shock wave and study the high temperature combustion processes for various gases. The first ST was constructed by P Vieille [Vieille P., 1899]. However, it was not until 1937 that widespread interest was stimulated by the British scientists Payman and Shepherd [Payman et al.,1937], whose work led into designing of high pressure “pure” ST in which a shock wave was initiated by rupturing a diaphragm separating gases in high and low pressures sections [Payman et al., 1946]. Since then various developments have been made including optical access to visualize and record the processes inside the ST [Pfahl et al., 1996; Westbrook et al., 1998]. They are now commonly employed for studying auto-ignition at high pressures and temperatures.

A ST is basically a closed tube which is divided into two sections by a diaphragm. The two sections are at substantially different pressures. Depending on the shock pressure and temperature required, diaphragms are usually made from cellophane, aluminium, copper or steel. Fig. 1.2 shows the schematic for a typical shock tube facility operation. The principle of operation is based on shock wave theory. A shock wave is generated when the diaphragm that separates the low and high pressure sections is broken. The shock wave propagates to the low pressure section and instantaneously compresses the test mixture. The separation distance between the incident shock and contact surface dictates the upper limit of the test time in shock tubes as shown in Fig 1.3. Conventional shock tubes are limited to 1-3ms test time [Samitra et al., 2011; Huang et al., 2004], but recent advances, which includes extending the driver section, have increased the testing times. For example, the Princeton group attained testing times of up to 55 ms [Campbell et al., 2015].

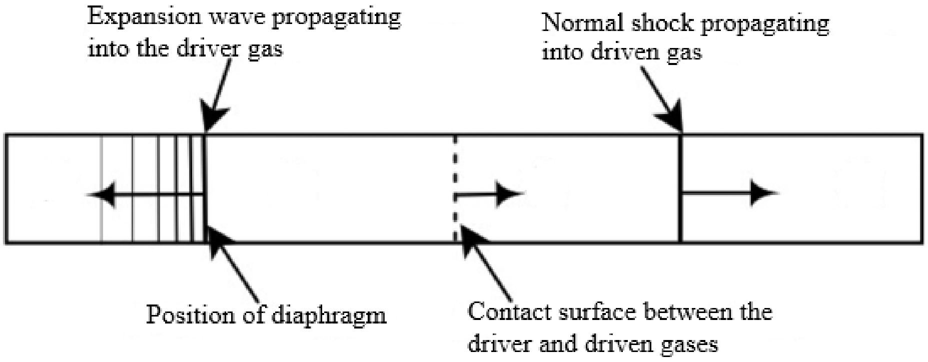

Figure 1.2. Schematic of shock tube operation. [Quinn et al., 2013].

Measurements of τ in the ST are usually derived from the measured pressure traces within the test section and detection of CH-radical band emissions [Pfahl et al., 1996], as shown in Fig. 1.4. Due to limitations in their testing times, ST are more suited for measuring relatively shorter τ values at higher temperatures. The main advantage of ST over other devices is its capability to compress the test mixture instantaneously using incident and reflected shocks and thus reduce the influences associated with the compression process. Moreover, Stanford group developed an aerosol ST which use modified end wall section to permit filling with aerosol mixture [Davidson et al., 2008]. This enabled measurements of vapour-phase ignition delay times of low vapour pressure fuels and fuel surrogates such as JP-7 and *n*-dodecane without the need of heated ST and separate mixing chamber.

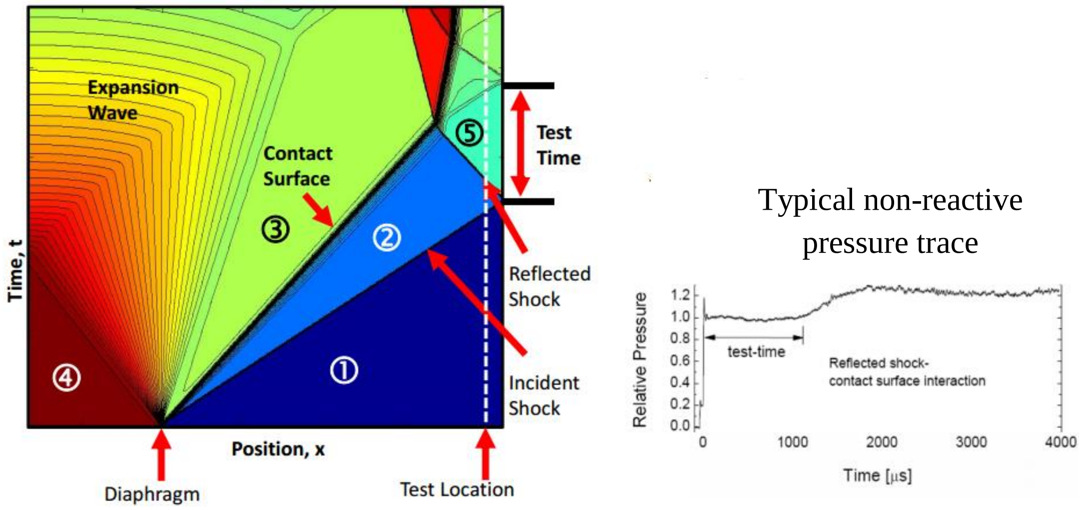

Figure 1.3. Wave system in the shock tube and typical non-reactive pressure measurements showing testing time [Mathew et al., 2015].

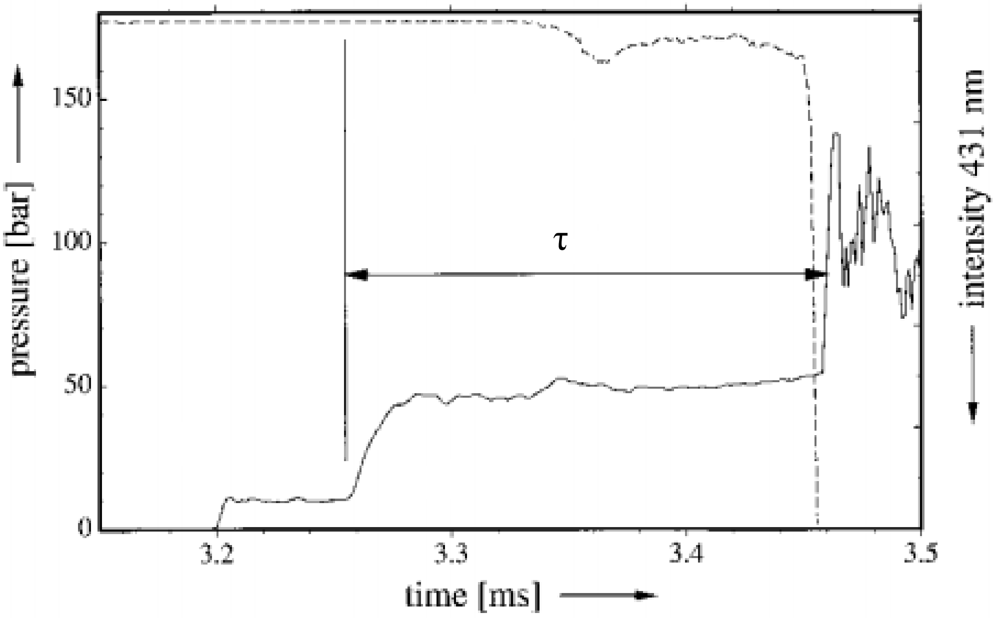

Figure 1.4. Pressure history and CH-band emission for n-decane, 5.0MPa, 885K, stoichiometric [Pfahl et al., 1996].

1.5.2 Flow reactors.

Like ST, these devices are cylindrical tubes with hot turbulent air flow, as shown in Fig. 1.5. Fuel is rapidly injected into the stream of hot air at the throat of high velocity nozzle, and mixing takes place downstream. Usually the tube is covered with heaters to ensure uniform temperature. Auto-ignition occurs after fuel/air mixing and is observed by means of light emissions or a sudden temperature rise of at least 50K [Eric et al., 2007]. τ is measured as the time between the fuel/air mixing to the point of ignition, and the initial point of fuel/air mixing is usually detected using a laser detection system, as indicated in Fig. 1.6.

Most flow reactors operate in the pressure range of 0.1-3.0MPa and at a maximum temperature of 1000K. However, due to difficulties associated with perturbations in the mixing region, they are commonly used to measure the longer τ values, in excess of 100 ms [Petersen et al., 2007, Beerer, 2009].

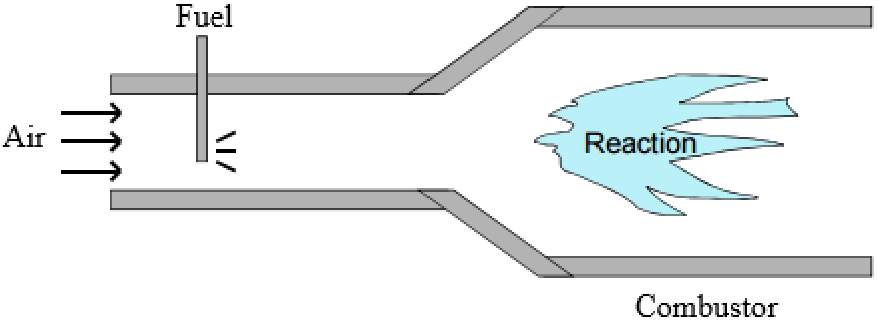

Figure 1.5. Schematic of flow reactor [Beerer D., 2009].

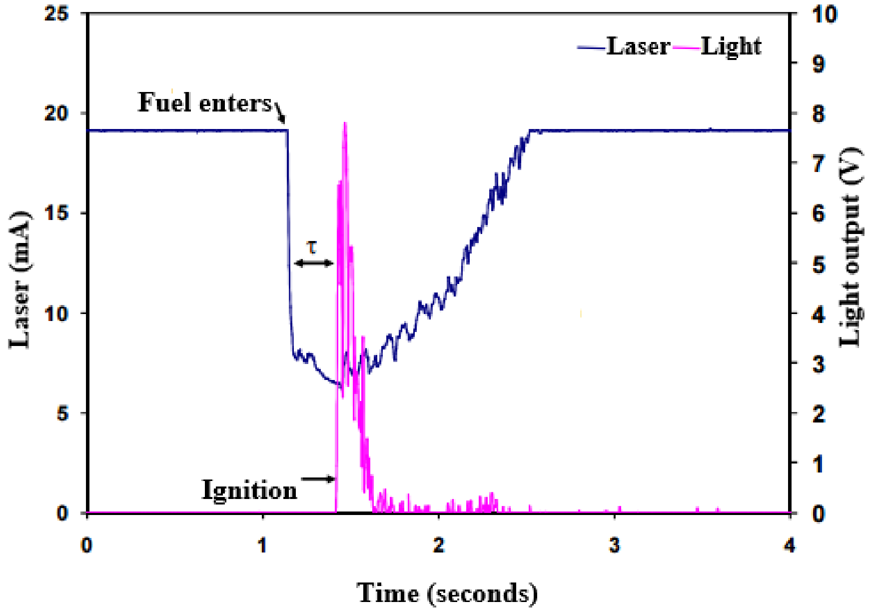

Figure 1.6. τ definition using laser and light output in flow reactor [Beerer et al., 2009].

1.5.3 Rapid Compression Machines (RCM).

This is a single stroke compression facility, where compression is achieved by a simple piston-cylinder configuration, as shown in Fig. 1.7. The motion of the piston is driven by high pressure at one side, at the other is the reactant mixture. The compression must be rapid otherwise reaction will occur during compression. It is difficult to attain as rapid a compression as that in a ST. However, RCMs are capable of sustaining fairly constant pressure and temperatures after compression for about 120 ms, compared to that of, at most, 55 ms in a ST. [Mittal et al., 2007].

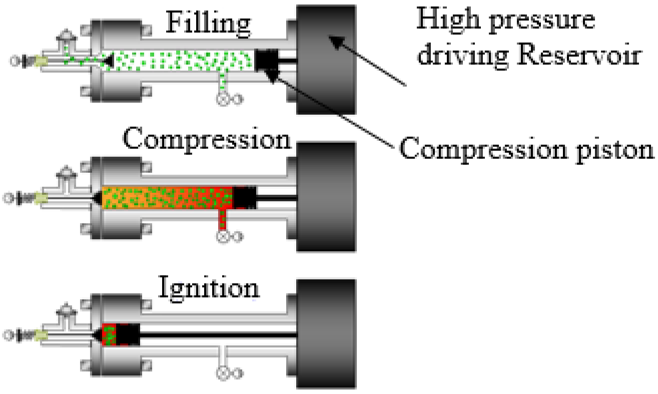

Figure 1.7.Schematic of RCM operation [University of Illinois, 2014].

In RCMs, τ is obtained from pressure records and τ is usually defined as the duration from the end of compression (t = 0) to the point of maximum rate of pressure rise (i.e maximum dP/dt) [Gersen et al., 2010; Westbrook et al., 1998; Gallagher et al., 1998; Mittal et al., 2008], as shown in Fig. 1.8. Other definitions have been used, such as the elapsed time from the end of compression to the time when pressure reaches 20 or 50% of the maximum pressure rise [Ihara et al., 2009; Tanaka et al.,2003; Mittal et al., 2007]. Because of the rapid rise in pressure during ignition, all these methods produce similar results. Fig 1.9 summarises typical boundaries for the measured τ values for each device.

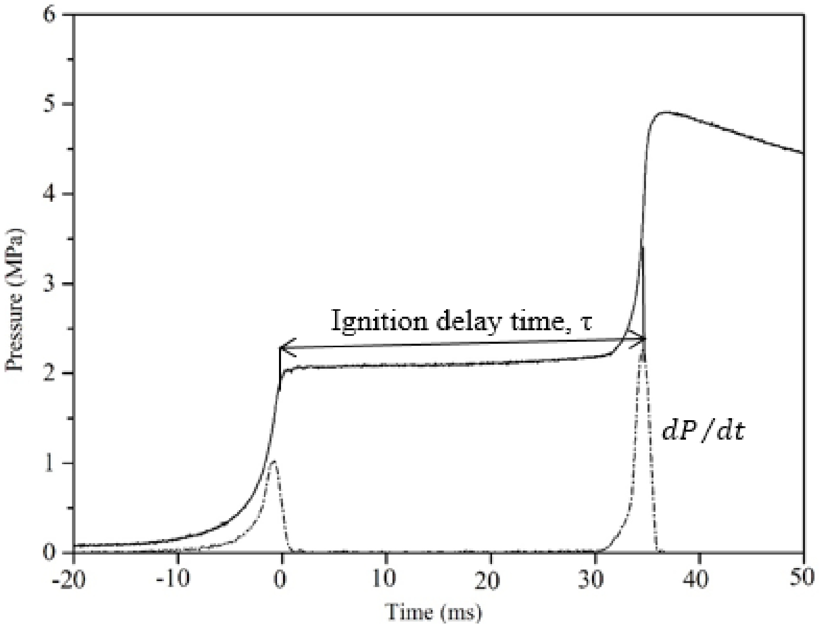

Figure 1.8. Typical pressure trace in the RCM showing Ignition delay time definition.

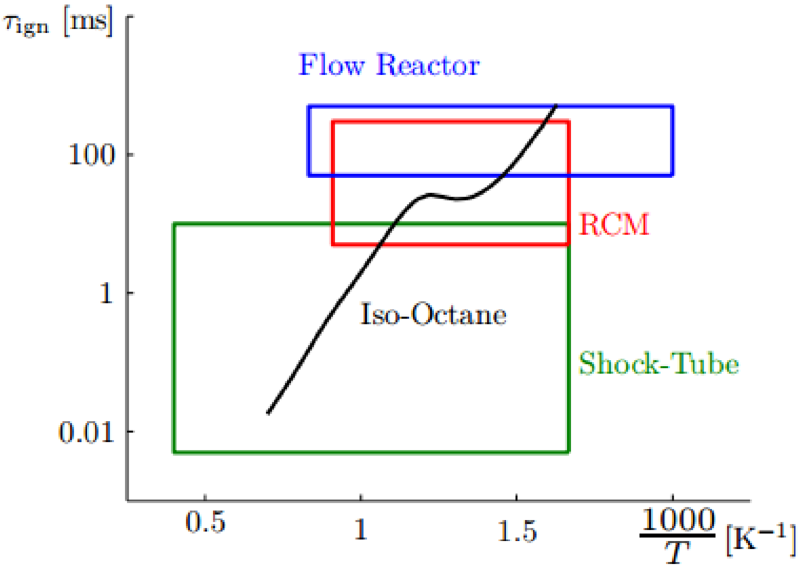

Figure 1.9. Typical operational boundaries of ST, RCM and flow reactors. A comparison to a representative ignition delay curve of *i*-octane is included [Grogan et al., 2015]; ignition delay of *iso*-octane is obtained from the reduced mechanism of Pepiot-Desjardins and Pitsch [Pepiot-Desjardins et al., 2008] at an equivalence ratio of 0.6 and a pressure of 2.0 MPa.

1.6 Auto-ignition (AI) chemistry of hydrocarbons.

The chemistry of hydrocarbon oxidation is very complex. A sequence of thousands of different elementary chemical reactions can take place during combustion. This section gives only the basic elementary chemistry involved during ignition of hydrocarbon fuels. In the present work no intermediate species were measured, only ignition delay times. Nevertheless, since the τ_i values of different hydrocarbons at different conditions are fundamentally controlled by their oxidation chemistry, it is aimed to give an overview of how reactions unfold at different temperatures. Reviews of detailed chemical mechanisms for alkanes and other hydrocarbons can be found in Battin-Leclerc [2008] and Simmie [2003].

A general understanding of hydrocarbon oxidation mechanisms has been developed over many years, and it is widely accepted that in a simple static combustion system, there are two distinct regions with different reactions behaviours which depends on the temperature of the fuel, on one side there is slow, low temperature reaction and the other side high temperature explosive reactions [Barnard et al., 1985].

AI chemistry is mainly controlled by the chain branching reactions, which change with temperature and concentration. In the initiation process atoms or radicals are produced by either dissociation of the fuel molecule (RH) or by reaction between fuel and oxygen, to produce alkyl radical R, hydrogen H and hydroxide OH. This process is basically hydrogen abstraction for saturated hydrocarbons, such as alkanes. For unsaturated hydrocarbons addition of oxygen to the double bonds results in the formation of aldehydes.

$$RH \rightarrow R + H \tag{1.1}$$

$$RH + O_2 \rightarrow R + OH \tag{1.2}$$

Decomposition of fuel molecules (Eq.1.1) is dominant at high temperatures, while at low temperatures dissociation is too slow and (Eq. 1.2) dominates. It is also important to note that these reactions are very slow because unimolecular dissociation (Eq. 1.1) would require an activation energy, equal or greater, than the bond dissociation energy of the fuel molecule.

Hydrogen atom abstraction can also be initiated by fuel reaction with hydroxyl radical (OH) using the following reaction.

$$RH + OH \rightarrow R + H_2O \tag{1.3}$$

The production of alkyl radical, R, results in other important reactions that propagate the chain reactions with increasing temperature. The main reactions are decomposition and oxidation of the alkyl radical. The alkyl radical may decompose to alkenes and another alkyl radical:

$$RCH_2CHR' \rightarrow R + CH_2 = CHR' \tag{1.4}$$

The reaction of the alkyl radical with oxygen is very important, leading to the formation of the alkylperoxy radical RO_2, which is essential to the formation of many combustion products.

$$R + O_2 \rightarrow Alkene + HO_2 \tag{1.5}$$

$$R + O_2 \leftrightarrow RO_2 \tag{1.6}$$

The RO_2 radical may undergo a wide variety of reactions, but of particular importance is the hydrogen abstraction which can occur internally (isomerisation) and result in the formation of the hydroperoxyalkyl radical QOOH, where Q represents C_nH_{2n} species. External hydrogen abstraction might occur, provided RO_2 has a sufficient life time.

$$RO_2 \rightarrow QOOH \rightarrow Products \tag{1.7}$$

The equilibrium of Eq. 1.6 tends to move to the left as the temperature increases [Barnard et al., 1985], promoting the production of more alkenes and the HO_2 radical.

The products from alkyl peroxide isomerisation usually include aldehydes. At temperatures below 400°C the lowest aldehyde (formaldehyde) is stable and takes no part in branching. The higher aldehydes may cause some degenerate branching reactions, generating large amounts of the degenerate branching agent, hydroperoxide-HO_2.

$$CH_3CHO + O_2 \rightarrow CH_3CO + HO_2 \tag{1.8}$$

The increased amount of hydroperoxide from Eqs. 1.5 and 1.8 retards the branching process and overall reaction rate, and is the primary mechanism for the occurrence of Negative Temperature Coefficient (NTC) behaviour for alkanes, where ignition delay times increase with increase in temperature. This phenomenon occurs in the intermediate temperature range of 750-850K [Griffiths et al., 1993; Minetti et al., 1994; Vranckx et al., 2013; Mittal et al., 2014]. The presence of peroxides in the radical pool has been reported in [Bardwell et al., 1951] as inducing cool flame ignition, prior to the main explosive ignition. This is commonly known as two stage ignition. The first stage is characterised by a blue luminescent cool flame and the second by a more intense high temperature explosion. [Falconer et al., 1983] have shown that cool flames represent the explosion of accumulated peroxides, as concentration of peroxides were found to reach peak concentration a few milliseconds before the cool flames, and decreased sharply soon after cool flame had occurred. Figure 1.10 shows typical pressure measurements in RCM indicating the two stage ignition of stoichiometric *iso*-octane at 2.0 MPa, as measured in the present study.

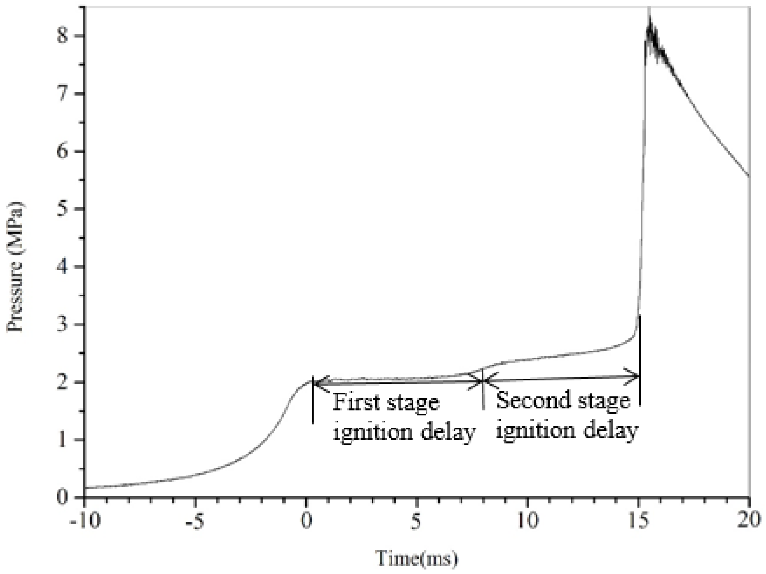

Figure 1.10. Pressure trace for iso-octane combustion in RCM showing the two stage ignition phenomena.

As the temperature is increased, further chain branching occurs, leading to the production of hydrogen peroxides

$$HO_2 + RH \rightarrow H_2O_2 + R \qquad (1.9)$$

$$HO_2 + HO_2 \rightarrow H_2O_2 + O_2 \qquad (1.10)$$

These are followed further with the chain branching reaction:

$$H_2O_2(+M) \rightarrow 2OH(+M) \qquad (1.11)$$

These reactions become more important at higher temperatures [Barnard et al., 1985] and eventually cause the rate of reaction to increase again with temperature.

For aromatics, their C-C and C-H bonds are substantially stronger than those of alkanes and therefore their low temperature oxidation initiation is usually through reaction with the OH radical which may abstract a hydrogen atom or add directly to the ring's π-system, generating an allylic type radical system. These two pathways compete and contribute to the combustion chemistry of aromatic species. Addition of OH to the aromatic ring is more prevalent at 298K [Atkinson, 1994]. Once a radical is generated either on the aromatic ring or side chain of toluene, rapid oxidation can occur. At high temperatures, initiation occur through different routes. Emdee et al. [1992] and Dagaut et al. [2002] proposed that the toluene combustion mechanism is most sensitive to its reaction with O_2 (H-abstraction) to form the benzyl radical and HO_2. The benzyl radical can further decompose to form acetylene and cyclopentadienyl or react with an additional O_2 and decompose to form phenyl and formyl radicals (via benzalydehyde, $C_6H_5 - C(=O)H$). Djurisic et al. [2001] and Sivaramakrishnan et al. [2005] summarised the overall toluene auto-ignition reaction to proceed through $C_6H_5CH_3 \rightarrow C_6H_5CH_2 \rightarrow C_6H_5CHO \rightarrow C_6H_5CO \rightarrow C_6H_5 \rightarrow C_6H_5O \rightarrow C_6H_5OH$, followed by the ring breaking reactions. The major consumption of toluene was found to be due to the reaction of $C_6H_5CH_3 + OH$.

For alcohols, the presence of a hydroxyl group brings about different behaviour of its associated rate constants and product channels compared to hydrocarbons. These effects include pre-reaction complexes when reacting with OH that cause negative temperature dependence in their rate constants at low temperature [Zhou et al., 2011]. Also their molecular structure allows faster reaction of the 1-hydroxyl radical with reactive molecules and radicals such as O_2 and OH compared to an analogous hydrocarbon radical [Silva et al., 2009]. Key chemical mechanisms that drive alcohol auto-ignition are described in Section 4.4.3.

As demonstrated, the temperature plays a vital role in determining the fuel oxidation progress and its route. Different intermediate radicals are generated which speed up, or retard, the reactions and this affects the overall auto-ignition characteristics of a fuel at different temperatures. Measurements of τ for hydrocarbon fuels under varying temperatures, pressure and concentration, provide a good input towards validation of the detailed chemical kinetics models, and broaden our understanding of how these intermediate radicals interact. Moreover, numerical simulations such as Tomlin et al. [1992]; Tauranyi et al. [2015]; Bansal et al. [2015] have been able to use experimental measurements and detailed chemical mechanisms to reduce these complex mechanisms into fewer steps and reactions which can be extrapolated to conditions where experiments have not been performed.

1.7 Use of experimental ignition delay times for chemical kinetic studies. (Case of RCM)

Measurements of ignition delay times in controllable conditions such as in shock tubes and RCMs are important for understanding low to high temperature fundamental auto-ignition chemistry under engine-like conditions. Complementary combination of RCM and shock tube data has allowed validation and refinement of various reaction mechanisms over a wide range of pressures and temperatures. Various mechanisms such as that of *iso*-octane [Curran et al., 2002], *n*-heptane [Westbrook et al., 2011] and toluene [Pitz et al., 2001] have been successfully validated using experimental ignition delay times and are now widely used as building blocks for reaction mechanisms for the surrogate blends such as in Cancino et al. [2009].

Direct comparison between the measured ignition delay data and predictions of reaction mechanism is not always possible because experimental measurements are usually subjected to facility dependent effects such as mixture non-homogeneity, pre-reactions during compression and heat loss during and after compression. Therefore, careful interpretation of these data need to be made before they can be used by modellers. Mixture inhomogeneity is usually overcome by proper design of the reaction chamber and piston as will be discussed in Section 3.2.3, but heat loss is quantified by experimentally measured pressure traces using non-reactive mixtures. These measurements quantify the amount of pressure drop as a result of heat loss in a particular facility, numerical models are therefore generated to match the pressure history of non-reactive mixture to account for the heat loss effect. Two main approaches are typically used; one is the addition of heat loss term in the energy equation while keeping the reaction chamber volume constant e.g. in Ribaucour et al. [2000] while the other is to specify a volume expansion term while applying the adiabatic core assumption e.g. in Tanaka et al. [2003]. Comparison of these two approaches with the CFD simulation of non-reactive RCM experiments using N_2 in Mittal et al. [2006], showed that the latter approach was found to be computationally valid because it matched the CFD pressure and temperature for a longer period than the former one.

The procedure for obtaining volume expansion term is as follows: for compression stroke, an empirically determined parameter is added to the time dependent actual geometric volume of the combustion chamber in order to match experimental pressure measurement and thus simulate the heat loss during compression. After compression, the effective volume history is calculated from the actual measured pressure using the adiabatic core relation in eqn. 1.12,

$$v(t) = v_o(P(t)/P_o)^{1/\gamma} \tag{1.12}$$

Mittal et al. [2007] have used a detailed chemical kinetic mechanism to simulate ignition delay times for syngas, and their results agreed fairly well with experimental pressure traces for both reactive and corresponding non-reactive using volume expansion approach. The excellent agreement between pressure traces during and after compression indicates the adequacy of the heat transfer model described above. Furthermore, computationally a study of H_2 ignition in RCM by Mittal et al. [2014] showed that zero dimensional simulations in conjunction with the approach of volume expansion performs very well in predicting ignition delay as compared with the results obtained by CFD simulations.

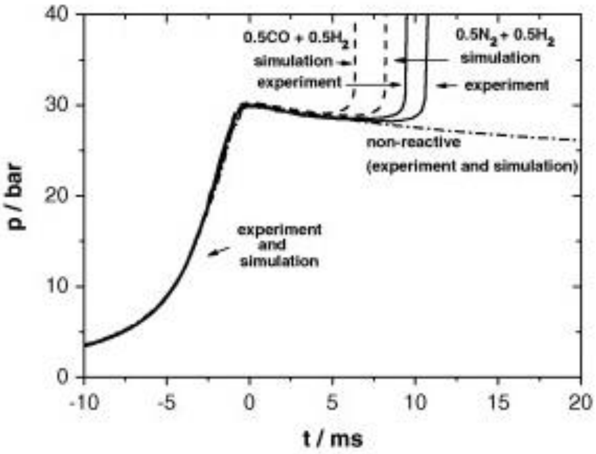

Figure 1.11 Experimental and simulated pressure records for 0.5CO/N_2 + 0.5H_2 in a mixture comprising (CO/N_2 + H_2)/O_2/N_2/Ar = 12.5/6.25/18.125/63.125 and the equivalent non-reactive composition compressed to 30 bar and 1007.0 ± 0.5 K. [Mittal et al., 2007]

During compression, radicals can start to accumulate and affect the overall measured ignition delay times (as will be well described in Chapter 3). This effect can be captured when simulations are conducted based upon initial conditions from the start of compression covering the entire experiment. Comparisons were made using dimethyl ether (DME) in Mittal et al. [2008], between (1) simulations which used the initial experimental conditions to simulate the entire compression and post end of compression processes and (2) simulation used only the post end of compression processes using end of compression as initial conditions. At higher temperatures, calculated ignition delay times using end of compression as initial conditions gave longer delay times by about 60% compared to that which used initial experimental conditions, whereas at lower temperatures the difference is only about 7%. This indicates that the technique of using end of compression as an initial condition failed to capture the effect on delay times caused by pre-reactions during compression. It is therefore recommended to simulate the entire experiment process to include compression stroke and post compression.

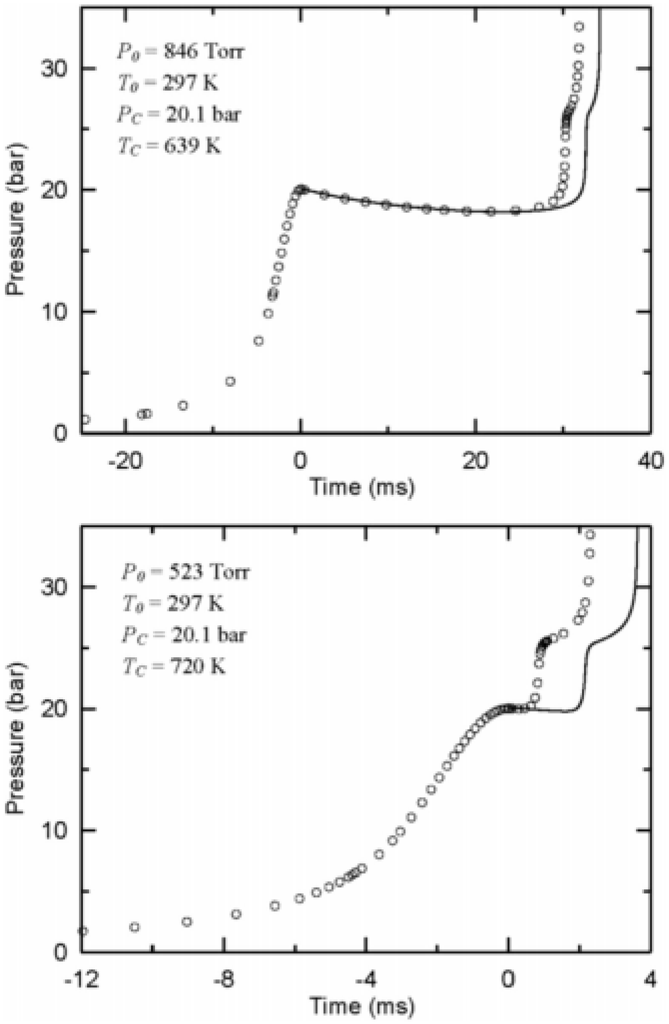

Figure 1.12 . Effect of the compression stroke on modelled pressure traces for a DME/O_2/N_2 mixture (1/4/30 M composition). Open symbols represent calculations performed considering the RCM compression stroke; lines are results obtained by initializing the calculations at the end of compression for the compressed pressure and temperature conditions listed and using the initial mixture composition. The heat loss effect is included in both calculations. [Mittal et al., 2008].

1.8 Thesis outline.

This thesis is divided into six Chapters. A brief introduction to their content is highlighted below.

- **Chapter 2** This Chapter gives a description and the operation procedures of University Leeds and University of Cape Town RCMs with their associated modifications. It also includes techniques which are used for measuring ignition delay times in RCM.
- **Chapter 3** In this Chapter, issues related to the deviation of RCM operation from ideal conditions are discussed and corrections are made for the measured delay times to account for non-ideal conditions in RCM operations and measurements using experimental data from seven different RCMs around the world.
- **Chapter 4** This Chapter presents the experimental measurements of ignition delay times for various individual fuels and their blends at different equivalence ratios and temperatures. The purpose of this work is first to test the performance of the machine after modifications by comparing the results with the existing literature results and then measurements are made for the blends of Toluene Reference Fuel (TRF) surrogate with ethanol and *n*-butanol to study the effect of alcohols on the AI behaviour of a TRF surrogate.
- **Chapter 5** This Chapter introduces a blending law which is based on the measured ignition delay times of the constituent fuels.
- **Chapter 6** This Chapter concludes this study by summarising the important findings as well as giving recommendation for future research.

CHAPTER 2: EXPERIMENTAL APPARATUS, TECHNIQUES AND MODIFICATIONS.

2.1 Introduction.

A Rapid Compression Machine is, essentially, a piston inside a cylinder. Its purpose is to rapidly compress a combustible mixture to a higher temperature and pressure at which its auto ignition characteristics can be studied. As in the present work, such machines find application in the study of engine fuels because they are a reasonable representation of a single stroke compression ignited engine. There are different RCM designs and techniques but they all have the same main objectives of rapidly compressing the mixture while producing the minimum amounts of heat and mass loss, turbulence and pressure oscillations due to piston oscillations. The operation of RCMs was discussed in Chapter 1 and results from several are compared and discussed in Chapter 3. This chapter describes the design and measurement techniques for the two RCMs used in the present work. One was a recently developed machine at the University of Cape Town (UCT-SAFL) and the other was a significantly modified version of a well-established machine at the University of Leeds. These machines are very different in a number of ways and each has its advantages and disadvantages. Together they have provided valuable insight into auto-ignition of fuels and fuel blends as discussed in Chapter 4.

2.2 University of Leeds RCM.

The Leeds RCM was initially developed at Shell Thornton Research Centre by Affleck and Thomas [Affleck et al., 1968]. It was subsequently acquired by the Chemistry Department at the University of Leeds in the 1970’s and much published work was undertaken with it by J. Griffiths et al. [e.g. Griffiths et al., 1996; Griffiths et al., 1988; Griffiths et al., 1993; Griffiths et al., 1997]. Finally, it was transferred to the School of Mechanical Engineering at Leeds where it was significantly developed from 2010 by the present author and R. Mumby as part of an EPSRC research grant [Sharpe et al., 2009].

2.2.1 Main design and configuration.

The Leeds RCM was designed and constructed based on one half of a dual opposed piston RCM from Shell Thornton research centre [Affleck et al., 1968]. Shown in Fig. 2.1(a) is a photograph of the complete system and its corresponding interior sectional view. It is a single piston horizontal machine which is pneumatically driven by compressed air and damped hydaulically. This technique is widely used by other RCMs [Mittal et al, 2006; Dracy et al., 2014; Lee et al., 2012] due to its proven ability. The Leeds RCM is approximately 2m in length and 1.5m height. It is capable of achieving a range of compression ratios between 10.5 and 13.58, attained by varying the compression stroke between 170mm-230mm. The stroke variation was achieved by adjusting the number of removable spacers which varied the length of the hydraulic chamber and consequently the initial volume before compression.

The machine consisted of three main sections, A: The driving air reservoir, B: The hydraulic oil chamber and C: The combustion cylinder and chamber. These sections were interconnected by a piston assembly.

Each of these sections and piston assembly are discussed below.

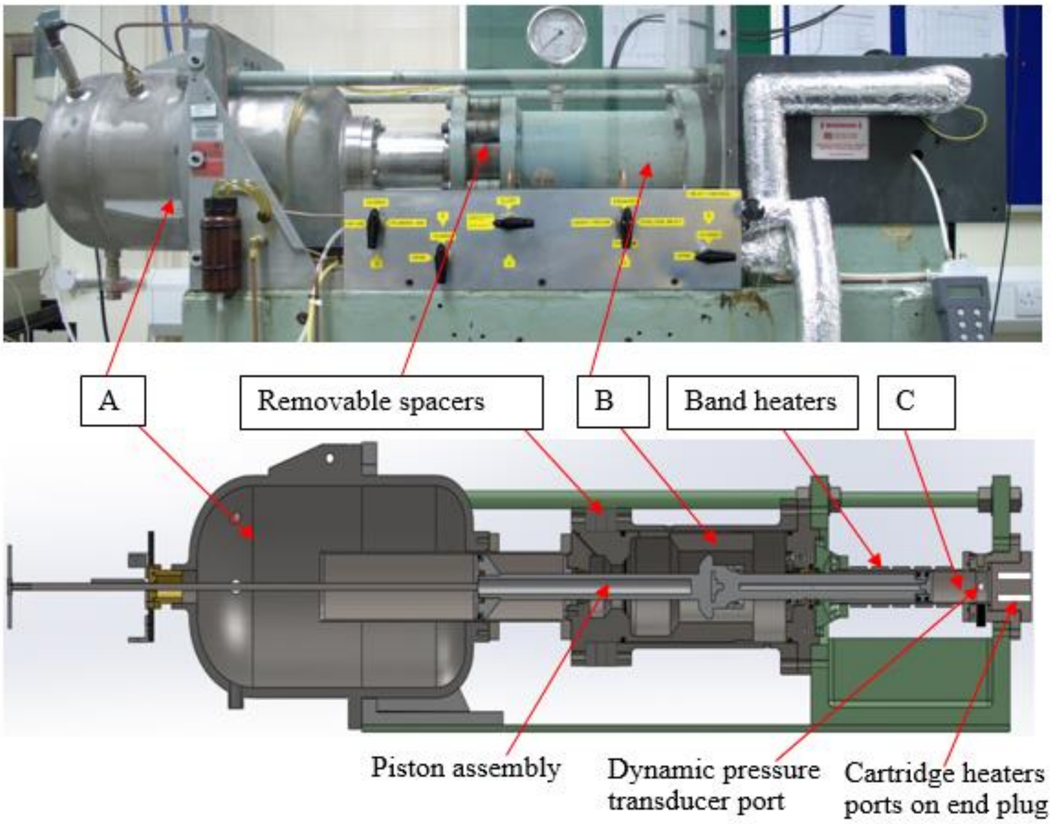

Figure 2. 1. University of Leeds RCM showing main sections.

2.2.2 Driving air reservoir.

The piston was driven and held at its final position by compressed air from the driving air reservoir. The reservoir was capable of handling up to 2.0 MPa, but in practise a driving pressure of 1.4 MPa was used. This is because higher pressures would exceed the piston holding force and cause the piston to move before firing. The reservoir was connected to two main pressure line feeds; one was the low pressure from the compressed laboratory air (limited to 0.7 MPa) and the other was the high pressure from a compressed air tank (regulated at 2.0 MPa). A pressure relief valve was put in place and was set at the activation pressure of 1.9 MPa.

2.2.3 Hydraulic oil chamber.

The hydraulic oil chamber section, shown as section B in Fig. 2.1, was between the driving air tank and combustion chambe. This was used to hold the piston in place before firing and it was also used for piston damping. Using the hydraulic oil, the high speed piston assembly was damped through the use of a damping ring and groove mechanism, as shown in Fig. 2.2. In this mechanism as the damping ring enters the damping groove, the small volume of oil that is trapped between the ring and groove is highly compressed and the pressure that is generated in the hydraulic oil acts as the transfer of kinetic energy from the moving piston rod and the piston is damped and brought to a halt. The precise machined clearance between the damping ring and groove is vital for the fast and smooth deceleration, this clearance is designed to give progressive venting of the hydraulic oil back to the oil reservoir at a rate which gives fast and uniform piston decelaration.

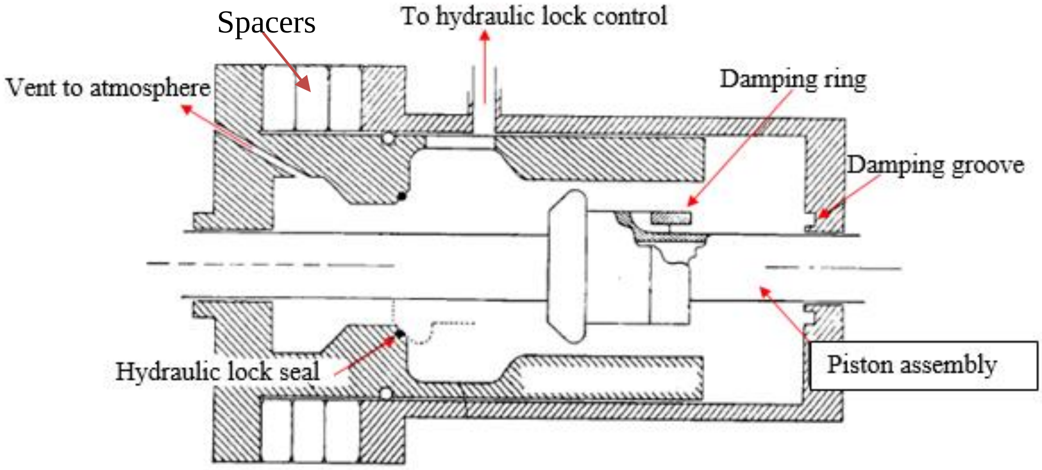

Figure 2.2. Sectional view sketch of Leeds RCM showing piston damping mechanism.

2.2.4 Combustion cylinder and chamber.

The combustion cylinder and chamber, shown as section C in Fig. 2.1 and detailed in Fig. 2.3, were both made of stainless steel with the cylinder having a bore diameter of 46 mm and 228 mm length; and a stepped combustion chamber having a diameter of 44.5mm and 19.5mm length. The combustion chamber was designed to withstand high pressure generated during combustion and had ports for pressure transducer and gas inlet/outlet. Special care was taken in design of gas inlet/outlet port to minimize the dead volume in the combustion chamber by using a poppet valve. The end plug of the combustion chamber was made of mild steel and had six ports machined for inserting cartridge heaters for heating the combustion chamber.

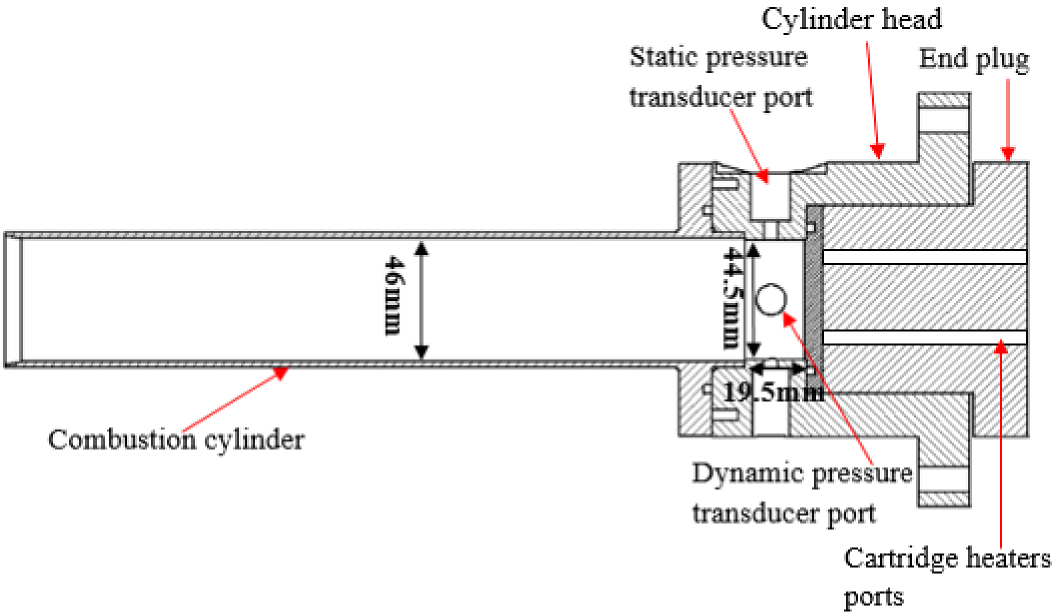

Figure 2.3. Combustion cylinder and chamber detail.

2.2.5 The piston assembly.

The piston assembly connected between the three main sections of the Leeds RCM. Shown in Fig. 2.4 are different parts of the piston assembly. It was machined from stainless steel and had two ends with a damping ring in the middle. One end was the driving piston which was in contact with the driving compressed air and the other was the driven/compression piston which was used for compressing the mixture in the combustion chamber. The ratio between the driven and drive piston diameters was 1:2 thus allowing the driving air pressure needed to hold the piston assembly after compression to be a factor of 4 smaller than the pressure in the combustion chamber.

The compression piston was fitted with Teflon seals to ensure excellent sealing during compression, the driven/compression piston head was made of aluminium.

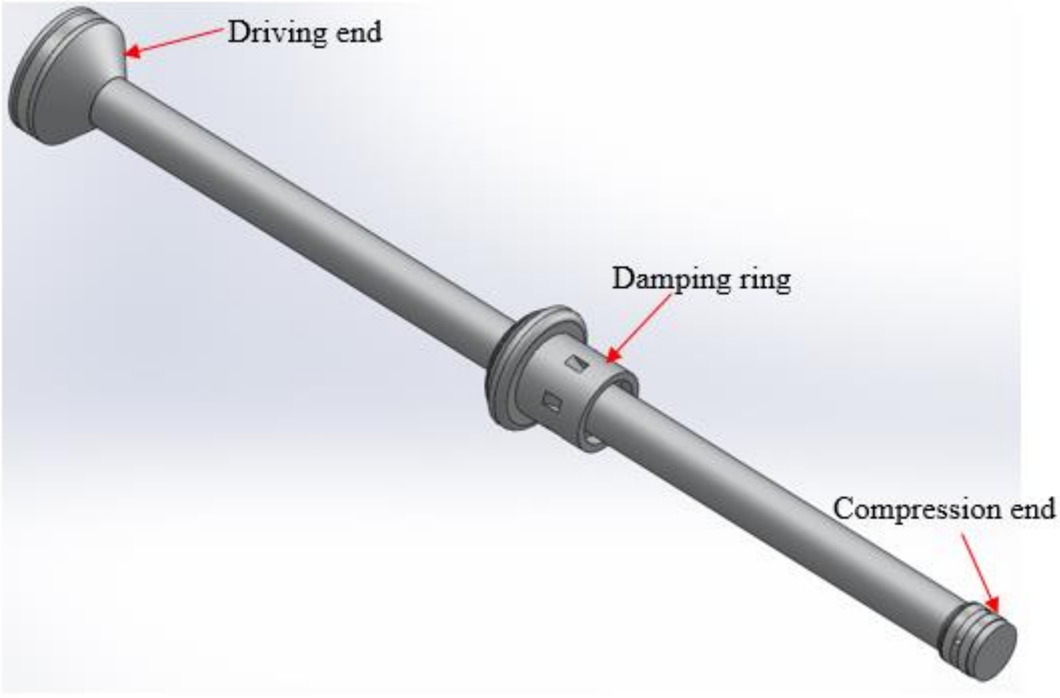

Figure 2.4. Piston rod assembly.2.2.6 Mixing Chamber.

To avoid errors caused by inconsistent mixture preparation in the combustion chamber, a separate fuel mixing chamber was used. In the mixing chamber the liquid fuel is pre-vapourized and mixed with the oxygen and other diluents to make a homogeneous reactive mixture, the use of the mixing chamber increases efficiency, control as well as safety. For reasons of compactness, a constant volume, high pressure system was used as shown in Figs. 2.5 and 2.6. This system was developed by the present author and R.Mumby, stress analysis was first conducted during designing to ensure safe and proper operation, calculations are shown in appendix A. The chamber had a cylindrical shape with an cap at each end, the two caps were connected to the middle turbular part with external restraining bolts. The end plates were made from 303 (EN 1.4305) stainless steel and a turbular section from 316L (EN 1.4404) stainless steel. Ports were made for gas inlet, fuel injection, pressure transducer and mixture outlet.

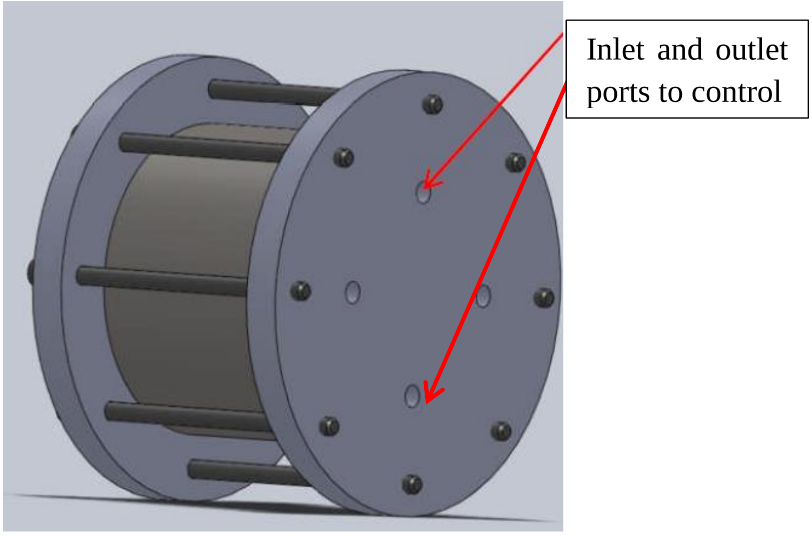

Inlet and outlet ports to control

Figure 2.5. Fuel mixing chamber (front view).

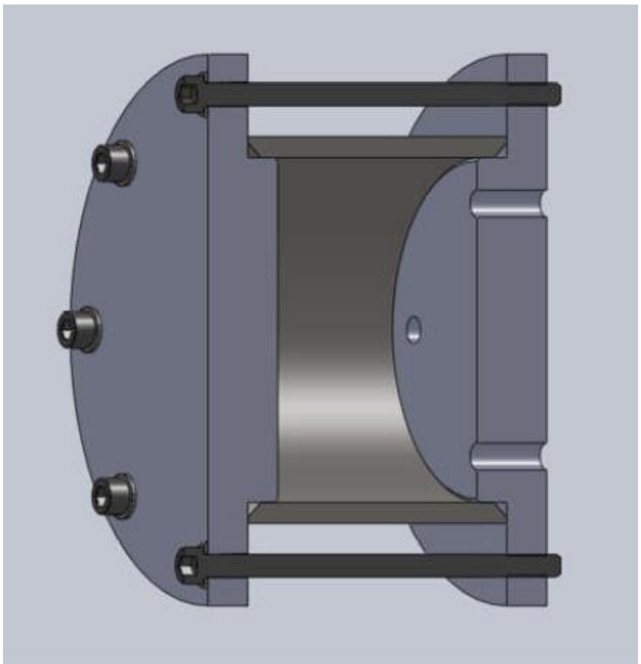

Figure 2.6. Fuel mixing chamber (cross section view)

2.2.7 Auxiliary equipments.

2.2.7.1 Pressure instrumentation.

The pressure measurement was made by dynamic or static pressure transducers depending on the requirements. These were located, respectively, on the side and top of the combustion chamber as shown in Fig 2.3. Initial pressure in the combustion chamber was measured by a static pressure transducer COMARK C9557 with a measuring range of 0 MPa to 0.8 MPa absolute pressure. For measuring pressure in the combustion chamber during and after compression, several dynamic pressure transducers were investigated because of the importance of accurate dynamic pressure recordings, but with the complication of large temperature variations. This is discussed in Section 2.2.9.1. The piezoelectric dynamic pressure transducer Kistler 6045A was chosen to be used in the Leeds RCM. This transducer was mounted flush to the wall of the combustion chamber and could withstand a maximum pressure of 25 MPa and operating temperatures of -20^{o}C to 350^{o}C. The pressure inside the mixing chamber was measured by a static pressure transducer UNIK 5000 with maximum pressure of 0.4 MPa. Pressure in the driving air reservoir was measured by a RS (3100 series) pressure transducer with a maximum pressure of 2.5 MPa. All the static pressure transducers were connected to the control box and wired to digital display units which had measurement resolution of 0.0001 MPa. The dynamic pressure transducer in the combustion chamber was connected to the charge amplifier Kistler 5015 which converted the generated charge into voltage (0-10V). The data acquisition (DAQ) board NI PCI-6110 which featured a dedicated analogue-to-digital converter (ADC) for each channel, was used to digitise the voltage from the charge amplifier. This DAQ had 12 bit resolution and therefore with sensivity set at 20bar/volt it gave smallest measurable increment of 0.00244 volts and $4.88*10^{-4}$ MPa. Sampling was performed at 50 kHz.

2.2.7.2 Temperature instrumentation.

To ensure uniform initial heat distribution within the combustion cylinder and chamber prior to compression, different heating arrangements were tried and the optimum was chosen. This is discussed in Section 2.2.10. The combustion cylinder was heated by 5 different band heaters each with 375W power and a cylinder head heated by 6 cartridge heaters fitted circumferentially in the end plug with 10W/m each.

The lines that take the fuel from the mixing chamber to the combustion chamber are 4mm diameter stainless steel pipes. These pipes were wrapped up with a heating cable to ensure no fuel condensation occurs along the line. The RS constant wattage heating cable with a power of 20W/m was used. These heaters were capable of heating up to 200^{o}C. A flexible polyethylene pipe insulation was also used for increased efficiency. The mixing chamber was heated by a single Mica band heater fitted around its tubular section with 2 KW power.

The initial temperature in the combustion cylinder and chamber prior to compression, and that of the mixture pipeline were measured using K-type thermocouples each placed on the surface of the metal which it measured. It was not possible to measure transient temperature during compression and combustion. Instead, this was estimated as discussed in Section 3.2.2 of Chapter 3. The temperatures were displayed and controlled using PID temperature controllers.

2.2.7.3 Piston displacement measurements.

To accurately measure the displacement of the piston assembly during operation, several methods and approaches were considered as discussed in section 2.2.11. A class 2 laser which was targeted, at a slight angle, onto a reflecting circular plate attached to the piston extension rod, was chosen as a suitable method, as shown in Fig. 2.7. The displacement of the reflected beam was measured by a 2D linear displacement laser sensor, model LK-G82 from Keyence and recorded at a sampling rate of 20 KHz by its own independent control unit. This converted the digitally measured displacement to analogue output of +/- 10v which can be read by LabView VI. This system had a measurable range of 30 mm and a resolution of 0.6 mm.

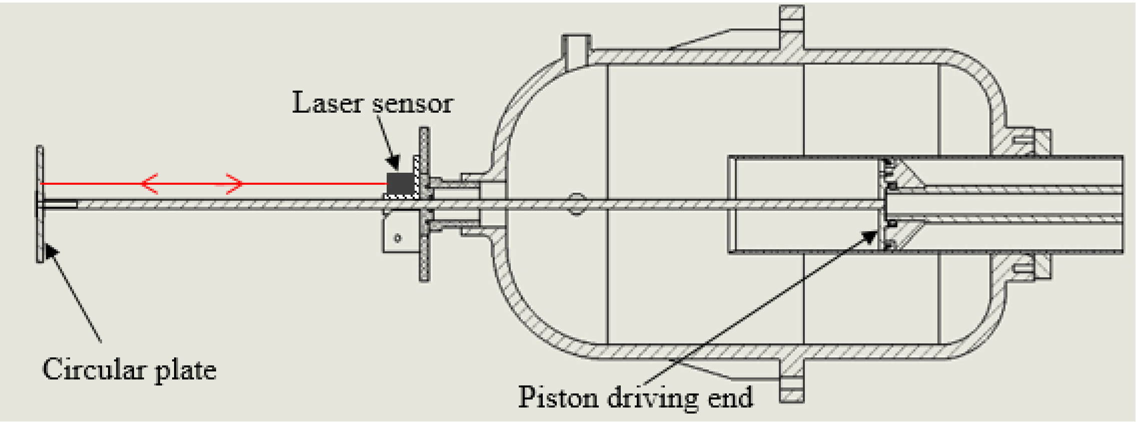

Figure 2.7. Piston displacement measurement system.

2.2.8 Mixture preparation and machine operation.

Fuel-air mixtures were prepared in a separate mixing chamber (Section 2.2.6). The mixing chamber was first heated to a pre-determined temperature to ensure a test fuel would be fully vapourised. For most fuels tested in this work this temperature was typically 80^{o}C. This was followed by a purging of the mixing chamber to remove all residuals by flushing it with pressurised laboratory air for about 2 minutes. The chamber was then filled with laboratory air up to 0.2 MPa and finally evacuated to less than 0.002 MPa. This process was repeated twice using dry air to ensure that there was less than 0.01% residual gas from the previous mixture. The temperature within the chamber and volume of liquid fuel injected was pre-determined so that fuel partial pressure was less than its vapour pressure; this was done to ensure that the liquid fuel was fully vapourized.

An excel spreadsheet was created to perform the partial presure calculations based on the type of fuel and conditions. Shown in Fig. 2.8 is the variation of pressure with temperature for a stoichiometric mixture of *iso*-octane and air. The solid line shows the *iso*-octane vapour pressure at different temperatures and the dotted horizontal line is its partial presure when the total mixture pressure was 0.2 MPa. The dashed vertical line is at 80^{o}C which is the typical mixture preparation temperature in the present work. The plot shows that the fuel is potentially fully evaporated down to a temperature of about 40^{o}C. The pre-determined liquid volume of fuel was injected into the mixing chamber under partial vacuum through a stainless steel Luer-lok inlet. After fuel injection, the increase in pressure (the fuel partial pressure) was measured and was typically found to be within +/- 0.0001 MPa of that expected from a partial pressure calculation. After fuel injection, the gaseous components, usually comprising various amount of N_2, CO_2, Ar and O_2 as discussed in Section 3.2.4. in Chapter 3, were carefully introduced into the mixing chamber using the high precision needle valves and the fuel mixture was left in the chamber for about 2 hours for proper mixing before it was used.

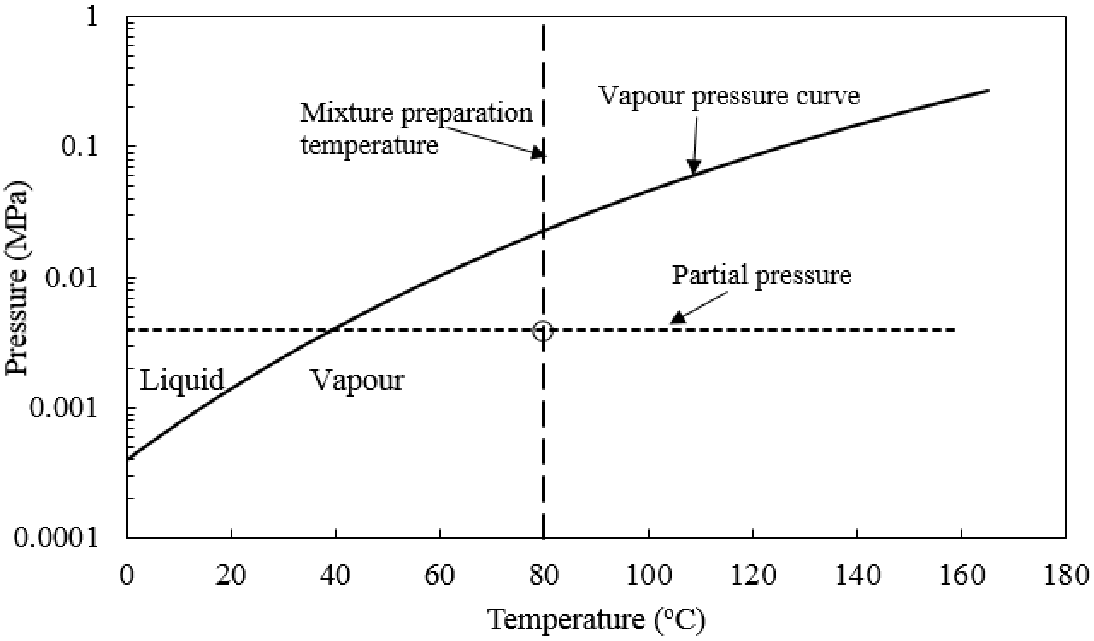

Figure 2.8. Vapour pressure and partial pressure for stoichiometric *i*-octane in the mixing chamber, showing mixture fully vapourised at preparation temperature 80^{o}C.

Once the mixture was prepared, the RCM combustion cylinder and chamber walls were heated to the pre-determined initial pre-compression temperature. Similar to the mixing chamber, the combustion chamber was flushed of all residual gas from the previous experiment by pressurising the chamber with laboratory air up to 0.2 MPa and then evacuated to less than 0.002 MPa to ensure less than 0.01% residual gas. The pre-determined amount of reactant mixture from the mixing chamber was introduced into a combustion chamber through a high precision needle valve.

The hydraulic oil was then pumped into the oil chamber, using a hand pump, up to 4.0 MPa. This ensured the piston assembly (shown in Figs 2.1 and 2.4) was held in its initial position before firing. The driving air was next fed into the driving reservoir in two stages. First, laboratory compressed air was introduced at the available maximum pressure of about 0.7 MPa. This was then topped up with compressed nitrogen gas to yield a total driving pressure of 1.4 MPa.

Once the mixture had been introduced into the combustion chamber and attained the required temperature, and once the hydraulic and driving pressures were as required, the machine was fired by use of a triger button which was electrically connected to the solenoid valve in the hydraulic oil chamber. This vented the hydraulic oil back into the hand pump, thus reducing its pressure/force. Once the driving force exceeded the hydraulic oil force, the piston was driven forward to compress the mixture in the combustion chamber. A trigger signal was also sent to the DAQ card for collection and recording of pressure and piston displacement data.

A special labview virtual instrument (VI) was produced by the present author to collect, display and save the pressure measurements within the combustion chamber during and after compression. Also, this VI collected and saved data from piston displacement measurements, described in section 2.2.7.3. Shown in Fig. 2.9 is a block diagram for the VI used and Fig. 2.10 is the user interface with typical results obtained from stoichiometric *iso*-octane compression at end of compression pressure 2.0 MPa. For the top plot in Fig. 2.10, the white line shows the pressure measurement while the red line is the piston displacement, and the bottom plot shows the rate of pressure change, the vertical axis measures the magnitude (pressure, displacement and rate of pressure change in this case) and the horizontal axis measures time.

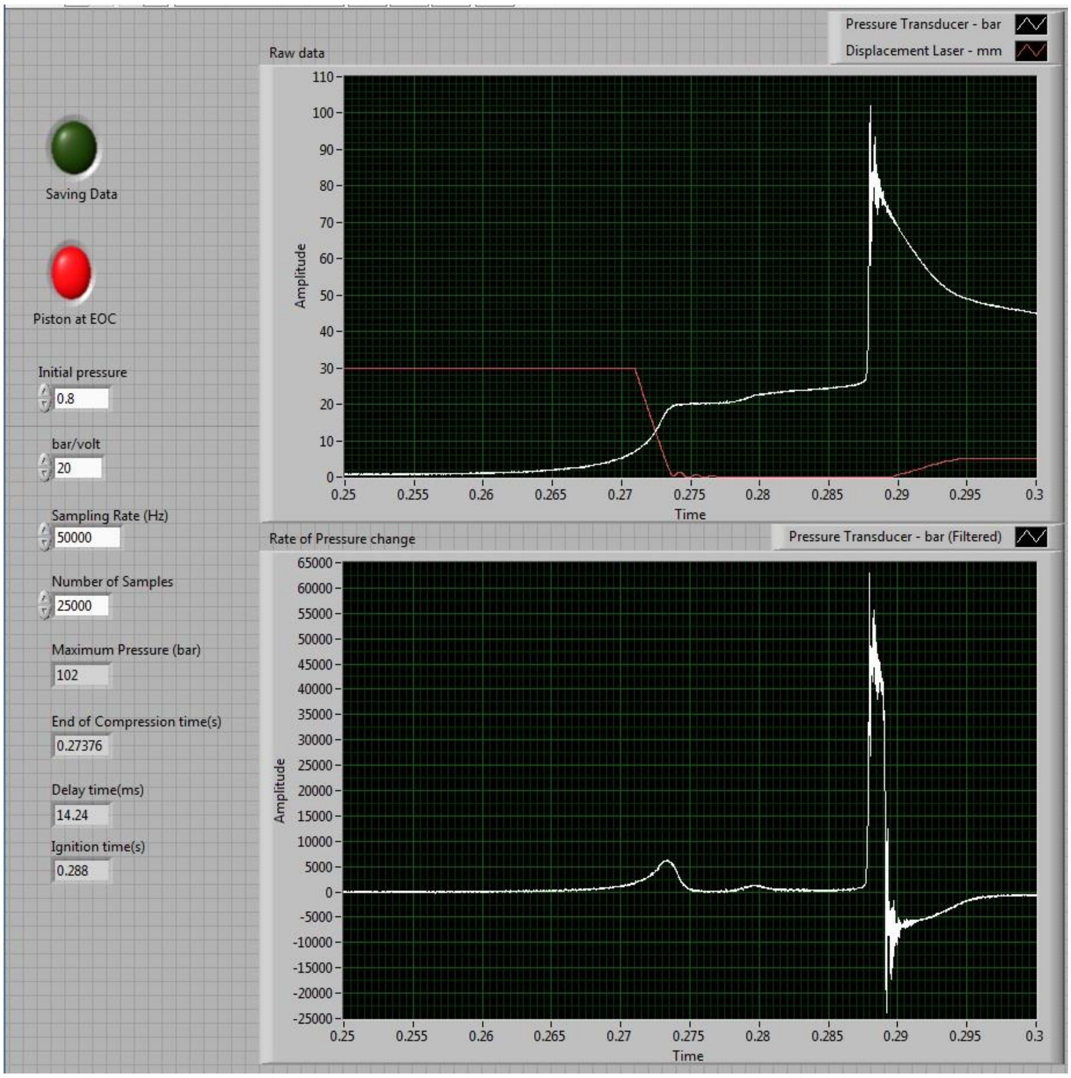

Initial pressure 0.8

bar/volt 20

Sampling Rate (Hz) 50000

Number of Samples 25000

Maximum Pressure (bar) 102

End of Compression time(s) 0.27376

Delay time(ms) 14.24

Ignition time(s) 0.288

Figure 2.9. Typical pressure trace for stoichiometric *iso*-octane captured by Labview VI.

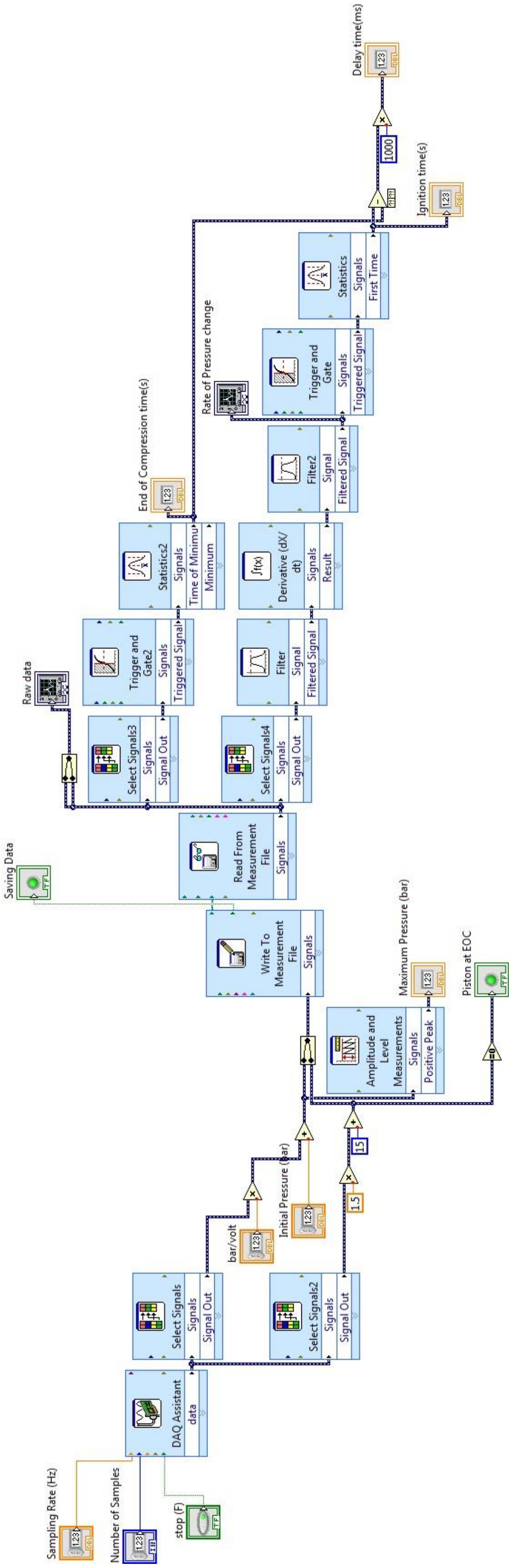

Figure 2.10. Block diagram for the Labview VI used for data collection in Leeds RCM

2.2.9 Modifications made to Leeds RCM during the course of this research.

2.2.9.1 Pressure measurements and thermal shock error protection.

The accurate measurement of pressure in the RCM can not be over-emphasised. Pressure results are used to derive the temperature of the fuel-air mixture in the combustion chamber as well as ignition delay times as will be described in Chapter 3. Measurements of pressure histories during and after compression in the RCM usually use dynamic pressure transducers, their preference comes from high frequency response, accuracy, durability and repeatability. The Leeds RCM uses a piezoelectric dynamic pressure transducer. This type of transducer uses special piezoelectric crystals which generate charge when force is applied, the charge obtained is then amplified and converted into voltage using a charge amplifier. The crystals are properly packed in the stainless steel housing and use a thin stretched diaphragm as its sensing face. In a steady thermal condition, the sensitivity to change of these transducers is very small (less than 1%), but when exposed to very high rates of temperature changes the accuracy is highly degraded. The sudden change of temperature imposes thermal stresses on the transducer diaphragm and its housing, and in response it results in momentary deformation/expansion which eventually lessens the preload force on the crystals, causing a negative signal output and hence gives an erroneous pressure signal.

Previous experiments from RCMs by Mittal et al. [2013] have shown that a thermal shock error of 0.5 MPa was experienced at the end of compression when nitrogen was compressed. This is about an 18.5% reduction in pressure from when the transducer was protected from thermal shock. Similar results have been reported in engines by Lee et al. [2005], Randoplh [2010] and combustion bombs by Dibbern et al. [2009].

To ensure accurate pressure measurements, it is therefore vital to evaluate the amount of thermal shock error in the present RCM. Experiments were therefore conducted to measure the effects of different thermal shock protections on pressure transducer measurements. All experiments were conducted using air at atmospheric initial conditions and fixed compression ratio of 13.58. Temperature gradients of up to 110K/ms are achieved during compression. Four different commonly used techniques for thermal shock protection were tested at these conditions. These are recess mounting, silicon grease, Room Temperature Vulcanizing (RTV) silicon rubber, and vinyl tape. To obtain accurate results, pressure transducers were first calibrated using two reference pressure transducers 6052C and 6045A from Kistler, these transducers have very low thermal shock error of less than +/- 1%. The charge amplifier Kistler 5015 was sent to the manufacturer for calibration. A total of four different Kistler pressure transducers (601A, 701A, 7005 and 6061B) were tested. These were the available transducers in the laboratory store commonly used in different rigs including RCM. 6061B is a water cooled transducer designed to minimize the thermal shock error by cooling the crystal housing during measurements. A 7005 has a reinforced diaphragm to enable measuring higher pressures of up to 60 MPa, 601A has very high natural frequency making it suitable for applications where vibrations are high and 701A has high sensitivity for increased accuracy. These were tested simultaneously using specially designed end plugs in which they were mounted.

Two types of end plugs were designed and manufactured, one for flush mounting and the other was for recess mounting as shown in Figs. 2.11 and 2.12. Dimensions of the slots are based on the size and shape of the transducers tested.

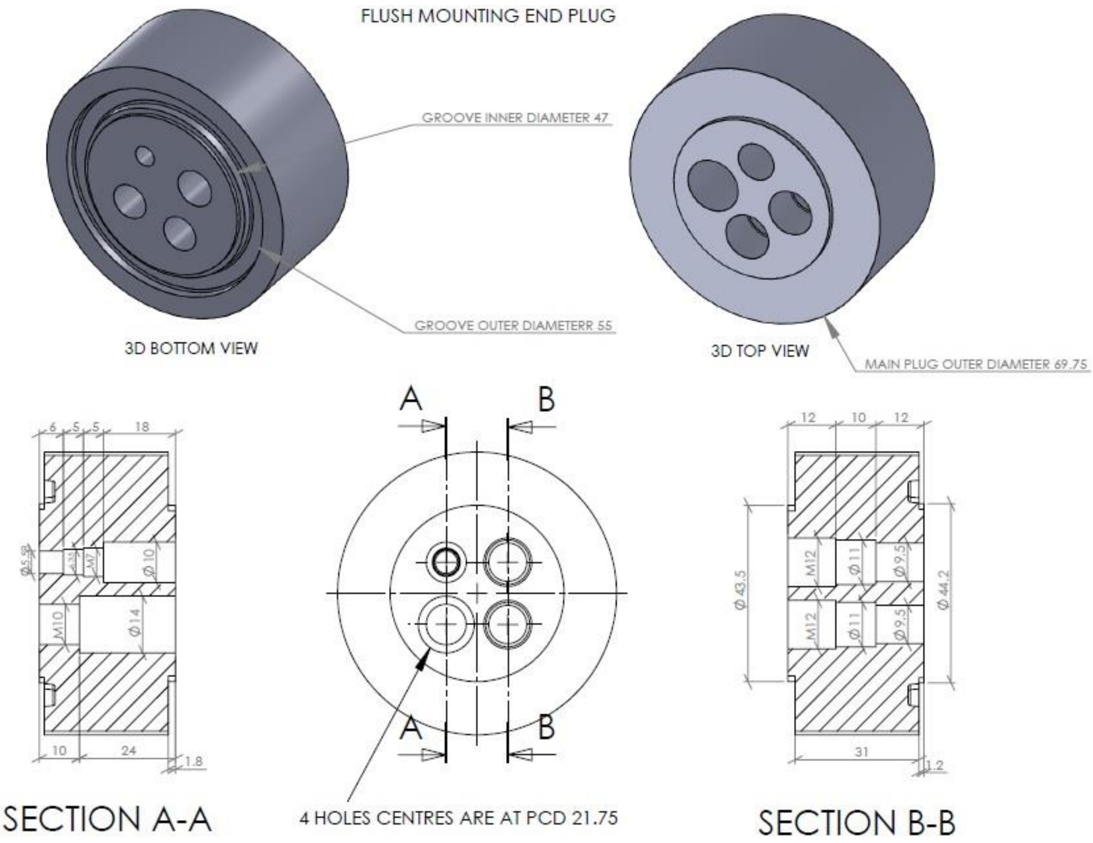

Figure 2.11. End plug for flush mount pressure transducers

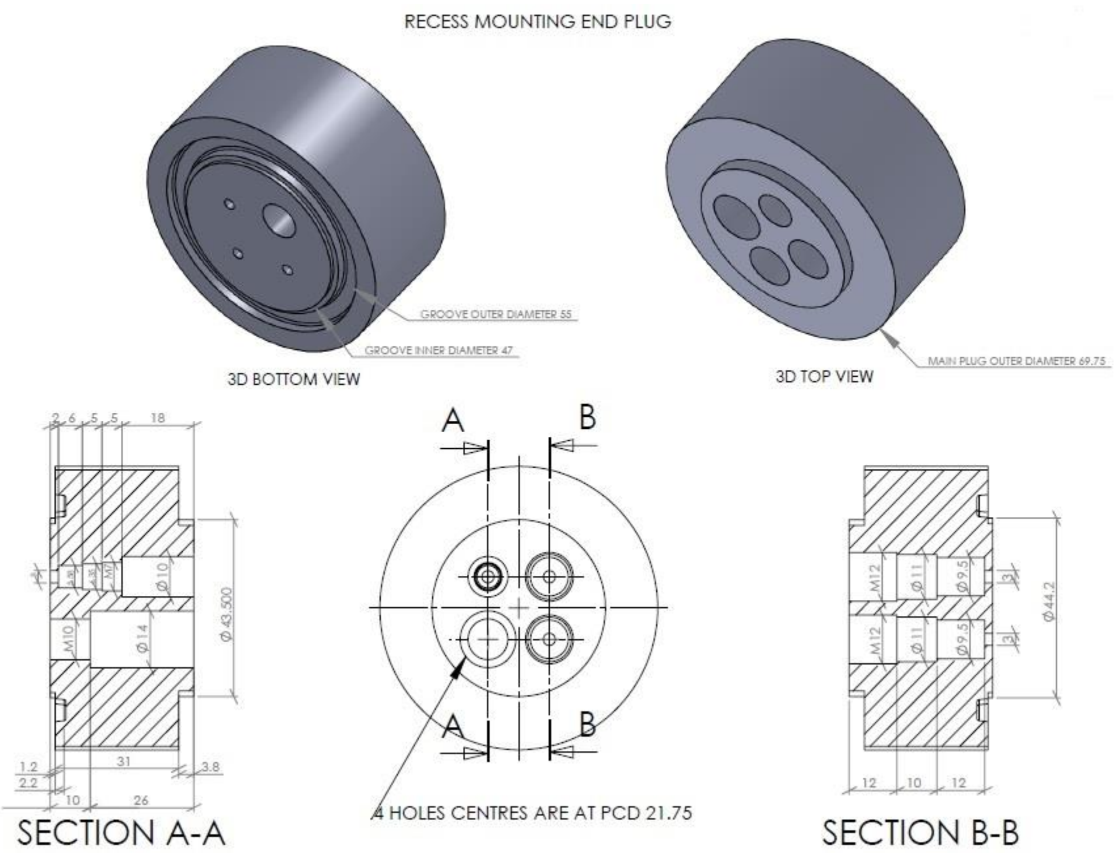

Figure 2.12. End plug for recess mounted pressure transducers.

1. Thermal shock test.

The initial test was conducted to check the amount of thermal shock error for each transducer. The pressure measurements were made simultaneously with all transducers flush mounted using the end plug in Fig. 2.11. Shown in Fig 2.13 are the pressure readings for the five transducers (including reference transducer) when air was compressed from an initial pressure of 0.1 MPa and temperature of 293K. The time zero in Fig 2.13, and for all other similar plots in this section, denotes the time when the piston reached the end of compression (EOC). In this test, the magnitude of thermal shock error was measured by the pressure difference between the measurements with the reference transducer (6045A) and the one being compared. Values are shown in Fig. 2.14.

Transducers 601A and 701A show the maximum effect to the thermal shock, they record the lowest end of compression pressures of all the transducers tested, a difference of 0.11 MPa (3.6%) is seen at the end of compression. The water cooled 6061B shows the least deviation from the reference transducer 6045A. Transducer 7005 recorded less pressure drop at the end of compression than 601A and 701A. However, a sharp pressure drop was seen after the end of compression, this could be due to the lower thermal response of its reinforced diaphragm. All transducers showed reduced pressure difference after the compression which indicates their recovery from the thermal shock effect as time progressed.

With the exception of the water cooled transducer 6061B, all other pressure transducers were noticeably affected by the thermal shock due to the very rapid temperature rise during compression. Different methods commonly used for thermal shock protection were investigated by the present author and are reported in the following Sections.

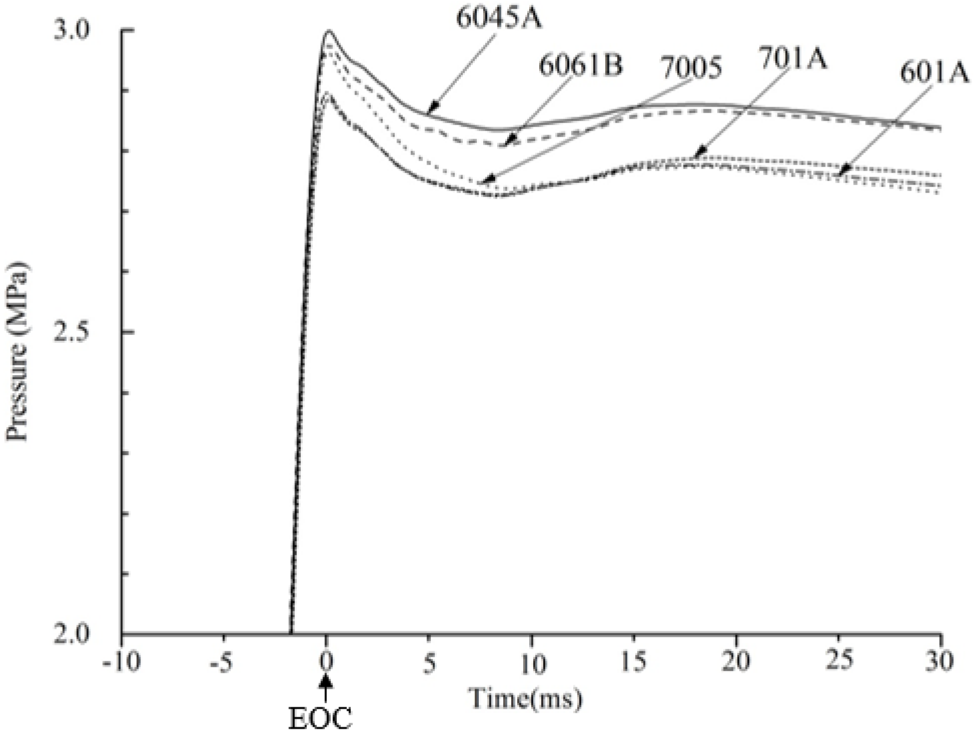

Figure 2.13. Air pressure traces in the RCM during and after compression. Measurements were made using five different pressure transducers simultaneously.

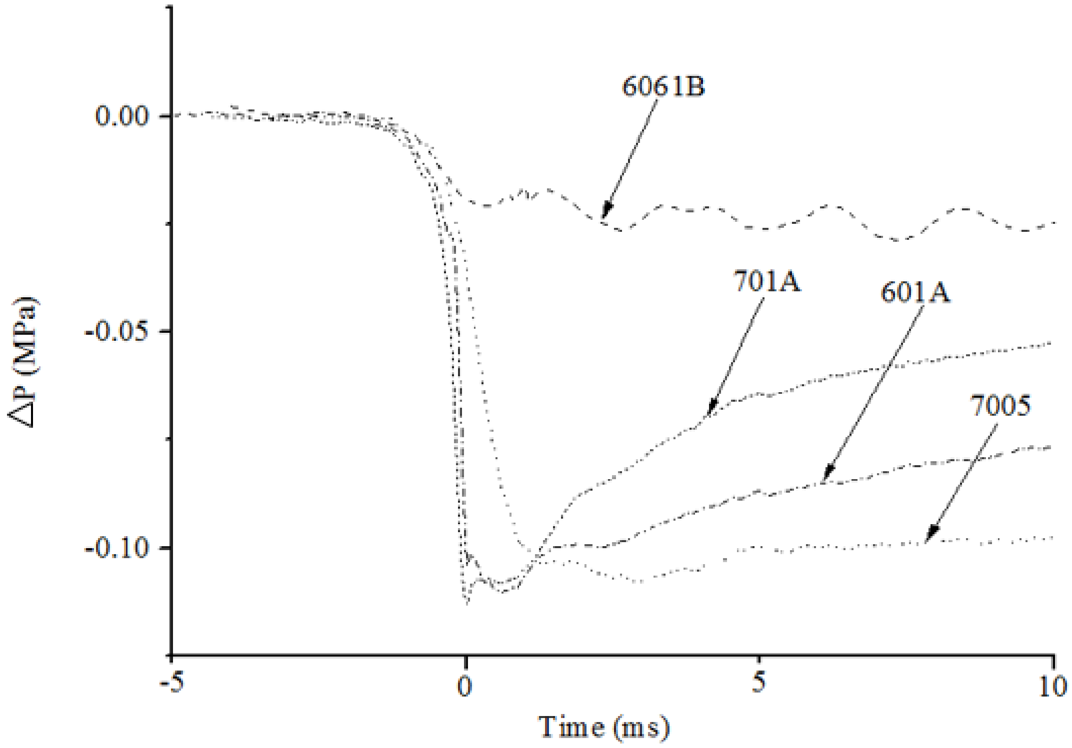

Figure 2.14. Magnitude of thermal shock error using pressure difference between the reference, 6045A and that under test.

2. Flush mounting and surface coating method.

In this method of thermal shock protection, the pressure transducers were flush mounted and a coating was applied on the face of the transducer diaphragm. Vinyl tape and RTV silicon rubber have been suggested by manufacturers as one of the methods for thermal shock protection because they delay the thermal effects for the duration of measurements [PCB piezotronic, 2015], it is most relevant for short duration measurements such as in shock tubes and RCMs. In this work, a vinyl tape and a 1mm coating of Loctite 5399 RTV rubber were applied separately over the face of flush mounted pressure transducers and the pressure measurements were taken. Shown in Figs. 2.15 to 2.18 are pressure traces for the different transducers when mounted flush with the chamber walls, with and without the protective coatings over the transducer diaphragm. The effect of the vinyl tape is minimal for the 601A and 701A transducers in Figs. 2.15 and 2.17. However, results for the 7005 in Fig. 2.18 shows a slight increase in pressure at the end of compression when the tape is present. Interestingly, the vinyl taped water cooled transducer 6061B recorded lower pressure at and after the end of compression compared to its corresponding non-taped measurements. This suggests that, although vinyl tape can protect the transducer diaphragm against thermal shock, it also makes transducers less sensitive to rapid pressure change as seen in Fig 2.17 for the 6061B. This effect negates the thermal shock protection advantage. There was no change in recorded pressure for 601A and 701A when a coating of Loctite 5399 was applied whilst for 7005 there was a slightly higher pressure reading with the surface coating. Therefore, with the current RCM set up, using flush mounted transducers tested in this work, a vinyl tape and Loctite 5399 coatings have very minimal effect in protecting transducers 601A, 701A and 6061B against thermal shock. Transducer 7005 was well protected when coated with vinyl tape, a pressure increase of 0.12 MPa from its non-protected recordings was obtained at the end of compression. However, an abrupt pressure drop within 4 milliseconds after the end of compression was seen, which suggests that the vinyl tape could only delay the heat flux reaching the transducer for a very short time and thus cause only a temporary thermal protection.

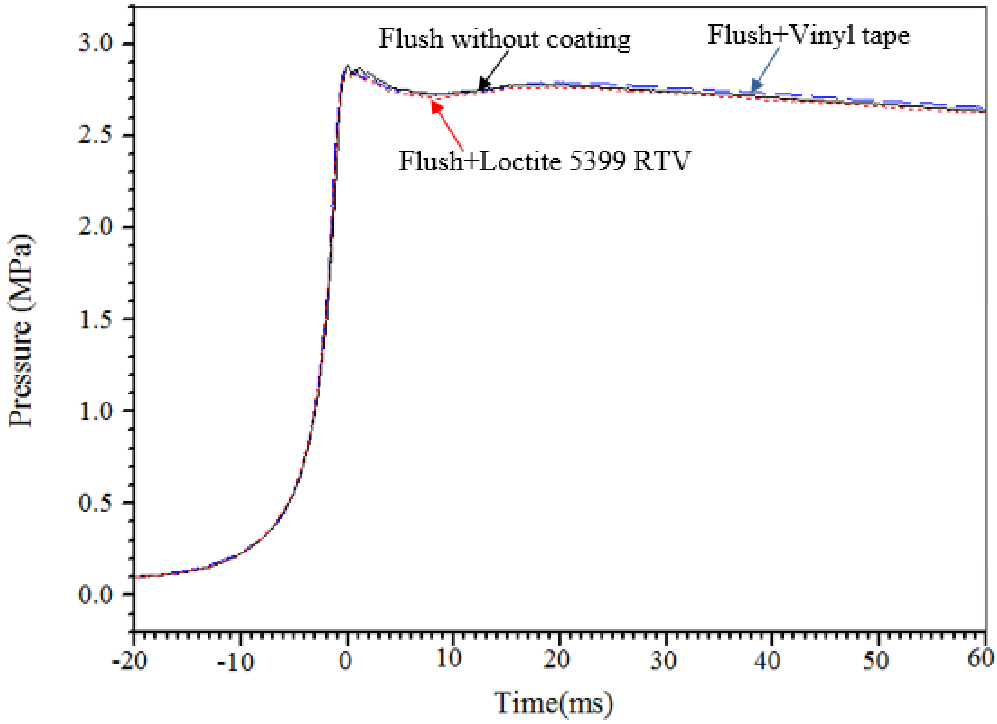

Figure 2.15. Pressure traces for air with atmospheric initial conditions using pressure transducer 601A flush mounted, with and without coatings

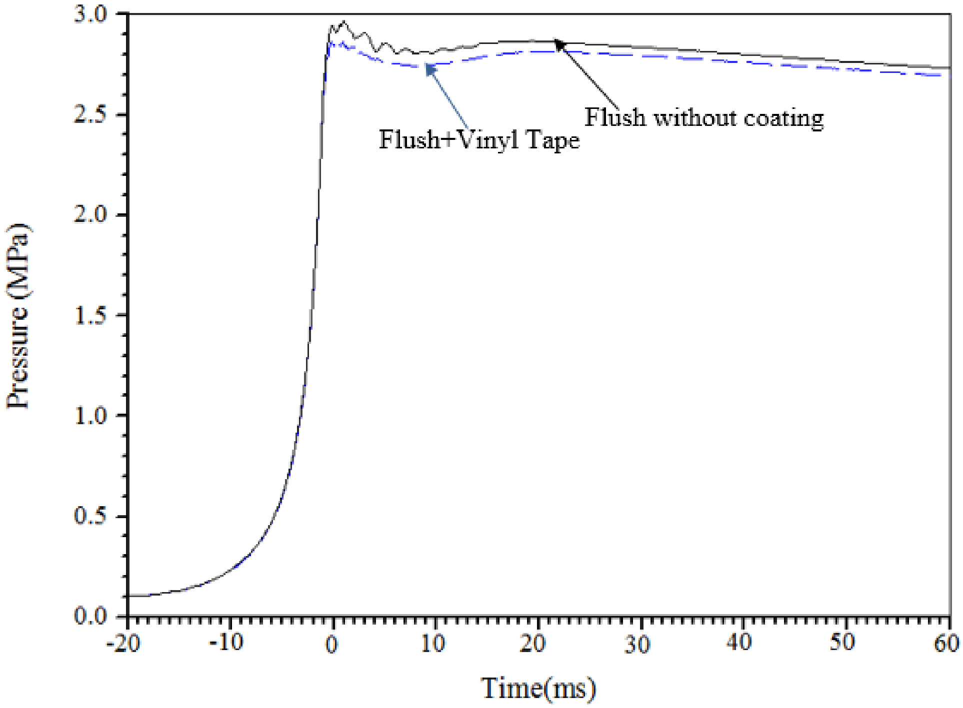

Figure 2.16. Pressure traces for air with atmospheric initial conditions using pressure transducer 6061B flush mounted, with and without coatings.

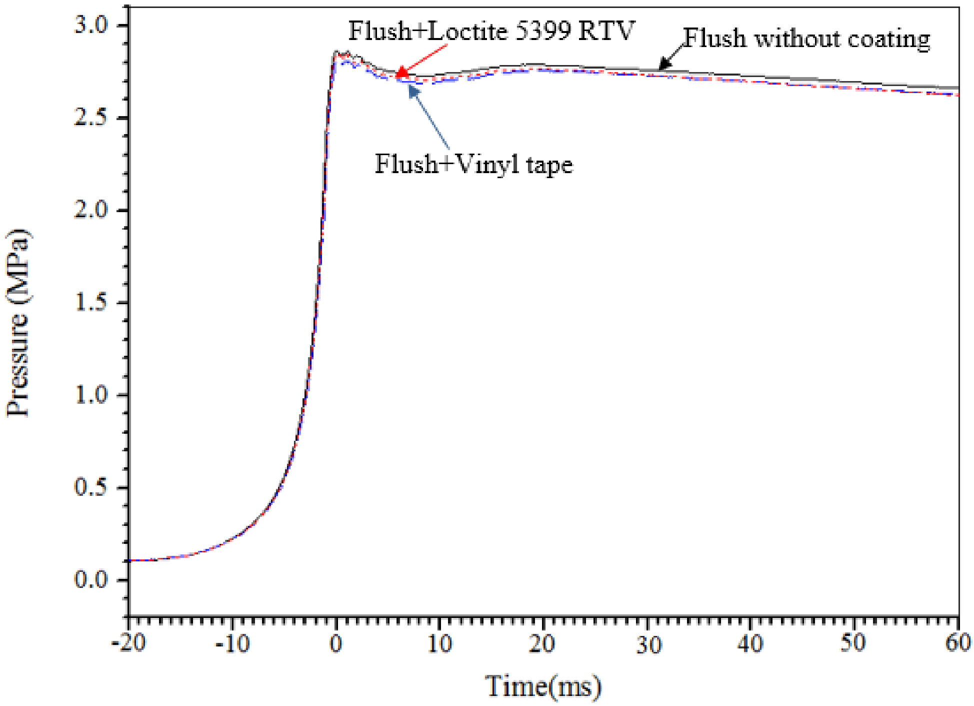

Figure 2.17. Pressure traces for air with atmospheric initial conditions using pressure transducer 701A flush mounted, with and without coatings.

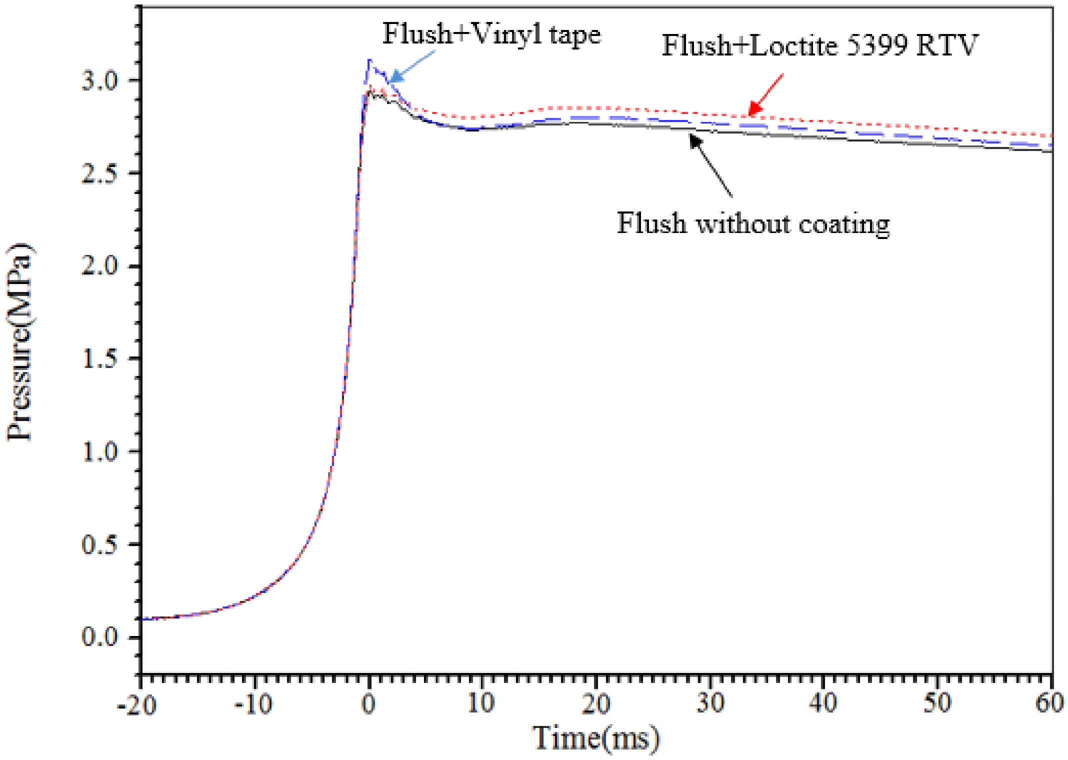

Figure 2.18. Pressure traces for air with atmospheric initial conditions using pressure transducer 7005 flush mounted, with and without coatings

3. Recess mounting and silicon filling method.

The recessed mounting technique involved mounting a pressure transducer in a recessed position from the wall of the combustion chamber, the aim is to protect the transducer diaphragm from coming into contact with hot gases within the combustion chamber. It is a common method especially used in engines where the transducers are repeatedly exposed to high temperature flames. A combination of mounting a pressure transducer in a recess position and filling a recess hole with a silicon grease or rubber has also been suggested by manufacturers [PCB group, 2015].

In this work, tests were conducted with three pressure transducers (601A, 701A and 7005) using the recess mounted end plug shown in Fig. 2.12. Three types of silicon fillings were tested, these were 2 pack RTV, Loctite 5399 RTV and silicon grease. Shown in Figs. 2.19-2.21 are the pressure traces for recessed mounted transducers when with and without RTV coatings. Also for comparison, pressure records for flush mounted transducers without coating are included.

For all transducers tested, the recess mounted measurements, with or without coatings, recorded lower pressures compared to when flush mounted. Application of both RTV coatings (Loctite 5399 and 2 pack) in the recess mounted transducers reduced the transducer's sensitivity and lead to measurements that were significantly lower than those measured without coating. However, when silicone grease was applied, and pressure records were compared with those of recess without coatings, a pressure increase of 0.1483 MPa for 601A and 0.19 MPa for 7005 was obtained. This increase is equivalent to about 55% recovery from pressure drop caused by thermal shock as was shown in Fig 2.14. There was a slight pressure increase for 701A compared to when recessed and non-coated.

Therefore, in the current RCM set up, transducers 601A and 7005 can be fairly well protected from thermal shock effects using the recess mounting technique together with the silicon grease. However, the new Kistler pressure transducer models, such as the one used as the reference in this work (6045A), have better thermal shock error properties compared to those tested in this work even with the different protection methods tried, thus transducer 6045A was acquired from Kistler and it was used for the remainder of this work.

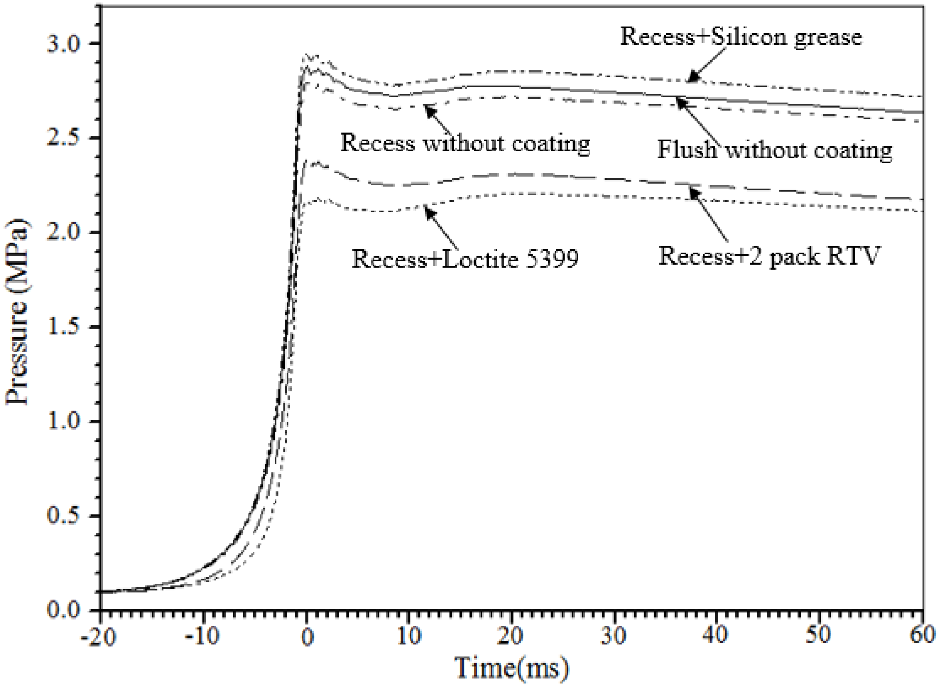

Figure 2.19. Pressure traces for air with atmospheric initial conditions using pressure transducer 601A when recess mounted with and without coating, and when flush mounted without coating.

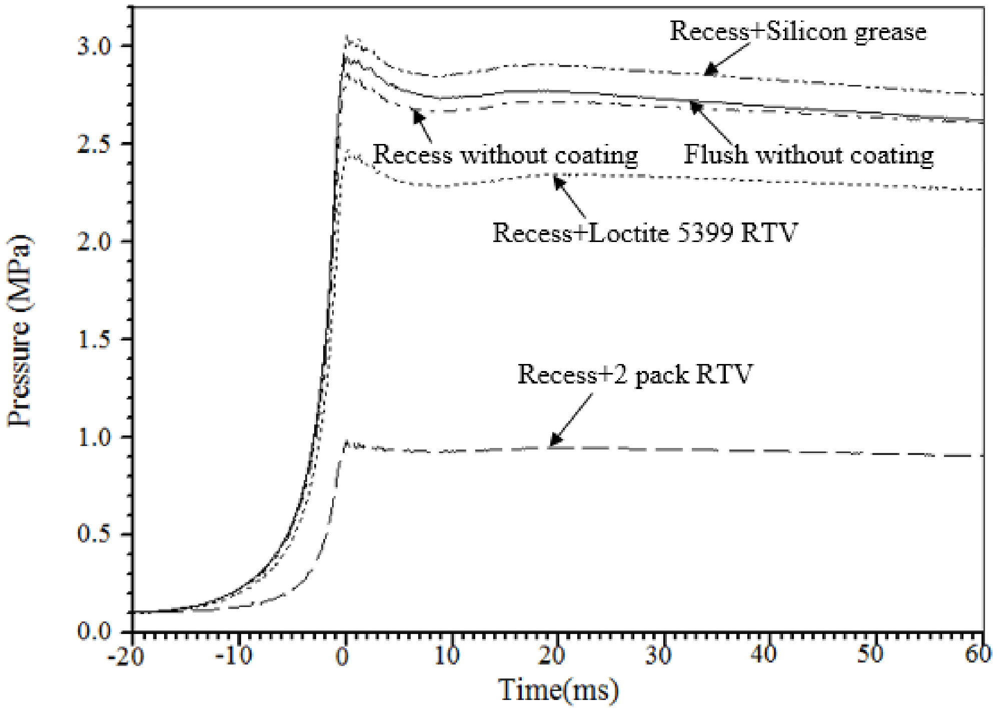

Figure 2.20. Pressure traces for air with atmospheric initial conditions using pressure transducer 7005 when recess mounted with and without coating, and when flush mounted without coating.

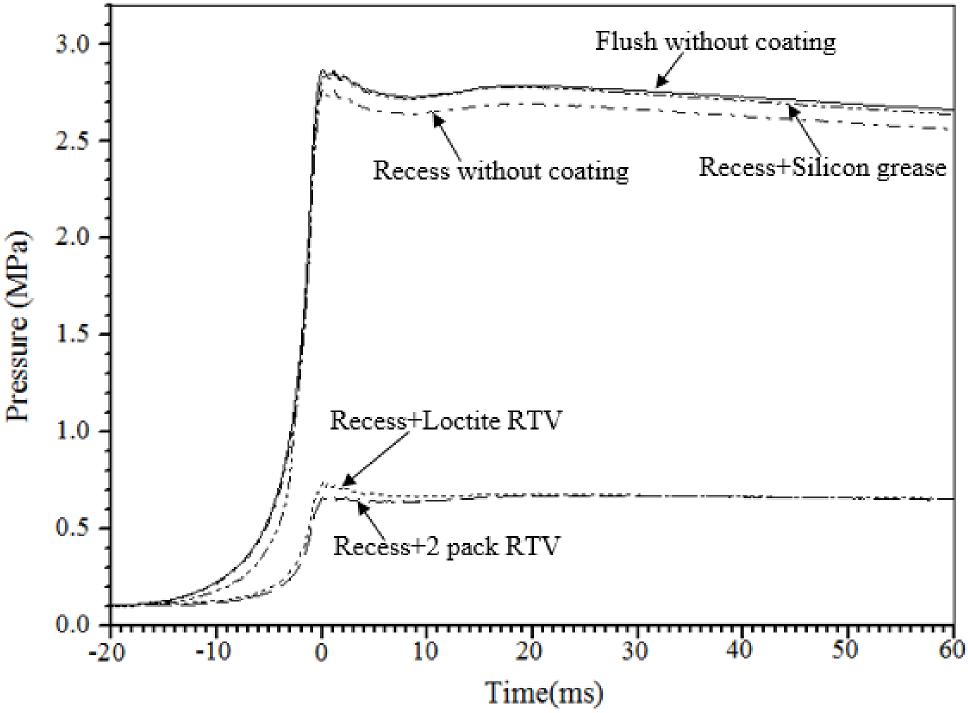

Figure 2.21. Pressure traces for air with atmospheric initial conditions using pressure transducer 701A when recess mounted with and without coating, and when flush mounted without coating.

2.2.9.2. Combustion cylinder and chamber heating modifications.

Among other things such as fuel concentration and pressure, autoignition properties depend on temperature. Therefore, one of very important feature of an RCM is its capability to control the initial temperature of the combustible mixture before compression. Initially, heating was only achieved by using the band heaters installed on the combustion cylinder, and there was no heating on the combustion chamber end, which was in contact with the machine’s frame metal block, as shown in Fig. 2.1. This arrangement frequently resulted to an overheating of combustion cylinder and not enough heating was attained on the combustion chamber end. Different heating arrangements were then tried by the present author to ensure uniform temperature throughout the combustion cylinder and chamber at the start of compression. Temperature measurements were taken longitudinally along the centre of the combustion cylinder and chamber for air at atmospheric conditions. These mesurements were made using a type K thermocouple which was protected within a ceramic tube. The tube had markings on the outside to enable determining the position of the thermocouple in the combustion cylinder and chamber. A special end plug with a hole machined at the centre, for inserting the ceramic tube, was used. During measurements, the ceramic tube was carefully pushed through to the chamber length and measurements were taken every 20mm.

Different methods were investigated. Fig. 2.23 shows three curves of temperature distribution within the combustion cylinder using two heating arrangements. One (black curve) using two band heaters, each with 375W and 30mm wide, which are fitted around the combustion cylinder, one on each end and both set at 70^{o}C, and another arrangment (red curves) using a combination of 5 band heaters each with 375W around combustion cylinder and six cartridge heaters 50W each fitted circumferentially into the walls of the end plug, as shown in Fig.2.22. The length axis in Figs. 2.23 was measured from the combustion chamber end to the piston face as shown in Fig. 2.22. Therefore, a value of 0 mm represents chamber end face and a value of 245mm represents the length of the combustion chamber at the start of compression. It is clear from Fig. 2.23 that when using only band heaters on the combustion cylinder, a substantial variation in temperature along the length of the combustion chamber is obtained, with the lowest temperature, at the cylinder head, being some 35^{o}C below the maximum temperature which ocured at approximately the mid point between cylinder head and piston face.

Fairly uniform temperature distributions were obtained, at different set temperatures, when a combination of band heaters on combustion cylinder and cartridge heaters on the end plug were used. This heating arrangement was therefore chosen as the optimum heating solution and was used for the rest of this work.

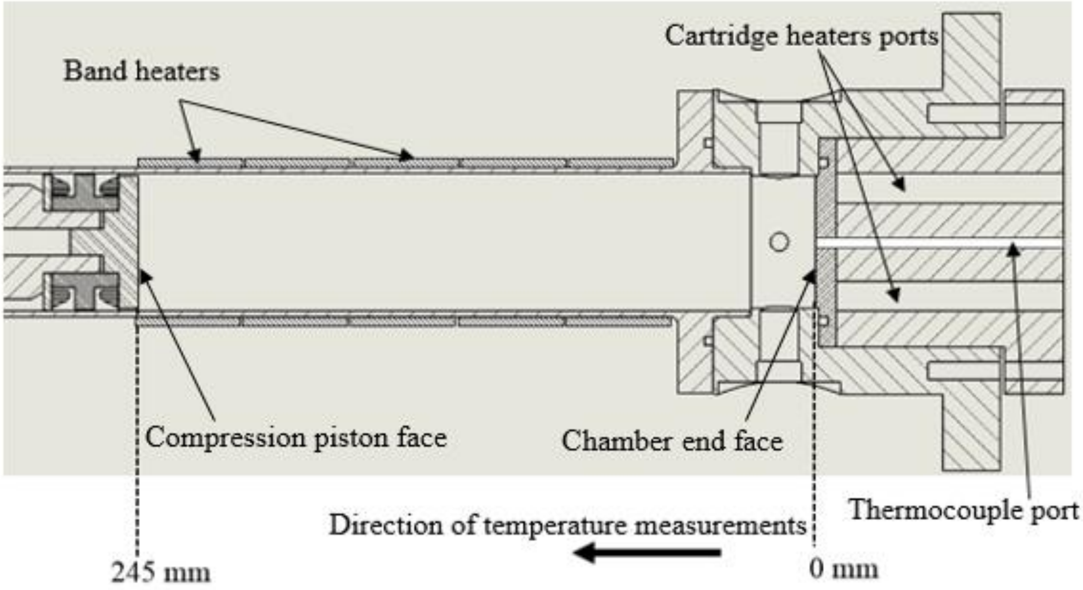

Figure 2.22. Combustion cylinder and chamber heating arrangement.

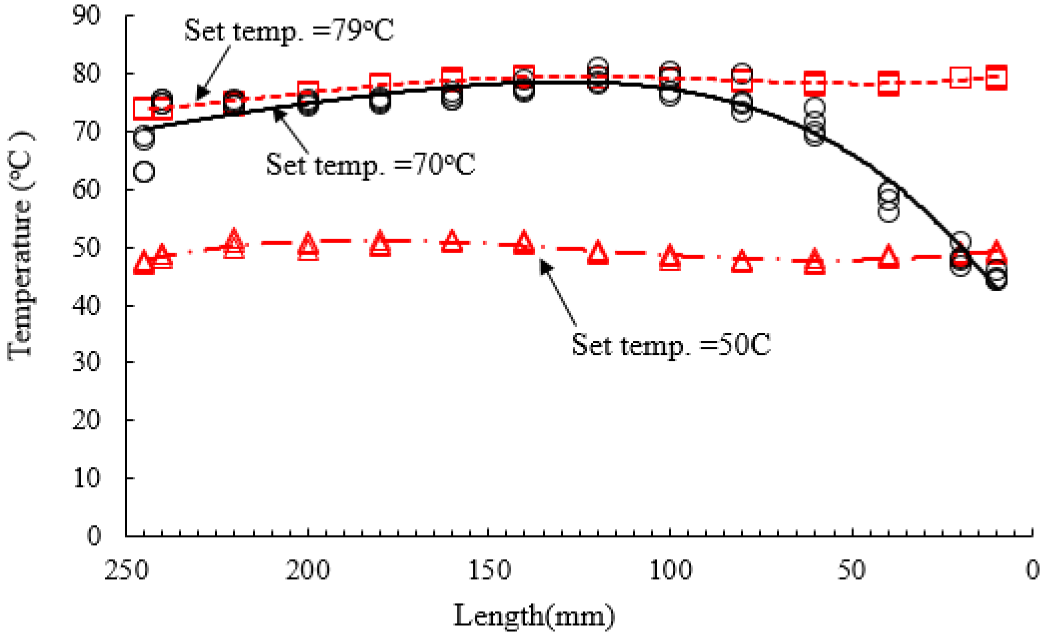

Figure 2.23. Temperature distribution along the centre of the combustion cylinder and chamber, at different set temperatures, using two different heating arrangements.

2.2.9.3 Piston position/displacement measurements.

Prior to the start of this work, no means of measuring the piston position was available. However, the present author believed that this was an essential requirement. This was particularly so because any piston bounce after the end of compression would affect the volume, hence pressure and temperature, during the autoignition delay period. Further, the reactant temperature can be inferred, as will be discussed in Section 3.2.2, from the changing volume of the chamber during compression.

Initially, a linear potentiometric displacement transducer (PS-C15) was used for measuring piston position as shown in Fig. 2.24. A slider arm was attached to the end of the driving piston while the other end was fixed on the end cap of the driving air reservoir. However, this was unreliable and suffered from frequent failures. Therefore, an improved system was designed and implemented by the present author. An extension rod was connected to the driving piston and a high speed camera was used to film the rod movement past an externally installed fixed ruler as shown in Fig. 2.25. However, this method required manual synchronisation of high speed movie images with digitally recorded pressure records. It proved to be very time consuming and prone to errors.The final solution, used throughout the rest of this thesis comprised a class 2 laser system, where a laser beam was targeted, at a slight angle, onto a reflecting circular plate attached to the driving piston extension rod. Details of this system are described in section 2.2.7.3. Given the initial interest was to capture piston behaviour, such as bounce or creeping, at the final stages of compression, a KEYENCE laser model LK-G82 was chosen. It has a measurable range of 30 mm which is sufficient to accurately measure these behaviours.

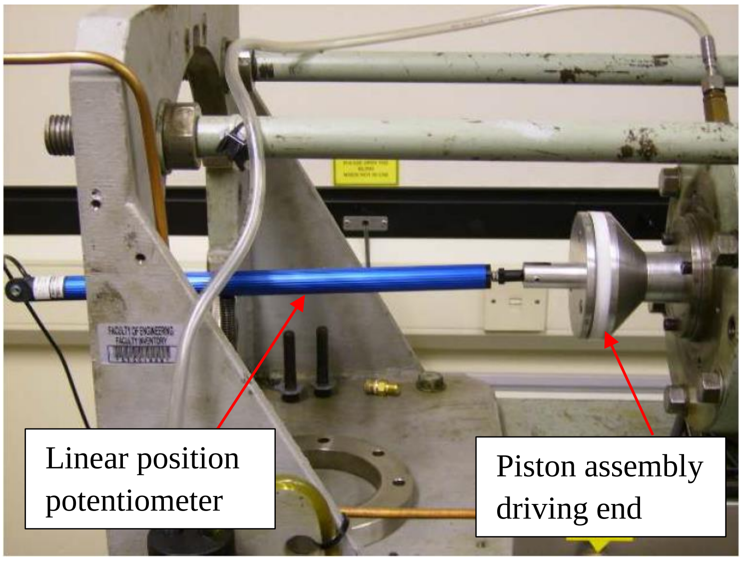

Figure 2.24. Piston displacement measurement system using a linear position potentiometer.

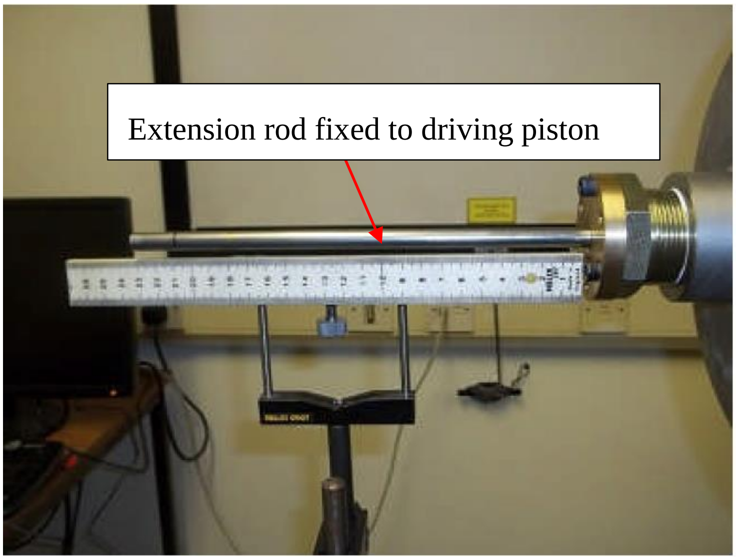

Figure 2.25. Piston displacement measurement system using a high speed camera and externally installed fixed ruler.

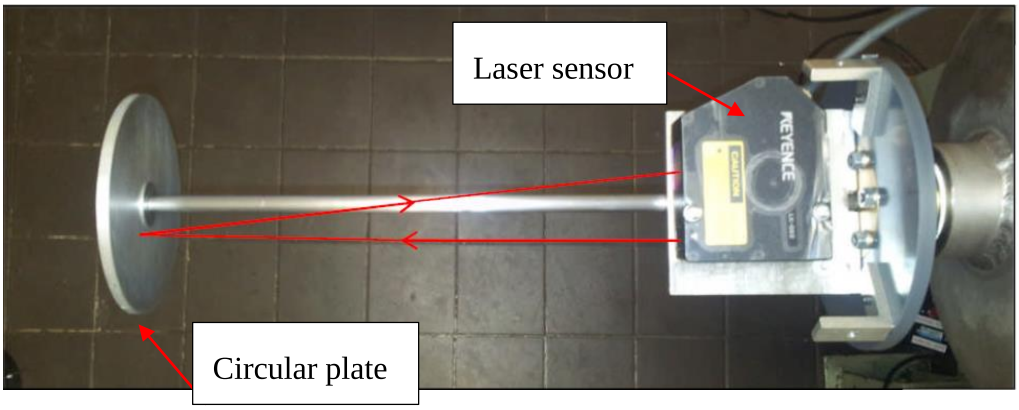

Figure 2.26. Piston displacement measurement system using a class 2 laser system.

2.2.9.4 Piston damping.

As explained in Section 2.2.3, the hydraulic piston damping mechanism requires very accurate clearance between the damping ring and groove so as to ensure smooth and progressive piston damping. Shown in Fig. 2.27 is the variation of piston position with time after the end of compression of air at an initial pressure of 0.1 MPa. The dashed line shows measurements obtained during initial tests before any improved piston damping was considered. It shows massive piston bounce in excess of 25mm, which was typical of all pressures investigated. Therefore, an investigation by the present author revealed a slight misalignment between the damping ring (see Fig. 2.2) and its mating groove. Therefore, the damping groove was remanufactured, to a high precision of 0.01 mm such that it was just enough for the damping ring to pass through. This, produced a rather abrupt piston arrest followed by a reduced bounce back due to combination of impact force from damping oil and the back pressure from the combustion chamber. The piston then creeped slowly to the end of compression position over an excessive period of time.

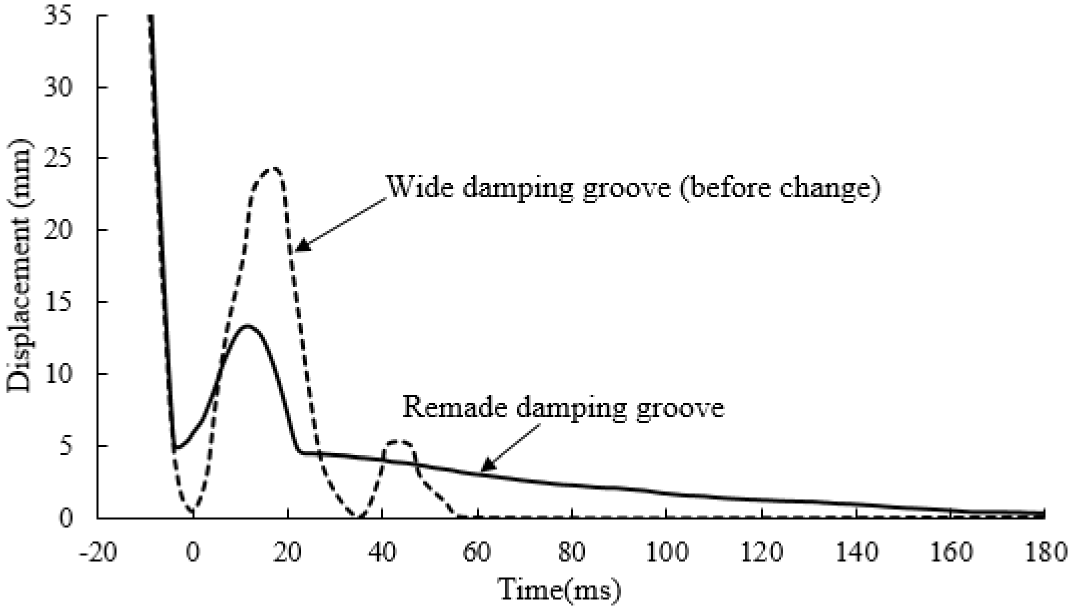

Figure 2.27. Piston displacement before and after damping groove change.

Improvements were obtained by experimentally varying the driving pressure and oil composition. The effect of changing the driving pressure is shown in Figs. 2.28 and 2.29.

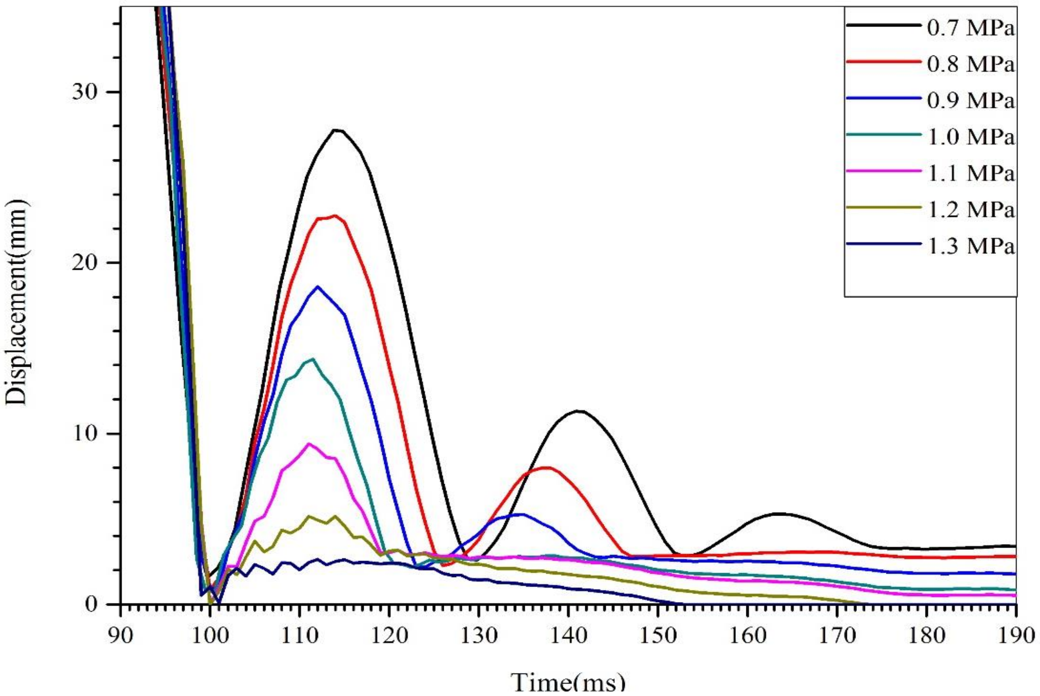

Figure 2.28 Piston displacement showing the effect of increasing driving pressure (P_{dr}) while keeping combustion chamber initial pressure (P_i) constant at 0.1 MPa.

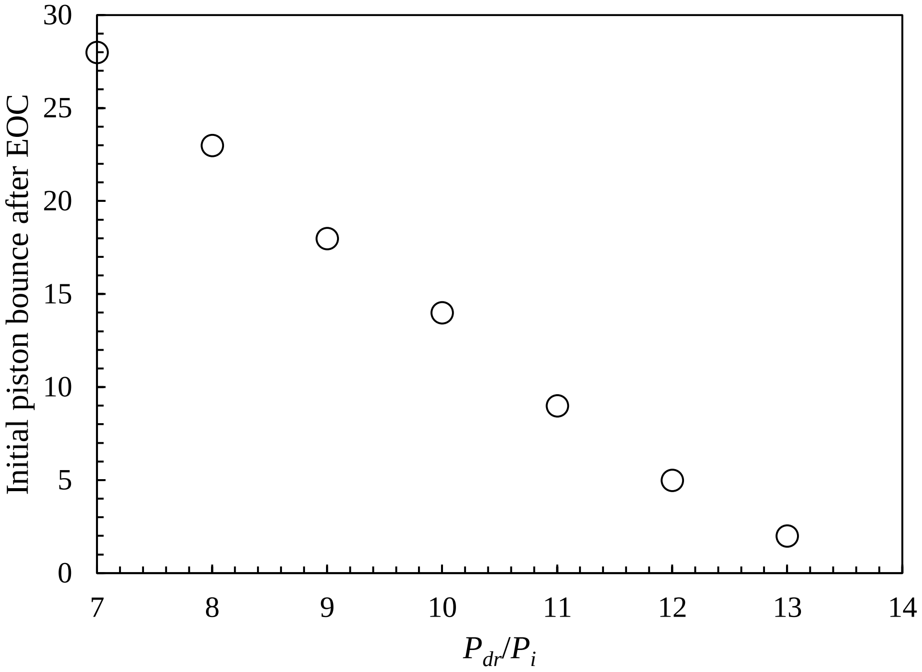

Figure 2.29. Piston bounce reduction with driving/initial pressure ratios

However, adequate damping required a significant redesign of the damping arrangement by the present author in collaboration with a collegue, Richard Mumby, as shown in Fig. 2.30. This comprised an alternative, and highly controllable, route through which the damping oil could leave the damping section.

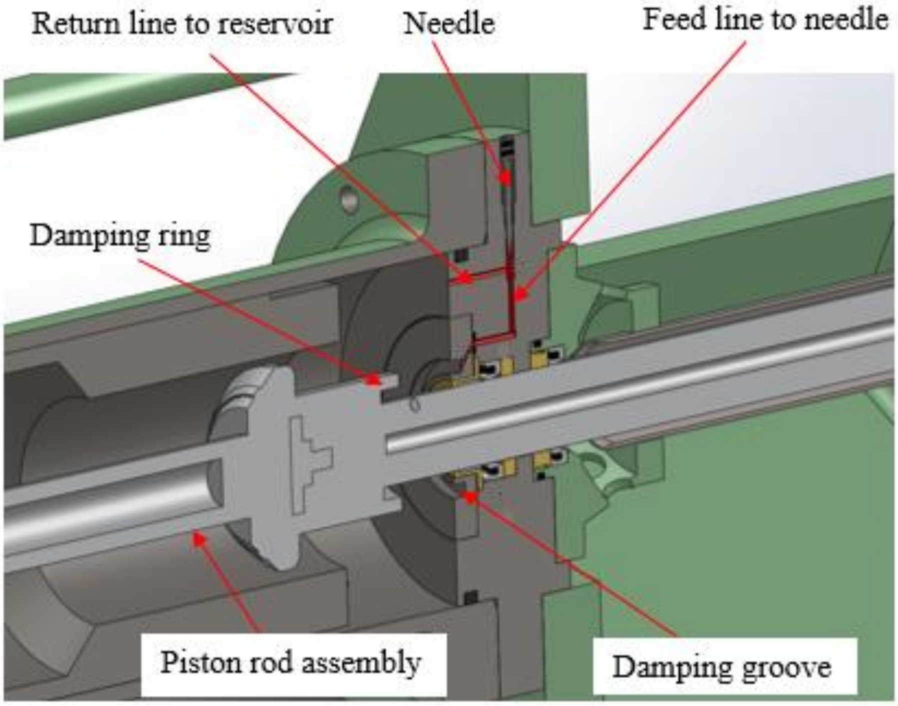

Figure 2.30. Needle valve damping mechanism.

It involved the use of alternative return paths from the back of the damping groove to the oil reservoir, which were regulated by needle valves as shown in Fig. 2.30. The use of the needle valve allowed precise control of the rate of oil displacement for a given driving cylinder to combustion chamber pressure ratio. Three equidistant needle valves controlled return paths were installed and these provided efficient and uniform damping as shown in Fig 2.31. Here, the variation of piston displacement with time is shown for a number of tests with different amounts of damping. The damping was characterised by the position of the needle valves in terms of the number of revolutions (turns) of the valve from fully clossed. Tests were made at a constant driving to initial chamber pressure ratio of 13, the curves in Fig. 2.31 show pressure measurements in the combustion chamber together with the corresponding piston displacement measurements. With the needle valve fully closed as shown by the black solid curve in Fig 2.31, the damping is very poor and similar to that shown by the solid line in Fig 2.27. As the needle valve is opened to 1 turn, the piston quickly attaines the end of compression position, without evidence of creep, before showing significant bounce back oscillations of about 2mm. With increased number of turns of the needle valve, the amount of bounceback and duration of bounceback oscillations diminishes. The maximum effect, and the best operating condition was found to be with 20 turns of the needle valve. It is possible that further design improvements may produce better performance, but the damping obtained with 20 turns was considered sufficient for the present work.

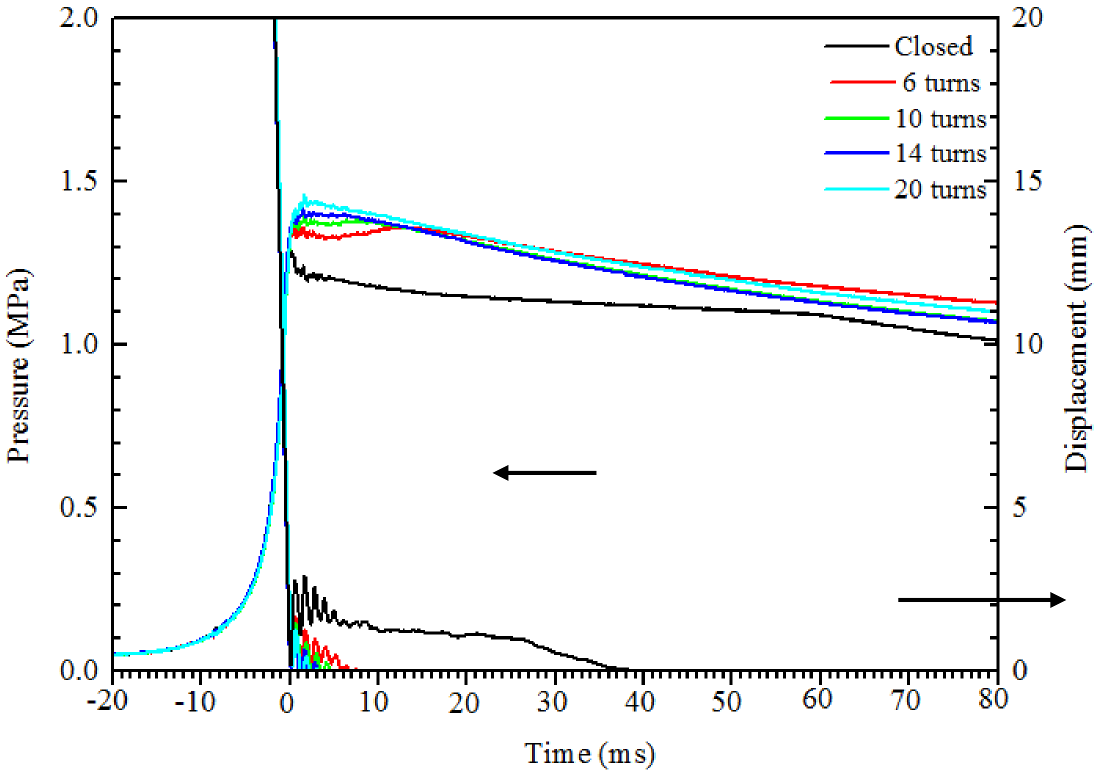

Figure 2.31. Pressure traces showing the effect of needle valves turning, at driving pressure of 1.3 MPa and initial pressure of 0.1 MPa.

Nevertheless, tests were conducted with damping oils of different viscosity. Highly viscous oil was more difficult to displace through the needle valves and required higher driving pressure to force it through the back of the damping groove. However, they had better damping behaviour than less viscous oil. Shown in Fig 2.32 are pressure measurements for air under the same conditions using three different damping oils. Shell Tellus 22 which has lower viscosity, Shell Tellus 68 with slightly higher viscosity and the most viscous Shell Tellus 220. The low viscosity oil allows more oil to be displaced from the back of the damping groove and thus the piston reaches near the top dead centre and achieves slightly higher pressure. However, a substantial piston bounce occurs making it less desirable for effective damping. With application of higher driving pressure to help push through the more viscous oil, Tellus 220 was able to give very good piston damping capabilitiy without rebound, as shown in the Fig 2.32.

Therefore, a high viscosity Shell oil Tellus 220 was chosen as a damping oil for all work reported in the rest of this thesis. This oil together with the use of three needle valves and high driving pressure of up to 1.4 MPa, yielded very rapid piston arrest, with good damping and without rebound, this was possible for end of compression pressures of up to 2.5 MPa.

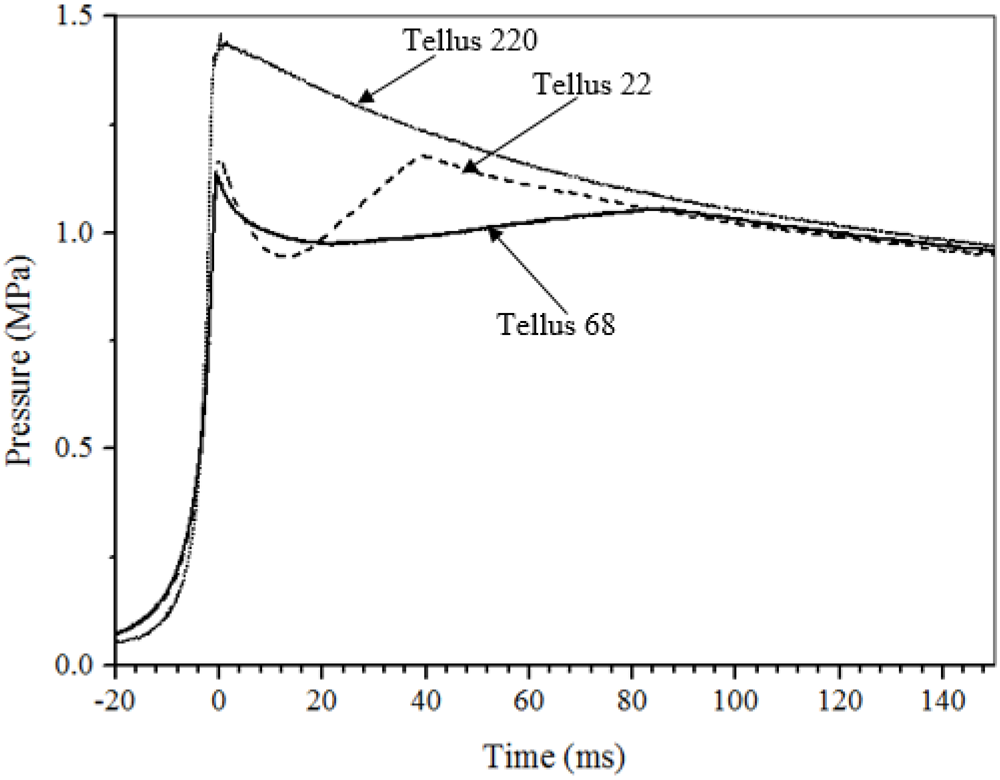

Figure 2.32. Pressure trace showing the damping effect of different damping oils.

2.3 University of Cape-Town RCM (UCT-SAFL RCM).

Shown in Fig 2.33 is a photograph of the RCM developed by the Sasol Advanced Fuel Laboratory (SAFL) at the University of Cape Town (UCT) [Ezevard, 2011]. In the present work, it is designated as UCT-SAFL RCM. While the piston driving mechanism was somewhat similar to most RCMs, the UCT-SAFL RCM used a novel concept for the piston arresting and damping mechanism. It utilised the principle of impact mechanics (like a Newton's cradle). It was capable of achieving higher compressed mixture pressures, of up to 4.0 MPa in the combustion chamber, than those currently achieved by the Leeds RCM (up to 2.5 MPa). The machine and its development have been fully described in Ezevard [2011]. This section gives a brief overview of the machine and its auxiliary components, followed by a description of the operating procedures used in the present work.

The UCT-SAFL RCM comprised four main systems as shown in Fig 2.33 and in the schematic of Fig 2.34. These are:

i.) The air delivery section which provided pneumatic pressure to drive the piston within the combustion cylinder;

ii.) The combustion chamber which comprised a cylinder and piston;

iii.) Momentum trap to stop the piston by transferring its momentum to a second rod;

iv.) Hydraulic damping unit to arrest the second rod.

Each of the four systems are discussed below.

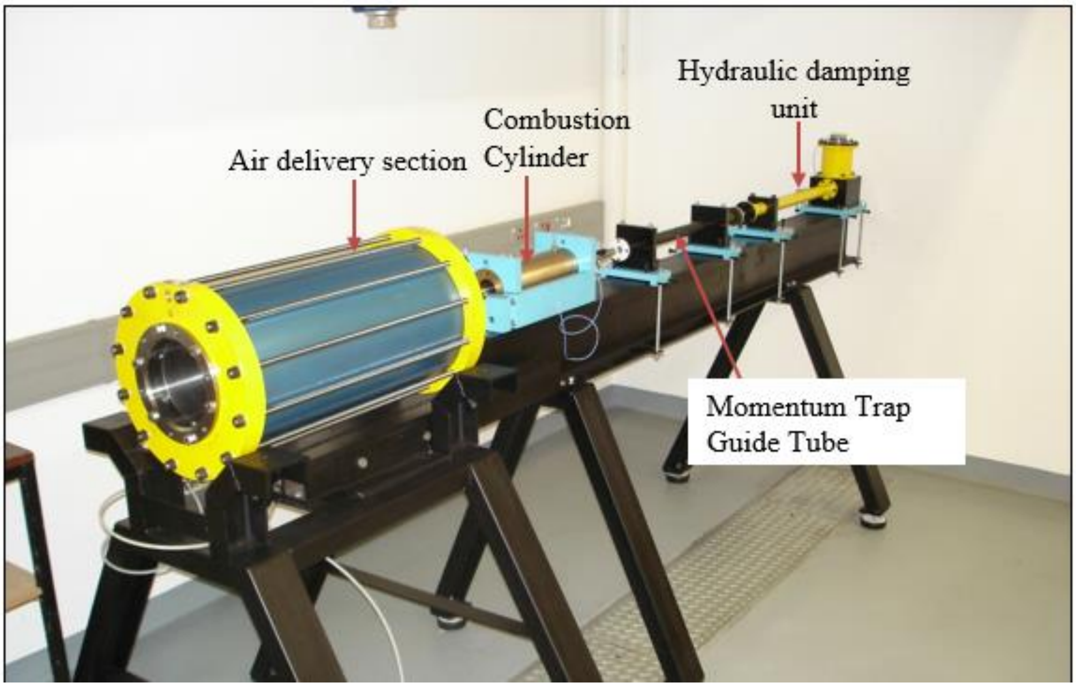

Figure 2.33. A picture of UCT-SAFL RCM showing the main sections.

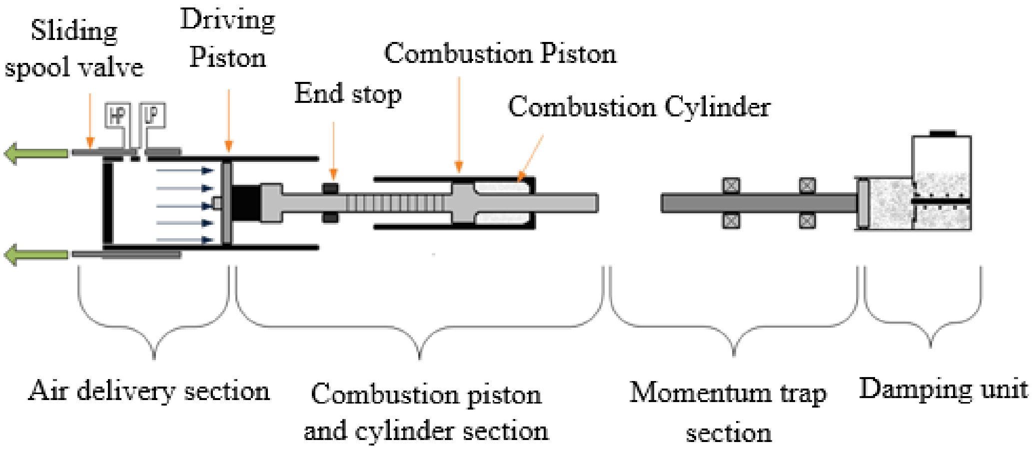

Figure 3.34. A schematic representation of UCT-SAFL RCM [Ezevard, 2011]

2.3.1 Air delivery and piston driving system

The combustion piston was connected directly to the driving piston which was located in the driving cylinder. Air pressure within the driving cylinder drove the combustion piston to its final position and then held it in place. A low pressure (LP) reservoir initiated piston motion followed by the high pressure (HP) reservoir which accelerated the driving piston to the end of compression.

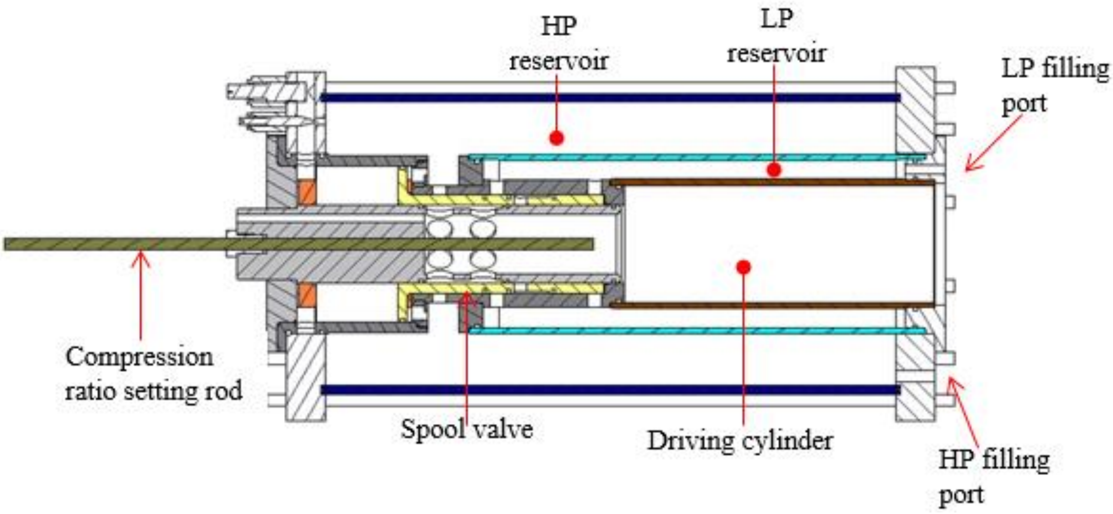

Figure 2.35. Section view of the air delivery system. [Ezevard, 2011]

2.3.2 Combustion piston and chamber section.

This system is shown in Fig. 2.36, it contained the combustion piston and cylinder. The combustion piston was machined from a solid metal rod and consisted of two enlarged sections. One of the enlarged sections was used to rest against the end stop which allowed for absolute positioning of the piston at the end of compression; the other was used for compressing the test mixture. The cylinder head was machined so that a section of the reduced cross-section of the piston rod protruded through the combustion chamber and acted as a point of contact with the momentum trap for piston stopping which is explained in Section 2.3.3. This design resulted in a semi-toroidal combustion chamber.

Six 250W cartridge heaters are fitted on the circumference of the combustion cylinder and controlled remotely on a PC using software written in LabView (Section 2.3.5). The cylinder pressure is measured by a water cooled dynamic pressure transducer AVL QC43D which is mounted in a machined recess in the cylinder wall.

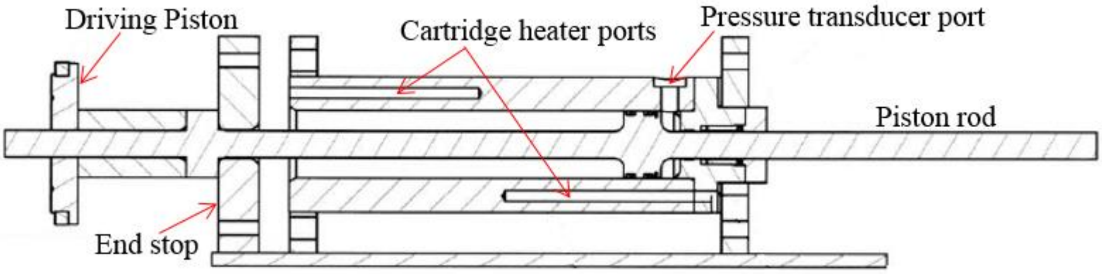

Figure 2.36. Section view of combustion cylinder. [Ezevard, 2011]

2.2.3 Momentum Trap.

One of the essential requirement of an ideal RCM is that the piston must accelerate instantaneously, stop instantaneously at the end of compression and have zero rebound. These requirements are impossible to achieve in a real machine and various designs have been produced to approximate these requirements. All such designs require compromises. The present design, shown schematically in Fig. 2.37, was unique in that it used the application of Newton's third law to transfer momentum from the combustion piston rod to a secondary rod (momentum trap) in a similar way to that of a Newton's cradle. However, implementation of this method is complex due to elasticity of working components and induced pressure waves generated in the materials. This is the subject of impact mechanics and its analysis is discussed in Spotts [1964]. Further, the present implementation makes use of an elongated piston rod which resulted in a toroidal combustion chamber with its associated increase in heat loss due to large surface area. Nevertheless, the system produced the fastest deceleration and minimum rebound of any RCM known at the time of writing.

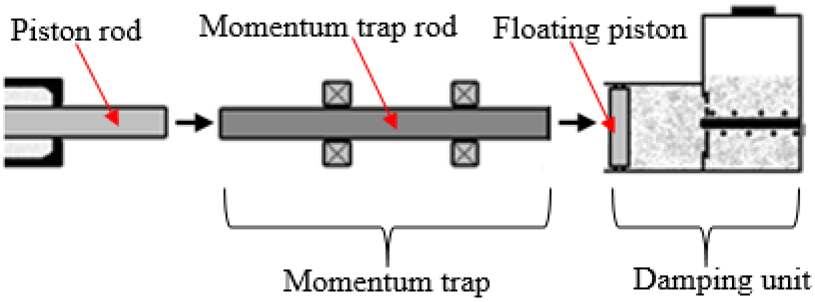

Figure 2.37. Schematic representation of momentum trap technique.

2.2.4 Damping Unit.

The momentum trap rod from section 2.3.3 was damped by a special hydraulic damping unit shown in Fig. 2.38. Inside this unit sits a floating piston which when coming into contact with the momentum trap rod, pushes the hydraulic fluid in front through an orifice plate.

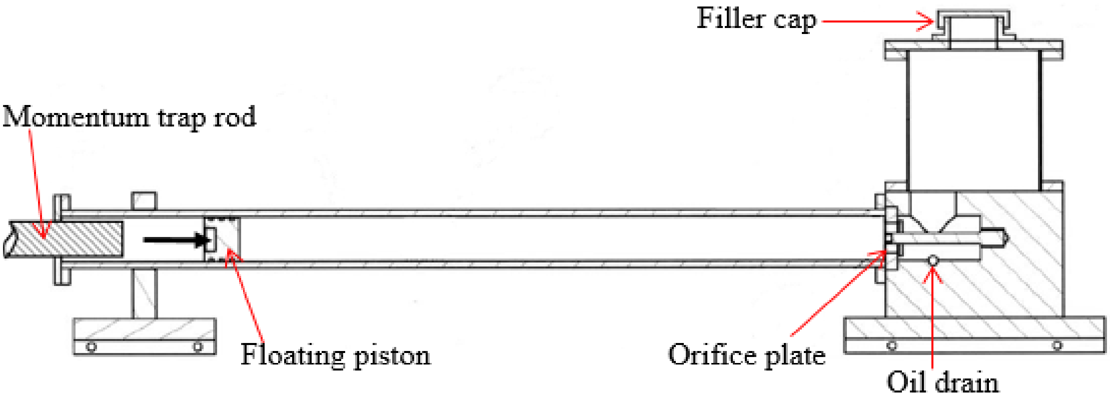

Figure 2.38. Section view of the hydraulic damper. [Ezevard, 2011].

2.2.5. Mixture preparation and Machine operation.

Similar to the Leeds RCM decribed in Section 2.2.6, a separate mixing chamber was used. Shown in Fig. 2.39 is a schematic of the mixing chamber. It is a collapsible cylindrical tank made of flexible aluminium ducting which was clamped at either end to the tank lid and base. A maximum of 20 tests including purge cycles between tests could be obtained from a full tank.

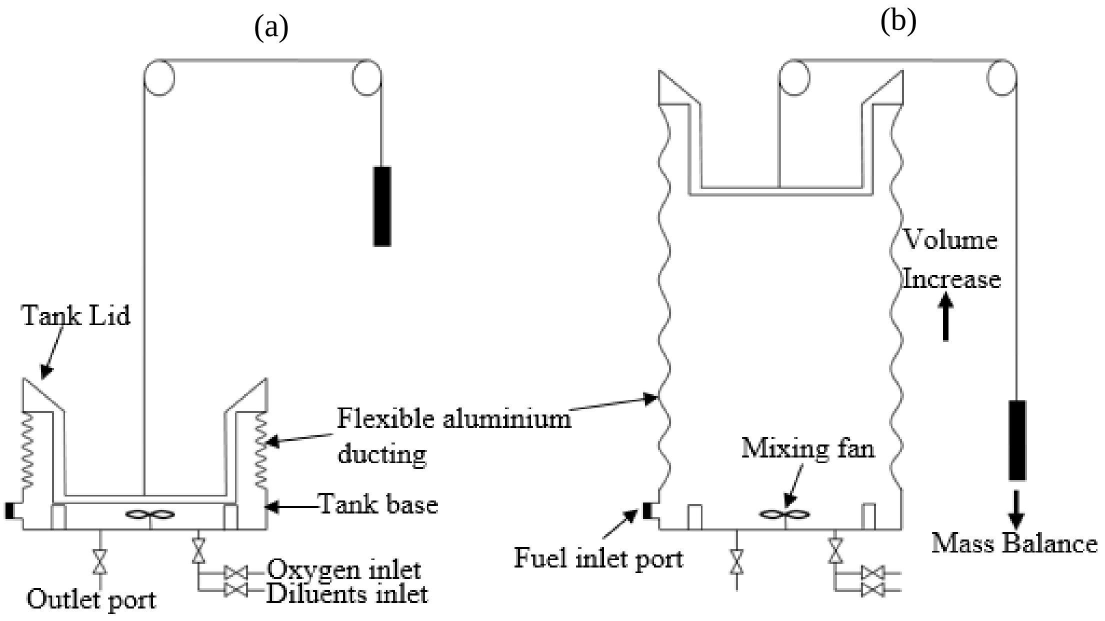

Figure 2.39. Schematic representation of mixing chamber at UCT-RCM, where (a) shows initial state of chamber before mixture was made and (b) after fuel and gas were let in.

The main internal features of the mixing chamber included a mixing fan for ensuring fast and thorough mixing, inlet ports for allowing gases (oxygen and diluents) into the chamber, outlet port to transfer the mixture to the combustion cylinder, a heating tray to ensure full fuel evaporation, fuel injection port, dead volume spacers to insure a dead volume at the "empty" position and provide a clearance volume for the mixing fan, and a safety burst diaphragm which would direct expanding gases away from the user in case ignition occurs in the mixing tank.

During filling, a mass balance which had the same weight as the tank lid was placed and diluent gases were added sequentially through the inlet port controlled by a needle valve. This extended the aluminium ducting and thereby increasing the tank volume accrued to a predetermined amount for each particular gas, Fig. 2.39(b) shows the tank volume increase as gases were added. Fuel was finally added using the needle onto the heating tray inside the mixing chamber. The mass was then removed during testing or purging.

The UCT SAFL RCM was fully automated using various circuits which were made up of several solenoids valves, sensors and pneumatic actuators. Operation of the whole system, except for filling the mixing chamber, was controlled by a computer programme, developed in Labview Software and running on a PC.

Tests were conducted by running different Labview Sub-VI (Virtual Instrument) which controlled different stages of the machine operation using the following sequence of operations;

1. Initial settings were made by entering the initial pressure, temperature, compression ratio and number of experiments to be conducted.

2. Purge cycle in which a mixture was transferred from the mixing tank to the combustion chamber for purging the combustion chamber from previous test.

3. Charge cycle in which an appropriate amount of mixture was filled into the combustion chamber.

4. Fire cycle in which a solenoid valve was opened and move a spool valve to allow compressed air into the driving cylinder and push the piston forward to compress the mixture in the combustion chamber.

CHAPTER 3: RCM IDEAL OPERATION AND CONSORTIUM STUDY OF MEASUREMENTS OF *ISO*-OCTANE IGNITION DELAY TIMES.

3.1 Introduction

Ignition delay times, τ, and excitation times are key parameters in the characterisation of auto-ignition [Fieweger et al., 1997; Lutz et al., 1988]. The latter time, during which the heat release occurs, is approximately on the micro-second time scale and at present has to be derived computationally [Gu et al., 2003]. Mentioned in Chapter 1, Shock tube measurements [Hanson et al., 2014] are well suited to the higher values of temperatures and pressure, and rapid compression machines, RCM, to the lower values [Sung et al., 2014]. Comparison of ignition delay times measured from different RCMs has not always been possible. This is due to difference in thermal behaviour within the combustion chamber during and after compression for each machine. These differences are mainly brought about by dissimilarities in operation characteristics such as compression times and piston vs chamber walls interactions. As will be shown in the following section, all RCMs deviate from their ideal behaviour each with different extent, and this will cause the ignition delay times of the same fuel and conditions to differ from different RCMs. This Chapter is divided into two main parts. The first part describes the key aspects of the operation of RCMs, including their limitations and methods to reduce those limitations, and the second part is aiming at characterising the discrepancies of measured ignition delay times from different RCMs by using their limitations and deviations from ideal performance.

3.2 Issues related to RCM ideal operation.

The design of any RCM is based around key aims which act as a machine’s performance criteria. However, these aims cannot be perfectly achieved in practise and for many years, RCM researchers have been developing methods to ensure that the machines run as close as possible to these aims. It is important to understand the limitations that arise in practise, in aiming to achieve these aims. This section describes the main characteristics that govern the operation of an RCM.

3.2.1 Ideal RCM operation and core gas hypothesis.

The accuracy of measured ignition delay times using an RCM depends on how close the actual operation of a given machine is to achieve these aims. After the compression, the aim is to achieve a uniform temperature of the charge. This is impossible throughout the charge and an adiabatic core is assumed. This assumes that the core gas away from the thermal boundary layer is compressed isentropically to a uniform temperature. Heat loss to the walls during and after compression is restricted to the thin boundary layer along the walls and the core charge is unaffected by the heat loss. This unaffected area is called the core region, in which the temperature is assumed to be uniform.

To meet this condition, RCMs should ideally compress the test gas very rapidly, minimising time for the heat transfer between the core gas and boundary layer to take place. This way the core gas can be considered as spatially uniform (homogeneous). Typical compression times for different RCMs, around the world, are in the range of 20-50 ms, but the most important part of compression is the final half of compression. Here the higher temperature and pressure promote both heat transfer and chemical reaction. This time is commonly known as t_{50}, and is in the range of 1-5 ms.

After compression, the reaction chamber volume should remain constant, with the piston coming to rest instantaneously, with no rebound. Temperature and pressure are then expected to stay constant throughout the delay period, and the main ignition occurs homogeneously throughout the mixture. Figure 3.1 shows a representative pressure trace within the reaction chamber for ideal RCM operation, time=0 is the end of compression.

3.2.2 Core gas temperature determination.

Measurements of ignition delay times are usually related to the end of compression conditions of pressure P_o and temperature T_o. Pressure is measured by using a high response dynamic pressure transducer usually installed flush with the reaction chamber wall. It is difficult to measure the temperature inside the reaction chamber directly during and after compression. Any intrusive measurement method, such as a thermocouple would affect the aerodynamics inside chamber. It is difficult to find thermocouple that can match the response time required. Non-intrusive optical methods are difficult to set up and require extensive calibration.

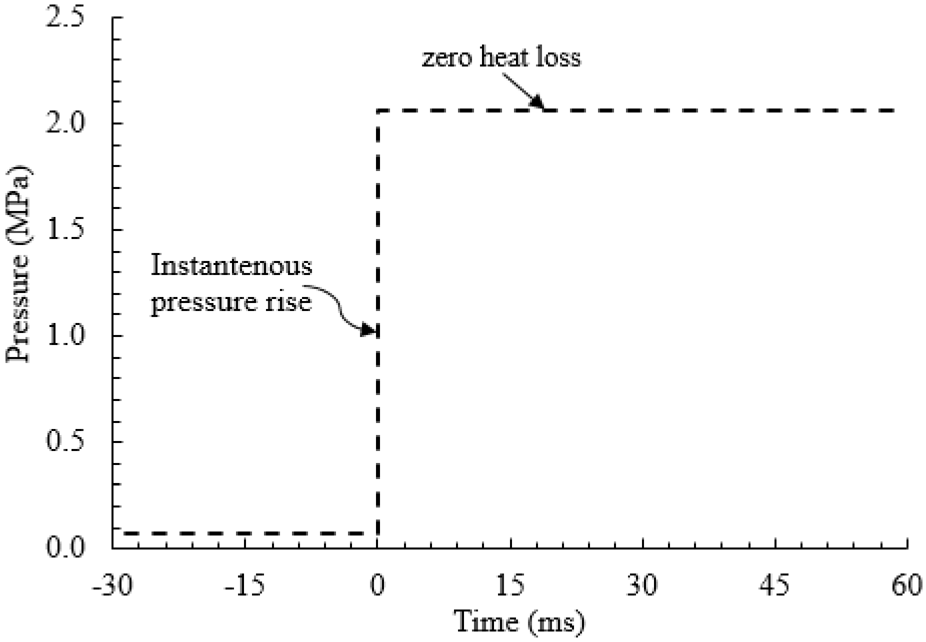

Figure 3.1 Pressure trace for ideal RCM operation.

Consequently the most common indirect method for determining the temperature is to use the adiabatic core hypothesis. This method has been previously validated experimentally [Das et al., 2012] and computationally [Mittal et al., 2008]. The truly isentropic temperature of the gas within the core region at the end of compression, T_{ad}, can be determined using the following relation:

$$\int_{T_i}^{T_{ad}} \frac{1}{\gamma - 1} \frac{dT}{T} = \ln(CR) \tag{3.1}$$

Where, T_i is the initial temperature, γ is temperature dependent specific heat ratio and CR is the volumetric compression ratio.

However, the compression is not perfectly isentropic and there is a small heat loss within the core gas, resulting in slightly lower values of pressure and temperature than predicted by isentropic compression. Previous studies by Desgroux et al. [1995] and Griffiths et al. [1993] have shown that, the adiabatic core assumption can be reasonably met by using an effective compression ratio modified by heat transfer to the wall. This effective compression ratio can be obtained by using the actual measured pressures within the core region by the following relation:

$$\frac{P_o}{P_i} = (CR)^{\gamma} \tag{3.2}$$

Based on this assumption, the end of compression temperature, T_o, is calculated from:

$$\int_{T_i}^{T_o} \frac{\gamma}{\gamma - 1} \frac{dT}{T} = \ln\left(\frac{P_o}{P_i}\right) \tag{3.3}$$

Where P_i is initial pressure, P_o is end of compression pressure and other variables are same as in Eq. (3.1).

3.2.3 RCM non-idealities, limitations and methods to overcome them.

Despite the adiabatic core assumption, one of the main deviations from ideal conditions is the heat loss. Heat loss during compression is limited by the short time scales associated with the compression. But compression is not instantaneous and heat loss occurs, making the pressure and temperature at the end compression lower than that predicted by the adiabatic assumption. After compression the heat loss is evident from the pressure drop in the measured pressure traces. For some machines and large ignition delay times the pressure drop could be near 20% as shown in Fig. 3.2 from Goldsborough [2012]. Such a drop is a severely limiting factor. For large delay times the heat loss can quench the chemical reactions and there can be no ignition. The measured ignition delay times are usually associated with the end of compression conditions of temperature and pressure but these conditions may not remain uniform during the delay time. Consequently, the measured delay times are not associated with end of compression conditions. In Section 3.3.2, a method of making allowance for these changing conditions is proposed.

The non-instantaneous compression can also impose another limitation due to the onset of chemical reactions during compression [Griffiths et al., 1993; Cox et al., 1996; Mohamed et al., 1998]. This is aggregated by slow compression and an increase in reaction rate with temperature. Thus, the compression time, particularly t_{50}, acts as a limiting factor for accurate delay time measurements of very reactive fuels. This is discussed on Section 3.3.3 and a method is developed to correct the measured delay times to the conditions at the end of instantaneous compression.

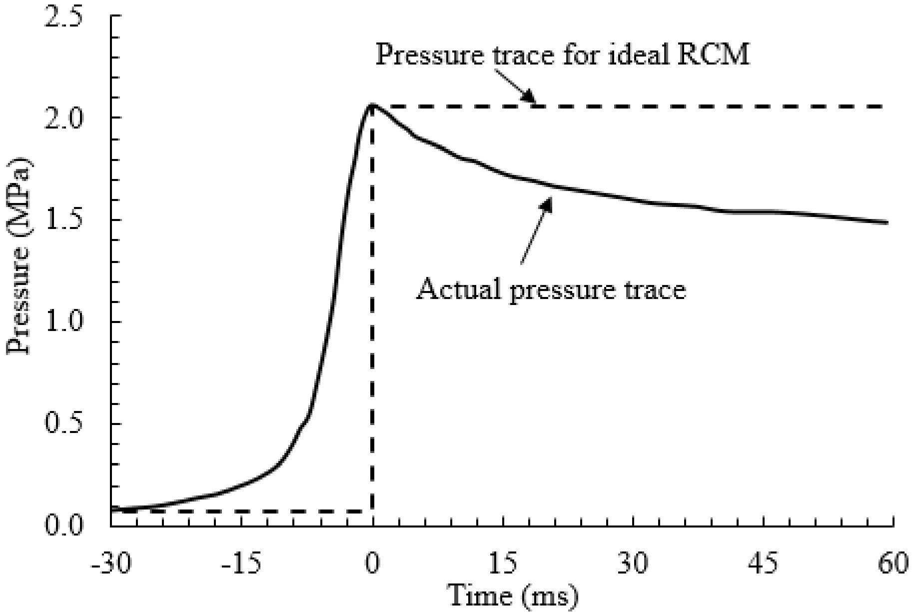

Figure 3.2. Pressure traces for actual [Goldsborough, 2012] and ideal RCM operations, showing pressure drop due to heat loss.

Ideally, the reactive mixture within the chamber remains a homogeneous mixture before, during and after compression. However, the high speed of the piston, when suddenly brought to rest at the end of compression can induce complex flows inside the chamber which can influence the temperature distribution in the reactive mixture. Several researches [eg. Lee and Hochgreb, 1998; Mittal and Sung, 2006; Wurmel and Simmie, 2005] have shown the generation of a roll up vortex caused by the piston scraping off the cold boundary layer during compression. This results in the mixing of colder gas from the cylinder wall with the hotter gases in the core zone, creating an inhomogeneous mixture inside the chamber, the exact nature of which cannot be accurately characterised.

In attempts to avoid this, modern RCMs use specially designed piston faces with crevices on the sides of the piston, designed to suppress the vortex formation during compression, and greatly limit the movement of colder gas to the core zone. Figure 3.3 illustrates vortex formation during the piston compression stroke and its suppression using the creviced piston [Sung et al., 2014]. Temperature fields within the combustion chamber, predicted by CFD, showed improved, more uniform temperature distributions when a creviced piston head was used, as opposed to the non-crevice piston head, as presented in Fig. 3.4 [Wurmel, 2004].

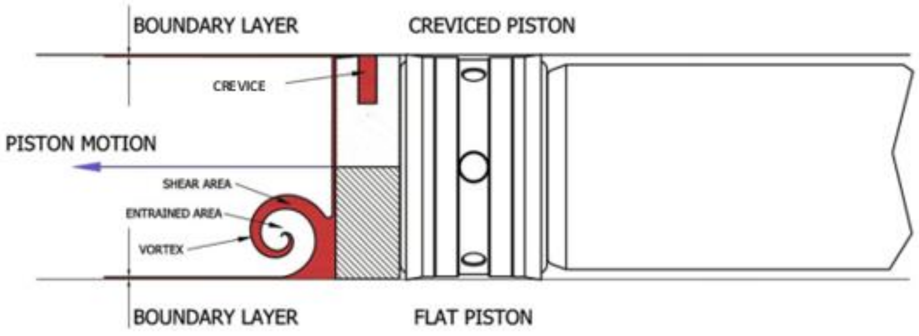

Figure 3.3. Illustration of creation of roll up vortex due to piston motion during compression (lower section) and containment of boundary layer through a crevice (upper section) through proper design [Sung et al., 2014].

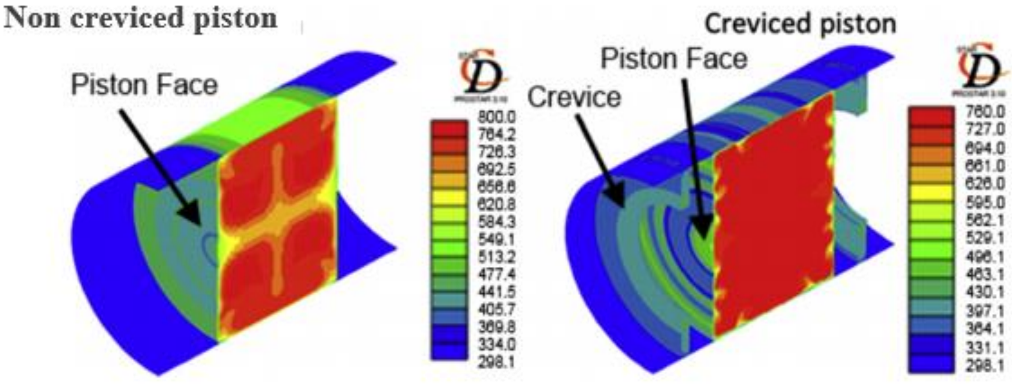

Figure 3.4. Comparison of predicted temperature fields at 10.4ms from the end of compression for N_2 gas using creviced and non-creviced piston heads [Wurmel, 2004].

A creviced piston introduces other multidimensional effects, specifically for fuels that manifest two staged ignition [Mittal et al., 2011]. During the first stage (cool flame) ignition, significant heat release can take place in the hotter core region, but with no heat release in the cooler crevices. This can cause additional mass transfer from the reaction chamber to the crevice volume, reducing the overall pressure and temperature rise. Mittal et al. [2013] have suggested the use of crevice containment method to overcome this problem. This employs a normal seal (O-ring) to isolate the crevice from the main reaction chamber when the piston reaches end of compression (Fig. 3.5). During compression, the crevice is connected to the reaction chamber to capture the roll up vortex but after compression they are disconnected to avoid mass transfer from the reaction chamber to the crevice.

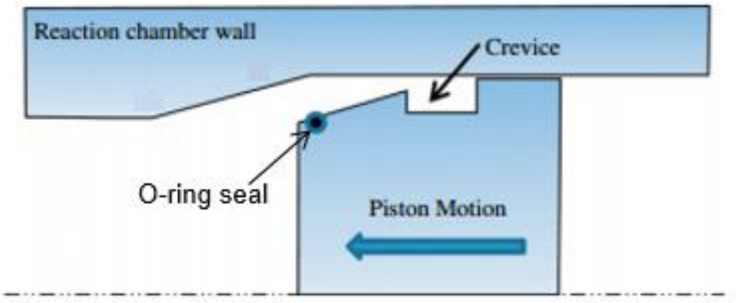

Figure 3.5. Schematic of stepped combustion chamber with O-ring seal for crevice containment [Mittal et al., 2012].

To achieve the same effect, the University of Leeds RCM had a slightly different arrangement between its piston head and combustion chamber. The machine uses a stepped combustion chamber with piston seals which are wider than the piston end (by 1.5 mm), therefore creating a gap between the cylinder wall and the actual piston end (Fig. 3.6). The roll up vortices generated from the movement of the seal against the cylinder will be rotated within this gap. At the end of compression, the piston end makes a close fit contact with the stepped combustion chamber entrance and thus essentially separates the chamber from the cold gas. This helps to suppress the cold gas entering the main combustion chamber as well as ensuring no mass transfer occurs between the crevice and main mixture during heat release.

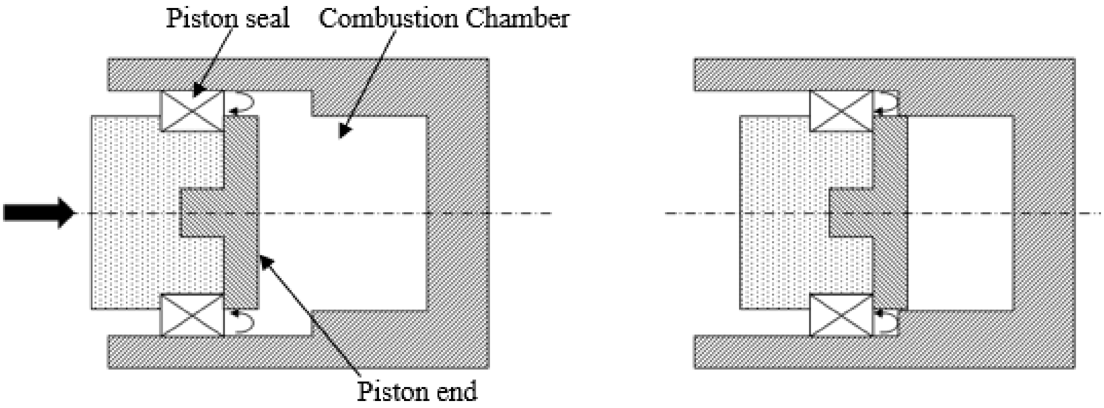

Figure 3.6. Sketch of the Leeds RCM piston and combustion chamber arrangement

Shown in Fig. 3.7 are CFD model results for heat distribution within the combustion chamber from the end of compression up to 50 ms after compression. The model was conducted by Dr. Gary Sharpe, University of Leeds, using air at initial conditions of atmospheric pressure and temperature. Only a small jet of cold stream gets into the combustion chamber at the end of compression. The bulk section virtually remains homogeneous during this time.

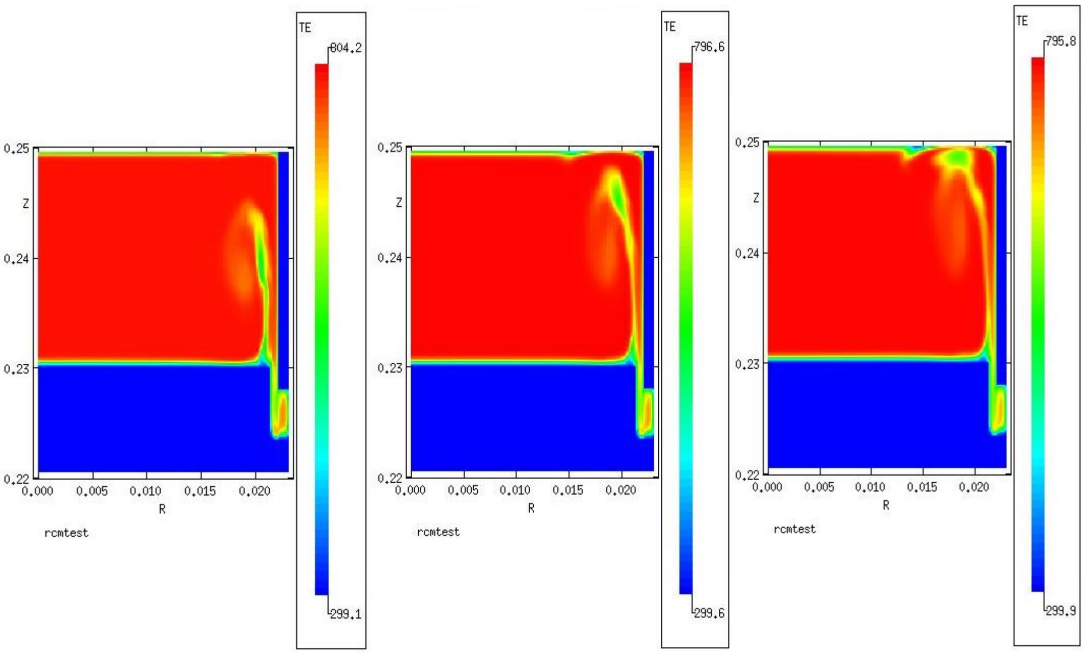

Figure 3. 7. CFD model for heat distribution for Leeds RCM combustion chamber

3.2.4 Use of diluent gases and their effects in RCM experiments.

Inert gases are normally used as diluents in the fuel mixture in order to change the specific heats and therefore increase the range of temperature that can be achieved at the end of compression. In RCM experiments, the reactant fuel is only a small fraction of the mixture volume (fuel mole fractions of < 2%) [Donovan et al., 2004]. The bulk of test gas mixture is made up of diluent gases which take no part in the chemical reactions, yet their thermal properties have the potential to affect the measured delay times. Wurmel et al. [2007] conducted experiments in an RCM using pure helium, xenon, argon and nitrogen, and compared their pressure traces during and after compression. As shown in Fig. 3.8 Xe, Ar and He have higher ratios of specific heats (γ) than N_2, and therefore from the same initial pressure and compression ratio, N_2 attains lower pressure and temperature at the end of compression pressure than monatomics. However, after compression N_2 shows the least whilst He shows the highest pressure drop, due to the higher γ and thermal diffusivity of He, see Table 3.1. Consequently, the use of He results in significant heat loss after compression and the measured delay times will be longer than with N_2. For this reason, He is not recommended as a diluent in RCM experiments, and Ar is preferred. However, care must be taken, especially when the ignition delay times measured are longer than 20 ms. Fig. 3.9 from Wurmel et al. [2007] shows the measured ignition delay times of 2, 3-dimethylpentane (DMP) using different diluent gases. Clearly, He as the diluent gives significantly longer ignition delay times than argon over a comparable temperature range.

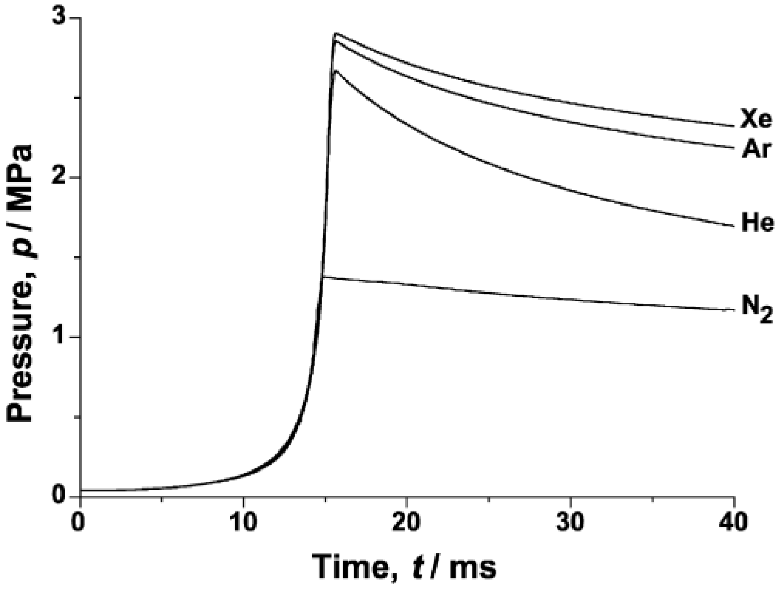

Figure 3.8. Pressure traces for typical diluent gases, compressed from the same initial pressure (0.04MPa) and temperature (298K) [Wurmel et al., 2007].

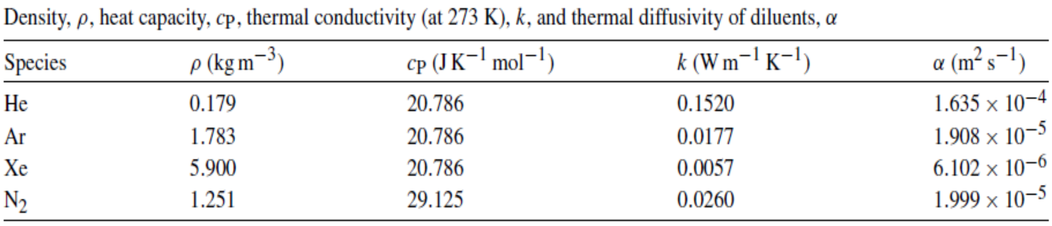

Density, ρ, heat capacity, c_P, thermal conductivity (at 273 K), k, and thermal diffusivity of diluents, α

Species	ρ (kg m^{-3})	c_P (J K^{-1} mol^{-1})	k (W m^{-1} K^{-1})	α (m^2 s^{-1})
He	0.179	20.786	0.1520	1.635×10^{-4}
Ar	1.783	20.786	0.0177	1.908×10^{-5}
Xe	5.900	20.786	0.0057	6.102×10^{-6}
N_2	1.251	29.125	0.0260	1.999×10^{-5}

Table 3.1. Thermal and physical properties of diluents used in RCMs. [Wurmel et al., 2007]

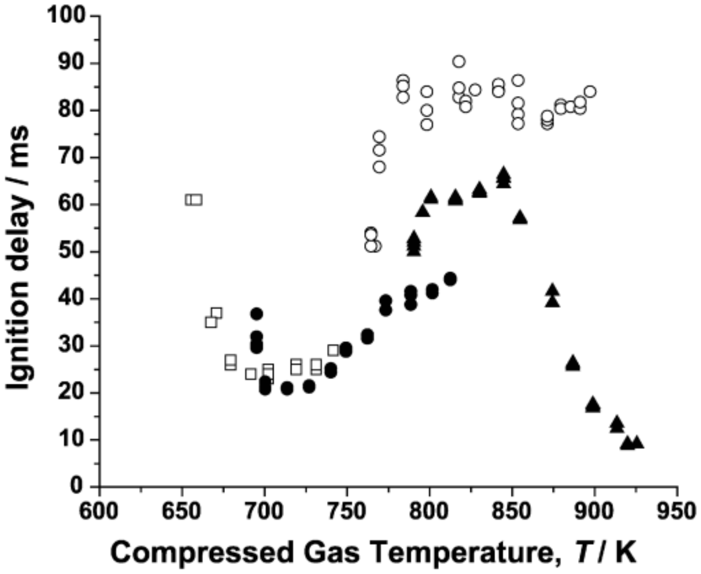

Figure 3.9. Ignition delay times of stoichiometric Dimethylpentane (DMP), Pressure 1.5 MPa; bath gas: (□) N_2 only, (●) 0.50 N_2:0.50 Ar, (▲) Ar only, (○) He only [Wurmel et al., 2007].

3.3 Characterisation of discrepancies of ignition delay times of *iso*-octane measured from different RCMs.

To advance our understanding of the non-ideal behavior of RCM operation, and how they affect the measured ignition delay times, an international collaborative effort was initiated by thirteen diverse research groups that included experimentalists, modellers, and theoreticians, with expertise in their use. The aim was to evaluate and understand the differences in the ignition delay times that were measured with the different RCMs [Goldsborough, 2012].

A Consortium was created for this initiative and it was agreed that the various machines, of different designs, should measure the ignition delay times of *iso*-octane under nominally the same conditions. The composition was to be stoichiometric, with a fixed oxygen content of 21%, pressure at the end of compression, P_o, of 2.0 MPa, and in the temperature range 650K-950K. The required variations of temperature at the end of compression, T_o, were to be attained by changing the initial temperature, varying the amounts of diluents with different specific heats (N_2, Ar and CO_2), or adjusting the compression ratio via stroke and/or clearance height modification. The results were submitted and collated by the workshop organisers, Argonne National Laboratory, and presented at the 2nd International RCM Workshop [Argonne National Laboratory, 2012].

The collection of experimental data from the consortium presented an opportunity to attempt corrections for the various experimental errors. The present Chapter analyses these diverse experimental measurements of delay time, τ_e, obtained from the different RCMs, in an attempt to increase understanding of the departures of the RCMs from their ideal performance, and suggest how allowances for these departures might yield more accurate values of τ.

3.3.1 Experimental Results and Derivation of τ_e

Figure 3.10 shows the experimental values of auto-ignition delay times, τ_e, following normal custom, plotted against $1000/T_o$, measured with the seven RCMs of the Consortium. Each point is identified by a numbered symbol, unique to the RCM of each participating group. Table 3.2 shows these assigned RCM numbers together with their corresponding groups. It can be seen that there is significant scatter in τ_e, especially at the intermediate and low temperatures. It is emphasised that the performances of all the RCMs are those at the time that the data were submitted to the Consortium. They are no guide to their present performance at the different centres.

Assigned RCM numbers	Participating group
RCM 1	Argonne National Laboratory
RCM 2	National University of Ireland Galway
RCM 3	University of Akron (with crevice containment)
RCM 4	University of Lille
RCM 5	University of Leeds
RCM 6	University of Connecticut
RCM 7	University of Akron (without crevice containment)

Table 3.1. Different participating groups with their corresponding assigned RCM numbers.

Three rather different compression pressure-time traces, aimed at attaining similar conditions, on RCMs 1, 5 and 6 are shown in Fig. 3.11. The experimental ignition delay time, characterised by P_o and T_o, is, the difference in the times measured from the end of compression (point *o* at time zero) to the maximum rate of pressure rise, designated as point *i* (i.e. $\tau_e = t_i - t_o$).

Clearly, the machines have different compression times, and because of the different rates of change of pressure and temperature, different degrees of reaction occur during compression. This contributes to the different values of τ_e. Other contributory causes are heat loss after compression, possible piston bounce, and non-uniform ignition. All these causes are considered in turn.

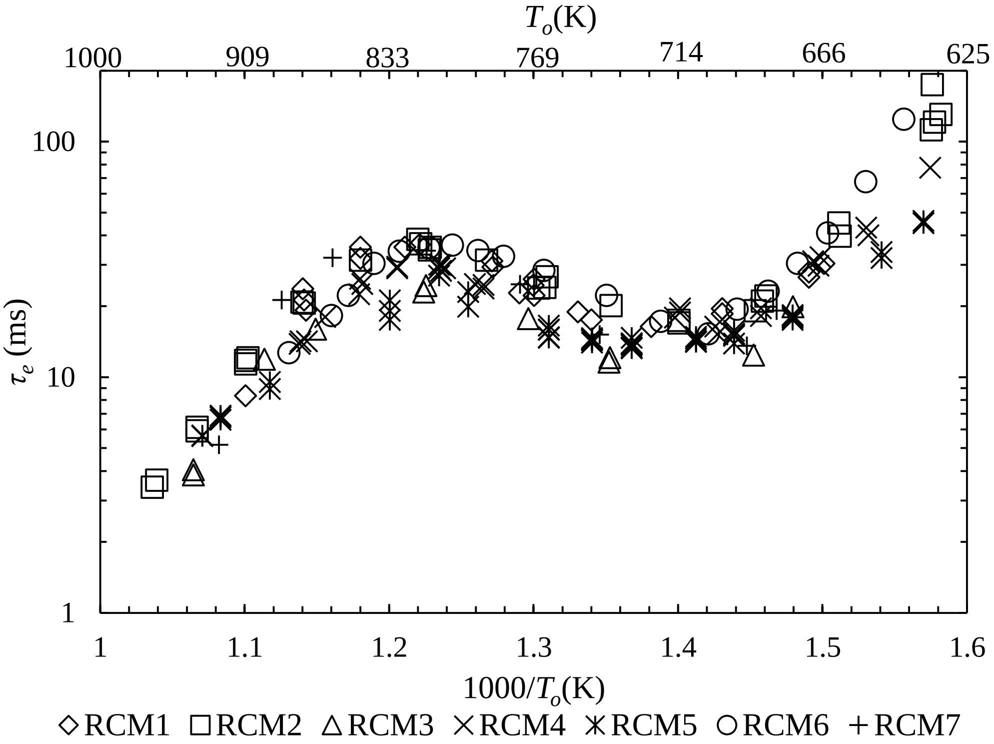

Figure 3.10 Auto-ignition delay times, τ_e, of stoichiometric *iso*-octane from the different RCMs, plotted against end of compression reciprocal temperature T_o (P_o~2.0MPa) [Argonne National Laboratory, 2012].

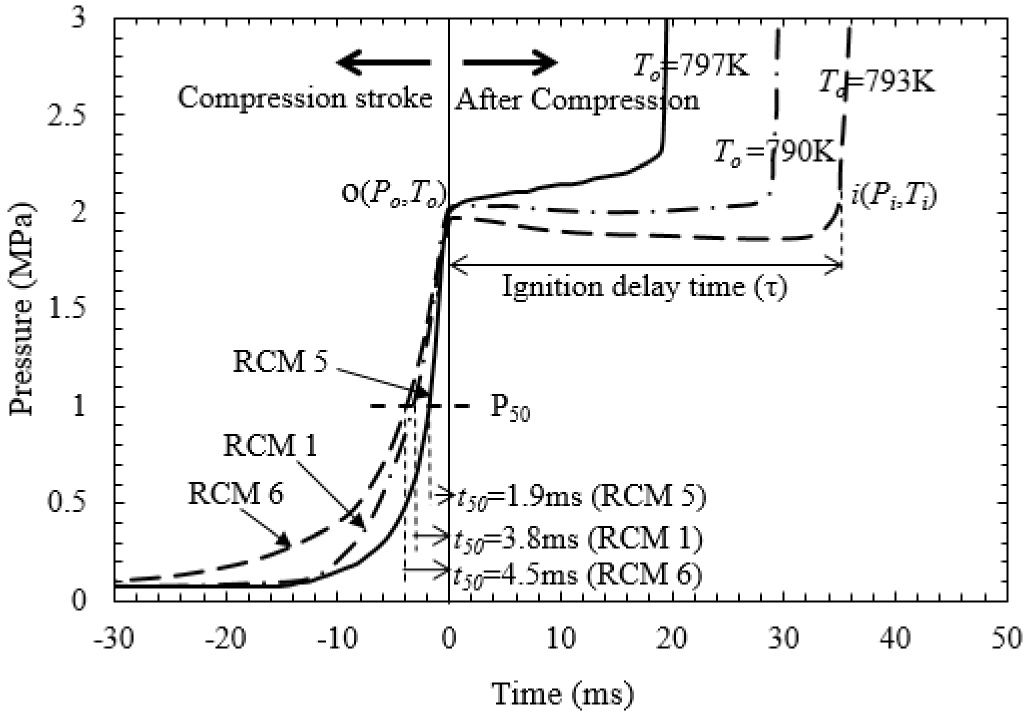

Figure 3.11 Pressure traces for RCMs 1, 5, and 6 at end of compression conditions (Po~2.0MPa, To= (790K-797K)).

3.3.2 Effects of heat loss.

3.3.2.1 Derivation of τ_m

During the cooling following compression, and due to any piston bounce, which is considered in detail in Section 3.3.4.2, the temperature of the adiabatic core, *T*, is determined from the measured pressure, *P*, using the isentropic law:

$$\frac{T}{T_o} = \left(\frac{P}{P_o}\right)^{\frac{\gamma-1}{\gamma}} \tag{3.4}$$

where γ is the ratio of specific heats for the mixture.

It is clear that the auto-ignition is not determined uniquely by the values at P_o and T_o, but by values that are continually changing. To allow for the changing values during the auto-ignition delay time, a mean temperature and pressure, T_m, and P_m, are calculated, and the original measured delay time τ_e is then attributed to these mean values, rather than to T_o and P_o.

The mean temperature is obtained from:

$$T_m = \frac{1}{t_i - t_o} \int_{t_o}^{t_i} T \, dt \tag{3.5}$$

and the mean pressure similarly, from:

$$P_m = \frac{1}{t_i - t_o} \int_{t_o}^{t_i} P \, dt \tag{3.6}$$

Leakage of reactants from the cylinder and combustion chamber, during and after compression, is assumed to be negligible.

The original experimental delay time τ_e is now attributed to T_m and P_m, rather than T_o and P_o.

Figure 3.12 shows the values of τ_e, as in Fig. 3.10, but now designated as τ_m for the mean temperature, T_m, plotted against 1000/T_m. Values of P_m ranged between 1.8 and 2.28 MPa. The solid line in Fig. 3.12 represents the polynomial curve fit through the data points. Comparison of Fig. 3.12 with Fig. 3.10 shows an improved agreement between the different RCMs, especially at the high and low temperature limits. However, a substantial scatter is still evident, particularly, in the negative temperature coefficient, NTC, region. It should be noted that there are fewer data points in this case. This is because not all the pressure traces were available at the time of analysis.

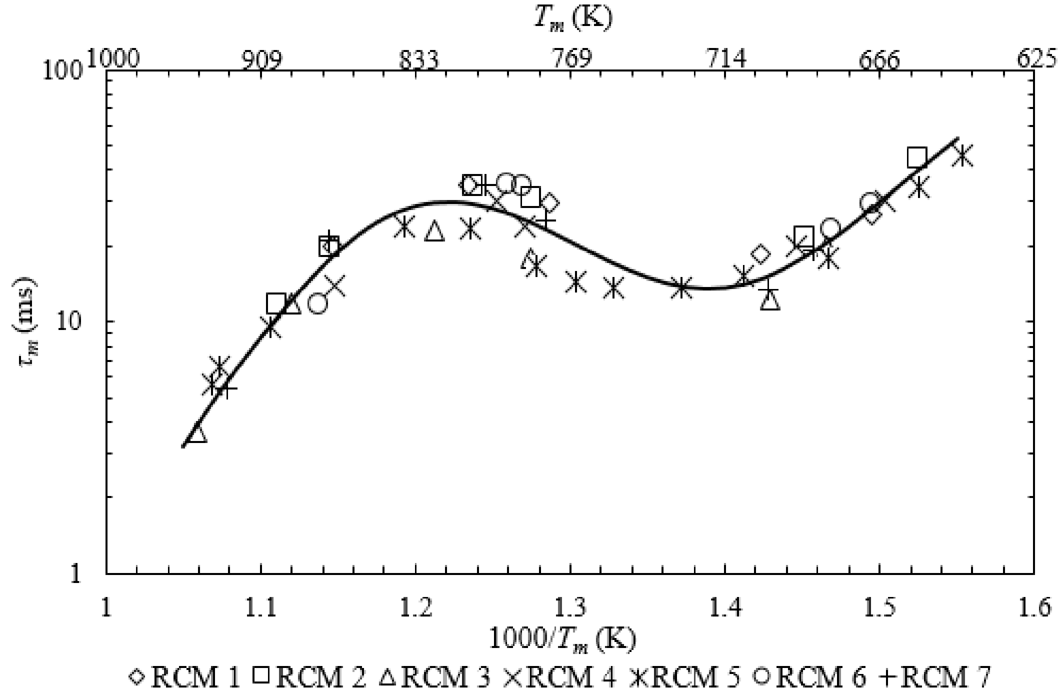

Figure 3.12 Delay time, τ_m, for stoichiometric iso-octane plotted against reciprocal mean temperature, T_m, P_m =1.8-2.28 MPa.

3.3.2.2 Derivation of τ_o

The measured delay times, τ_m, now associated with T_m and P_m, following convention, should be attributed to the values at the end of compression, T_o and P_o.The influence of this pressure change on τ was expressed by an inverse pressure proportionality, P^{-n}. Localised values of the exponent *n* were obtained from the pressure law adopted at the Argonne National Laboratory for iso-octane in the ranges of equivalence ratio, ϕ, 0.2-2.0, pressure 0.1-6.0 MPa and temperature 650K-2000K [Goldsborough, 2009]. Figure 3.13 shows these values of *n* for different temperatures at a pressure of 2.0 MPa and ϕ = 1.0.

The influence of temperature was expressed by:

$$\tau \,\alpha\, \exp(E/RT)\,. \tag{3.7}$$

Localised values of *E/R*, the activation temperature, were found, iteratively, initially by differentiating the values of $\ln\tau_m$ after applying the pressure correction, with respect to the inverse of T_m, using:

$$E/R = \partial \ln \tau_m / \partial(1/\ T_m) \quad . \tag{3.8}$$

Figure 3.14 shows the localised values of *E/R* found by differentiations of the curved line relationship in Fig. 3.12, throughout the temperature range.

Values of the revised delay time, τ_o, in terms of P_o and T_o, were found from those of τ_m using these values of *n* and *E/R* in the expression:

$$\tau_o(P_o, T_o) = \tau_m \left({}^{P_o}/_{P_m}\right)^{-n} exp\left({}^{E}/_{R}\left(\frac{1}{T_o} - \frac{1}{T_m}\right)\right) \tag{3.9}$$

The resulting values of τ_o for the seven different RCMs are plotted against $1000/T_o$ in Fig. 3.15. It can be seen that the scatter, particularly in the negative temperature coefficient, NTC, region, has been reduced.

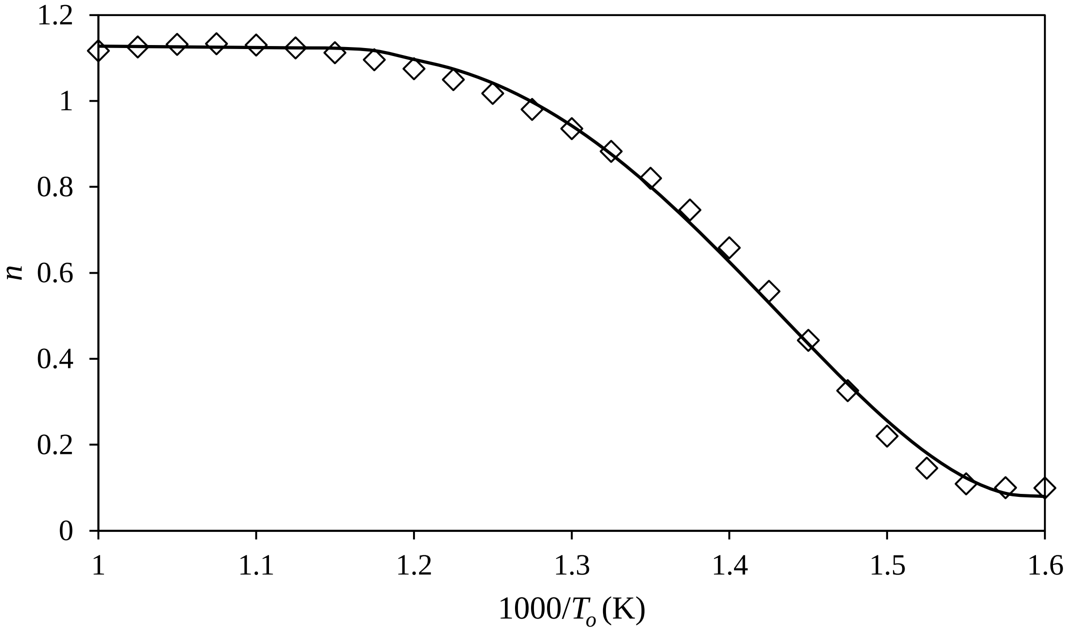

Figure 3.13 Values of n for stoichiometric iso-octane at P_o=2.0 MPa and different compression temperatures, T_o, from Goldsborough [2009].

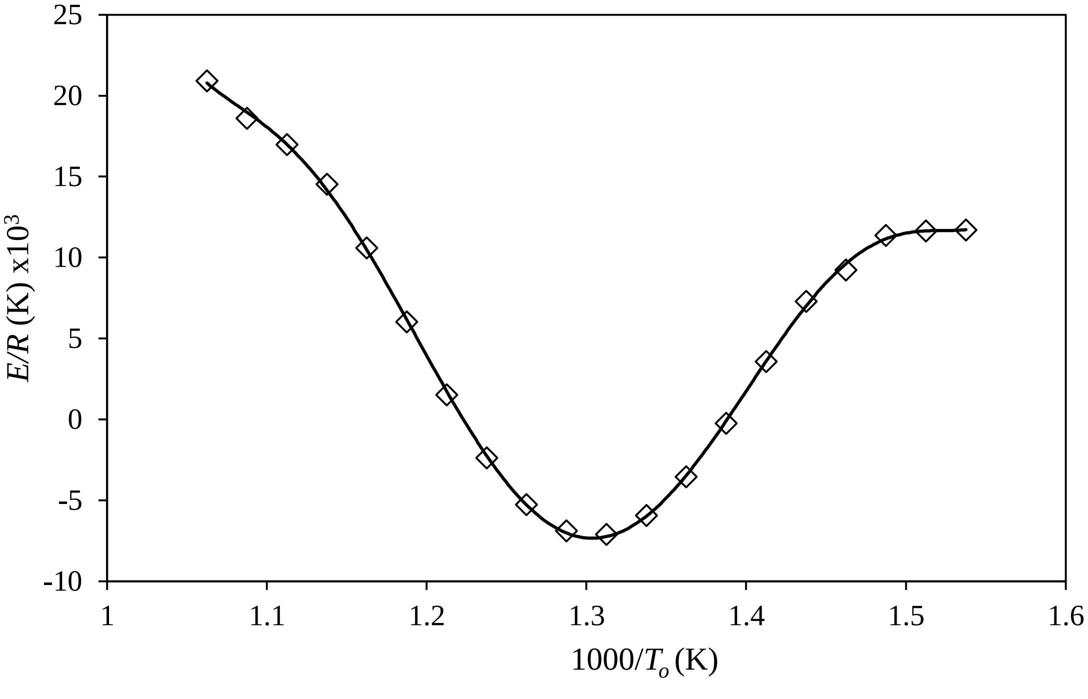

Figure 3.14. Localised activation temperatures, *E/R*, at P_o =2.0MPa, derived from Fig. 3.12.

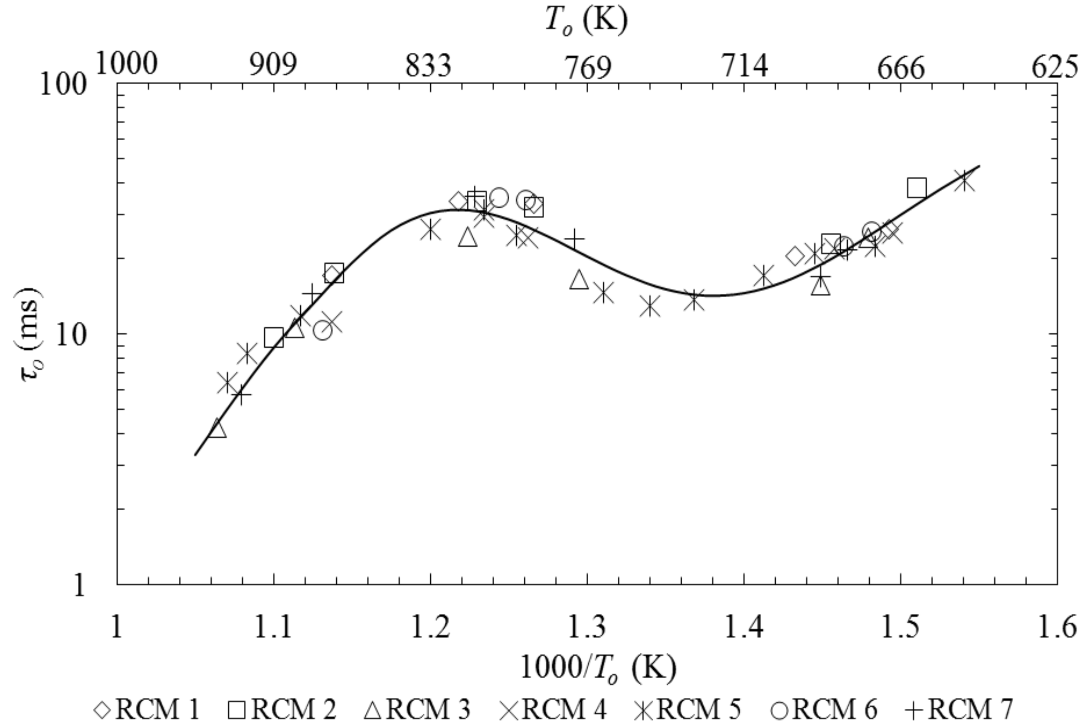

Figure 3.15. Corrected delay time, τ_o, of stoichiometric iso-octane for T_o, and P_o =2.0 MPa.

3.3.3 Effects of Reaction during Compression and Derivation of τ_c.

3.3.3.1 Livengood-Wu integral during compression.

It was proposed at the Workshop to employ the time, t_{50}, for compression from 50% of the peak pressure, P_{50}, to P_o to characterise the rapidity of compression. The significant increases in temperature during compression will initiate reaction, and the different compression pressure traces in Fig. 3.11 are indicative of the different degrees of reaction to be expected in each RCM.

An attempt was made to allow for this effect by evaluating the value of the Livengood-Wu integral (LWI) [Livengood and Wu, 1955] for the duration of the compression, at the end of which, P_o and T_o are attained. This integral evaluates the progress towards auto-ignition through an integration of the reciprocal ignition delay time with regard to time, under the changing P and T of the compression:

$$\int_{t_s}^{t_o} \frac{dt}{\tau(P,T)} = (LWI)_o, \tag{3.10}$$

where t_s and t_o are the times at the start and end of compression, respectively. The ultimate approach of the integral towards unity is a good guide of the progress towards auto-ignition.

Evaluation of the integral requires a knowledge of $\tau(P, T)$ under the changing conditions of P and T, at values below P_o and T_o. These values were obtained from the ignition delay correlation model generated in [Goldsborough, 2009]. The model is based on a detailed chemical kinetic mechanism of *iso*-octane auto-ignition and tested against 661 *iso*-octane experimental points from different RCMs and shock tubes. Very good agreement was attained between the model and experimental results in the pressure range of 0.1-6 MPa, and the temperature range of 650-2000K.

Fig. 3.16 shows typical calculated values of LWI during and after compression for different RCMs at more or less similar temperatures. Each RCM shows different progression towards *iso*-octane auto-ignition, values of $(\text{LWI})_o$ are extracted from such plots at time=0, which indicates end of compression. For different end of compression temperatures, T_o, the calculations of $(\text{LWI})_o$ showed, not surprisingly, that its value increased with T_o and that it had significantly different values for all the RCMs. Those with shorter compression times had smaller values of $(\text{LWI})_o$. Shown in Fig. 3.17 are plots of $(\text{LWI})_o$ for the different RCMs as a function of $1000/T_o$. Values of t_{50} also are given. There is significant scatter in the points, but clear trends nevertheless emerge, with $(\text{LWI})_o$ increasing with the higher reaction rates at higher temperatures, at which there is, on average, about 10% reaction progress towards auto-ignition. The compression time t_{50} for a given RCM remained unchanged.

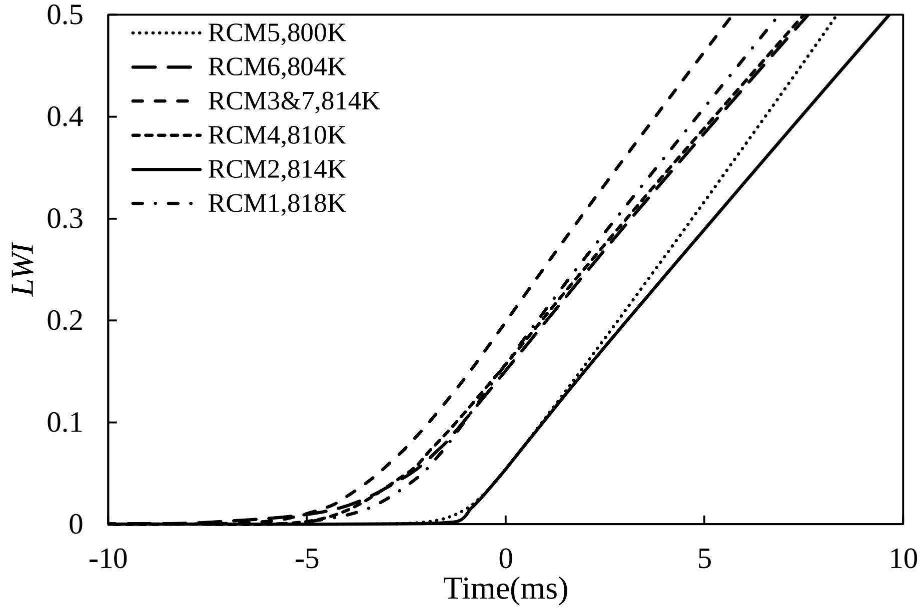

Figure 3.16. Calculated values of LWI during and after compression for different RCMs at similar temperatures.

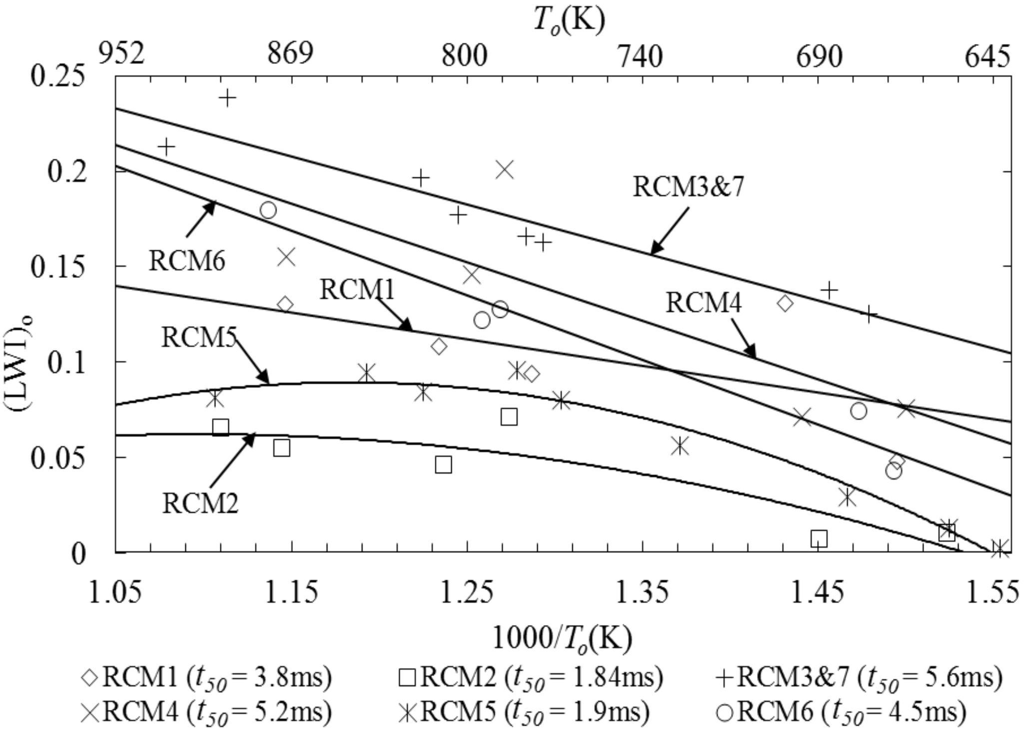

Figure 3.17. Calculated $(LWI)_o$ for different RCMs at selected temperatures T_o, P_o=2.0 MPa.

3.3.3.2 Derivation of τ_c.

From Fig. 3.17 it is possible to find the values of $(LWI)_o$ at any value of T_o for each RCM. Values of τ_o are known for all these conditions from the individual points in Fig. 3.15. These τ_o values are plotted against $(LWI)_o$ for all the different RCMs, at sequentially decreasing values of T_o in Figs. 3.18-3.21. The smallest error in the measurement of τ_o occurs at the lowest T_o, see, for example, Fig. 3.21. Ideally, the compression should be instantaneous, in which case (LWI)$_o$ would be zero. Consequently, in these figures, the values of τ_o are extrapolated to (LWI)$_o$ = 0, to give a corrected value of τ_o, namely τ_c. These "corrected" values, τ_c, are plotted against 1000/T_o by the full line curve on Fig. 3.22. The symbols indicate the originally measured RCM values of τ_e.

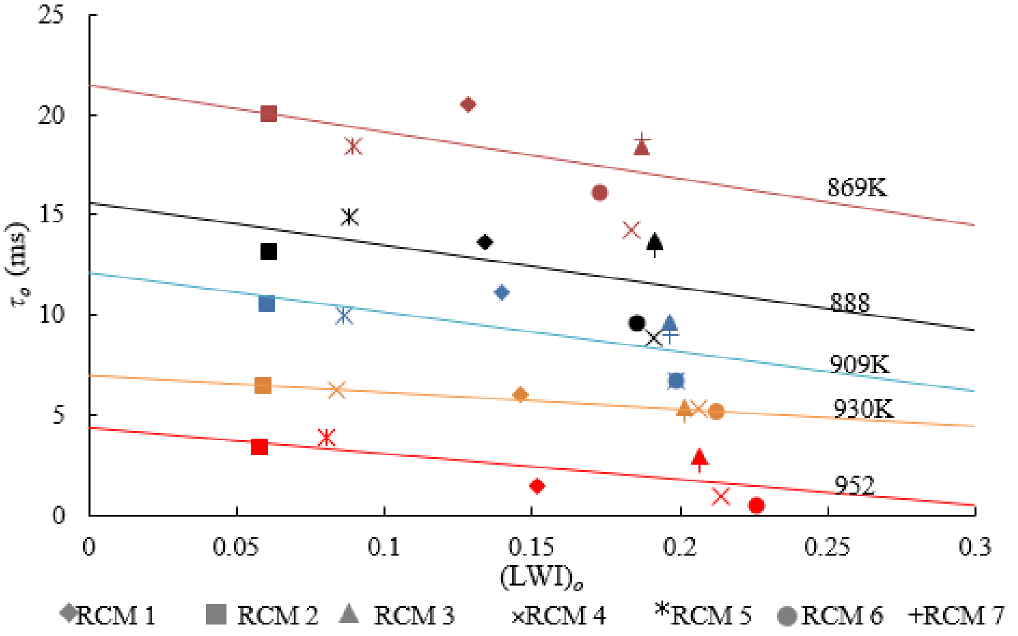

Figure 3.18. Derivation of τ_c from τ_o by extrapolation to (LWI)$_o$=0 for different RCMs, at different To, Po=2.0 MPa.

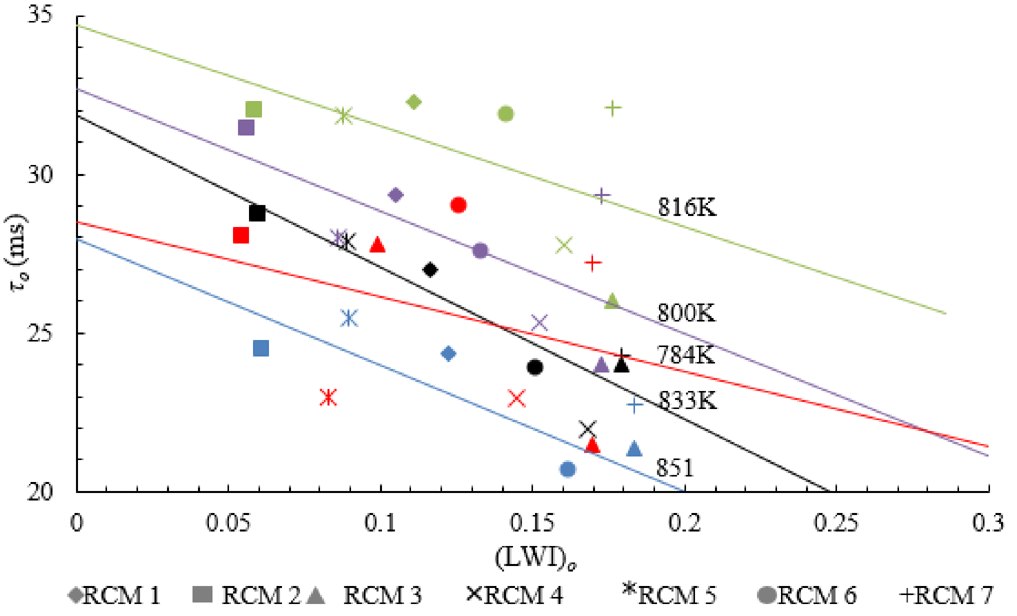

Figure 3.19. Derivation of τ_c from τ_o by extrapolation to (LWI)$_o$=0 for different RCMs, at different T_o, P_o=2.0 MPa.

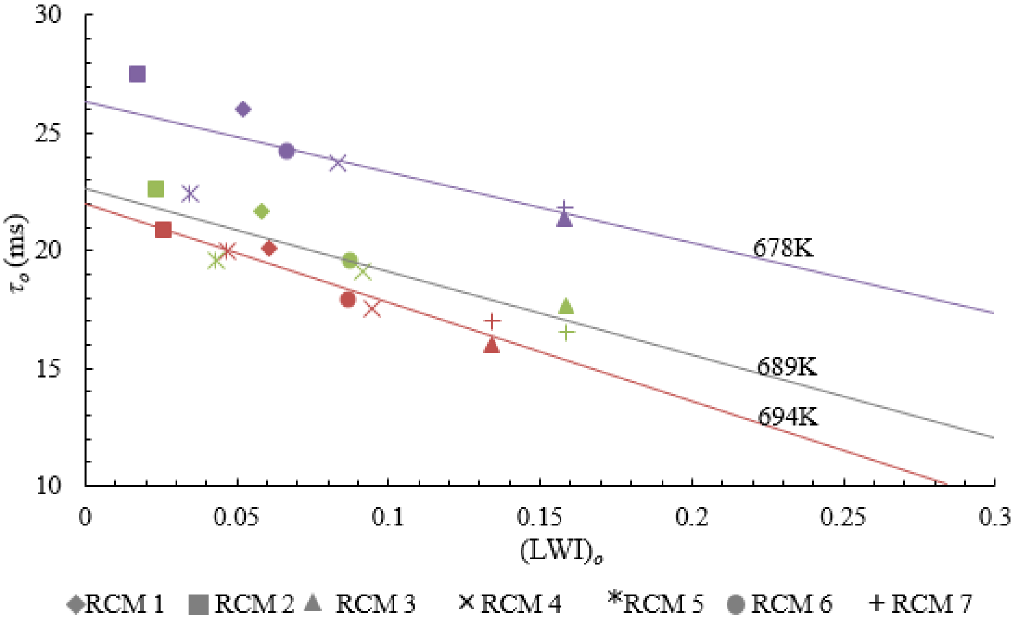

Figure 3.20. Derivation of τ_c from τ_o by extrapolation to (LWI)$_o$=0 for different RCMs, at different T_o, P_o=2.0 MPa.

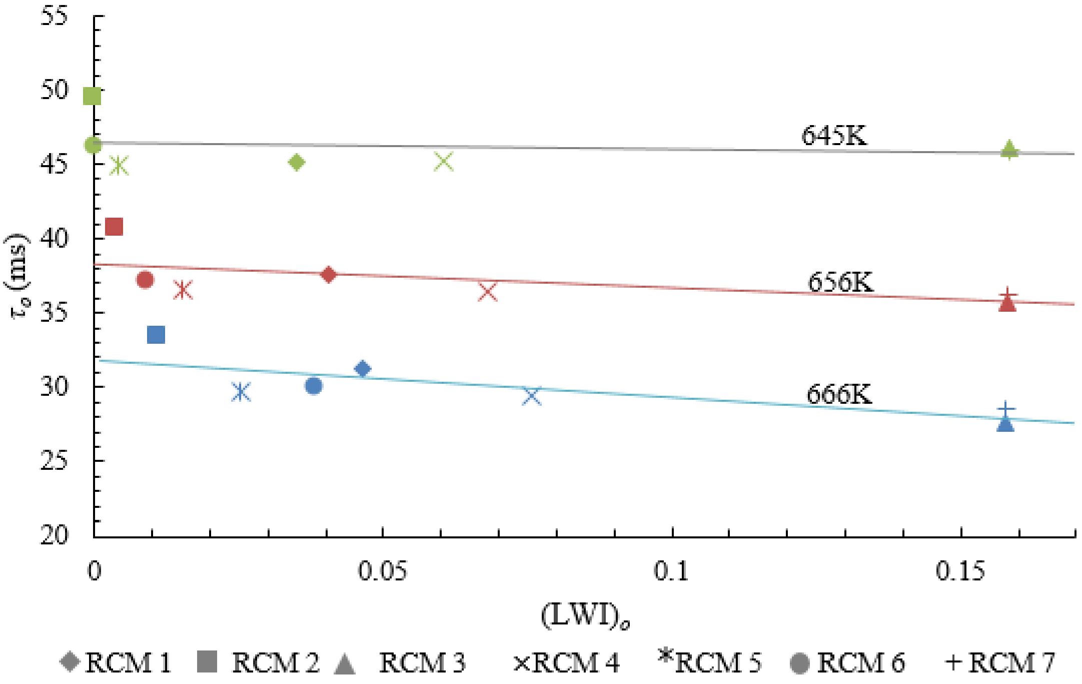

Figure 3.21. Derivation of τ_c from τ_o by extrapolation to (LWI)$_o$=0 for different RCMs, at different T_o, P_o=2.0 MPa.

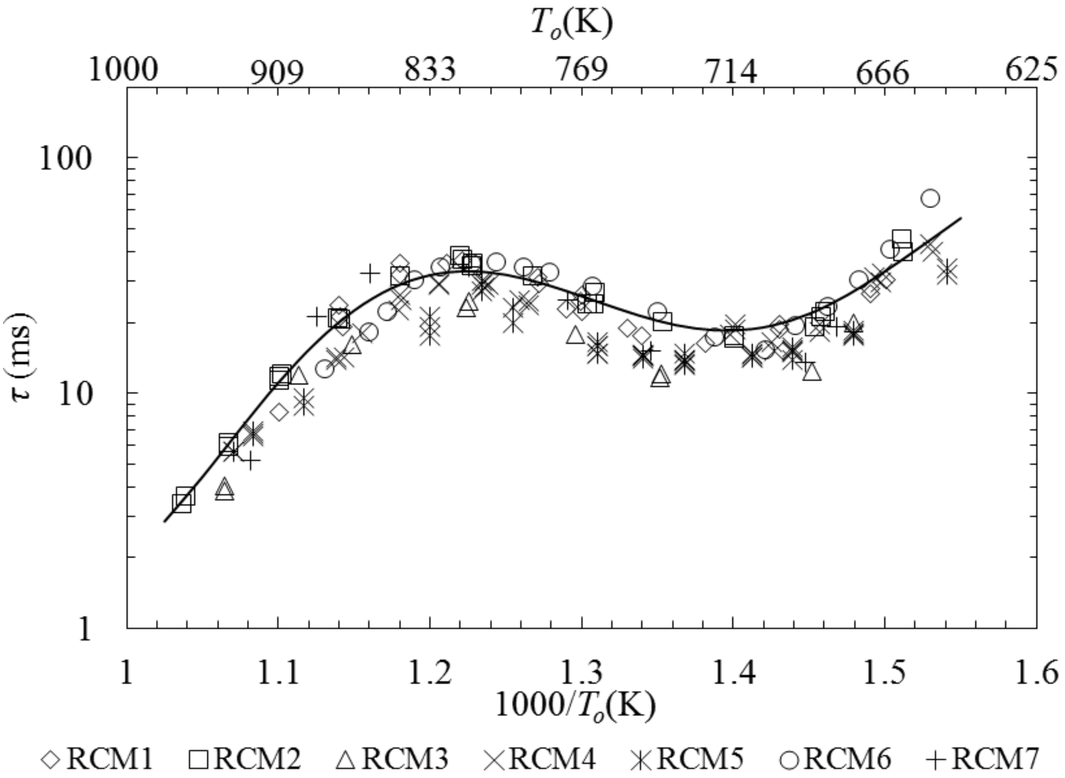

Figure 3.22. Continuous curve shows derived ideal “corrected” values of ignition delay times,τc, for stoichiometric iso-octane at the measured T_o and P_o=2.0 MPa. Symbols show original measured points, τ_e.

This methodology advantageously uses the different compression times of all the different RCMs to estimate the ignition delay for an ideal RCM. Apart from the low temperature values, where there is less reaction during compression, τ_c is higher than the original experimentally measured values and τ_o. In general, the values of τ_c are higher than those of τ_o, a consequence of the absence of reaction during compression. Values of *E/R* obtained from the full line curve in the figure were close to those originally derived, and a second round of computational iteration produced no significant change in τ_c.

Figure 3.23 summarises the different stages in this attempt to derive the ignition delay times for idealised RCM operation. The different lines are the polynomial curve fits from Figs. 3.10, 3.12, 3.15 and 3.22. They show the associated sequential values of delay times at each stage (τ_e, τ_m, τ_o and τ_c) plotted against 1000/T_o.

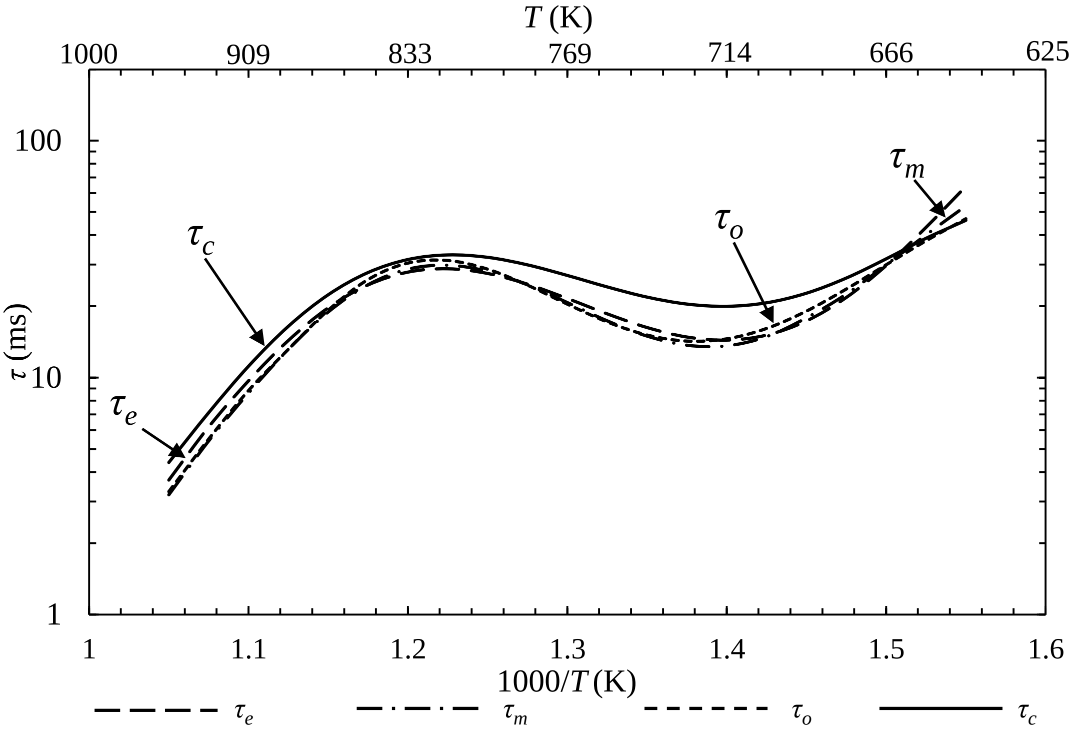

Figure 3.23. Original experimental, τ_e, and derived ignition delay times (τ_m, τ_o, τ_c) for stoichiometric iso-octane at P_o=2.0MPa.

It is very interesting to note in Fig 3.23 that the measured delay time error caused by reactions during compression is substantial compared to that caused by heat loss, there is no much difference between the corrected delay times based on heat loss, τ_o, and the original measured values, τ_e. It can also be noted that the largest overall correction is seen within the intermediate temperature range. Fig. 3.24 shows a plot of the difference between the final corrected values, τ_c, and the original measured values, τ_e, throughout the temperature range. It can be seen that the largest correction occurs at the temperature range where NTC behaviour occurs and diminishes towards the lower and higher temperatures. This shows measured delay times are more reliable at high and low temperatures but less so at the intermediate temperatures. Differences of up to 5.6 ms are obtained for this temperature range. It is also important to note that this correction may be different for different fuels due to their differences in reactivity. Therefore, it is difficult at this stage to generalise this correction for all fuels and conditions. More studies are needed from the consortium to enable such generalisations to be made. Nevertheless, this particular work has shown a possible way to make corrections to the measured ignition delay times caused by non-ideal behaviour of different rigs.

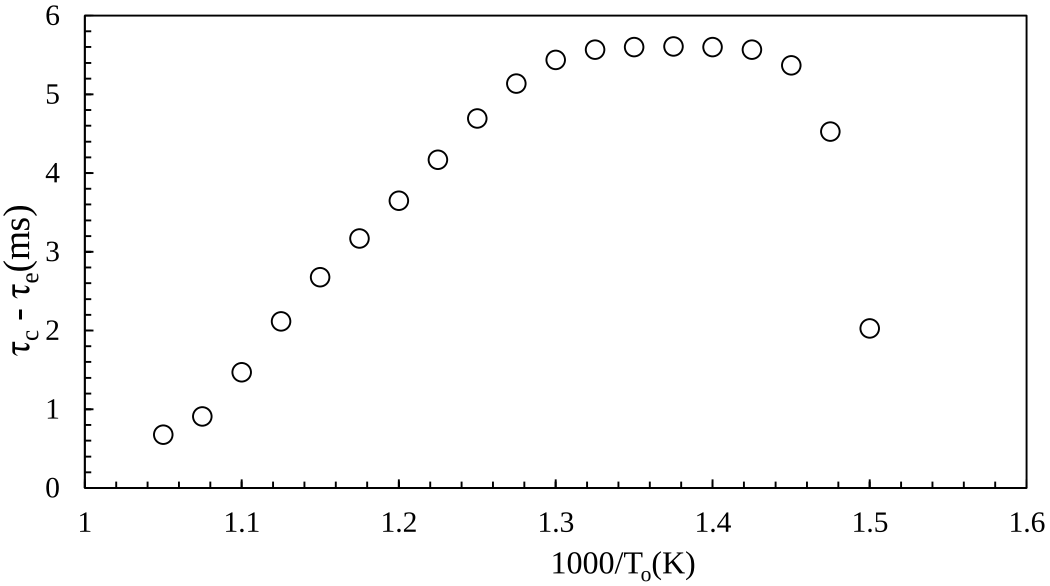

Figure 3.24. Difference between overall corrected values, τ_c, from experimental values τ_e throughout the temperature range.

3.3.4 Implications of the corrections to Leeds RCM measurements.

As it was discussed in section 3.2.3, the extent of reactions during compression is affected by the compression time. The longer the compression time the higher the amount of reactions during compression. NUIG (RCM 2) has the shortest compression time followed by Leeds (RCM 5) as shown in Fig. 3.17. Due to its relatively faster compression, correction of measured delay times to account for reactions during compression is limited to a maximum of 15% for Leeds RCM whereas for slower RCMs such as RCM 3 the required corrections were up to 36%.

The difference in the heat loss characteristics of these RCMs is mainly affected by their combustion chamber geometry and corresponding surface area to volume ratio (S/V). Since all RCMs studied in this work had cylindrical shape then their S/V ratio played a major role. It was not possible to get the actual dimensions of the combustion chambers and their crevices for different rigs in this study. However, it was evident that the RCMs with non-contained crevice after compression (RCMs 1, 2, 4, 6 and 7) had higher heat loss than others. This is due to their associated higher S/V ratio after compression, the additional crevice volumes result into increased ratio and hence higher heat loss. Shown in Fig. 3.25 is the amount of pressure drop after end of compression (t=0) for different RCMs and it can be seen that Leeds RCM (RCM 5) and Akron with crevice containment (RCM 3) show the least post compression pressure drop than others and this makes the required correction due to heat loss to be less significant for Leeds RCM. At lower temperatures where heat loss effects are maximum, Leeds RCM shows a maximum correction of delay times up to 2.5ms which is 7.4% decrease of original measured value, whereas RCM 7 shows a maximum decrease of 22%. This is in line with the results obtained in section 4.7 in chapter 4 when comparison for Leeds RCM was made between simulated delay times calculated using variable and constant volume approaches. No significant difference between them was obtained.

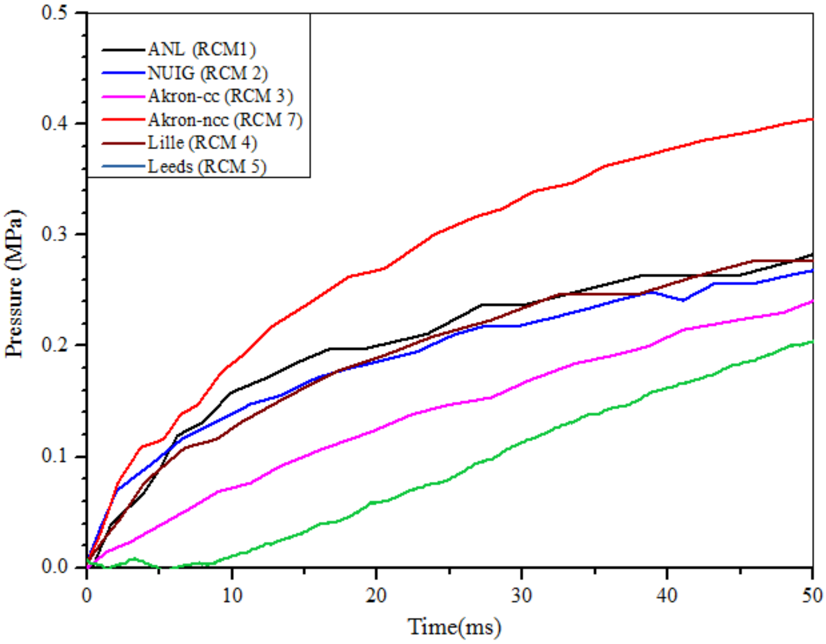

Figure 3.25. The amount of pressure drop with time after end of compression (t=0) for different RCMs.

For the rest of the data presented in this work pressure measurements of non-reactive mixtures for different fuels at different temperatures were compared and shown in Figs. 3.26-3.28 for three different temperatures. The pressure histories after compression were seen to follow the same trend which confirms that there is no substantial change in heat loss characteristics for the fuels studied in this work. Compression time was kept constant for all experiments during this work to ensure reactions during compression is minimum. Therefore, the corrections due to heat loss and reactions during compression for the rest of the data in this work can be considered to be within similar range to those seen by *iso*-octane in this chapter.

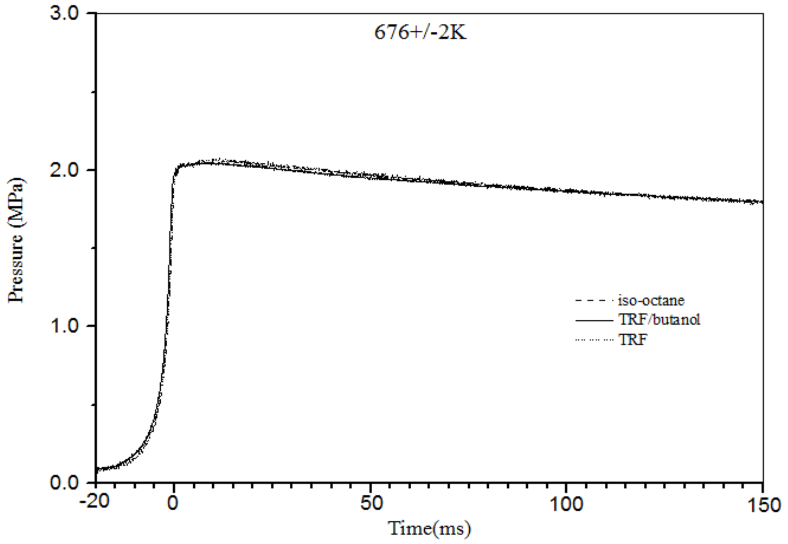

Figure 3.26. Pressure history for non-reactive mixtures at T_o=676+/-2K.

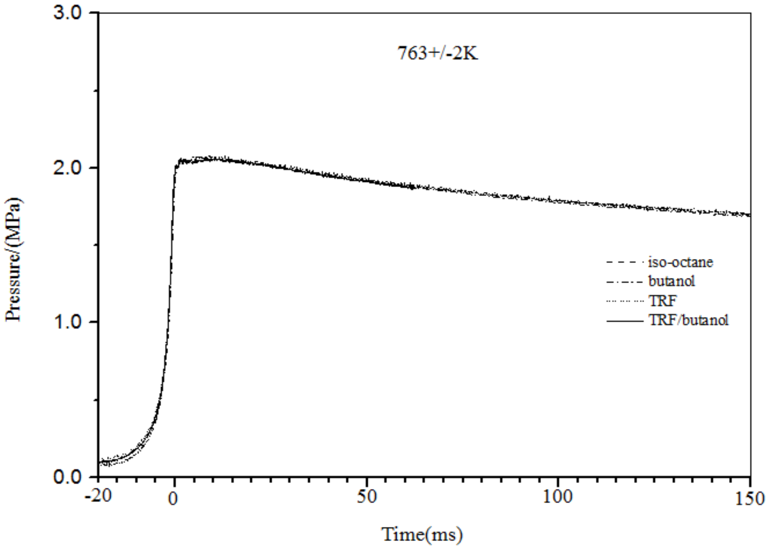

Figure 3.27. Pressure history for non-reactive mixtures at T_o=763+/-2K.

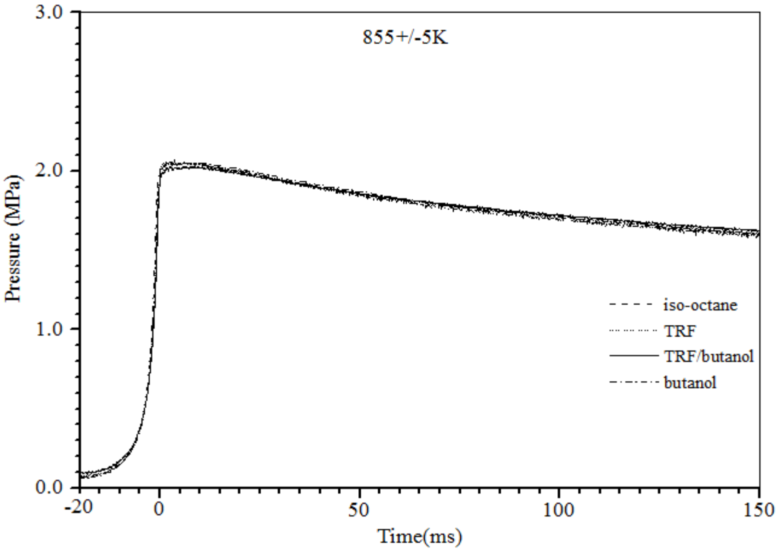

Figure 3.28. Pressure history for non-reactive mixtures at T_o=855+/-5K.

3.3.5 Overall Livengood-Wu integrals,. Auto-ignitive Explosions, and Piston Bounce.

3.3.5.1 The overall Livengood–Wu integral.

The ultimately derived values of auto-ignition delay time, τ_c, and the associated corrected experimental pressures and derived temperatures for each RCM, were employed to evaluate the Livengood-Wu integral, that now extended from the start of compression at time t_s up to the auto-ignition at point i, at t_i. Values of this integral, $(\mathrm{LWI})_i$, are given by:

$$\int_{t_s}^{t_i} \frac{dt}{\tau_c(P,T)} = (\mathrm{LWI})_i \qquad (3.11)$$

These are shown by the associated symbols for each RCM, plotted against $1000/T_o$, in Fig. 3.29. The best full line curve through the points has values close to unity, with a tendency to fall below unity at the highest temperatures.

This is in sharp contrast to values of the integral, that were based on the original experimental auto-ignition delay times, τ_e, temperatures and pressures, as indicated by Fig. 3.10, for the different RCMs. These integrals, the separate points for which are not shown, exhibited a much greater scatter and deviation from unity, with limits that extended to the broken curves in Fig. 3.29. The integral values based on τ_c are much closer to unity and this is indicative of improved accuracy.

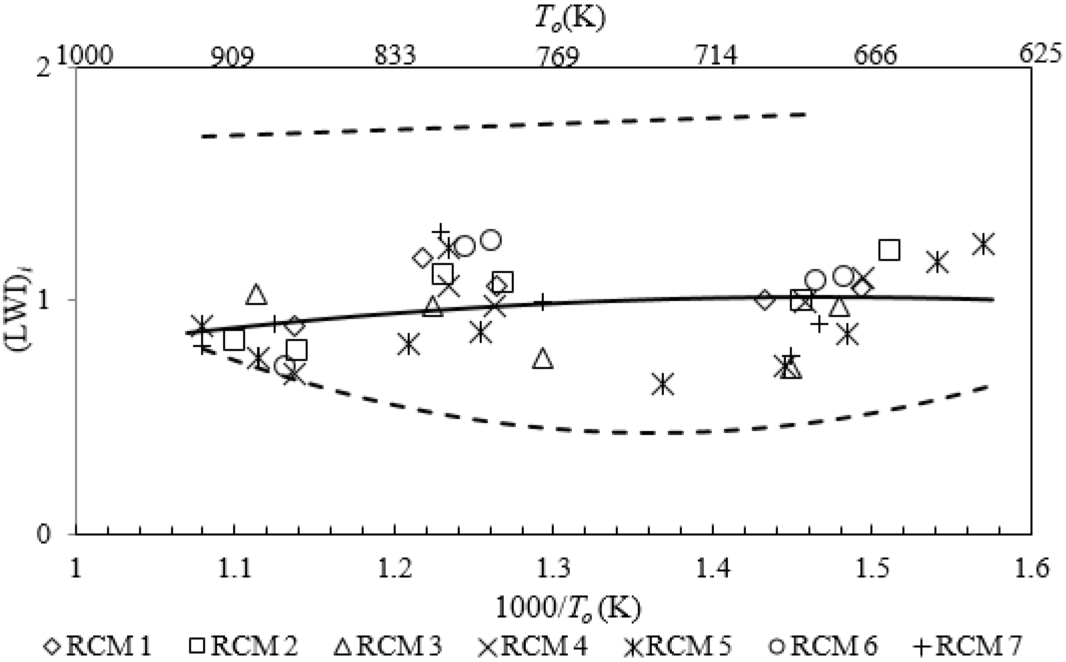

Figure 3.29. Calculated $(LWI)_i$ values using the original experimental temperatures and pressures in the different RCMs, but with the associated derived values, τ_c. Broken curves show the upper and lower limits of the integral when the original experimental values, τ_e, were employed in the evaluation.

The end of the auto-ignition delay time is marked by a rapid explosion, the severity of which increases with T_o. A single RCM, namely RCM5, was selected for a detailed study of such auto-ignition, and the pressure-time traces in Fig. 3.30 show this mounting severity, and the onset of pressure oscillations, over a range of T_o values. There are no oscillations at T_o = 650K, but they begin to emerge at T_o = 713K. The pressure traces show them to intensify as T_o increases.

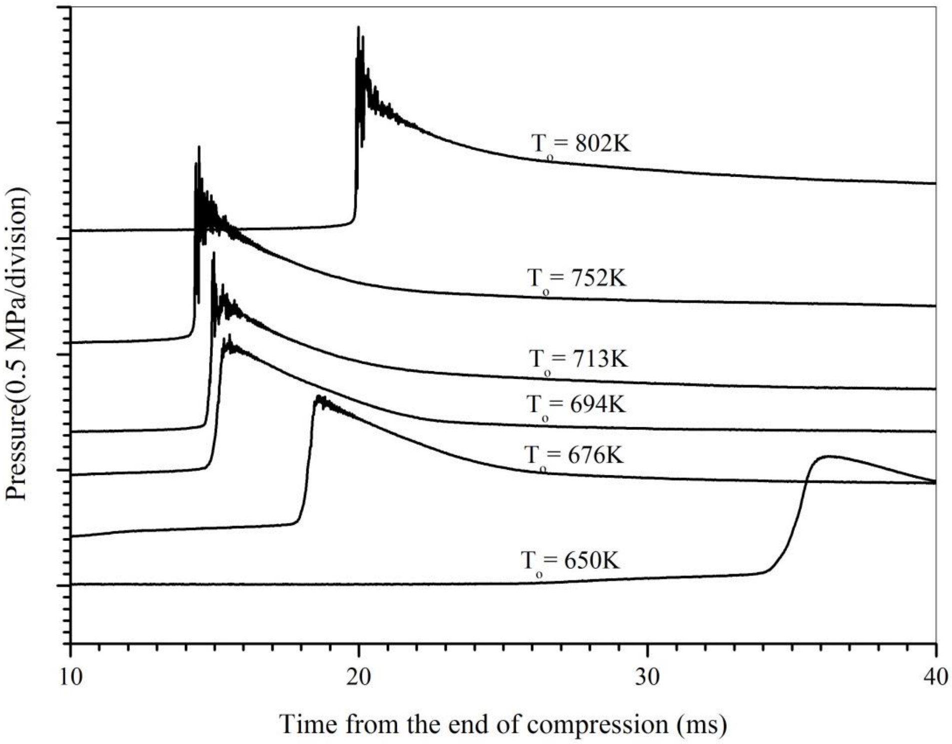

Figure 3.30. Pressure records from RCM 5 with auto-ignitions at six different end of compression temperatures, T_o. P_o = 2.0 MPa.

3.3.5.2 Piston bounce.

The question arises as to whether the high frequency pressure oscillations are gas dynamic manifestations of the explosion, or consequences of the piston re-bounding, or "bouncing", from its intended stationary position, and even oscillating about it. To explore this further, an attempt was made to measure the displacement of the extended piston rod optically, as described in Section 2.1.7.3. In normal operation the piston bounce was minimised, but in order to study its effects, controlled amounts of more extensive bounce were introduced by fine tuning of the piston damping mechanism and the compression pressure.

Air was compressed to 2.7 MPa in an initial investigation of controlled larger piston displacements. The sharply decreasing, near-vertical, line in Fig. 3.31 shows the rapid compression to time 0. Thereafter, the piston bounce is indicated by a positive displacement that diminishes relatively slowly as the piston returns to its intended position, with no displacement, after 18 ms. The volume of air is correspondingly increased and decreased, and the pressure decreased and increased. These changes induce an, assumed isentropic, cooling and heating, from which the associated pressure changes could be calculated. There was also cooling of the air due to heat transfer at the walls, apparent from the pressure record after 20 ms.

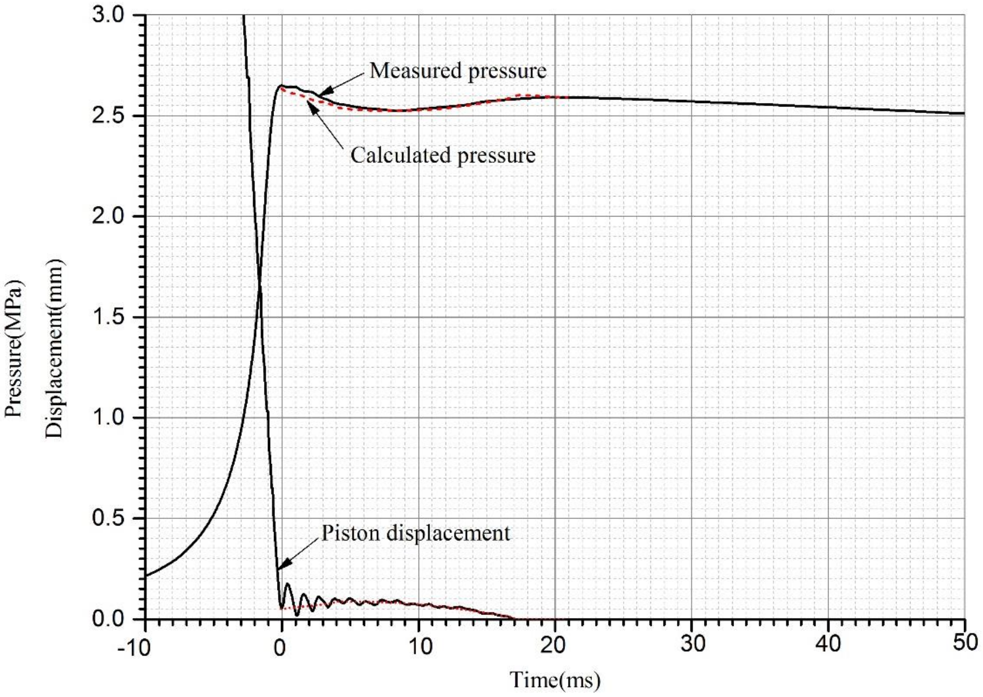

Figure 3.31. Pressure and piston displacement measurements for non-reactive mixture (air) with piston bounce.

The dotted pressure curve on Fig. 3.31 was calculated from these mean volume changes, neglecting the high frequency displacement oscillations, with the heat transfer inferred from the falling pressure after 20 ms. When allowance was made for the high frequency displacement oscillations the calculated pressures also showed such oscillations. The dotted, non-oscillatory, pressure curve on this figure was close to that measured by a high resonant frequency (≥80 kHz) Kistler 6045A dynamic pressure transducer. Importantly, the fact that the measured pressure trace only responded to the mean displacements, and not to the initial two high frequency cycles measured by the laser beam, implies that the origin of the high frequency component of the piston rod oscillation did not lie in the piston bounce. It would appear that the high frequency vibrations monitored by the reflected beam were generated by the combined RCM with its support structure, and the externally extended piston rod, laser head, and reflection plate.

3.3.5.3 Auto-ignition explosions.

Returning to the origins of the high frequency pressure oscillations, of the type shown in Fig. 3.30, at auto-ignition, Figs. 3.32 and 3.33 show the temporal variations of pressure and piston displacement during both the initial compression, and also the two contrasting auto-ignitions. As in all the auto-ignition delay time measurements, the piston bounce was minimised in these measurements. In contrast to the greater bounce in Fig. 3.31, in, both Fig. 3.32, T_o=650K, and Fig. 3.33, T_o=802K, the initial compression bounce is similar, and only occupies about 3 ms, with no significant associated pressure decrease after the compression. At auto-ignition the displacements are similarly comparable, but there are no significant pressure oscillations at 650K. In contrast, there are strong pressure oscillations at 802 K. After a delay of about 3 ms there is a greater displacement than at the end of compression, very similar in both cases. Only at 802K do strong pressure oscillations develop, and this occurs before there is any piston displacement. Clearly, the high frequency oscillations at auto-ignition at 802K are not related to piston bounce and there must be some other cause.

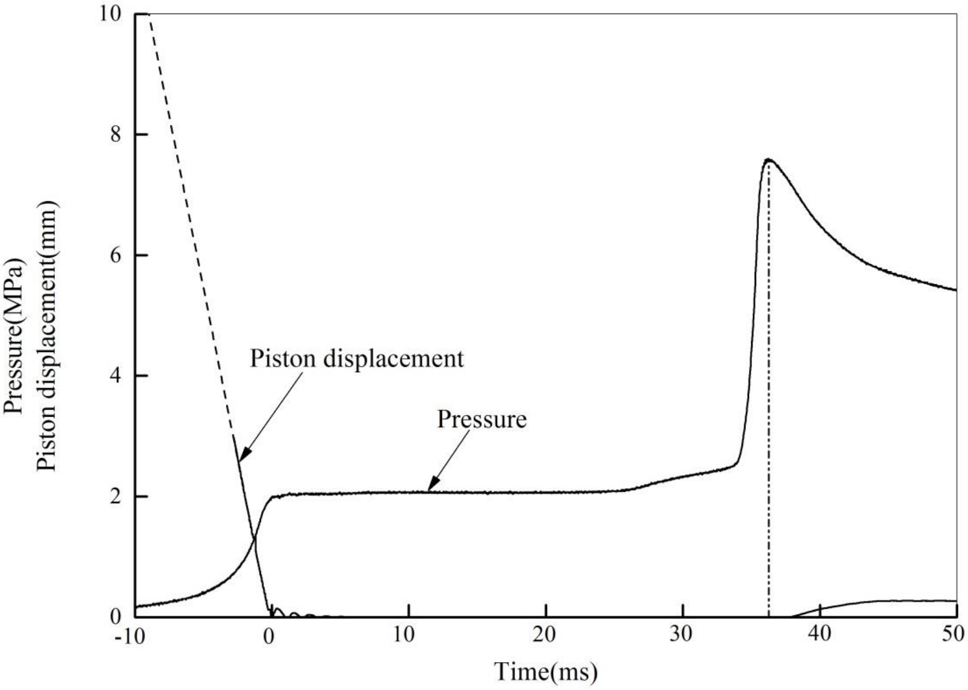

Figure 3.32. Pressure trace and piston displacement measurements at T_o =650K.

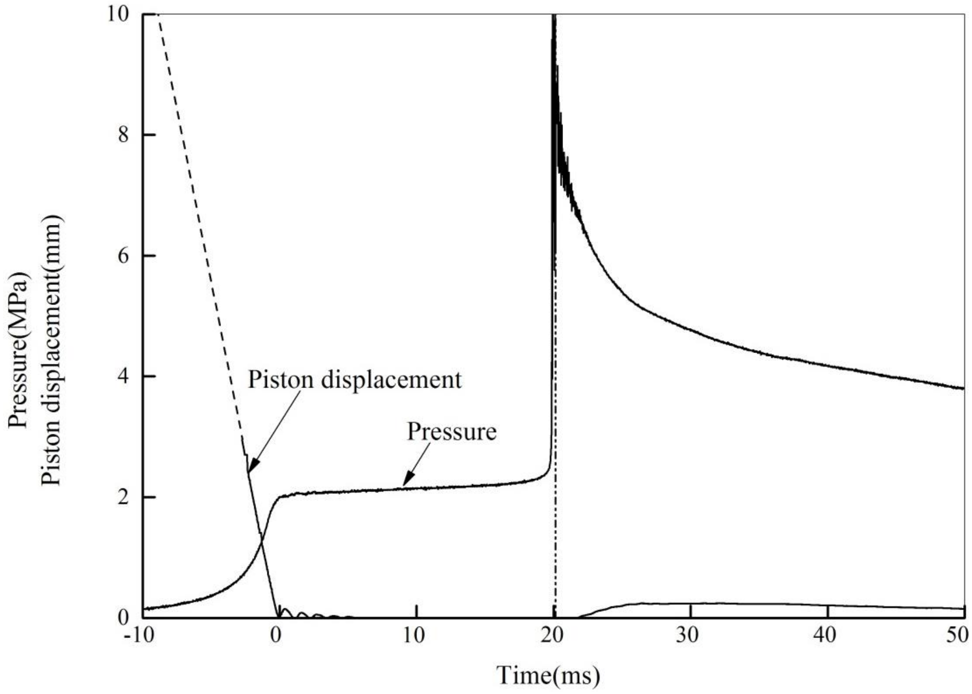

Figure 3.33. Pressure trace and piston displacement measurements at T_o =802K.

At the higher temperatures, the decrease in values of $(LWI)_i$ below unity with increasing temperature in Fig. 3.29 suggest the possibility of hot spot auto-ignitions that are more reactive and stronger than the milder ones at lower temperatures. Hot spot temperature elevations can be quite small, of the order 1K, which does not represent severe heterogeneity. Perfect homogeneity is unlikely, and it is normal for auto-ignition to be initiated at hot spots [Bradley, 1996]. Gradients of reactivity at hot spots can induce appreciable localised velocities, u_a, which at a spherical hot spot of radius, r, are given by $\partial r/\partial \tau$. When this gradient is associated with a temperature difference [Gu et al., 2003]:

$$u_a = \partial r/\partial \tau = (\partial r/\partial T)(\partial \tau/\partial T)^{-1} \tag{3.12}$$

[Meyer and Oppenheim, 1971] showed experimentally that "strong ignitions" were associated with low values of $(\partial \tau/\partial T)$ and "mild ignitions" with high values of both $(\partial \tau/\partial T)$ and τ. [Fieweger et al.,1997] suggested in their shock tube studies that localised low temperature auto-ignitions were mild, with ensuing slower flame speeds and an absence of pressure oscillations. In contrast, at higher temperatures the auto-ignitions were strong, with a higher rate of change of the energy release rate and the generation of shock waves. The evidence of Figs. 3.29, 3.32 and 3.33 is in line with these observations.

At low values of $\left(\partial\tau/\partial T\right)$ u_a can become appreciable and approach the acoustic velocity, a. The pressure pulse amplitude, generated by the rate of change of the heat release rate at a hot spot, increases in proportion to $(u_a/a)^2$ [Bradley and Kalghatgi, 2009]. If the excitation time is short enough for sufficient energy to feed into the pressure pulse, a detonation can develop [Gu et al., 2003]. The relevance of hot-spot auto-ignition to the intensity of engine knock is discussed in Bates et al. [2015].

3.3.5 Summary.

The diversity of the different RCMs has been advantageously utilised to increase understanding of the departures of the RCMs from their ideal performance. It is emphasised that the performances of all the RCMs are those at the time that the data was submitted to the Consortium. They are no guide to their present performance at the different centres. Allowances have been made for the effects of reaction during compression, the heat loss thereafter, and piston bounce. The different corrections to the measured auto-ignition delay times result in an increase in their values at intermediate and high temperatures. Auto-ignition is usually at hot spots, which initiate a flame or a propagating auto-ignition that, depending upon the strength of the associated shock wave, might initiate detonation. The strong pressure oscillations observed at the higher temperatures arise from this evolution.

More accurate values of auto-ignition delay times can be derived when

(i). Piston bounce is minimised.

(ii). The compression time is minimised, and allowance made for the effects of reaction during compression.

(iii). Corrections are made for the heat loss and any piston bounce during the auto-ignition delay time.

(iv). The mixture should be homogeneous. Even so, ignition is likely to occur initially at a hot spot. This may not introduce serious error. Ideally, homogeneous auto-ignition should occur in a thermal explosion, but this is usually not possible [Gu et al., 2003].

CHAPTER 4: MEASUREMENTS OF AUTOIGNITION DELAY TIMES.

4.1 Introduction

This Chapter presents the experimental results of ignition delay times of the selected synthetic fuels and their blends. The Rapid Compression Machine described in Chapter 2 was employed to measure the instantaneous pressure within the combustion chamber during and after compression. Ignition delay times were obtained from these pressure traces, as defined and described in Section 1.6.3. The measured ignition delay times are attributed to the end of compression conditions, of pressure, P_o, and temperature, T_o. An isentropic law is used to determine the temperature T_o of the adiabatic core in the combustion chamber;

$$\frac{T_o}{T_i} = \left(\frac{P_o}{P_i}\right)^{\gamma-1/\gamma} \quad , \tag{4.1}$$

where T_i, P_i are the initial temperature and pressure, and T_o, P_o are those at the end of compression temperature and pressure, and γ is the ratio of specific heats. The initial pressure P_i, initial temperature T_i and γ were varied to attain a required end of compression pressure P_o. Variations of γ were made by changing the diluent (Ar, N_2 or CO_2) and/or its concentration in the mixture. The chemical kinetic effects of these diluents on the measured ignition delay times were assumed to be negligible.

The results in this Chapter are presented in terms of pressure traces during and after compression, and ignition delay times are derived from pressure traces measured at different end of compression temperatures.

The fuel and "air" mixture was premixed in the separately heated mixing chamber for 1 hour to ensure proper mixing, as described in section 2.2.6. The required volume of each fuel injected into the mixing chamber was obtained from their mole fraction and total pressure as explained in Section 3.3, and the partial pressure obtained from addition of each individual fuel was checked against the calculated partial pressure and the values were always within ±100 Pa. The temperature and pressure were based on the vapour pressure of the individual fuel, and in the case of the fuel blends, the settings were based on the lowest vapour pressure of the fuel components mixed. This ensured all individual fuels in the blend are fully vapourised. The fuels used and the test conditions are summarised in the tables in each section. The experimental results presented in this Chapter are compared, where possible, with those of other researchers.

4.2 Selection of fuels.

Commercial gasolines contain different classes of hydrocarbons. Tests have shown that up to 80% (by weight) of the gasoline composition consists mainly of alkanes and aromatics [Thomas et al., 1984], of which, more than 12% are aromatics with an appreciable amount of toluene [Diehl et al., 1993]. In this work, the branched alkane (*i*-octane), linear alkane (*n*-heptane) and aromatic (toluene) are chosen as representative of existing commercial gasolines. In addition, alcohols (ethanol and *n*-butanol) are selected because of their growing importance, as described in Chapter 1.

There are few ignition delay measurements for pure *n*-butanol and its blends with other fuels, something the present work attempts to rectify. Ignition delay measurements are made for pure *i*-octane, toluene and *n*-butanol followed by those of blends of *i*-octane/*n*-butanol, toluene/*n*-butanol, toluene/*n*-heptane/*i*-octane/*n*-butanol and toluene/*n*-heptane/*i*-octane/ethanol.

4.3 Blending of fuel/air mixtures.

In all the fuel/air blends in the present work, the blended mixtures have the same equivalence ratio, $\emptyset$. Mixtures have been designated in different ways: by mass, mole and liquid fuel volume. In so far as reaction in terms of moles, conversion between different units is often necessary. This section gives general expressions for conversion between the different units.

From the fundamental definition of stoichiometry, equivalence ratio, $\emptyset$, is given as;

$$\emptyset = \frac{(F/a)}{(F/a)_s} \quad , \tag{4.2}$$

where F is the number of moles of fuel and a is the number of moles of air, and a suffix s indicates a stoichiometric mixture.

$$\text{Thus,} \quad a = \frac{(F/\emptyset)}{(F/a)_s} \quad . \tag{4.3}$$

The total number of moles for fuel and air mixture is given as;

$$F + a = F + \frac{(F/\emptyset)}{(F/a)_s} \quad . \tag{4.4}$$

One mole of fuel/air mixture is comprised of;

$$\frac{F}{F + \frac{(F/\emptyset)}{(F/a)_s}} \text{ fuel } + \frac{(F/\emptyset)\,/(F/a)_s}{F + \frac{(F/\emptyset)}{(F/a)_s}} \text{ air, which} \tag{4.5}$$

$$= \frac{\emptyset}{\emptyset + (a/F)_s} \text{ fuel } + \frac{(a/F)_s}{\emptyset + (a/F)_s} \text{ air} \tag{4.6}$$

If there are x_1 moles of mixtures 1 and x_2 moles of mixture 2, the composition of the blend for these mixtures will be;

$$\left[\frac{1}{\emptyset + (a/F_1)_s}(\emptyset + (a/F_1)_s)\right] x_1 + \left[\frac{1}{\emptyset + (a/F_2)_s}(\emptyset + (a/F_2)_s)\right] x_2, \tag{4.7}$$

If there is one mole of mixture then $x_1 + x_2 = 1$.

At the same $\emptyset$, the ratio moles of fuel 1/moles of fuel 2 is given as:

$$\frac{(\emptyset + (a/F_2)_s)}{(\emptyset + (a/F_1)_s)} \frac{x_1}{x_2} \quad , \tag{4.8}$$

Blends are not always composed of binary constituent fuel/air mixtures, sometimes more than two constituent mixtures are in the blend. In general, the fractional number of moles of all the constituent mixtures is:

$$\sum_{i=1}^{N} \left[\frac{\emptyset}{\emptyset + (a/F_i)_s} + \frac{(a/F_i)_s}{\emptyset + (a/F_i)_s}\right] x_i, \quad \text{with} \tag{4.9}$$

$$\sum_{i=1}^{N} x_i = 1, \tag{4.10}$$

The above form of Eq. (4.8) is helpful because it separates fuel moles and the moles of air. It makes possible to express the mixture in terms of either its fractional fuel ratio or fractional fuel/air ratio for a particular constituent mixture. For example, the mole fraction of constituent fuel/air mixture 1 is:

$$\left[\frac{\emptyset}{\emptyset + (a/F_1)_s} + \frac{(a/F_1)_s}{\emptyset + (a/F_1)_s}\right] x_1 \Bigg/ \sum_{i=1}^{N} \left[\frac{\emptyset}{\emptyset + (a/F_i)_s} + \frac{(a/F_i)_s}{\emptyset + (a/F_i)_s}\right] x_i \tag{4.11}$$

Fuel/air constituent mixtures blends can also be presented in terms of their fractional mass weighting. For example in a binary mixture, the ratio of mass of fuel/air constituent 1 to that of fuel/air constituent 2 is:

$$\left[\frac{\emptyset M_{F,1}}{\emptyset + (a/F_1)_s} + \frac{(a/F_1)_s M_a}{\emptyset + (a/F_1)_s}\right] x_A \left(\left[\frac{\emptyset M_{F,2}}{\emptyset + (a/F_2)_s} + \frac{(a/F_2)_s M_a}{\emptyset + (a/F_2)_s}\right] x_2\right)^{-1}, \tag{4.12}$$

where M_F is fuel molecular weight and M_a is that for air.

Finally, for practical reasons relative amounts of liquid fuels are often measured volumetrically. If V_1/V_2 is relative volume of fuel 1 to fuel 2 then the mole ratio of fuel 1 to fuel 2 is;

$$(V_1/V_2)(\rho_{F,1}/\rho_{F,2})(M_{F,2}/M_{F,1}) \quad = \quad \frac{(\emptyset + (a/F_1)_s)\, x_1}{(\emptyset + (a/F_2)_s)\, x_2} \tag{4.13}$$

where ρ_F, M_F are liquid fuel densities and molecular masses, given in the Table (4.1) for the different fuels studied in this work.

	Molecular mass, M_F (g/mole)	Density, ρ_F (kg/m^3)
i-octane (C_8H_{18})	114.23	690
n-heptane (C_7H_{16})	100.21	684
Toluene (C_7H_8)	92.14	865.14
n-butanol ($C_4H_{10}O$)	74.12	806.11
Ethanol (C_2H_6O)	46.07	789

Table 4.1. Fuel densities, obtained from supplier’s technical data sheet, and molecular masses for the fuels studied in this work.

The volume of liquid fuel injected into the mixing chamber was derived from the mole fraction of fuel to fuel and air. The total number of moles in the mixing chamber was obtained from its total volume and the conditions of pressure and temperature during mixing using the ideal gas expression.

$$n_{total} = \frac{PV}{RT} \tag{4.14}$$

Moles of fuel needs to be injected in the mixing chamber at these conditions will be;

$$n_F = x_F * n_{total} \tag{4.15}$$

These moles are converted into liquid volume using the following expression;

$$v_F = \frac{n_F M_F}{\rho_F} \tag{4.16}$$

4.4 Single fuels results.

Table 4.2 summarises the individual pure fuels and conditions under which they were tested.

Fuel	Condition		
	∅	Pressure (MPa)	Temperature(K)
iso-octane	0.8,1.0,1.2	2.0	640-940
Toluene	0.5	1.0-1.5	1090-1170
	1.0	2.0	915-1050
n-butanol	0.5	2.0	730-945
	1.0	2.0	666-862

Table 4.2. Testing conditions for single fuels.

Repeatability tests were performed to confirm that same results can be reproduced for the same initial conditions. Fig. 4.1 shows 5 different pressure traces for non-reactive mixture (air), measured separately. The curves are in very good agreement which confirm high repeatability. During the course of this work, at least 3 repeats of experiments were performed for each condition. Measurement of total spread between maximum and minimum measured ignition delay times were made and presented by error bars. These were determined by first calculating the mean of collected data points for a particular temperature and then the difference between maximum value and mean was determined to get positive error bar and the difference between minimum value and mean to get negative error bar.

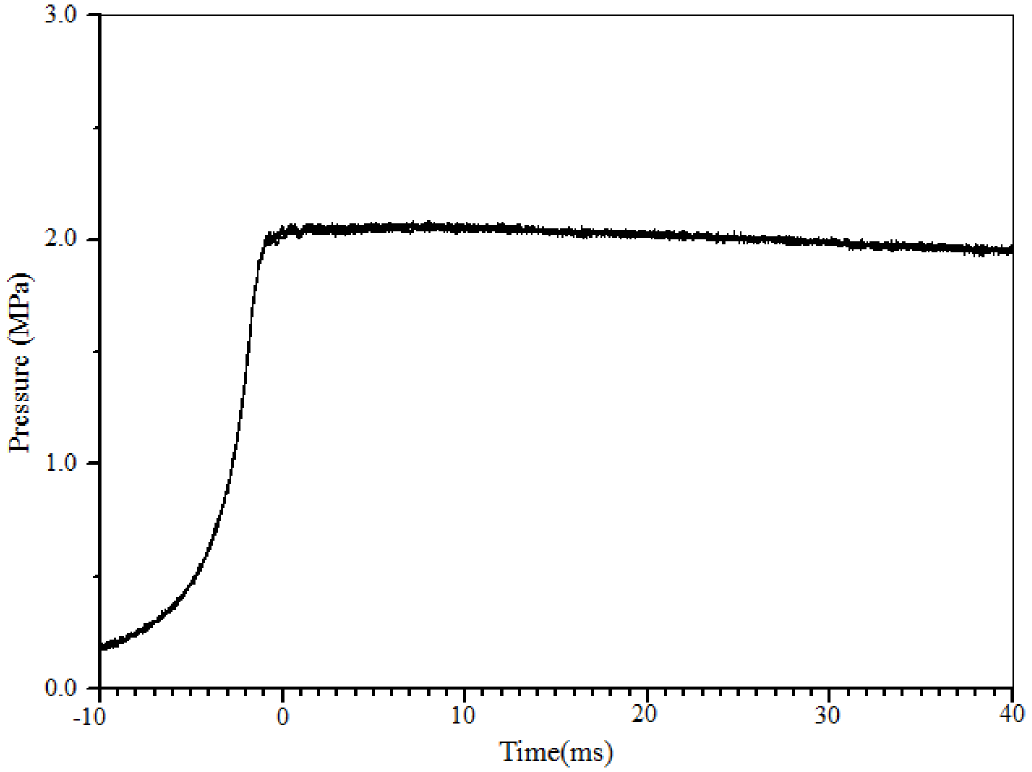

Figure 4.1 Repeatability test for Leeds RCM using pressure history for non-reactive mixture (air).

4.4.1 *iso*-octane.

Shown in Figs. 4.2-4.4 are measured RCM pressure records for stoichiometric, lean (Ø=0.8) and rich (Ø=1.2) *iso*-octane when compressed to a pressure of 2.0 MPa at different compression temperatures. At low to medium temperatures (650K-802K), the occurrence of two stages of ignition is evident, where the first stage is usually attributed to the occurrence of cool flames and the second stage to the main exothermic ignition. At higher temperatures (>900K) a non- cool flame, single stage, main ignition is obtained. Fig. 4.5 shows the corresponding ignition delay times derived directly from these pressure traces. The negative temperature coefficient (NTC) behaviour, where the reaction rates decreases with the increase of temperature, is seen in the medium temperature range (725K-833K). These results agree fairly well with those obtained by other researchers [e.g Griffiths et al., 1993; Westbrook et al., 1998; Davidson et al., 2005; Fieweger et al.,1994]. The effect of equivalence ratio is more pronounced in the NTC region, where the lean mixture (Ø= 0.8) shows an increased delay time, relative to the stoichiometric mixture, while the rich mixture (Ø=1.2) results in a reduced delay time. At higher temperatures there is no significant change of delay times for the equivalence ratios studied in this work, while at the lower temperatures the trends are similar to those in the NTC regime.

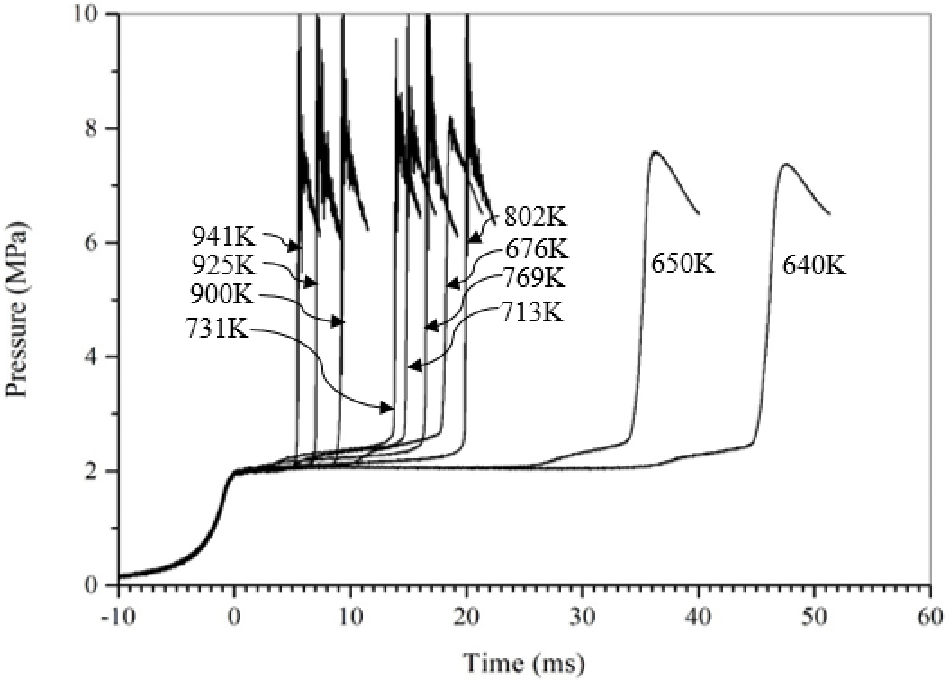

Figure 4.2. Pressure records for stoichiometric (Ø=1) *iso*-octane at the end of compression pressure 2.0 MPa.

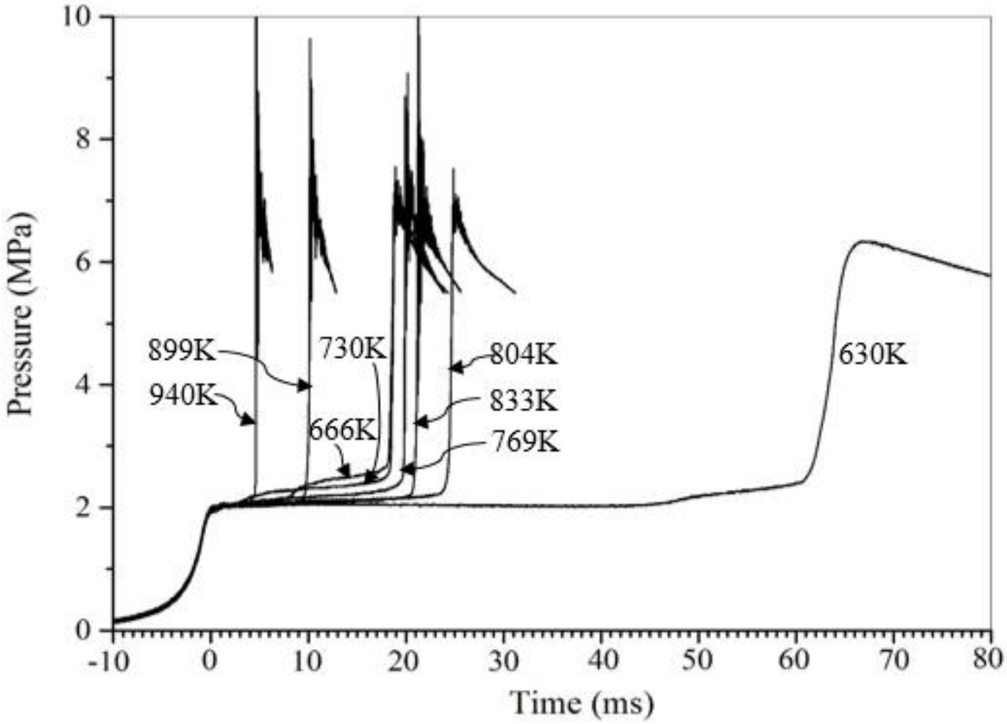

Figure 4.3. Pressure records for lean (Ø=0.8) *iso*-octane at the end of compression pressure 2.0 MPa.

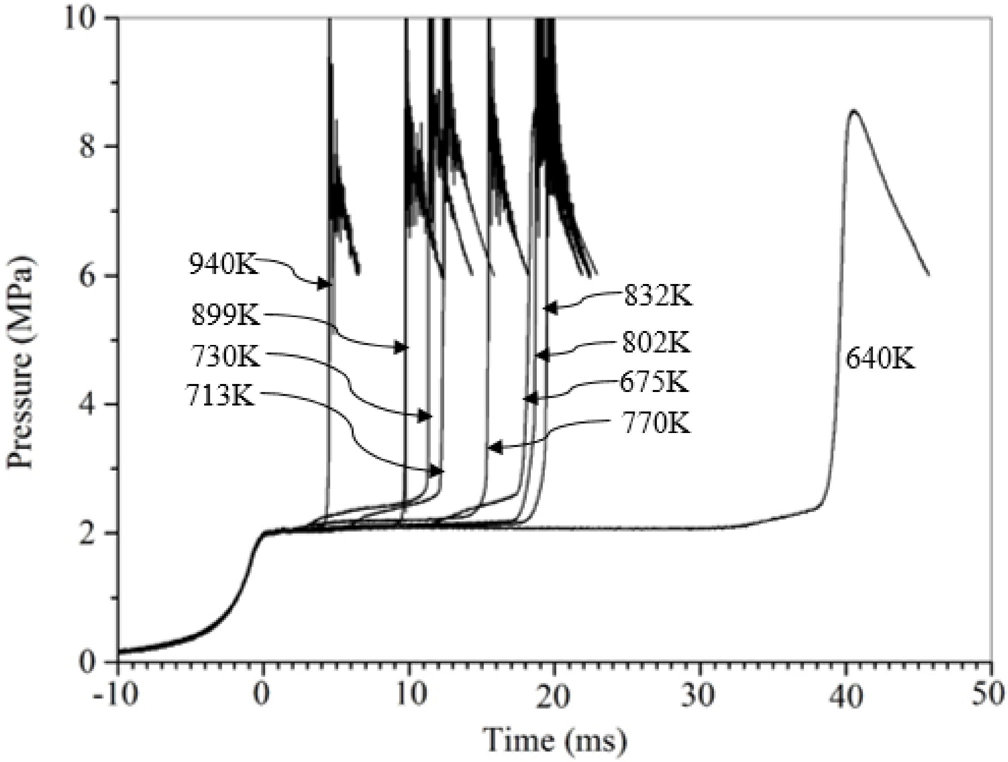

Figure 4.4. Pressure records for rich (Ø=1.2) *iso*-octane at the end of compression pressure 2.0 MPa.

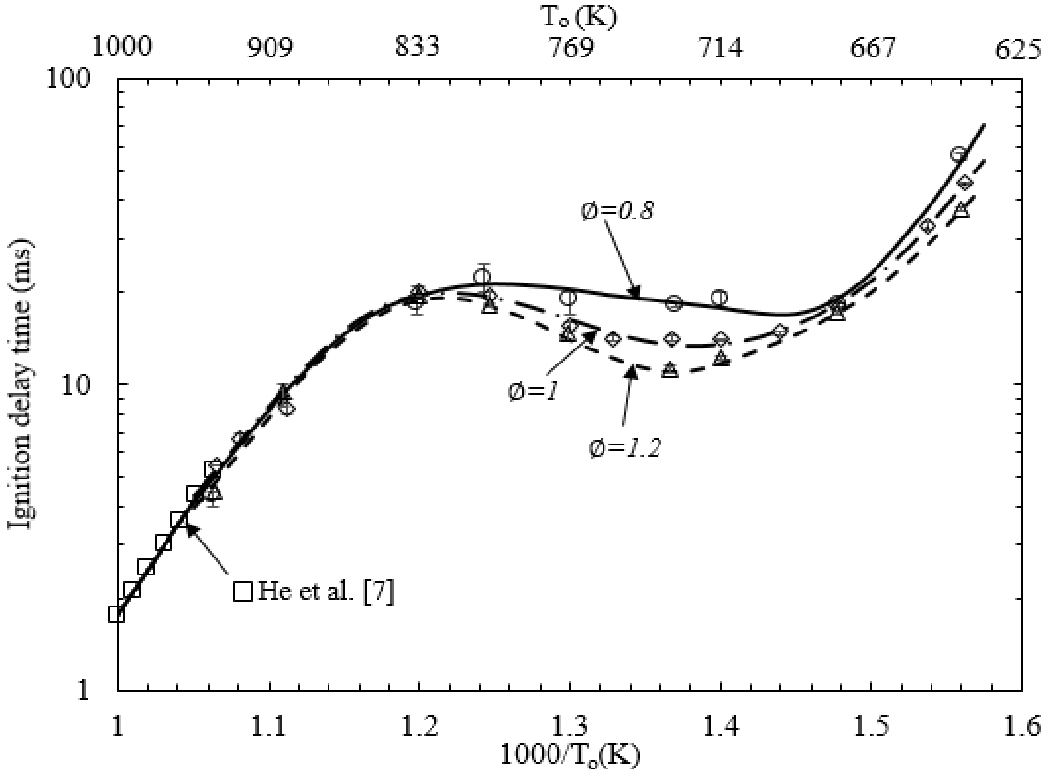

Figure 4.5. Ignition delay times for stoichiometric (Ø=1), lean (Ø=0.8) and rich (Ø=1.2) *iso*-octane at compressed pressure of 2.0 MPa.

Comparison of *iso*-octane ignition delay times obtained from Leeds RCM and those measured using UCT RCM under the same conditions of pressure, temperatures and concentration are shown in Fig. 4.6. Leeds RCM measures shorter τ that UCT RCM, throughout the temperature range studied. This is due to higher heat loss that is experienced by the UCT RCM. The UCT RCM, as described in Chapter 2, has a protruding piston rod that goes in the middle of the combustion chamber. This additional cool mass resulted in increased heat loss within the combustion chamber during and after compression, and thus longer delay times were measured. Shown in Fig 4.7 are the pressure records for the two devices at the same end of compression pressure of 2.0 MPa and temperature 895K, the heat loss with associated longer delay times is evident in these records. It is therefore not possible to compare results quantitatively between these two rigs, extensive comparison of results measured from different rigs at different research groups under the same conditions of pressure, temperature and concentration were discussed in detail in Chapter 3.

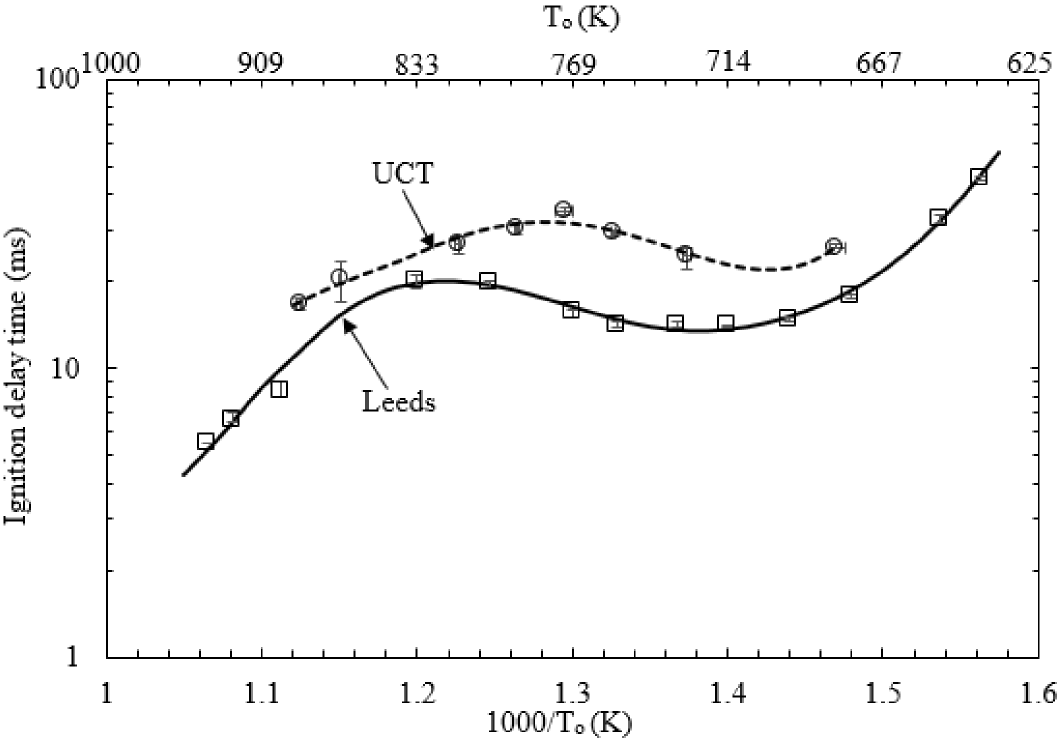

Figure 4.6. Ignition delay times for stoichiometric *iso*-octane at compressed pressure of 2.0 MPa measured using UCT RCM and Leeds RCM.

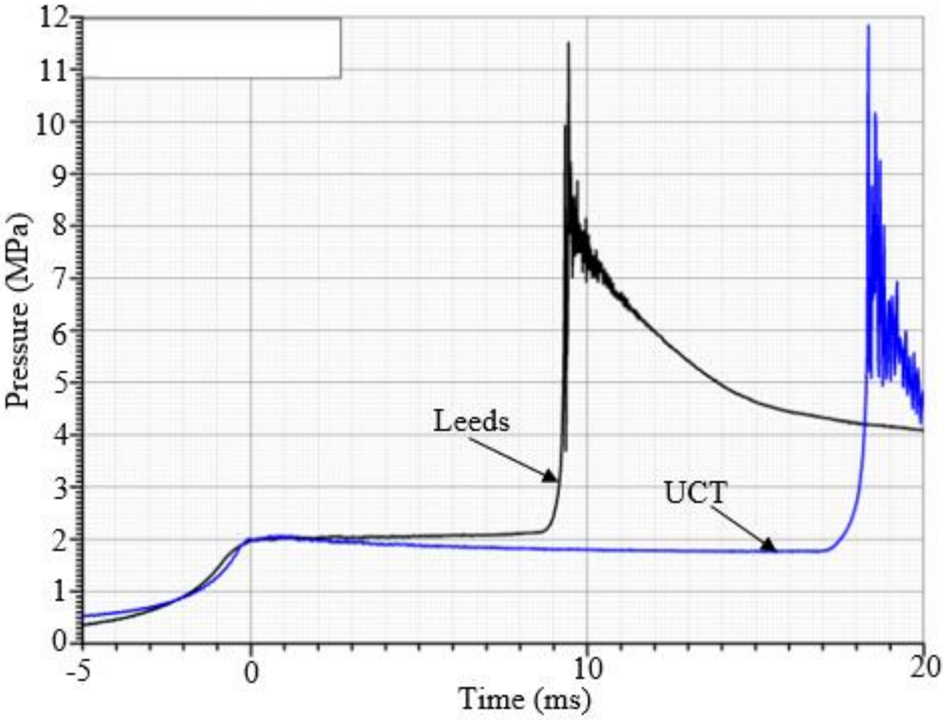

Figure 4.7. Pressure records for stoichiometric *iso*-octane at the end of compression pressure 2.0 MPa and temperature 895K, measured from UCT and Leeds RCM.

4.4.2 Toluene.

Pressure records for stoichiometric toluene/air mixture at different compression temperatures and a compression pressure of 2.0 MPa are shown in Fig. 4.8. The delay time versus reciprocal temperature relationship shown in Fig. 4.9 is very different from that for *iso*-octane in Fig. 4.5, with the complete absence of an NTC regime. This trend is common to aromatic hydrocarbons, as revealed by experiments and chemical kinetic simulations under different conditions [Mittal et al., 2007; Davidson et al., 2005; Roubaud et al., 2000; Shen et al., 2009]. For temperatures below 900K, with τ >100ms, the delay times were too large to be measured accurately. There was appreciable non-homogeneity within the cylinder and the core gas had lost heat to the chamber walls, to the extent that the mixture became non-ignitable. Previous RCM work at Lille [Roubaud et al., 2000] showed that stoichiometric toluene could not auto-ignite below 917K at 1.7 MPa. Comparison with other published measurements for RCMs and Shock Tubes are shown in Fig. 4.10 for lean ($\emptyset$=0.5) toluene mixtures, in the pressure and temperature ranges of 0.9-1.4 MPa and 1090-1170 K. Very good agreement is obtained for the current results with those from Davidson et al. [2005] and Shen et al. [2009]. There is however, substantial difference with the results of Mittal et al. [2007] at low temperatures. The principal reason, amongst others, would appear to be the amount of heat loss experienced by the mixture during the extensive delay time, a problem addressed in Mittal et al. [2007] and in Chapter 3.

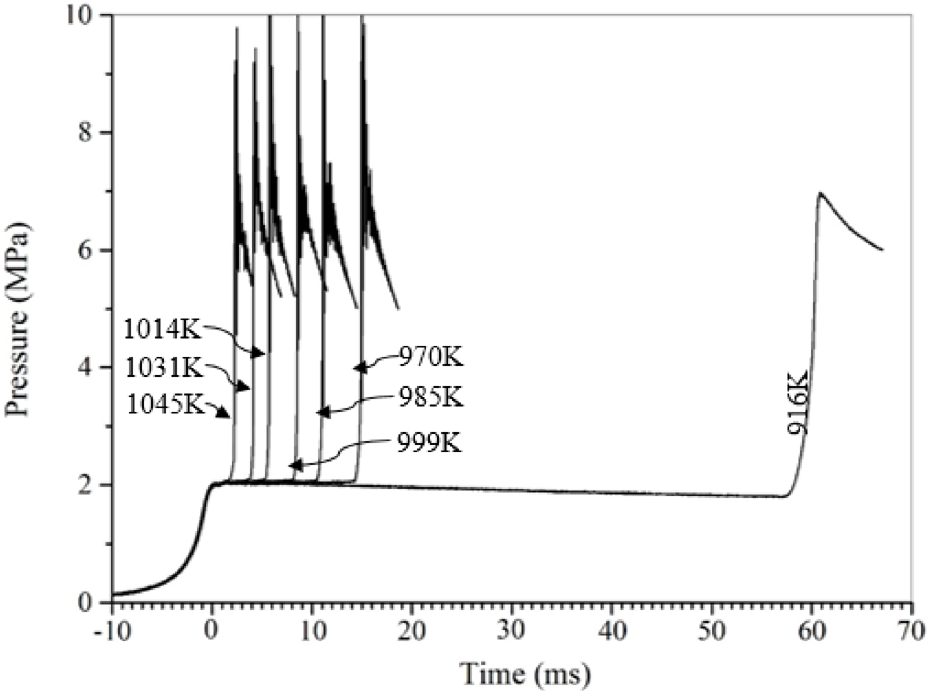

Figure 4.8. Pressure records for stoichiometric toluene/air at compression pressure of 2.0 MPa.

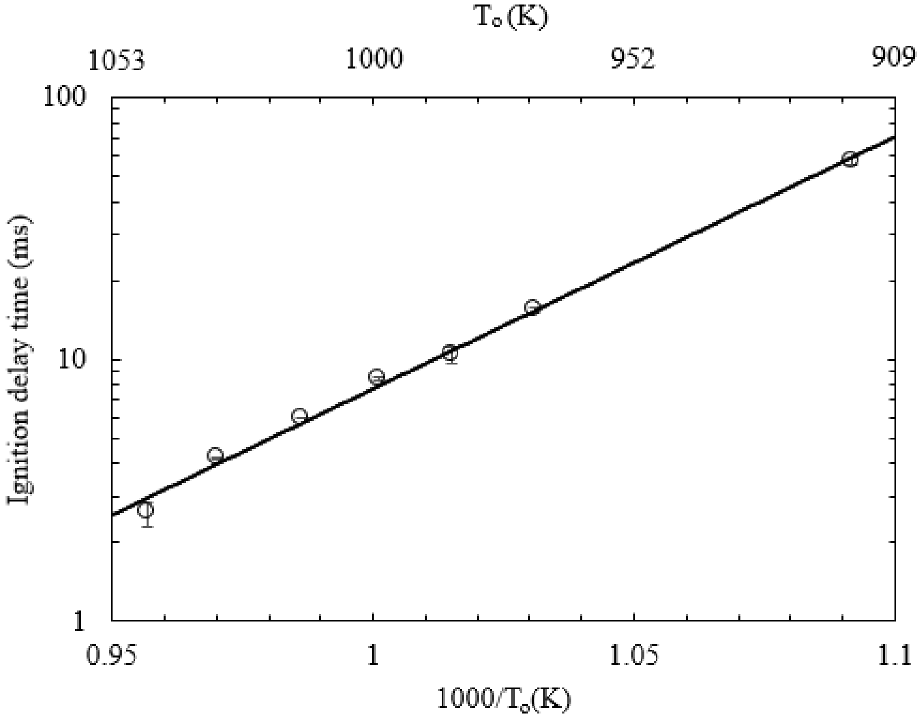

Figure 4.9. Ignition delay time for stoichiometric toluene/air at a compression pressure of 2.0 MPa.

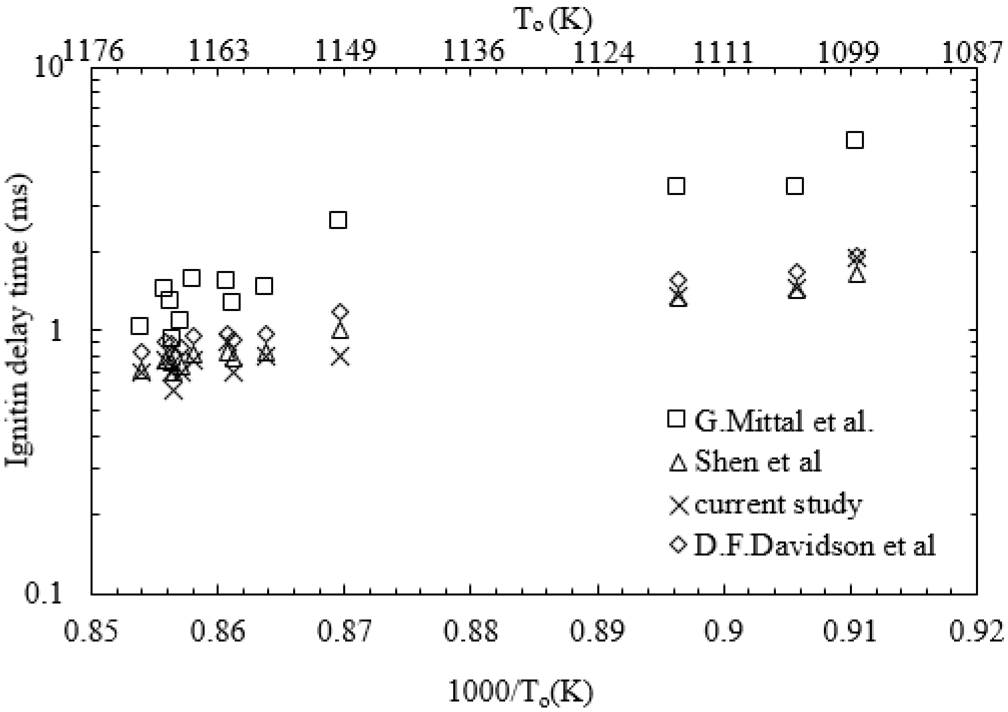

Figure 4.10. Comparison of ignition delay times from different researchers for lean (Ø= 0.5) toluene/air at a compression pressure of 1.0-1.5 MPa.

4.4.3 *n*-Butanol.

The pressure records for *n*-butanol also show that they have single stage ignition, with a near-linear change in τ, with no NTC, throughout the temperature range. Figs. 4.11 and 4.12 show the records for stoichiometric (Ø=1) and lean (Ø=0.5) mixtures. For both equivalence ratios the ignition delay time generally decreases with increase of temperature, while the leaner mixture has longer ignition delay times throughout the temperature range. A monotonic change in the slope is clear in Fig. 4.13 for a stoichiometric mixture in the temperature range (705K-725K). This finding is similar to that obtained by Heuffer et al. [2013]. No ignition measurements were possible for the lean mixture at temperatures lower than 730K.

The key mechanism driving auto-ignition of *n*-butanol are well described in Dagaut et al. [2008], Moss et al. [2008], Sarathy et al. [2012] and Black et al. [2010]. Here only a summary of reaction pathways suggested by Sarathy et al. [2012] for low and high temperatures is given. At low temperatures, the first chain branching process is the addition of molecular oxygen to fuel radicals (hydroxybutyl) which leads to formation of a chain branching radical hydroxyalkyl peroxy (ROO) and hydroperoxide radical (HO_2). The formation of HO_2 essentially inhibits the low temperature ignition behaviour of butanol, however it can be an important reaction during blending with other fuels as will be discussed for the case of toluene in section 4.5.2. The second step involves the isomerisation reaction where intramolecular H-abstraction of ROO occurs to form hydroxyalkyl hydroperoxide radicals (QOOH) which further propagates the chain reaction. QOOH further reacts with molecular oxygen to form hydroperoxyalkylperoxy radicals (OOQOOH) which then isomerise to form carbonyl alkylhydroxy hydroperoxides and OH. The last reaction path for the low temperature oxidation is the decomposition of carbonyl alkylhydroxy hydroperoxides to form the OH radical, small oxygenated radicals and stable oxygenates (i.e aldehydes or ketones). For high temperatures, the most important and relatively faster reaction is the H-abstraction of the weaker alpha C-H bond by OH radical. This bond is weaker than similar bonds in alkanes due to the nearby presence of the OH group. The importance of this reaction is reduced with increasing temperature as contribution from HO_2 chemistry and formation of H_2O_2 becomes more significant [Miller et al., 2005].

The model described above has been validated using different experimental studies such as premixed laminar flame velocity [Veloo et al., 2011], [Oßwald et al. 2011], [Hansen et al.,2011], ignition delay times from shock tubes and RCM [Weber et al., 2011], [Heufer et al.,2010], Vranckx et al.,2011], [Stranic et al., 2011] and species profile from jet-stirred reactors [C. Togbé et al, 2010], [Dagaut et al., 2009]. A wide variety of combustion data in these studies were well predicted using this model.

In this particular study, a comparison was made between measured τ values at $\emptyset$=1 and calculated values obtained from Energy Research Institute University of Leeds using numerical modelling and a detailed chemical kinetic model by Sarathy et al. [2012]. Details of this work are given in Agbro et al. [2015]. Very good agreement was obtained at intermediate temperatures between 735K and 793K, whilst an over prediction is seen at higher and lower temperatures as shown in Fig. 4.13.

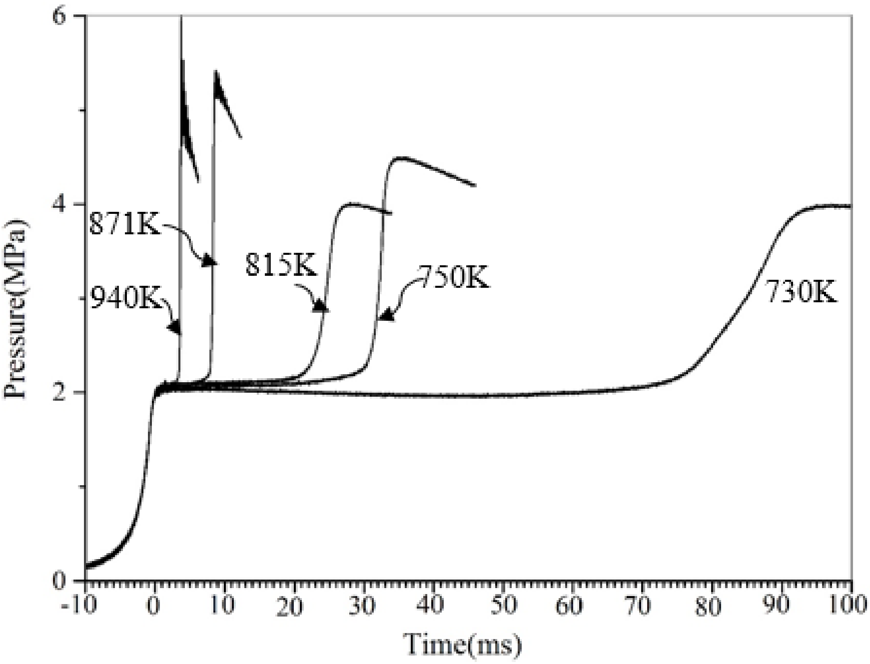

Figure 4.11. Pressure records for lean (∅= 0.5) *n*-butanol at a compressed pressure of 2.0 MPa.

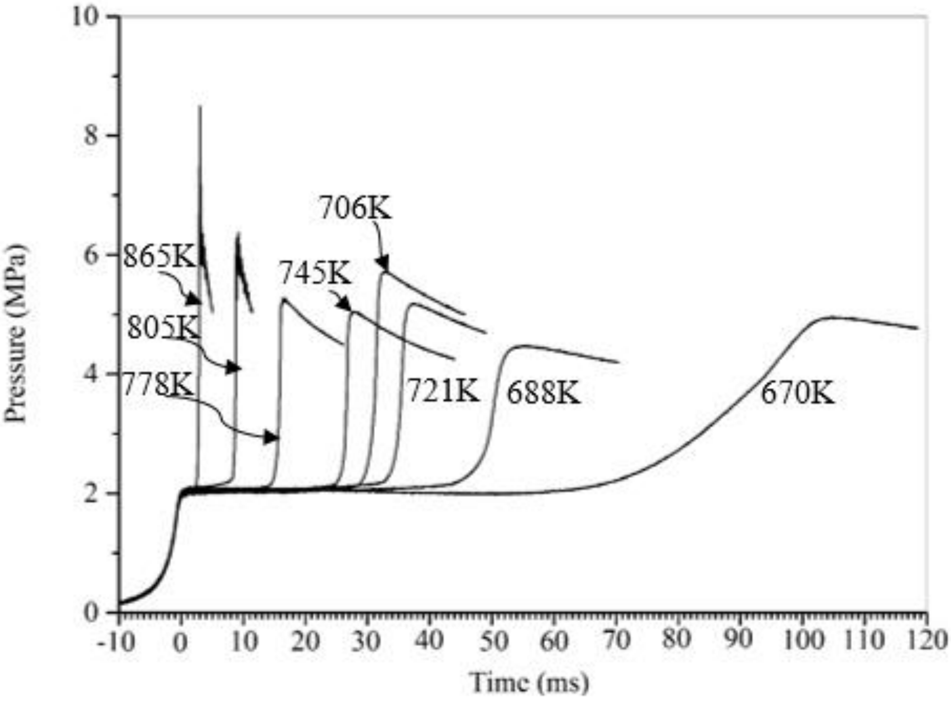

Figure 4.12. Pressure records for stoichiometric (∅=1) *n*-butanol at a compressed pressure of 2.0 MPa.

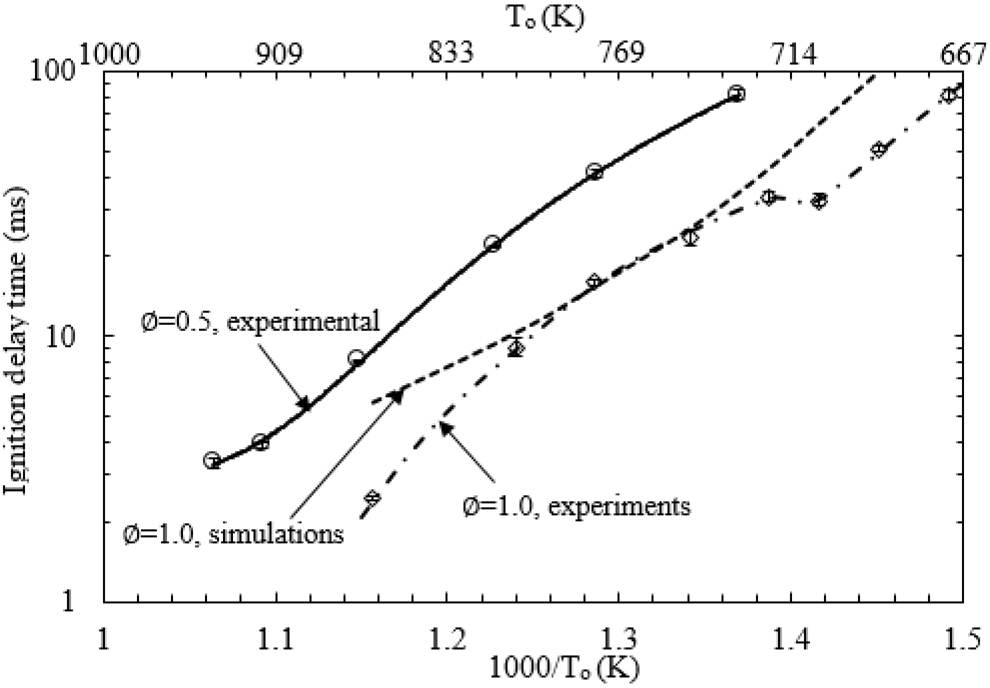

Figure 4.13. Ignition delay time of lean (Ø= 0.5) and stoichiometric (Ø= 1.0) *n*-butanol at a compressed pressure of 2.0 MPa.

4.5 Binary blend results.

The binary blends are those of *iso*-octane/*n*-butanol and toluene/*n*-butanol. These blends were selected to show the effect of *n*-butanol addition on the auto-ignition of paraffins and aromatics, represented by *iso*-octane and toluene, respectively. Table 4.3 shows compositions of the blends and the conditions under which they were tested.

	Constituents fuels			Fuel designation	Conditions		
	i-octane	toluene	*n*-butanol		Ø	Press. (MPa)	Temp. (K)
Fuel mole fraction	0.7	0	0.3	*I70*	1	2	650-926
Fuel mole fraction	0.5	0	0.5	*I50*	1	2	650-893
Fuel mole fraction	0	0.7	0.3	*T70*	1	2	735-1000
Fuel mole fraction	0	0.5	0.5	*T50*	1	2	690-917

Table 4.3. Composition and test conditions for binary blends of *iso*-octane/*n*-butanol and toluene/*n*-butanol.

4.5.1 *iso*-octane/*n*-butanol blends.

Figs. 4.14-4.16 show the experimental results for the *iso*-octane/*n*-butanol blends, all conducted at stoichiometric concentration and a pressure of 2.0 MPa. In general, at the higher temperatures the addition of *n*-butanol in the *iso*-octane mixture decreases the overall ignition delay time, while, at the lower temperatures it increases. This is due to the *n*-butanol delay times being lower than those of *iso*-octane at the higher temperatures, while they are higher at lower temperatures. The change of delay time due to the addition of *n*-butanol is not linear, Figs. 4.17-4.19 summarise the changes in delay time, as a function of the proportions of *n*-butanol in the blend mixture, at different temperatures.

At the higher temperatures (>760K), the addition of *n*-butanol decreases the delay time, and the trend can be presented by a second order function, as seen in Figs. 4.17-4.18. The middle temperature range, between 750K-660K in Fig. 4.16, shows an interesting behaviour where the addition of *n*-butanol increases the delay time but there is visually no difference in τ values between I50 and I70, whereas at the lowest temperature (660K) there is a significant increase.

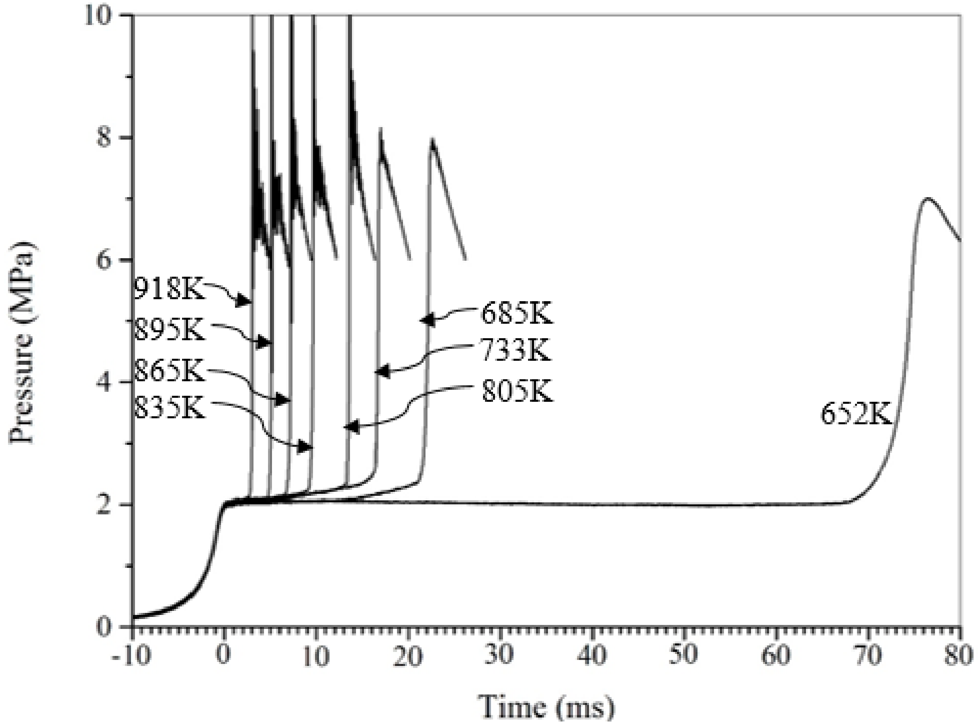

Figure 4.14. Pressure records for stoichiometric I70 blend at a compressed pressure of 2.0 MPa.

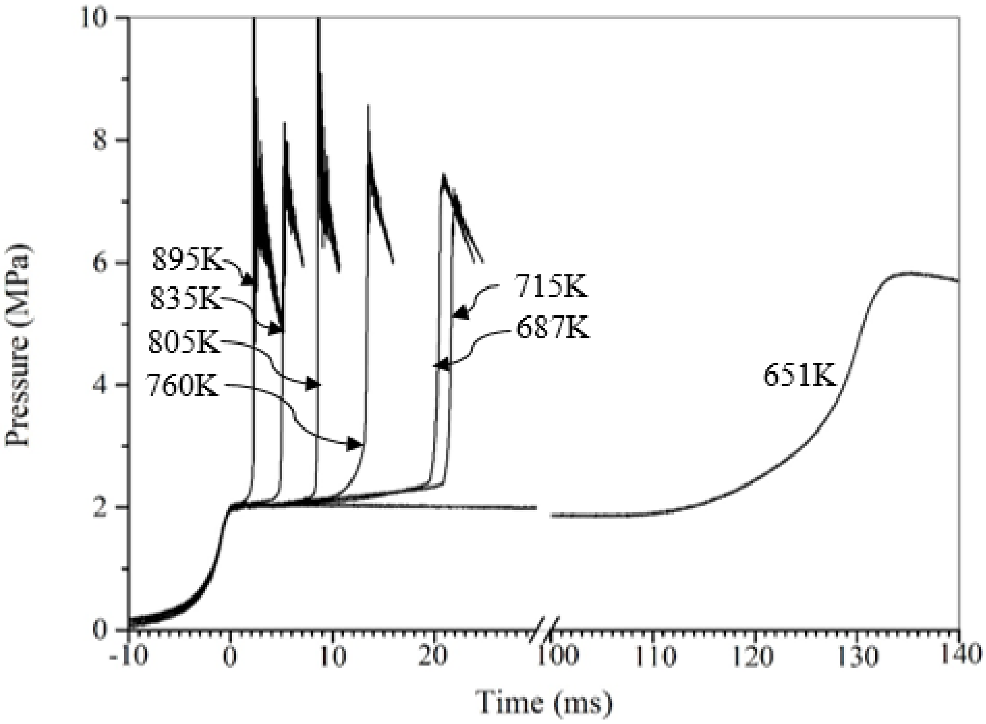

Figure 4.15. Pressure records for stoichiometric I50 blend at a compressed pressure of 2.0 MPa.

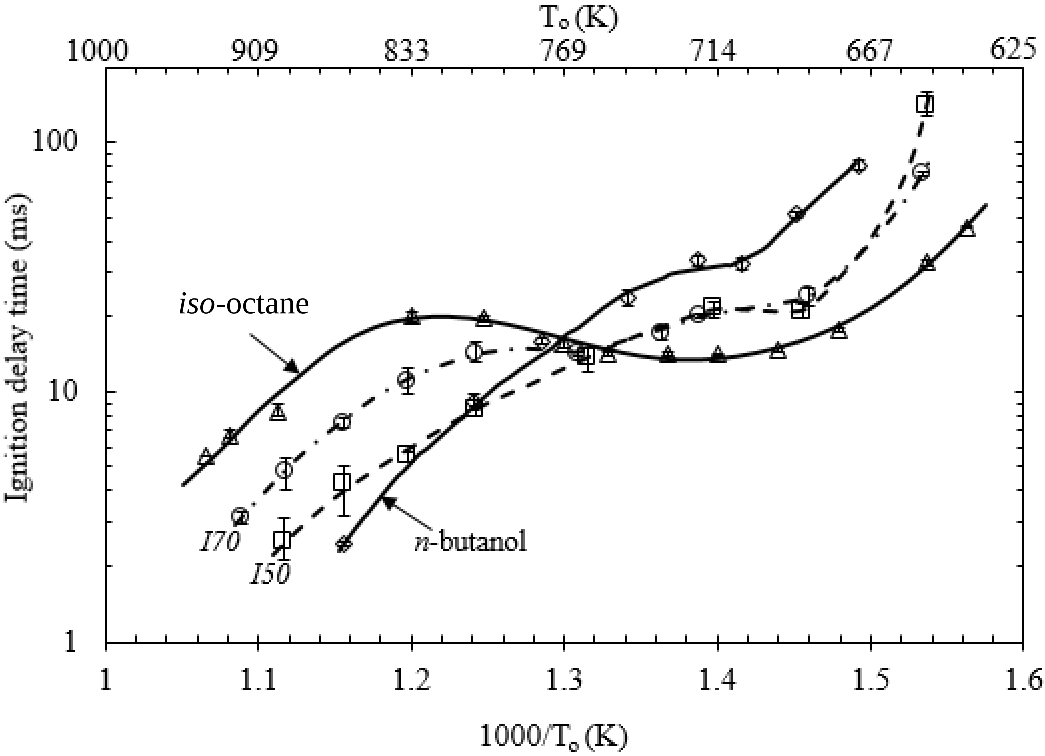

Figure 4.16. Ignition delay times for stoichiometric pure *iso*-octane, *n*-butanol and their blends *I70*, *I50* at a compressed pressure of 2.0 MPa.

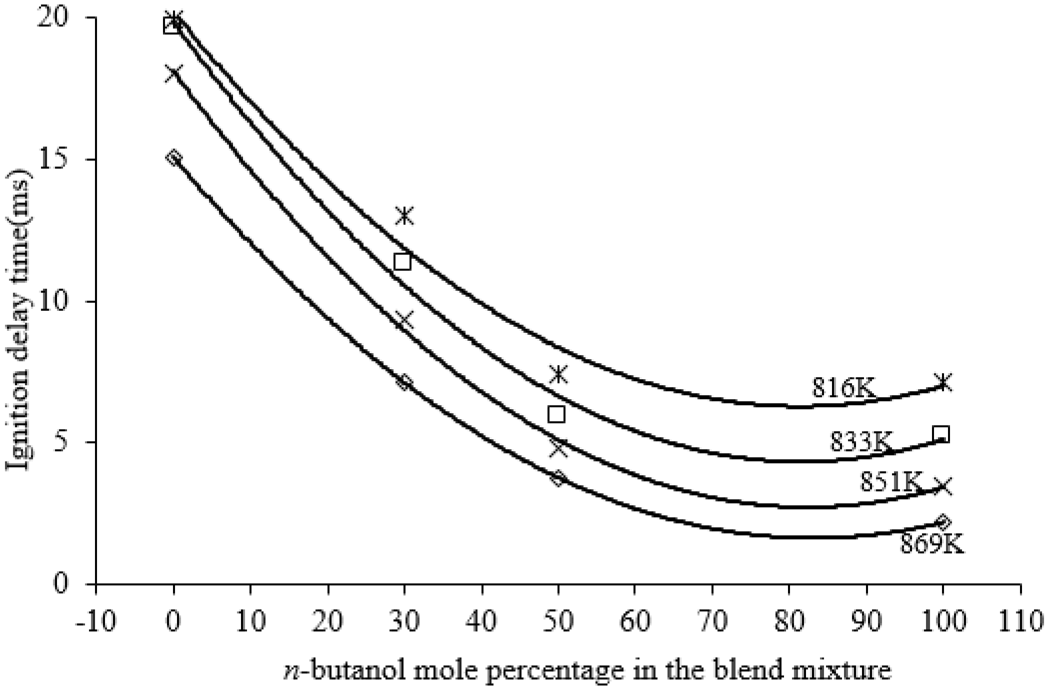

Figure 4.17. Ignition delay times of *iso*-octane/*n*-butanol at Ø=1.0 as a mole % of *n*-butanol in the blend mixture, at a compressed pressure of 2.0 MPa, in the temperature range (816K-869K).

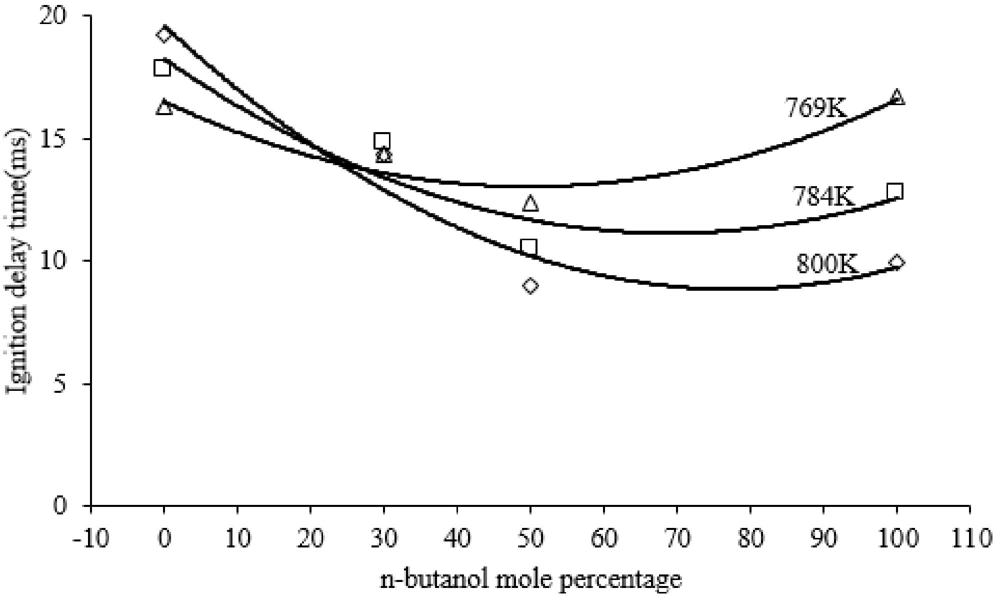

Figure 4.18. Ignition delay times of *iso*-octane/*n*-butanol at Ø=1.0 as a mole % of *n*-butanol in the blend mixture, at a compressed pressure of 2.0 MPa, in the temperature range (769K-800K).

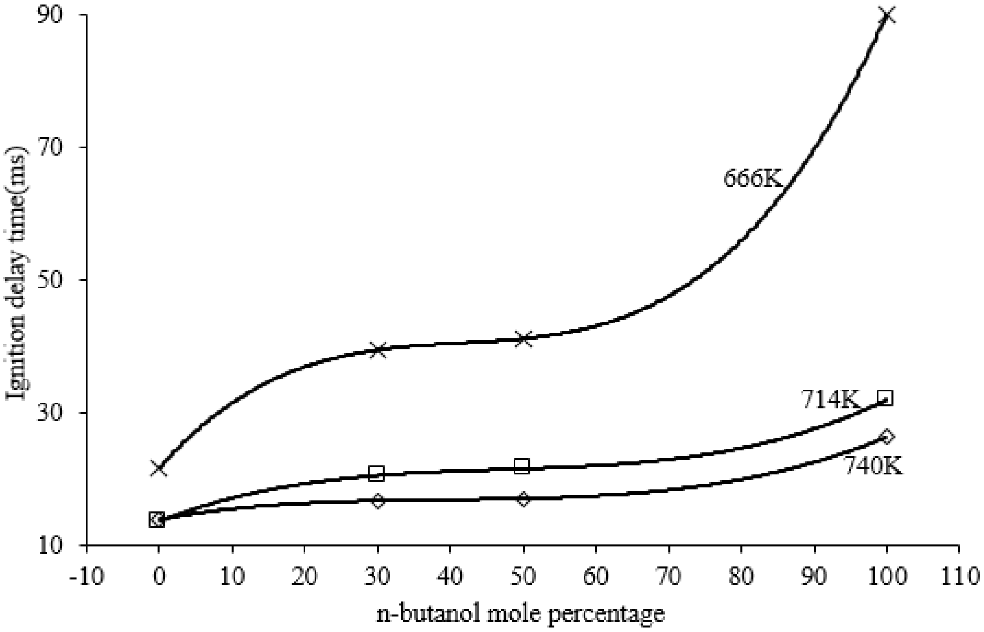

Figure 4.19. Ignition delay times of *iso*-octane/*n*-butanol at Ø=1.0 as a mole % of n-butanol in the blend mixture, at a compressed pressure of 2.0 MPa, in the temperature range (666K-740K).

The effect of pressure on I50 and I70 blends were investigated using UCT RCM. Measurements were made at 2.0 MPa and 4.0 MPa and results presented in Figs 4.20 and 4.21. For both blends, pressure increase results in shorter τ values. The NTC strength is also reduced with pressure increase. Using these results, pressure exponent, *n*, was calculated, for each blend, based on the relation $\tau \alpha P^{-n}$, and it was found that *n* values changes with temperature, with higher values of *n* obtained in the intermediate range and fairly constant values at higher and lower temperatures, as shown in Fig. 4.22.

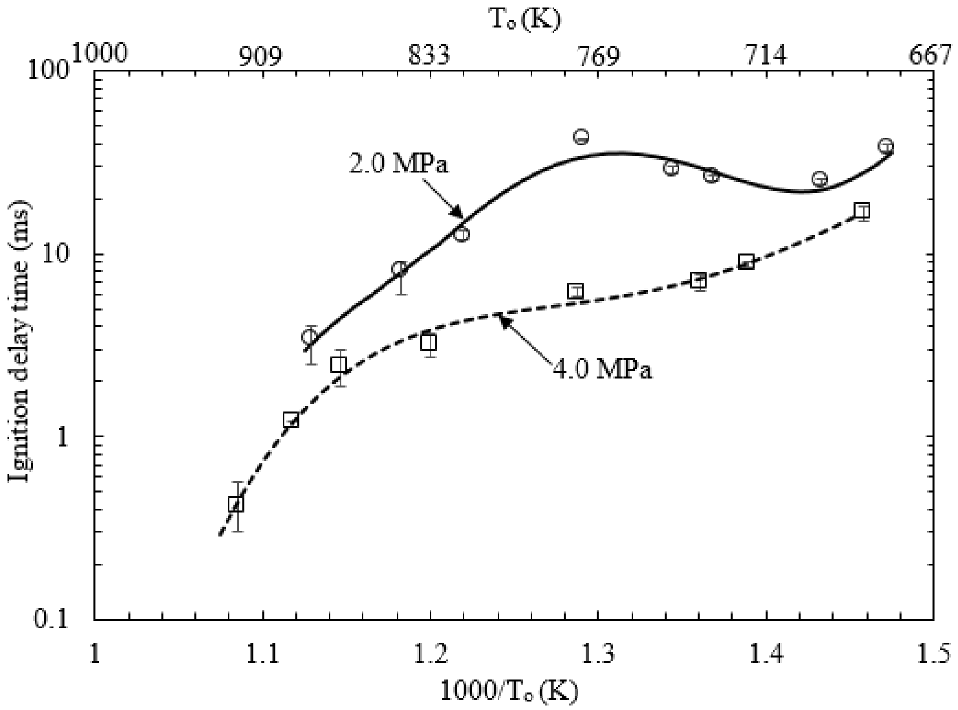

Figure 4.20. Ignition delay times for stoichiometric blend I70, at a compressed pressure of 2.0 MPa and 4.0 MPa.

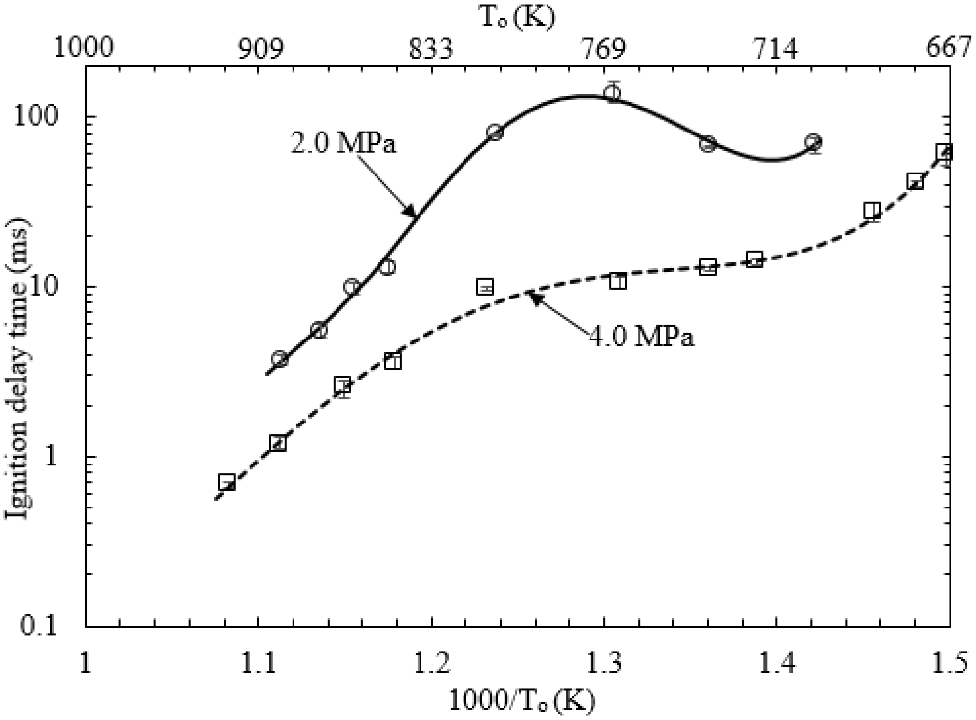

Figure 4.21. Ignition delay times for stoichiometric blend I50, at a compressed pressure of 2.0 MPa and 4.0 MPa.

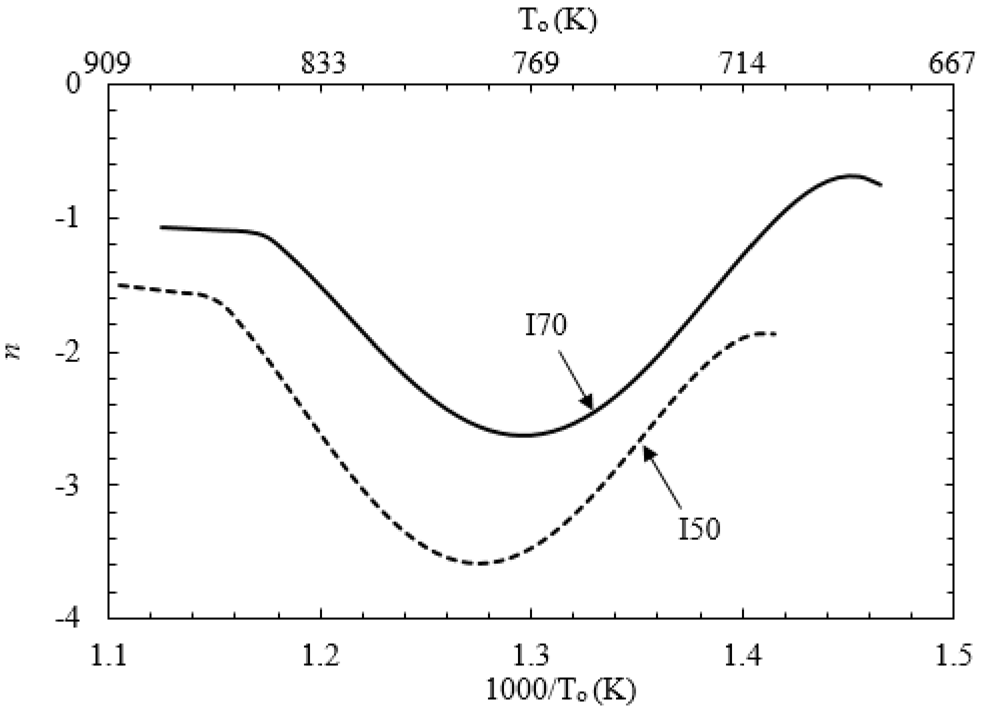

Figure 4.22. Values of pressure exponent, *n*, for stoichiometric blends I70 and I50 and different compression temperatures.

4.5.2 Toluene and *n*-butanol blends.

Figs. 4.23 and 4.24 show the pressure records for stoichiometric *T70* and *T50* blends at a compressed pressure 2.0 MPa, in which, single stage ignition was obtained with no NTC regime throughout the temperature range. The ignition delay times for the blends and the pure constituent fuels are shown in Fig. 4.25. Fig. 4.26 summarises the effect of increasing the percentage of *n*-butanol on the delay times. Generally, an increasing concentration reduces τ, particularly, at low temperatures. Interestingly, within a temperature range of 735K-835K, the ignition delay times of *T50* blend are slightly less than both constituent mixtures whilst those for *T70* are very close to those of *n*-butanol. This suggests that within this temperature range *n*-butanol generates chain branching radicals that overwhelm those created by toluene and thus *n*-butanol dominates the kinetics of the blend. This behaviour is analogous to the results reported for the auto-ignition studies of toluene/*n*-heptane blends from Di Sante [2012], Hartmann et al. [2011] and Vanhove et al. [2006]. In these studies, due to the difference in reactivity between toluene and *n*-heptane, the more reactive fuel (*n*-heptane) controls the kinetics of the blend. At lower temperatures, toluene has a high resistance to auto-ignition due to the lack of any forceful initiating reaction that could produce the chain carrier OH. *n*-heptane on the other hand, can readily generate the $OH^{\cdot}$ and $HO_2^{\cdot}$ radicals during its low temperature oxidation. The presence of these radicals results into cross acceleration effect, where the radicals produced during oxidation of *n*-heptane dramatically increase the oxidation rate of toluene compared to when toluene alone was oxidized. A detailed chemical kinetic mechanism for toluene/*n*-heptane blend developed by Andrae et al [2012] identified the main chemical reaction responsible for increase toluene consumption/reactivity due to cross acceleration effects as $C_6H_5CH_2^{\cdot} + HO_2^{\cdot} \rightarrow C_6H_5CH_2O^{\cdot} + OH^{\cdot}$.

Described in section 4.4.3, *n*-butanol generates HO_2 radicals at low temperatures and will therefore promote cross acceleration effects similar to that occurring in the case of *n*-heptane.

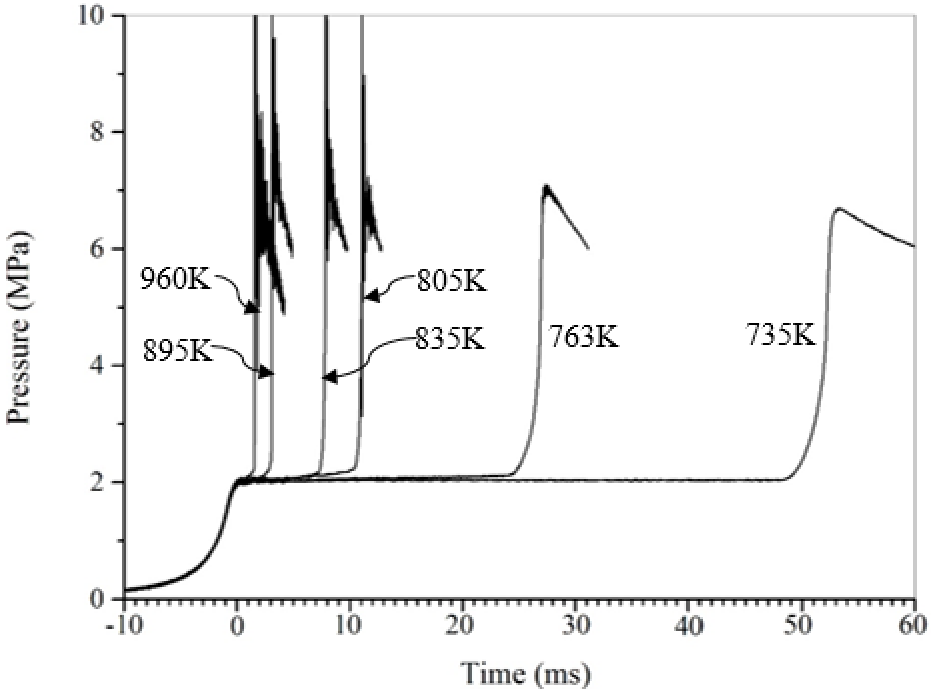

Figure 4.23. Pressure records for stoichiometric *T70* blend at a compressed pressure of 2.0 MPa.

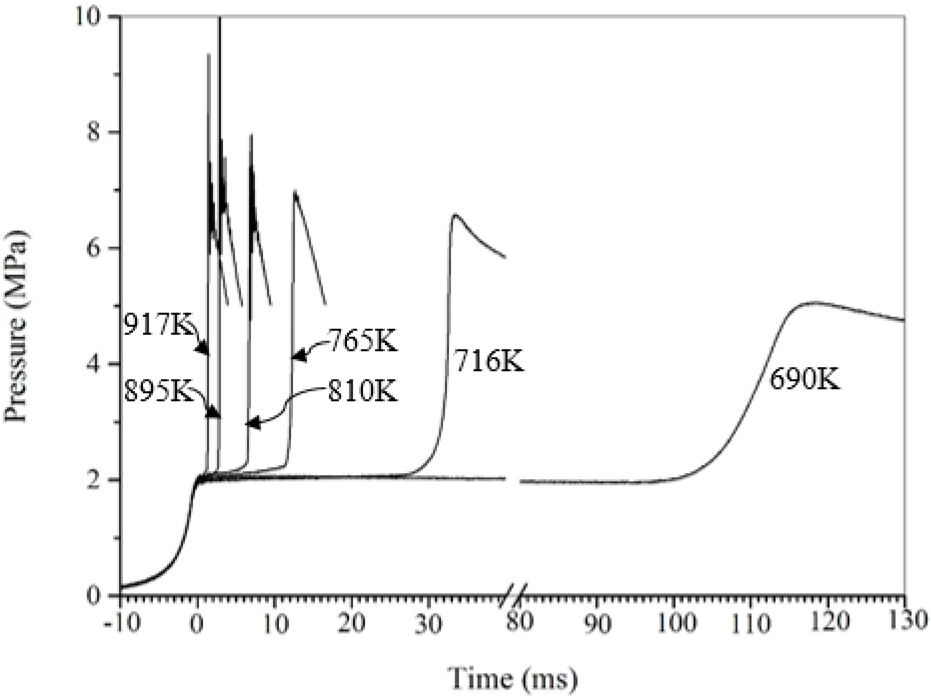

Figure 4.24. Pressure records for stoichiometric *T50* blend at a compressed pressure of 2.0 MPa.

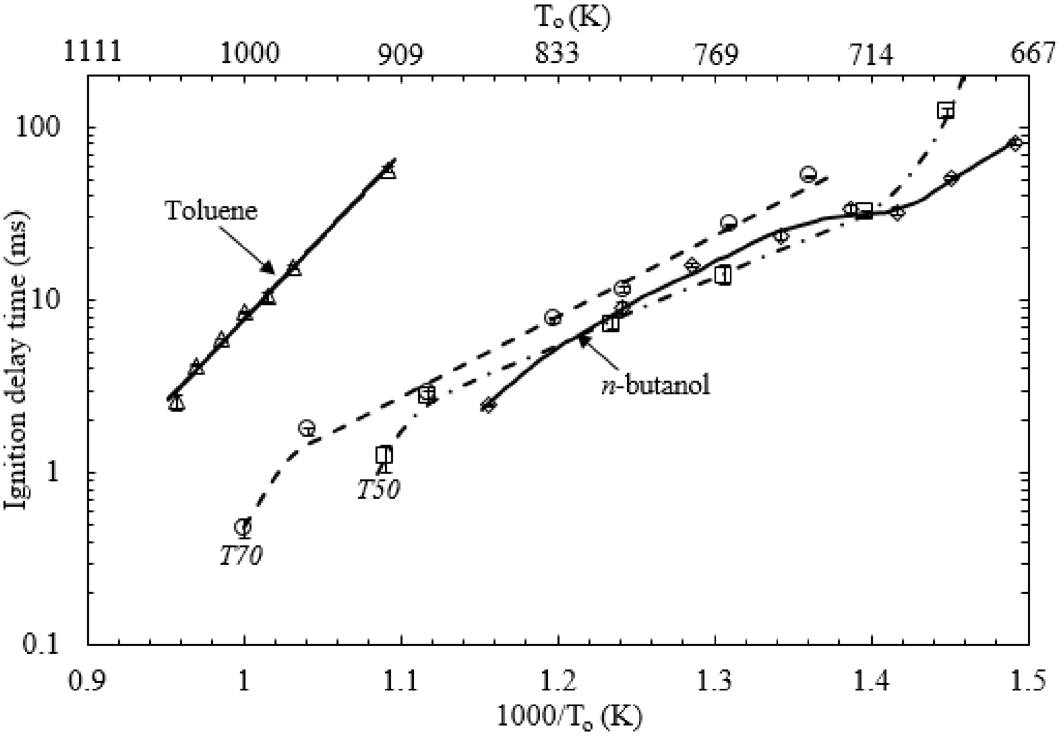

Figure 4.25. Ignition delay times for stoichiometric pure toluene, *n*-butanol and their blends *T70* and *T50* at a compressed pressure of 2.0 MPa.

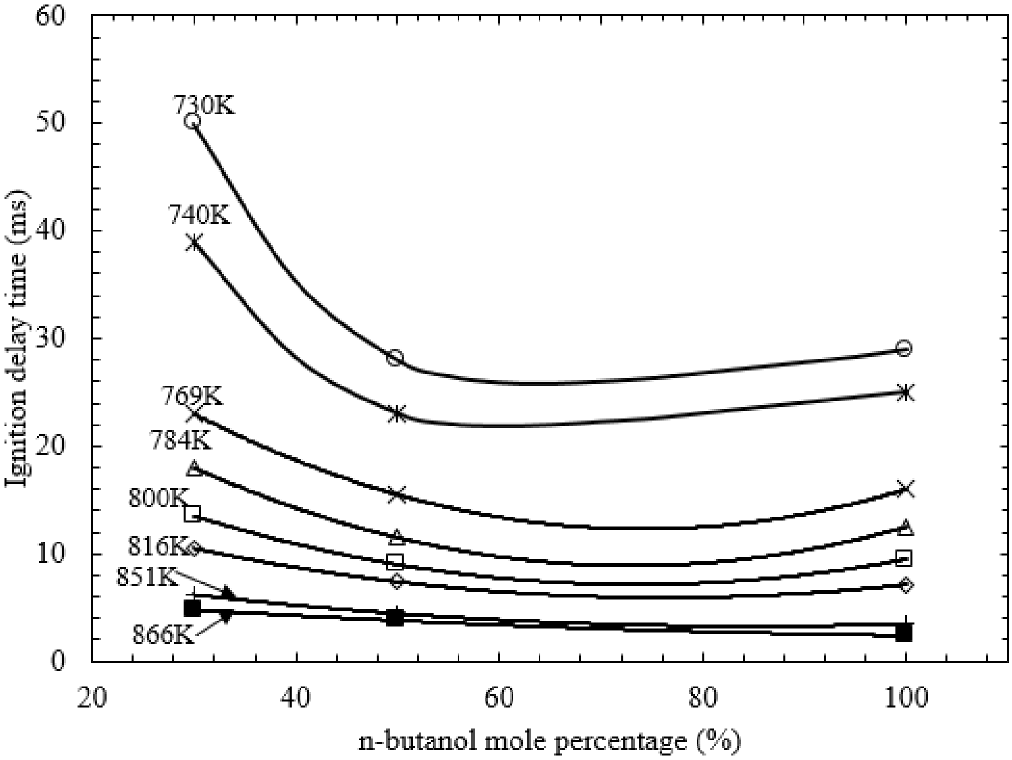

Figure 4.26. Ignition delay times of toluene/n-butanol at ∅=1.0 as a mole % of *n*-butanol in the blend mixture, at a compressed pressure of 2.0 MPa, in the temperature range (730K-866K).

4.6 Gasoline surrogate and its blends with alcohol.

4.6.1 Introduction.

The blending of gasoline and bio-based fuels is one of the methods of reducing the use of petroleum based fuels and eradicating its negative environmental effects. A surrogate for gasoline of growing importance is Toluene Reference Fuel (TRF), comprised of ternary blends of Toluene and PRF [Goutham et al., 2013; Cancino et al., 2009; Goutham et al., 2012]. Because of their importance, this chapter reports the ignition delay times of the blends of TRF and two bio-alcohols, namely ethanol and butanol. Ethanol has been proven to improve the anti-knock properties of gasoline. However, its use is not without disadvantages and these have been explained in Chapter 1. On the other hand, *n*-butanol provides an alternative to ethanol, without some of its disadvantages. Clearly, it is necessary to know how the autoignition times of respective blends of the gasoline surrogate, with *n*-butanol and ethanol, compare.

There are numerous proposed TRF surrogate mixtures in the literature [Vanhove et al., 2006, Morgan et al., 2010; Gauthier et al., 2004; Lenhert et al., 2009; Mehl et al., 2011] and the choice of surrogate composition depends on the end applications. In the present work, the objective is to measure the effect of alcohol on the ignition delay times of a typical high octane European standard gasoline. Morgan et al. [2010] was able to suggest a TRF mixture which was based on this standard, and in their work a response surface model was proposed which can give the composition of a mixture based on the specified values of RON and sensitivity. Using this model, it was possible to obtain the volume fractions of the three components (toluene, *n*-heptane and *iso*-octane) in TRF mixtures which can emulate gasoline with specified values of RON and MON. Calculations of the composition of a TRF mixture were made to emulate a high octane (RON=98.5 and MON=88) commercial gasoline (Gron 98 MK1). The obtained TRF comprised of 0.75418 toluene/0.05833 *iso*-octane/0.18749 *n*-heptane (by liquid volume fraction). Comparison of cylinder pressure profiles between Gron 98 MK1 and simulation results of the obtained TRF showed excellent agreement. This surrogate mixture is adopted in the present study and its equivalent fuel mole fraction is shown in Table 4.5. The liquid densities (ρ) were obtained from the supplied fuel bottles and were shown in Table 4.1.

4.6.2 Ignition delay times and pressure profiles for TRF blend.

The chosen TRF blend was tested in the RCM under stoichiometric conditions, at an end of compression pressure of 2.0 MPa, in the temperature range of 660K-960K. The results are presented in Figs. 4.26-4.27. In Fig. 4.27, the symbols represent the measured ignition delay times data while the solid line in the best fit line through these data, the decrease of ignition delay time with the increase of temperature is clearly seen for the higher and lower temperature ranges. In the mid-range temperatures, Fig. 4.26 shows two stages ignition whilst Fig. 4.27 shows a region of negative temperature coefficient (NTC) in the temperature range of 769K to 833K. These findings are similar to those obtained in the other heavy hydrocarbons such as PRFs [Fieweger et al., 1997; Halstead et al., 1977], gasoline and other TRFs surrogates mixtures [Goutham et al., 2013; Cancino et al., 2009; Goutham et al., 2012]. Shown in Fig 4.28 also is a comparison between the ignition delay time of the current TRF mixture with those of research gasoline (RD387) from Kukkadapu et al. [2012] and a gasoline surrogate from LLNL [Mehl et al., 2011] and Stanford A TRF mixture from Gauthier et al. [2004]. The solid line is the best fit line through the measured delay times for the current work. Measurements were made at stoichiometric conditions and an end of compression pressure of 2.0 MPa. All blends show to possess NTC behaviour. The current TRF measures longer ignition delay times throughout the temperature range due to its high content of toluene as shown in Table 4.5.

Blend	**Composition[a] (by volume)**
Current TRF mixture	5.833/18.75/75.418
Gasoline (RD387) [Kukkadapu et al.,2012]	42.3/9.5/26.4/4.7/16
Stanford A [Gauthier et al., 2004]	63/17/20/0/0
LLNL [Mehl et al., 2011]	57/16/23/4/0

[a] Composition order: *iso*-octane/*n*-heptane/toluene/olefins/napthenes

Table 4.4.Composition of gasoline and surrogates investigated in this and other studies.

	i-octane	*n*-heptane	toluene
Liquid fuel volume fraction	0.05833	0.1875	0.75418
Fuel mole fraction	0.0411	0.146	0.8125

Table 4.5. Constituents fuel proportions in the current TRF mixture, at Ø=1.

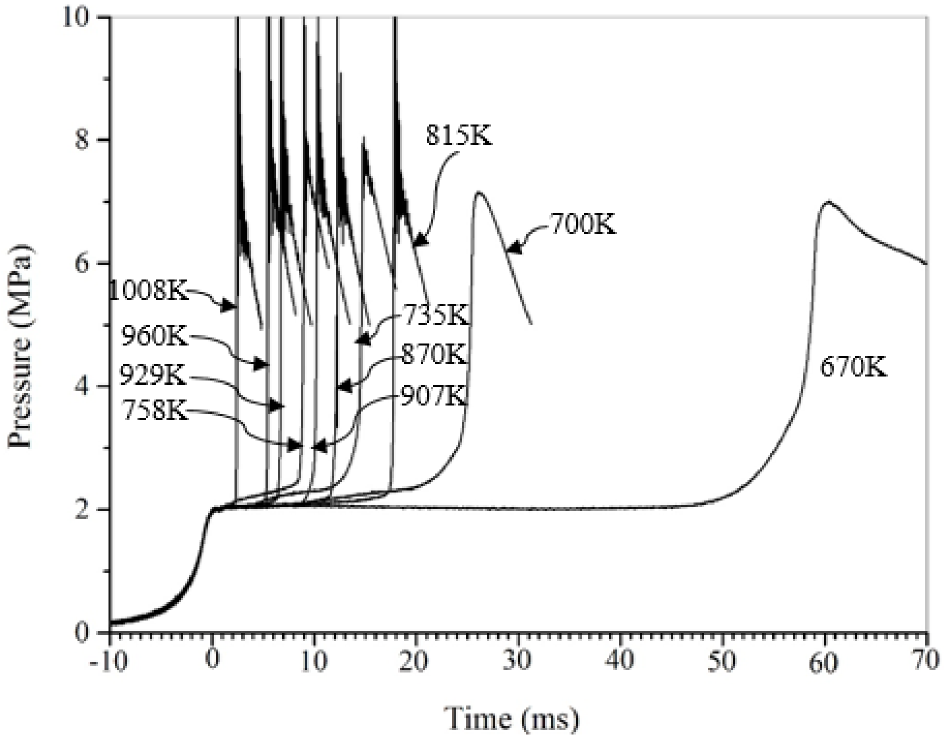

Figure 4.27. Pressure records for stoichiometric TRF/air (81.25% toluene/4.11% *iso*-octane/14.64% *n*-heptane (by mole) at a compressed pressure of 2.0 MPa.

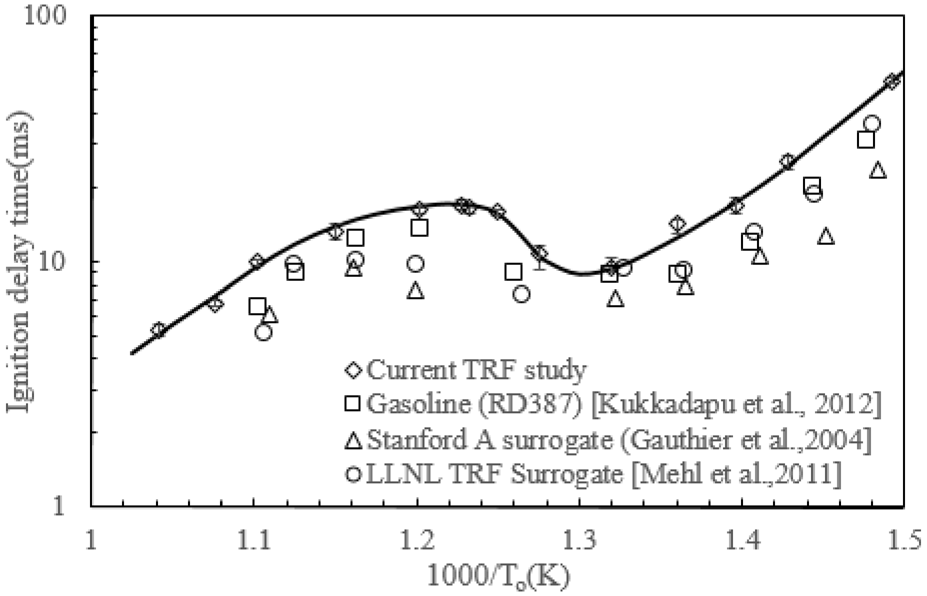

Figure 4.28. Ignition delay times for stoichiometric TRF/air at a compressed pressure of 2.0 MPa, compared with those of gasoline and other TRF surrogate at the same conditions.

4.6.3 Ignition delay times and pressure records for TRF/Ethanol blends.

As for the case of pure toluene, ethanol has very low reactivity at low temperatures. Experimental measurements of ignition delay times for pure ethanol have not been possible at low temperatures and pressures, a trend consistent with its high octane number. It is well known that high octane number fuels such as ethanol, methanol, MTBE etc are widely used as anti-knock additives due to their long ignition delay times especially at low temperatures [Lu et al., 2004], [De Caro et al., 2001], [Rothamer et al., 2012] as well as improving spark ignition engine performance [Kar et al., 2009], [Hsieh et al.,2002], [Wallner et al., 2009]. However, due to its very high sensitivity, ethanol has shorter ignition delay times at higher temperatures and this can enhance auto-ignition of the blended fuel. For example, in a study by Saisirirat et al. [2001], a blend of ethanol and *n*-heptane have been shown to suppress auto-ignition of *n*-heptane at low and intermediate temperatures while at high temperatures there was no significant change for low ethanol content. However, when it was increased to 57% by volume, *n*-heptane auto-ignition was enhanced and shorter ignition delay times were obtained. Tien et al. [2014] measured the change of traditional research octane number (RON) and sensitivity when ethanol was added to gasoline, PRF and TRF mixtures. For all these mixtures, addition of ethanol increased their RON and sensitivity values as shown in Fig. 4.29.

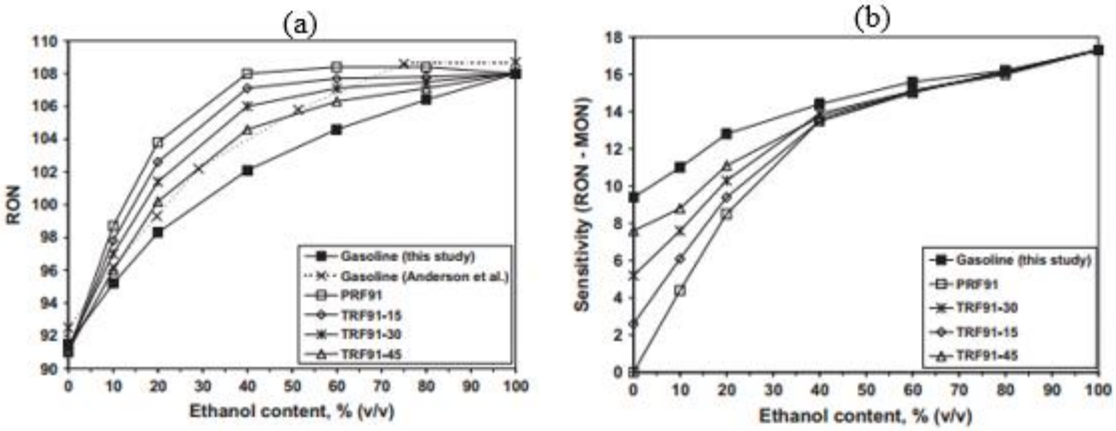

Figure 4.29. (a) Measured RONs and (b) Sensitivity for different ethanol/TRF blends versus ethanol content. Tien et al. [2014] is indicated as “this study” in the plot. Data from Anderson et al. [2002] is included for reference.

This Section reports ignition delay times for the blends of TRF/air and ethanol/air, with ∅=1.0 for both component mixtures. The experimental end of compression pressure was 2.0 MPa, in the temperature range of 700-1000K. The chosen TRF mixed with air at ∅=1.0 was blended with different mole proportions of ethanol/air also at ∅=1.0. The blends are characterised by the liquid volume percentage of ethanol in the liquid blend fuel. E25 indicates 25% liquid volume of ethanol in the blend mixture, the remainder is TRF mixture which is comprised of constituent fuels having the same ratio as that of pure TRF shown in Table 4.5. Table 4.6 shows all the blends tested, their composition in terms of liquid volume fraction and their equivalent fuel mole fraction in the blend. Table 4.7 shows the conditions under which they were tested.

	iso-octane	*n*-heptane	toluene	ethanol	Fuel designation
Liquid volume fraction	0.04375	0.14062	0.56564	0.25	*E25*
Fuel mole fraction	0.0248	0.0883	0.4903	0.3966	
Liquid volume fraction	0.02917	0.09375	0.37709	0.5	*E50*
Fuel mole fraction	0.0138	0.0493	0.2734	0.6635	
Liquid volume fraction	0.01458	0.04687	0.18855	0.75	*E75*
Fuel mole fraction	0.0059	0.0212	0.1175	0.8554	

Table 4.6. Liquid fuel blends designation and constituent proportions.

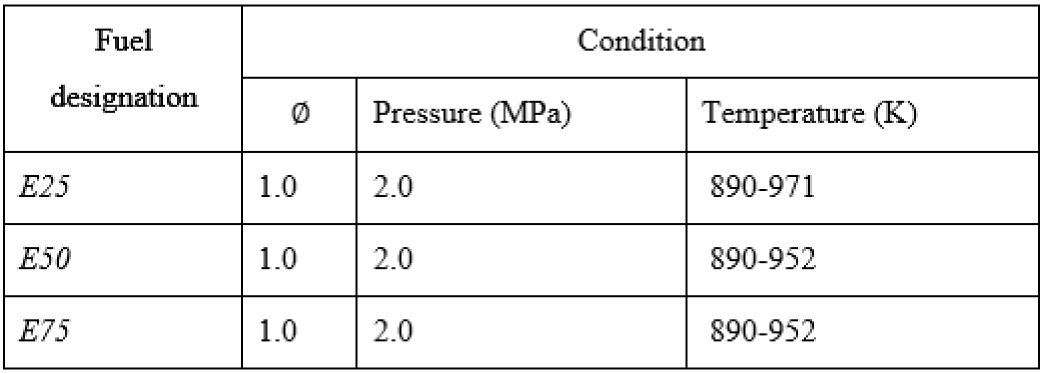

Fuel designation	Condition		
	Ø	Pressure (MPa)	Temperature (K)
E25	1.0	2.0	890-971
E50	1.0	2.0	890-952
E75	1.0	2.0	890-952

Table 4.7. Test conditions for chosen blends.

Pressure records and ignition delay times for the blends of TRF/air and ethanol/air at Ø=1.0 are shown in Figs. 4.30-4.33. The results from all three blends show single stage ignition under the conditions studied, with no NTC behaviour anywhere in the temperature range.

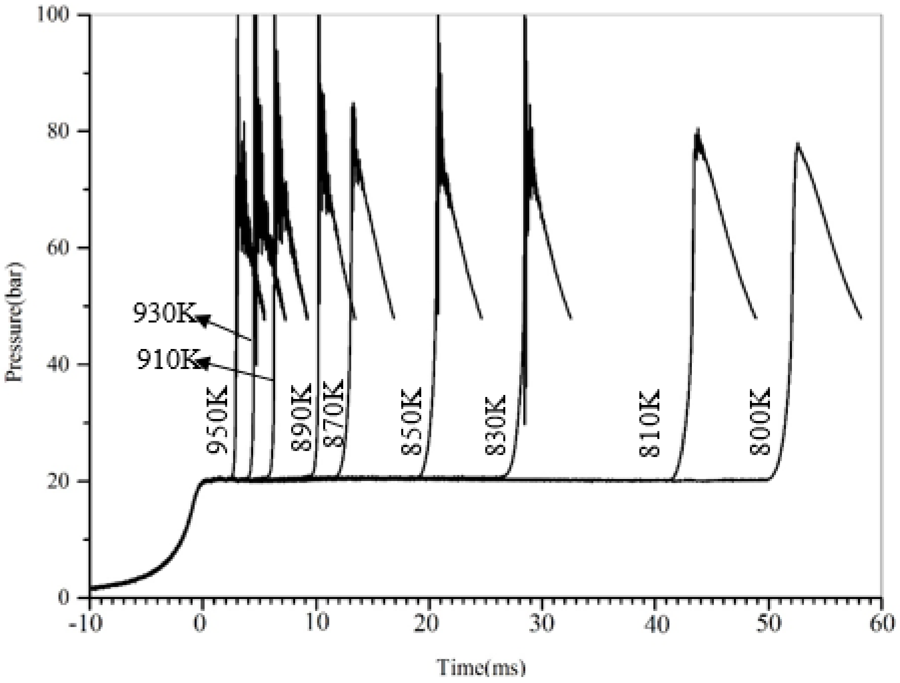

Figure 4.30. Pressure records for stoichiometric E25 blend at a compressed pressure of 2.0 MPa.

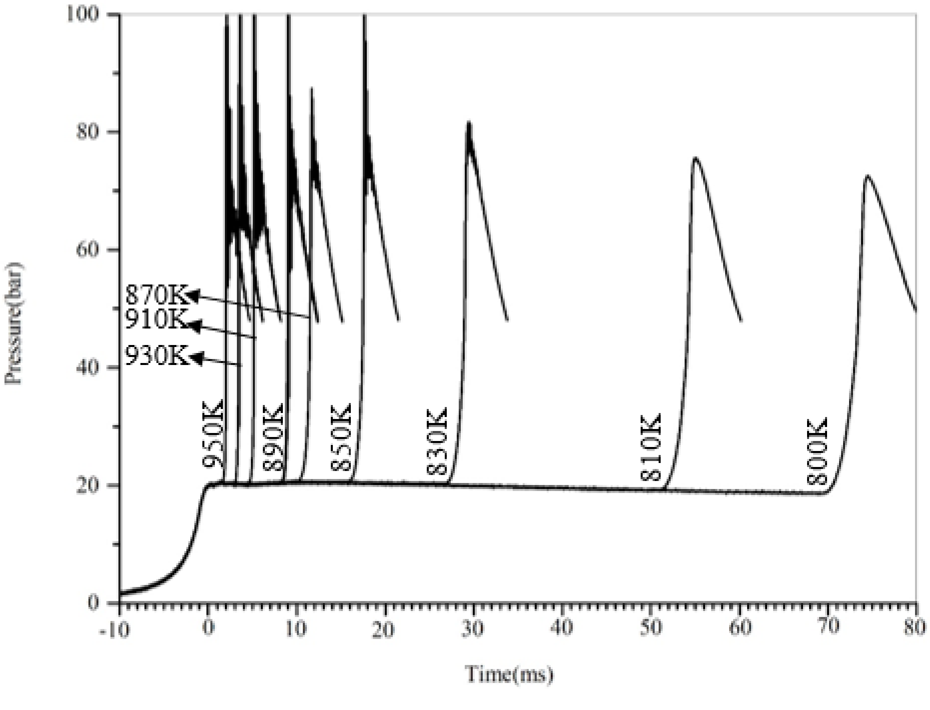

Figure 4.31. Pressure records for stoichiometric E50 blend at a compressed pressure of 2.0 MPa.

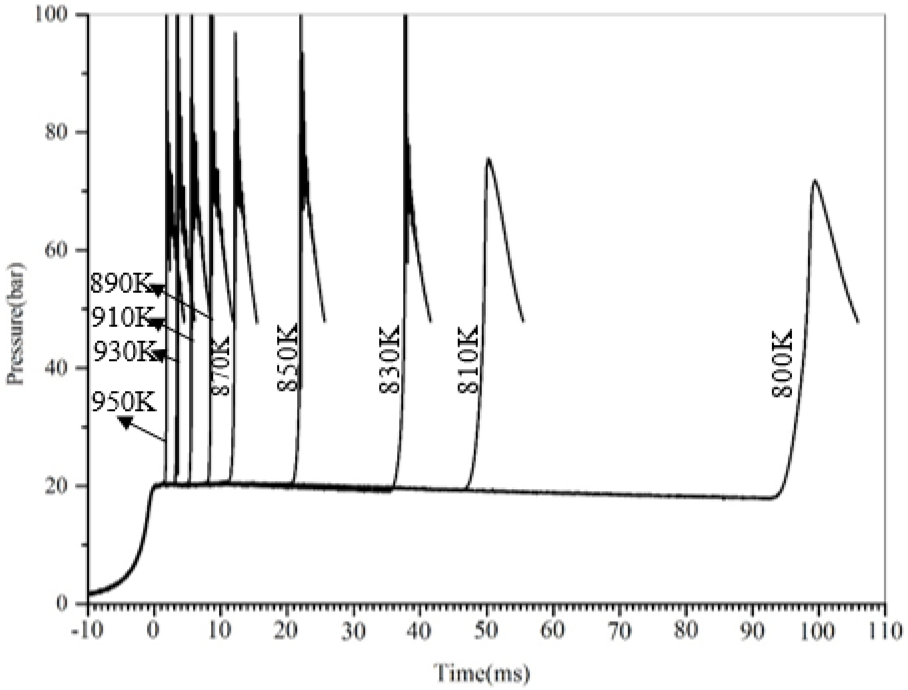

Figure 4.32. Pressure records for stoichiometric E75 blend at a compressed pressure of 2.0 MPa.

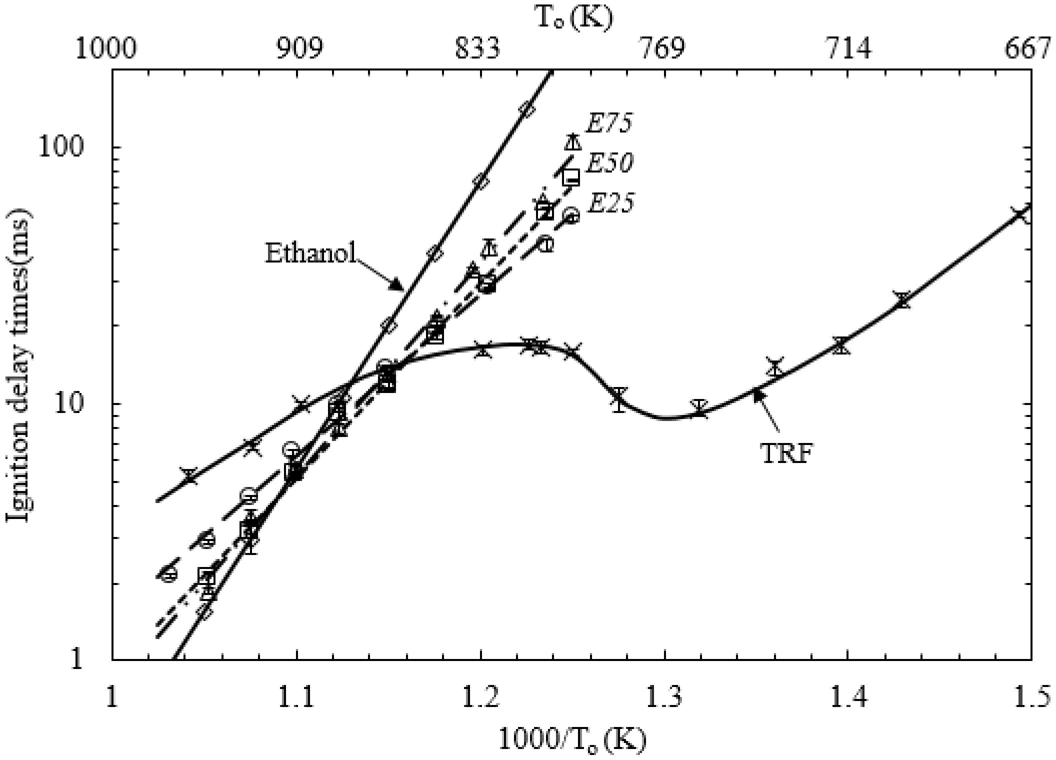

Figure 4.33. Ignition delay times for TRF/Ethanol blends at compressed pressure 2.0MPa.

Interestingly, NTC behaviour is only shown for the TRF on Fig. 4.33, whereas ethanol and the blends hardly show such a trend. This trend is in agreement with the results obtained by Yates et al. [2010], where addition of ethanol or methanol to the PRF80 mixture weakened its NTC behaviour which was eventually completely eliminated with higher content of ethanol. Fig. 4.34 summarises the change of ignition delay times of the blends with ethanol addition. At low temperatures < 860K, ethanol increases the resistance to auto-ignition and there is an appreciable increase in τ. In the mid-temperature range there is relatively small change in ignition delay times for all blends, with their delay times almost similar. In the range 860K-910K, τ values are slightly lower than those of the main components. At high temperatures > 910K, ethanol addition reduces the autoignition resistance of TRF, due to the shorter ignition delay times of pure ethanol. Similar results were obtained by Saisirirat et al. [2001] where ethanol addition to *n*-heptane supressed auto-ignition of *n*-heptane at low and intermediate temperatures and enhanced it at high temperatures.

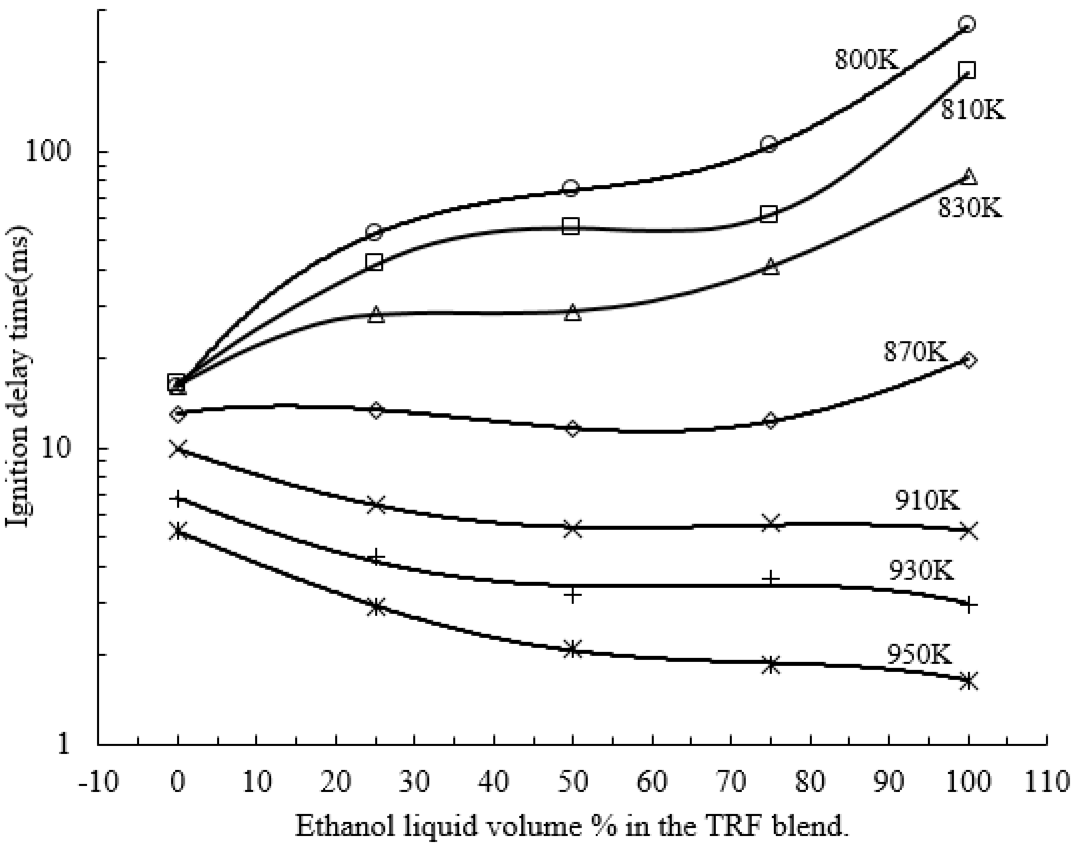

Figure 4.34. Change of ignition delay time with the proportion of ethanol in the blend for Ø=1.0, compressed pressure 2.0 MPa, in the temperature range 800K-950K.

4.6.4 Ignition delay times and pressure records for TRF/*n*-butanol blends.

Table 4.8 shows the composition and concentration of the TRF/air and *n*-butanol/air tested and Table 4.9 the test conditions.

	iso-octane	*n*-heptane	toluene	*n*-butanol	Fuel designation
Liquid volume fraction	0.04375	0.14062	0.56564	0.25	*B25*
Fuel mole fraction	0.0289	0.1031	0.5725	0.2955	
Liquid volume fraction	0.02917	0.09375	0.37709	0.5	*B50*
Fuel mole fraction	0.0182	0.0648	0.3598	0.5572	
Liquid volume fraction	0.01458	0.04687	0.18855	0.75	*B75*
Fuel mole fraction	0.0086	0.0307	0.1702	0.7906	

Table 4.8. Liquid fuel blends designation and constituents proportions.

Fuel designation	Condition		
	Ø	Pressure (MPa)	Temperature (K)
B25	1.0	2.0	671-917
B50	1.0	2.0	671-900
B75	1.0	2.0	671-855

Table 4.9. Test conditions for chosen blends.

Figs 4.35-4.37 show the pressure records for *B25*, *B50* and *B75* blends at different temperatures, two stages ignition is evident in the mid-temperature range for all blends. Fig. 4.38 shows the ignition delay times for all blends, where *B25* and *B50* show NTC behaviour, while *B75* behaves more like n-butanol with monotonic change at temperatures between 755K and 769K. Between 700K and 769K, the addition of *n*-butanol has insignificant effect on the ignition delay times of TRF, whilst at temperatures lower than 700K ignition delay times are increased, but *B25* has the same delay times as that of TRF at temperatures below 769K. At high temperatures, generally, the addition of *n*-butanol decreases delay times of TRF, and as for the TRF/ethanol blends, it can be seen that *B75* has delay times shorter than the individual components fuels at temperatures above 769K. The effect of *n*-butanol addition to TRF delay times at different temperatures is summarised in Figs. 4.39-4.40.

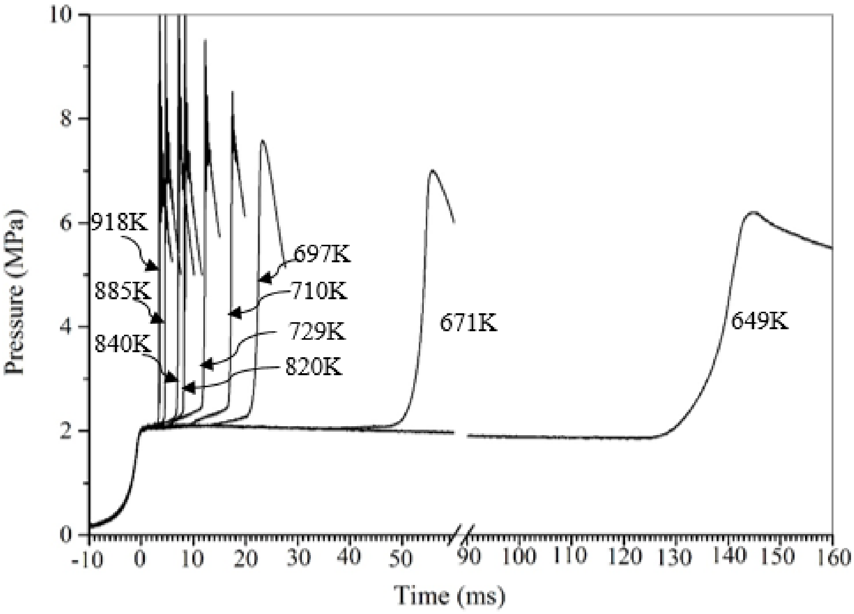

Figure 4.35. Pressure records for stoichiometric *B25* blend at a compressed pressure of 2.0 MPa.

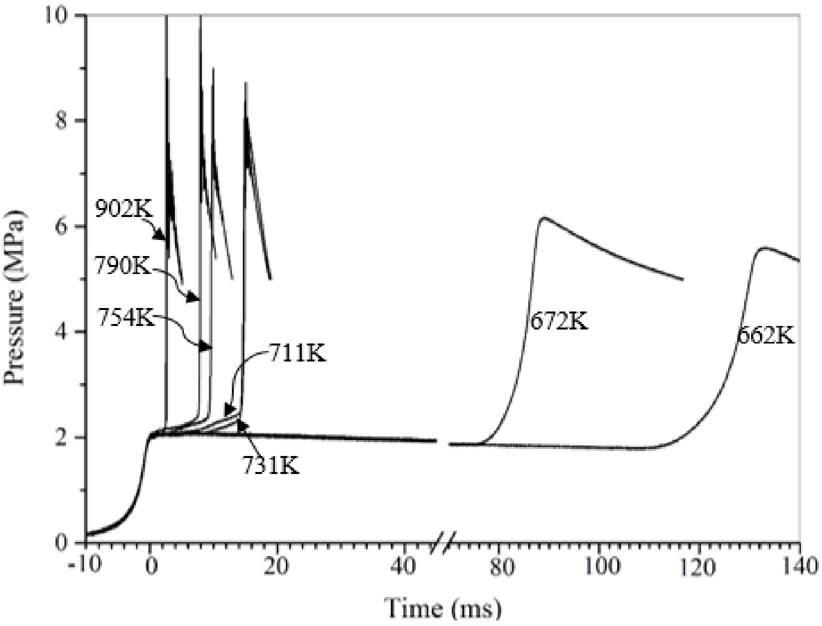

Figure 4.36. Pressure records for stoichiometric *B50* blend at a compressed pressure of 2.0 MPa.

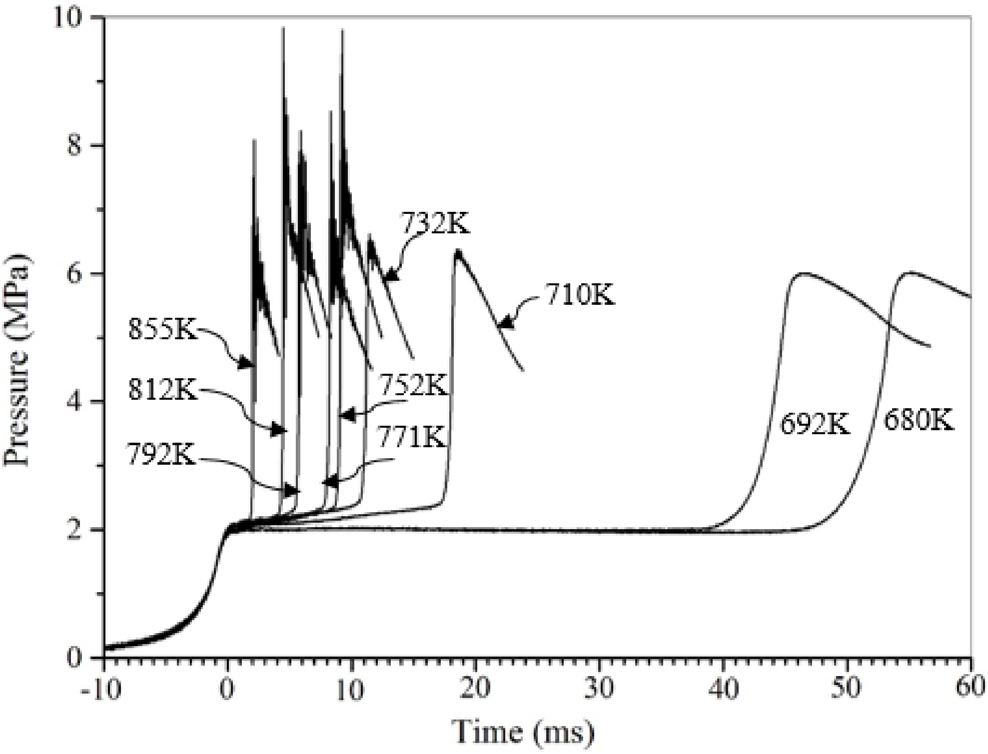

Figure 4.37. Pressure records for stoichiometric *B75* blend at a compressed pressure of 2.0 MPa.

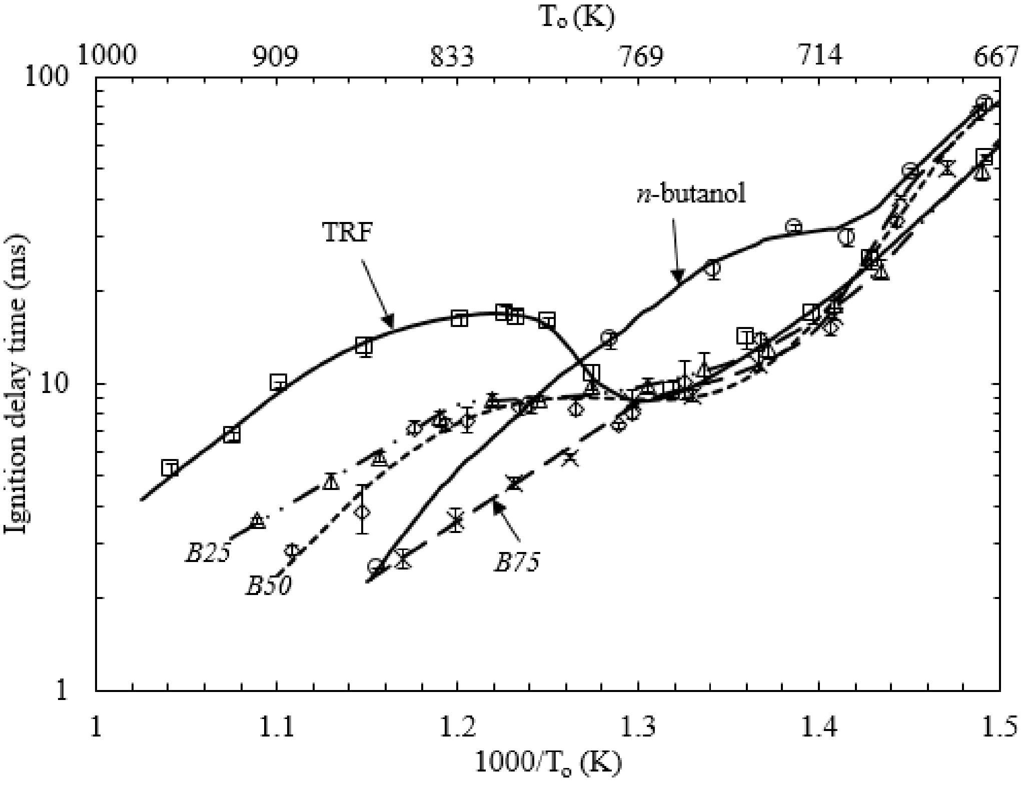

Figure 4.38. Ignition delay times for stoichiometric TRF/air and n-butanol/air blends at a compressed pressure of 2.0 MPa.

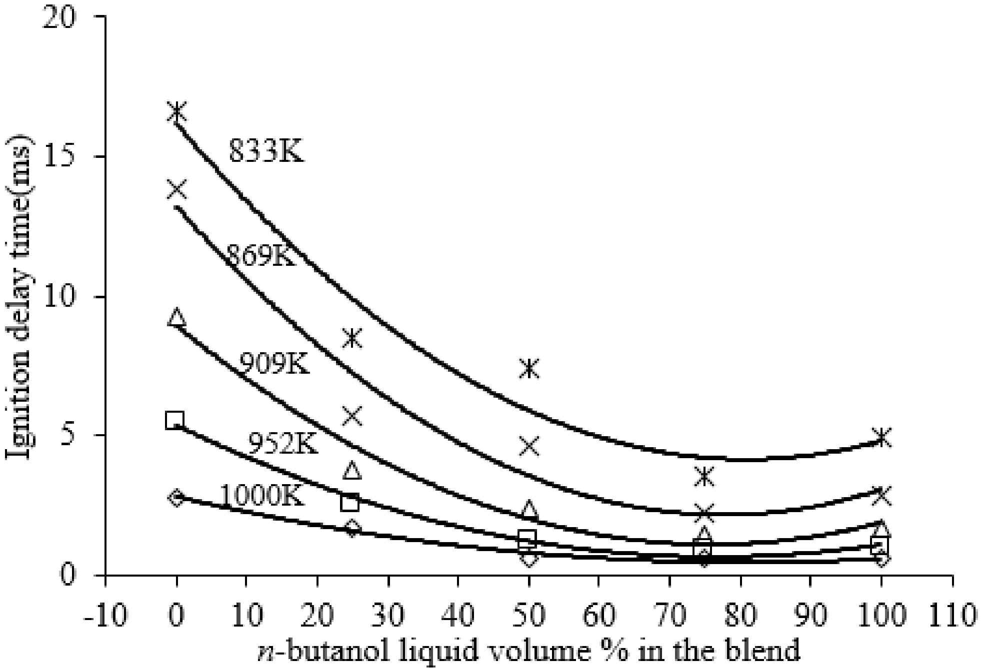

Figure 4.39. Change of ignition delay time with addition of *n*-butanol on TRF at stoichiometric condition, compressed pressure 2.0MPa and temperature range (833K-1000K).

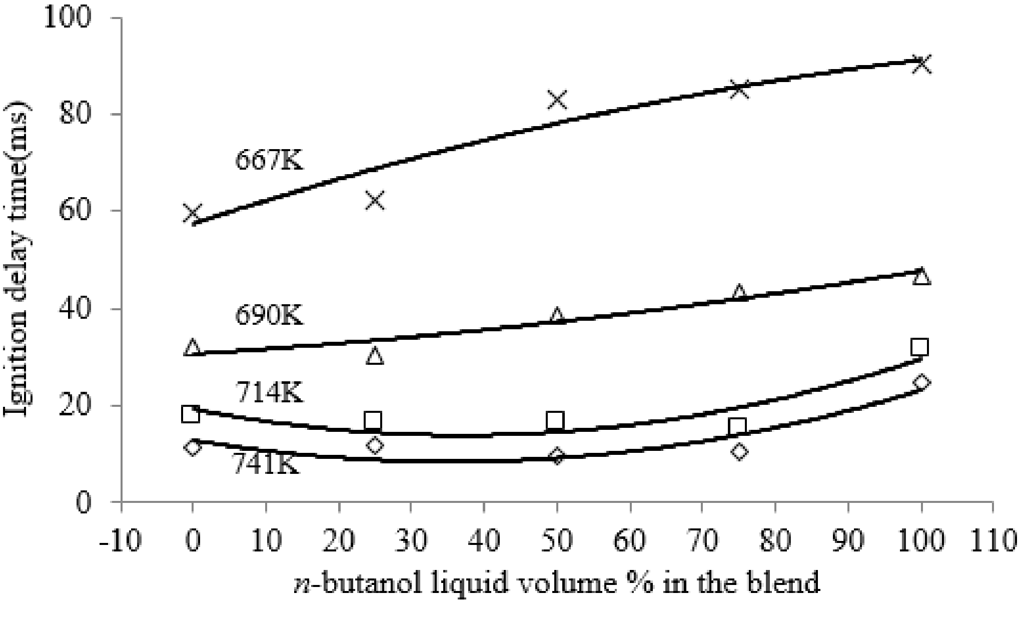

Figure 4.40. Change of ignition delay time with addition of n-butanol on TRF at stoichiometric condition, compressed pressure 2.0 MPa and temperature range (667K-741K).

4.7 Use of the experimental data in this work for simulation.

As discussed in Chapter 1, one of the main objectives of measuring ignition delay times in the RCM is to enable accurate modelling of the auto-ignition characteristic of a particular fuel at varying conditions of pressure, temperature and concentration using its chemical kinetics. Pressure traces for non-reactive mixtures are usually required to accurately simulate RCM experiments. This will help to account for heat loss during and after compression and also to avoid missing out any reactions that might have started to take place during compression. As pointed out in Section 1.7, non-reactive pressure traces with the same specific heat and initial condition of pressure and temperature as the reactive mixture are used to calculate volume expansion term using equation 1.12

Different RCMs have different extents of heat loss after compression due to their design and operating conditions. Those with substantial amounts of heat loss will necessitate the use of non-reactive pressure measurements for each particular fuel and condition in order to obtain a time dependent volume expansion term before carrying out chemical kinetic simulations. However, those with negligible heat loss will have their time dependent effective volume almost the same as that of the actual chamber and therefore simulations can be done using constant volume.

In this section comparison was made using Leeds RCM between the measured ignition delay times of TRF mixture and TRF/*n*-butanol blend at stoichiometric condition and end of compression pressure of 2.0 MPa and their corresponding simulations using constant volume approach (assuming negligible heat loss during delay period) and variable effective volume approach. Figs. 4.41&4.42 show the ignition delay times for these fuels using the two approaches (data measured and simulated by PhD student Edirin Agbro). Comparison with research gasoline RD387 from Kukkadapu et al. [2012] is also made. It can be seen that there is no substantial difference between the constant and variable volume approaches and therefore the experimental data in this work can be reasonably simulated using constant volume approach because all measurements were made at similar conditions to those shown in Figs 4.41&4.42. However, it should be noted that, since the heat loss characteristic for a particular machine depends on operating conditions, then non-reactive pressure traces need to be measured for new operating condition and run simulations using variable effective volume to compare with constant volume.

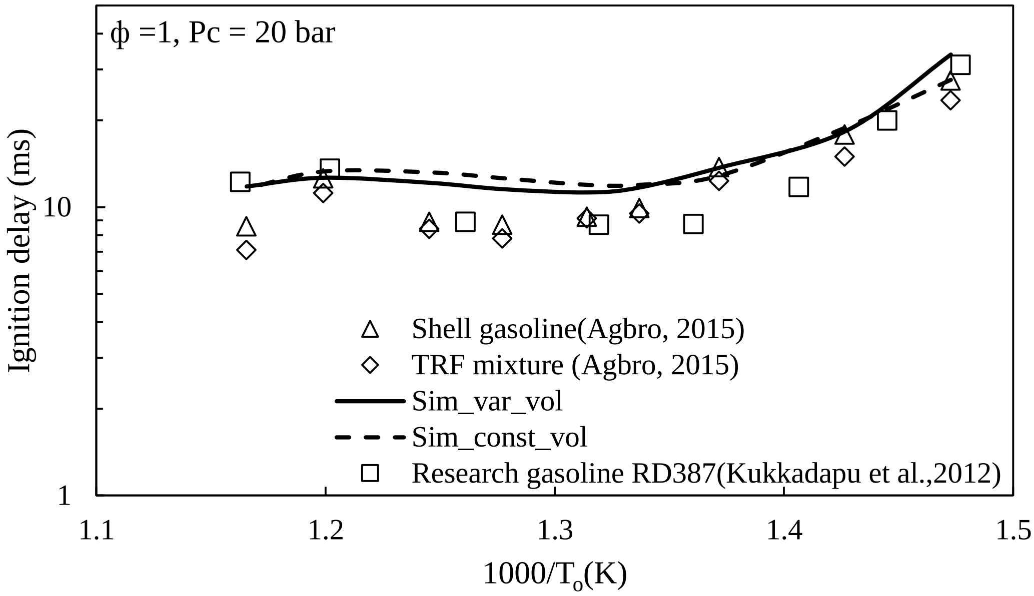

Figure 4.41. Comparison between measured and simulated of ignition delay times for gasoline and TRF mixture. Simulations were run using constant and variable volume approaches.

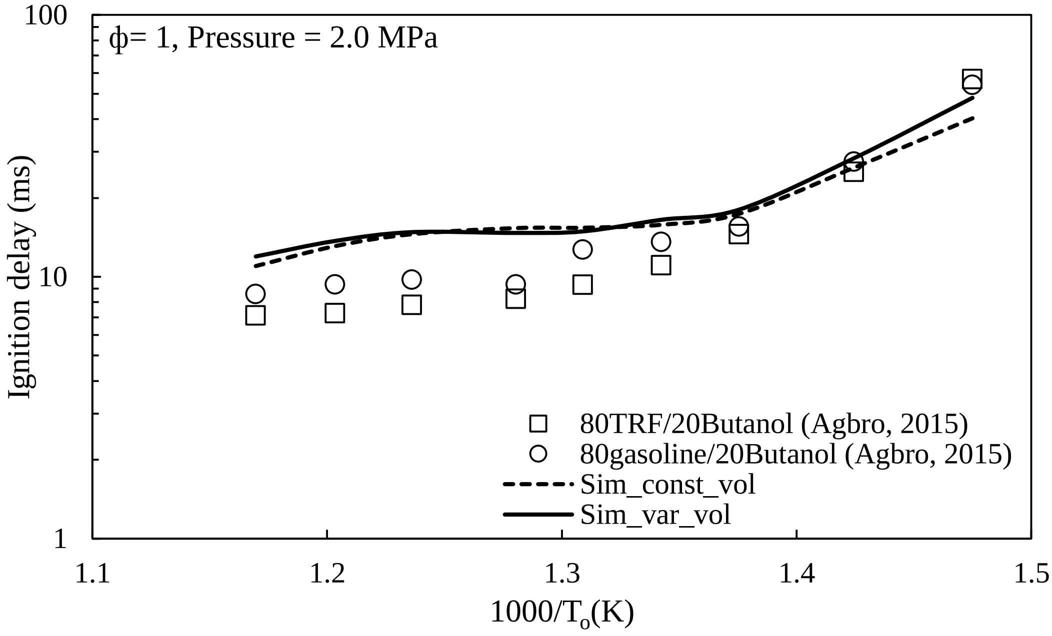

Figure 4.42. Comparison between measured and simulated of ignition delay times for gasoline/butanol and TRF/butanol blends. Simulations were run using constant and variable volume approaches.

4.8 Summary.

Comparison of measurements taken from Leeds and UCT RCMs at the same conditions have shown to differ. The main reason for this difference is due to their difference in heat loss behaviour, with UCT shows higher heat loss and thus measures longer delay times than Leeds.

Butanol is considered as one of the alternative biofuels which can potentially replace ethanol. Its effect on the ignition delay times of *iso*-octane and toluene was studied in this Chapter. Addition of *n*-butanol in *iso*-octane and toluene show a rather different outcome. *iso*-octane was made more reactive at higher temperature and thus shorter delay times were measured, and less reactive at lower temperatures with longer delay times. Toluene reactivity was significantly increased with butanol addition throughout the temperature range.

Comparison of addition of *n*-butanol and ethanol on TRF gasoline surrogate was also made, and Fig 4.43 shows a summary of the effect of adding equivalent amount of ethanol and *n*-butanol to the TRF surrogate in the temperature range between 800K and 952K. The curves are the difference between the measured delay times of the blends and that of pure TRF, $\Delta\tau$. The “zero” horizontal line represents pure TRF. Within this temperature range, *n*-butanol and ethanol have generally shown to have similar effect on TRF ignition delay times at lower temperatures and higher temperatures, where τ values of TRF are increased at lower temperatures and decreased at higher temperatures. Ethanol starts to increase τ values of TRF at substantially higher temperatures compared to *n*-butanol. Interestingly, in the temperature range between 709K and 752K addition of *n*-butanol has no substantial effect to the τ values of TRF.

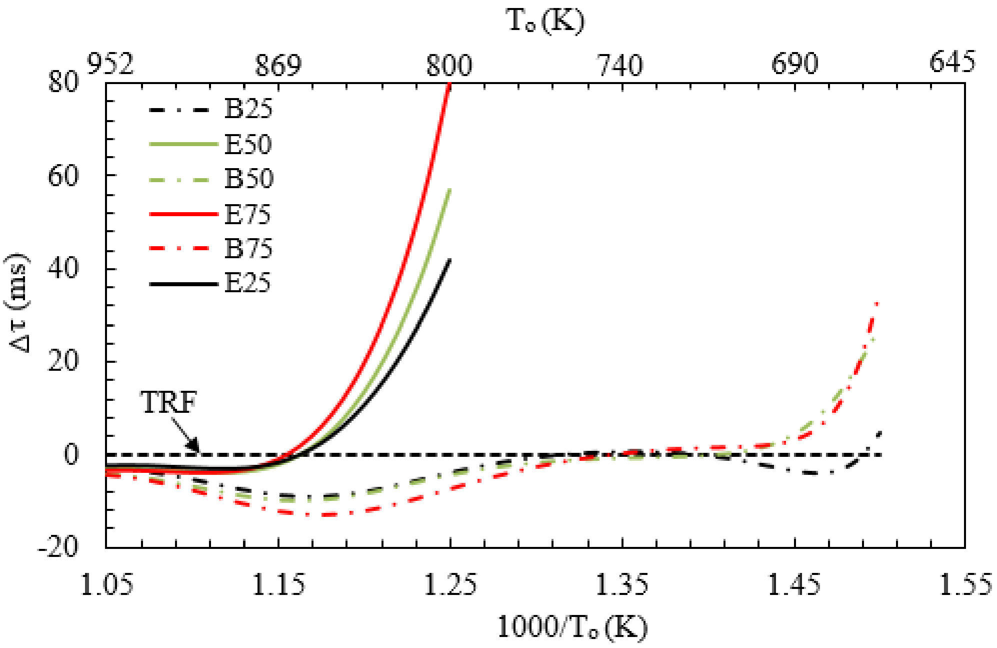

Figure 4.43. Ignition delay time difference between those of the blends and pure TRF at the end of compression pressure of 2.0 MPa.

CHAPTER 5: AUTOIGNITION BLENDING LAW.

5.1 Introduction

To be able to predict the auto-ignition behaviour of fuels under varying conditions of pressure, temperature and composition would be a very powerful tool. It could be used to increase and optimise engine performance and reduce pollution, as well as act as a safety tool for fuel storage. In an era which searches for new sources of liquid fuels, the optimal blends of different classes of fuel for efficient power generation with clean combustion have to be found. A major factor in the selection of these blends is their auto-ignition behaviour under varying conditions of pressure, temperature and concentration. It is therefore beneficial to develop auto-ignition blending laws that are able to predict the ignition delay times of different fuel blends.

Numerous empirical ignition delay correlation models have been proposed by different research groups [Yates et al., 2010; Qin et al., 2001; He et al., 2005; Goldsborough, 2009; Zhu et al., 2015; Li et al., 2014]. These are usually for single pure fuel components at relatively high temperature and are validated against chemical kinetic and/or experimental measurements. Measurements of ignition delay times, τ, in shock tubes, RCMs, engines, and constant volume bombs, have shown them to be very dependent on temperature, pressure and fuel concentration [Yates et al., 2010; He et al., 2005; Zhu et al., 2015; Li et al., 2014; Goutham et al.,2012]. A useful simplification is to characterise auto-ignition behaviour of a fuel by a global one step mechanism represented by an Arrhenius expression:

$$\tau = AP^{-n}\exp(E/RT), \tag{5.1}$$

where A and n are calibrations factors that change with fuel/air concentrations and temperature.

These empirical models have been used successfully to predict τ for both single component fuels and blends of different fuels under specified conditions. However, many of these models are only validated using fuels and/or conditions that do not show negative temperature coefficient (NTC) behaviour. This has been relatively easy and convenient, as the values of activation energy in these models are nearly constant over a wider temperature range. To the author’s knowledge only the empirical correlation model of

Goldsborough et al. [2009] predicts NTC behaviour of *iso*-octane, including different pressure and temperature conditions.

Practical gasoline and diesel fuels are composed of different classes of hydrocarbons in hundreds of different compounds, and their measured τ confirm negative temperature coefficient behaviour [Goutham et al., 2013; Fieweger et al., 1997; Herzler et al., 2007]. As described in Section 4.2, gasoline surrogate mixtures comprise a limited number of carefully selected individual hydrocarbons components, which collectively mimic the properties of the practical fuels, have been widely adopted. The use of these surrogate mixtures can simplify the derivation of τ values of blends based on the τ values for each constituent fuel. However, very little has been published on auto-ignition blending laws, a brief summary of which is highlighted below.

An extensive shock tube study of the ignition delay times of hydrogen and methane blends at pressures and temperatures, ranging from 800K to 2000K and 0.1 to 0.3 MPa, was conducted by Cheng and Oppenheim [1984]. The delay times of the blend mixture were correlated using the empirical expression,

$$\tau = {\tau_{H_2}}^{\beta} {\tau_{CH_4}}^{(1-\beta)}, \tag{5.3}$$

where τ_{H_2} and τ_{CH_4} are the ignition delay times for hydrogen and methane, and β is the mole fraction of hydrogen in the mixture. Very good agreement was obtained at the tested blends and conditions. Further studies were conducted by Gersen et al. [2008] for the stoichiometric blend mixtures of hydrogen and methane at higher pressure (1.0-7.0 MPa) in the temperature range 950K-1060K. Their results led to an Arrhenius like empirical relation for determining the delay times of their blend mixtures, incorporating the pressure and temperature dependency of ignition delay time for the pure individual fuels to be blended, of the form:

$$\tau = {A_{H_2}}^{\beta} {A_{CH_4}}^{(1-\beta)} \left(\frac{P_c}{T_c}\right)^{n_{H_2}\beta + n_{CH_4}(1-\beta)} \exp\left(\frac{E_{H_2}\beta + E_{CH_4}(1-\beta)}{RT}\right). \tag{5.4}$$

Recently, Sileghem et al., 2015 have suggested the use of an energy fraction α_i instead of mole or volume fraction x_i used in Cheng and Oppenheim [1984]. α_i, see below, is the heat of reaction of one fuel in the blend as a fraction of the total heats of reaction. Their method yielded a relatively good agreement with PRF-methanol blends calculated from detailed chemical kinetics.

$$\alpha_i = \frac{\Delta c {H_i}^{o} x_i}{\sum_{i=1}^{n} \Delta c {H_i}^{o} x_i}\,, \tag{5.5}$$

where ΔcH_i is the heat of reaction of the mixture components. The delay time for the blend mixture was given as:

$$\tau_{blend} = \prod_{i=1}^{n} \tau_i^{\alpha_i}. \tag{5.6}$$

There have been no further reported tests of the validity of these methods with other blends. It would be interesting to check if these methods could accurately predict ignition delay times of other blends, especially those that show NTC behaviour.

In this Chapter, an attempt is made to formulate a mixing rule that can be used to predict the ignition delay time of fuel blends using the ignition delay times of the fuel components under different conditions of pressures and temperatures, including the NTC region, and to compare this new approach with the reported existing ones.

5.2 A suggested auto-ignition blending law.

A two parameter blending law is developed for binary mixtures based on the fractional mole weighting of the principal parameters in an Arrhenius expression, *A* and *E/R*, at constant pressure:

$$ln\tau = lnA + (E/RT). \tag{5.7}$$

This method will be termed, the linear by mole (LbM) method. The ignition delay time of the mixture of two fuels B and C to form a blend D will then be given as;

$$ln\tau_{D(LbM)} = x_B(lnA_B + (E/RT)_B) + x_C(lnA_C + (E/RT)_C), \tag{5.8}$$

with x_B and x_C are the mole fractions of fuel B and C in the mixture of fuel B and C. The two fuels are assumed to be mixed with air at the same value of ϕ. The values of *E/R* for individual fuel components are obtained from Eq. (5.9), and the values of *A* are obtained from the measured values of τ and *E/R* for a given pressure, using Eq. (5.10);

$$E/R = dln\tau/d(1/T), \tag{5.9}$$

$$A = \tau\exp(-E/RT). \tag{5.10}$$

Eq. (5.8) allows for different activation temperatures, *E/R*, and for values of *A* to change, but only linearly, with fractional fuel concentration.

As shown in Chapter 3, for fuels which show NTC behaviour, the values of E/R and A vary with temperature and therefore using the actual values of these parameters at a particular temperature will potentially enable more accurate prediction of ignition delay time of blends with and without NTC behaviour. This makes LbM method different to those suggested by Cheng and Oppenheim, [1984 and Gersen et al. [2008] which were only designed and tested for fuels without NTC behaviour and at high temperatures.

5.2.1 Blends investigated.

The predicted data points employing this approach are compared with the experimental results. Some values were obtained by other workers and some in the course of the present studies. The fuel blend mixtures studied in this work are given in Table 5.1 together with the source from which relevant data were obtained.

Fuels		Data source for fuel/air		Data source for blends
B	C	B	C	
CH_4	H_2	[Gersen et al.,2008]	[Gersen et al.,2008]	[Gersen et al.,2008]
i-C_8H_{18}	n-C_7H_{16}	[Fieweger et al., 1997]	[Fieweger et al., 1997]	[Fieweger et al., 1997]
C_7H_8	n-C_7H_{16}	[Herzler et al., 2007]	[Herzler et al., 2007]	[Herzler et al., 2007]
C_7H_8	n-$C_4H_{10}O$	[PW]	[PW]	[PW]
i-C_8H_{18}	n-$C_4H_{10}O$	[PW]	[PW]	[PW]
TRF*	n-$C_4H_{10}O$	[PW]	[PW]	[PW]
TRF*	C_2H_6O	[PW]	[Mittal et al.,2014]	[PW]

Table 5.1. Constituent fuels studied in this work and their source.

[PW] Present Work

[TRF*] Constituent fuels that make this TRF mixture are shown in Table 4.4 in Chapter 4.

5.2.2 CH_4/H_2 blends.

For these blends, experimental ignition delay times were obtained entirely from an external source, [Gersen et al., 2008] who used a shock tube, under stoichiometric conditions at pressures between 1.5 and 7.0 MPa, and temperatures between 950 and 1060K. The blends are presented as a mole fraction of hydrogen in a mixture of both fuels, ($H_2/(H_2+CH_4)$). In Gersen et al. [2008], ignition delay times for different pressures were presented in a single plot by dividing τ values with the ratio (P_o/T_o) raised to the pressure dependency, n, i.e $\tau/(P_o/T_o)^n$. Gersen et al. [2008] used constant values of the pressure dependency coefficients, for H_2 as -1.3 and CH_4 as -2.3 throughout the temperature range they studied. Also in their work, the values of n for the blends were obtained by mole weighting of the individual pure fuel values i.e. $n = n_{H_2}x_{H_2} + n_{CH_4}x_{CH_4}$, where x_{H_2} and x_{CH_4} are the mole fractions of H_2 and CH_4 in the blend.

To obtain τ predictions for the data presented in Gersen et al. [2008] using the LbM method, *E/R* values were obtained from the gradient of the curve for constituent mixtures (CH_4 and H_2) using Eq. (5.9) and corresponding values of *A* calculated from Eq. (5.10). Predicted values of τ were then calculated using Eq. (5.8). Figs. 5.1-5.3 show the results obtained from the LbM method, together with the experimental results from Gersen et al. [2008]. Excellent agreement is found between these sets of results for all blends, throughout the temperature range.

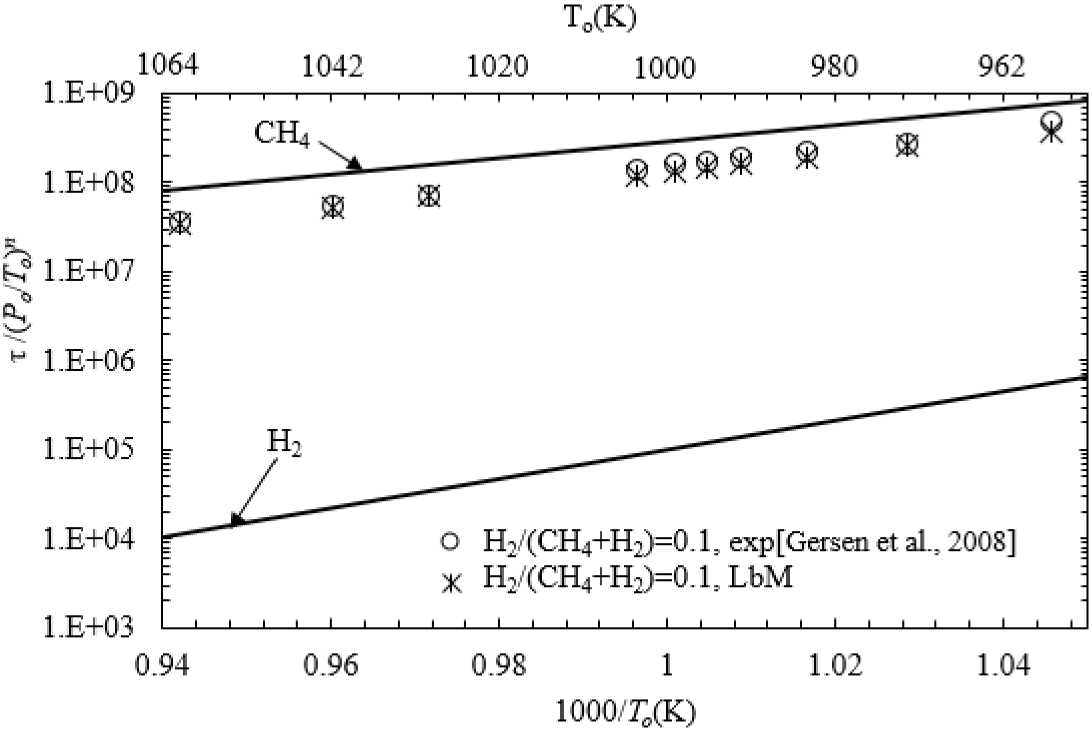

Figure 5.1. Ignition delay time divided by (P_o/T_o) to the power of pressure dependency n upon reciprocal temperatures for stoichiometric pure individual constituents (CH_4 and H_2) represented by solid lines and their blend, $H_2/H_2+CH_4=0.1$, represented by circles [Gersen et al., 2008], LbM results represented by asterisks. Pressure 1.5-7.0 MPa.

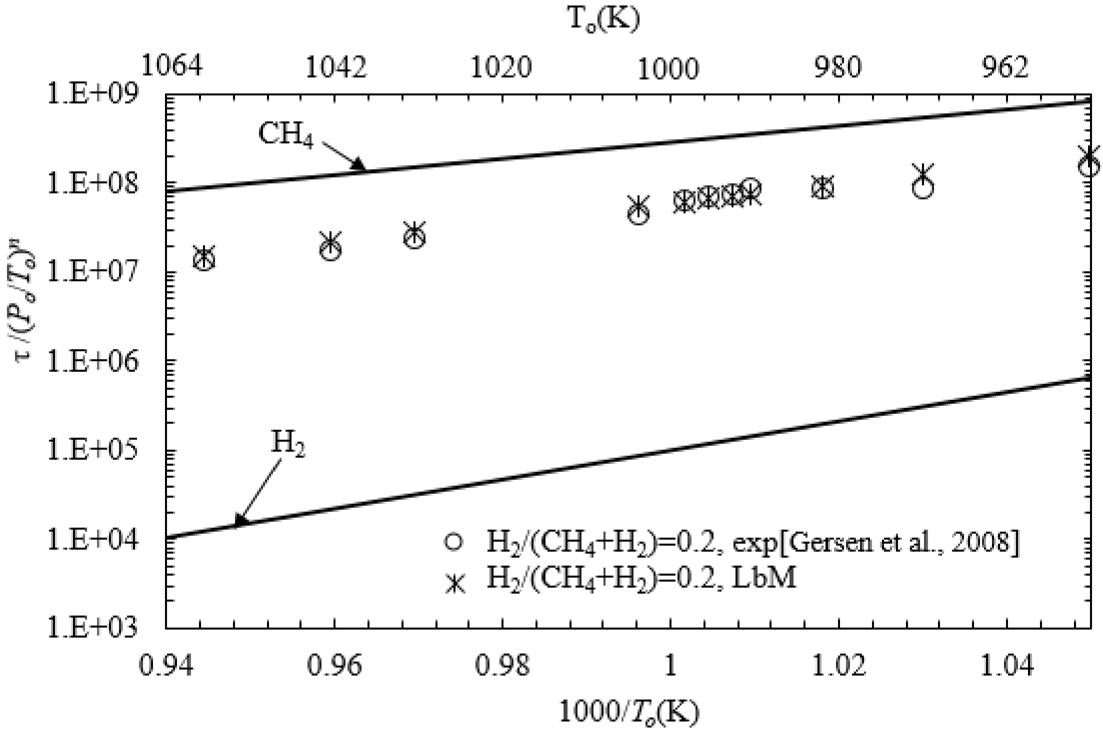

Figure 5.2. Ignition delay time divided by (P_o/T_o) to the power of pressure dependency n upon reciprocal temperatures for stoichiometric pure individual constituents (CH_4 and H_2) represented by solid lines and their blend, $H_2/H_2+CH_4=0.2$, represented by circles [Gersen et al., 2008], LbM results represented by asterisks. Pressure 1.5-7.0 MPa.

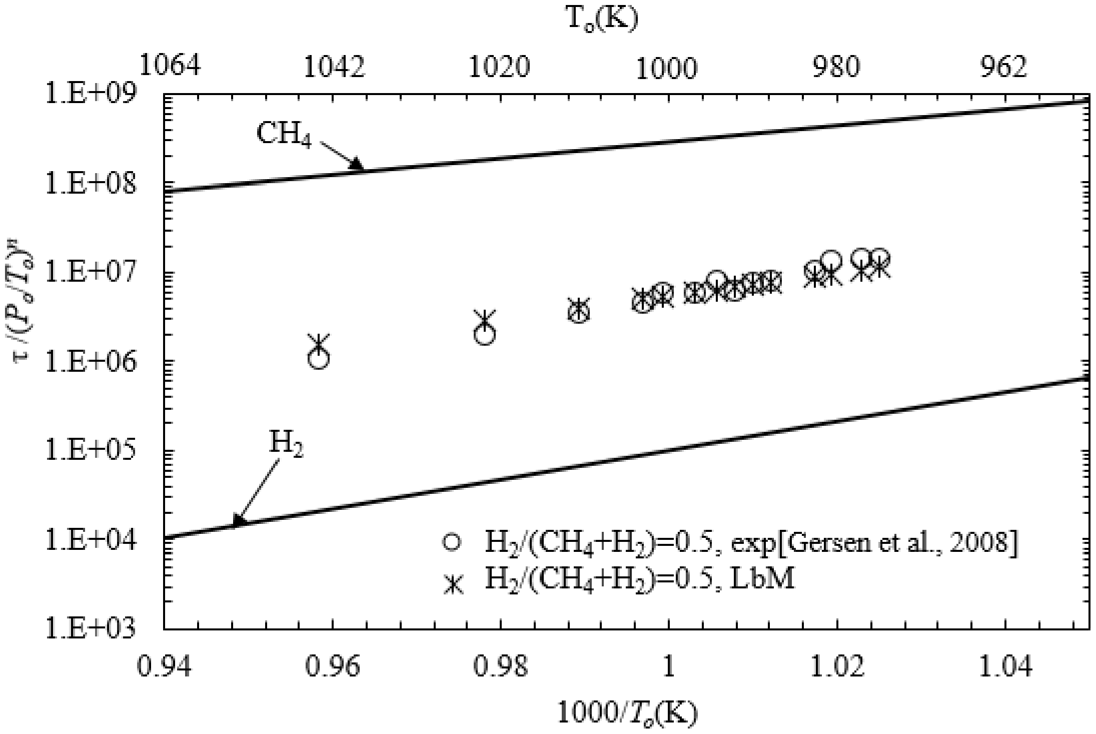

Figure 5.3. Ignition delay time divided by (P_o/T_o) to the power of pressure dependency n upon reciprocal temperatures for stoichiometric pure individual constituents (CH_4 and

H_2) represented by solid lines and their blend, $H_2/H_2+CH_4=0.5$, represented by circles [Gersen et al., 2008], LbM results represented by asterisks. Pressure 1.5-7.0 MPa.

5.2.3 Primary Reference Fuel (PRF) blends.

In this instance, experimental ignition delay times for different PRF blends of stoichiometric mixtures were obtained from an external source, namely [Fieweger et al., 1997]. Shock tube measurements of τ, for PRF60 (0.6 *iso*-octane/0.4 *n*-heptane, by liquid volume fraction), PRF80 (0.8 *iso*-octane/0.2 *n*-heptane, by liquid volume fraction) and PRF90 (0.9 *iso*-octane/0.1 *n*-heptane, by liquid volume fraction) were conducted with stoichiometric constituent mixtures at the pressure of 4.0 MPa and temperature range of 710K-1175K. The fuel mole fractions and fuel/air mole fractions for constituent fuels in PRF blends were obtained using Eqs. (5.10) and (5.11), with the liquid densities given in Table 5.1, in Section 4.3. Data sources are summarised in Table 5.2.

Fig. 5.4 compares the percentage moles of *iso*-octane/air in the PRF/air mixture with octane number. Similar conversion procedure was used for TRF/*n*-butanol and TRF/ethanol blends, which were prepared using liquid volumes. The results are summarised in Tables 4.5 and 4.7 in Sections 4.6.3 and 4.6.4.

	PRF mixture composition		Fuel Designation
	iso-octane	*n*-heptane	
Liquid volume fraction	0.6	0.4	PRF60
Fuel mole fraction	0.57	0.43	
Liquid volume fraction	0.8	0.2	PRF80
Fuel mole fraction	0.78	0.22	
Liquid volume fraction	0.9	0.1	PRF90
Fuel mole fraction	0.89	0.11	

Table 5.2. Composition of constituent fuels in the PRF mixtures.

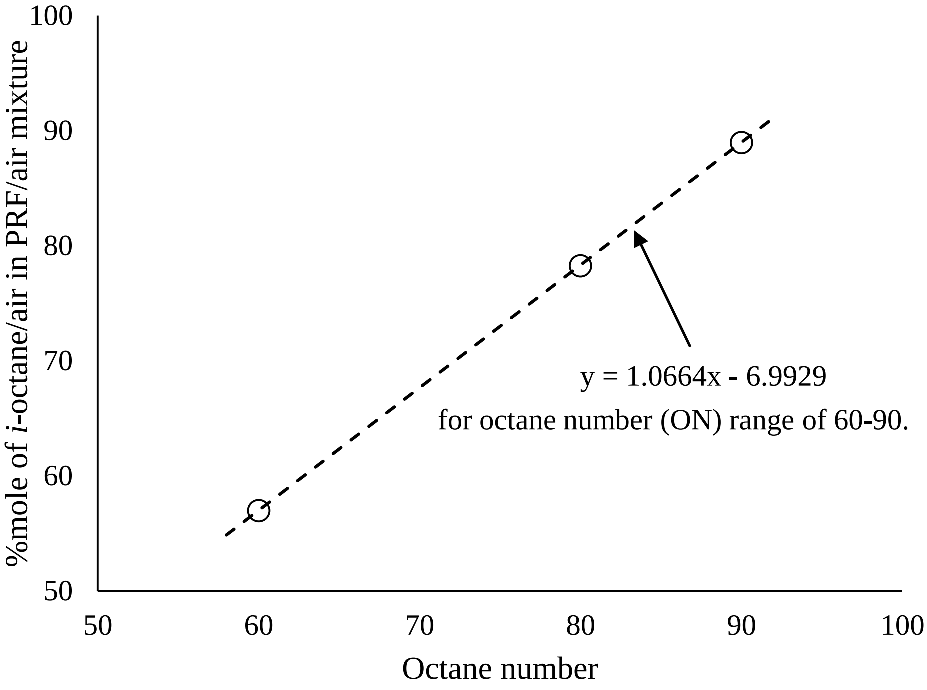

Figure 5.4. Percentage mole of i-octane/air in a PRF/air mixture vs octane number. The curve is the best fit line through the points.

Ignition delay times from the LbM method were obtained using Eq. (5.8). The obtained results, shown by asterisks, in Figs. 5.5-5.7, are in fair agreement with the experimental measurements, shown by circles, at the higher temperatures (T > 885K) but are over-predicted at the lower temperatures, where an NTC region develops. This trend is seen for all the PRF blends studied.

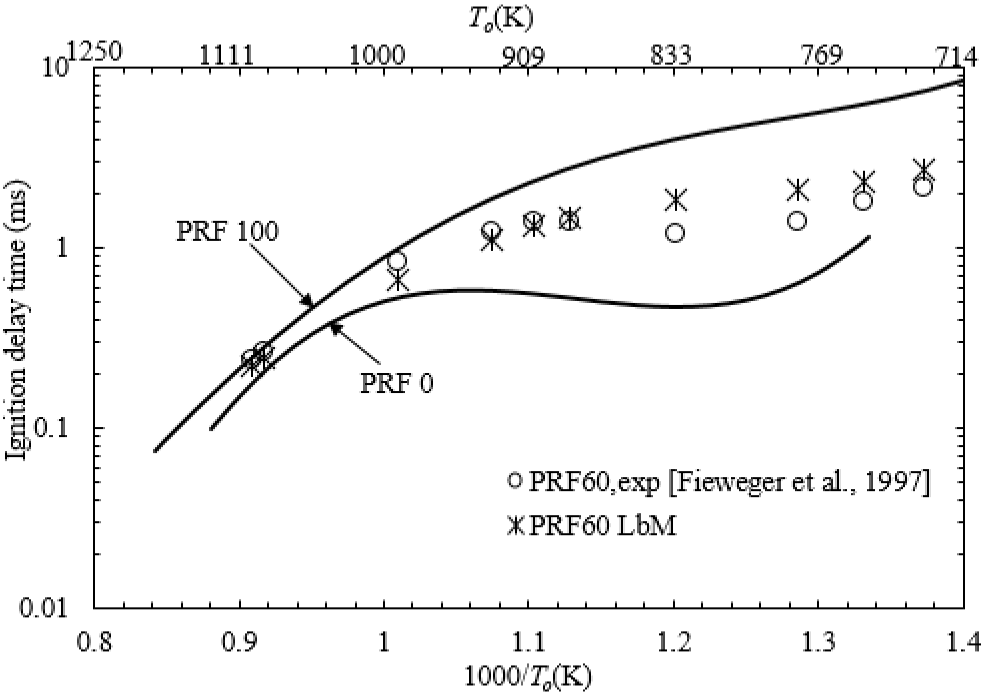

Figure 5.5. Ignition delay time versus reciprocal temperature for stoichiometric pure individual constituents (PRF0 and PRF100) represented by solid lines and their blend, PRF60, represented by circles, measurements made at 4.0 MPa. LbM results are represented by asterisks.

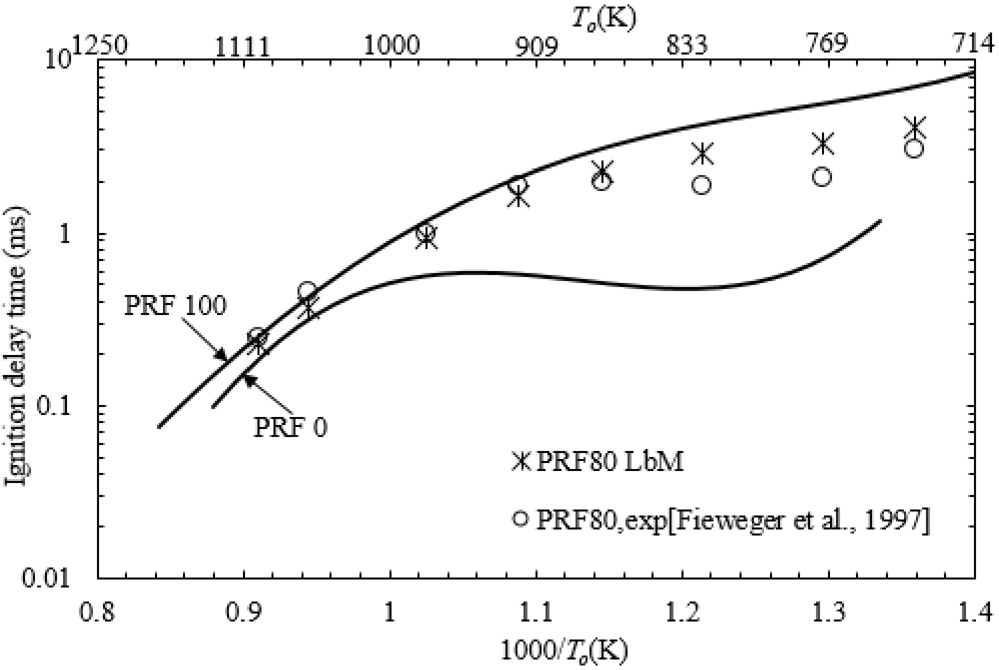

Figure 5.6. Ignition delay time versus reciprocal temperature for stoichiometric pure individual constituents (PRF0 and PRF100) represented by solid lines and their blend, PRF80, represented by circles, measurements made at 4.0 MPa. LbM results are represented by asterisks.

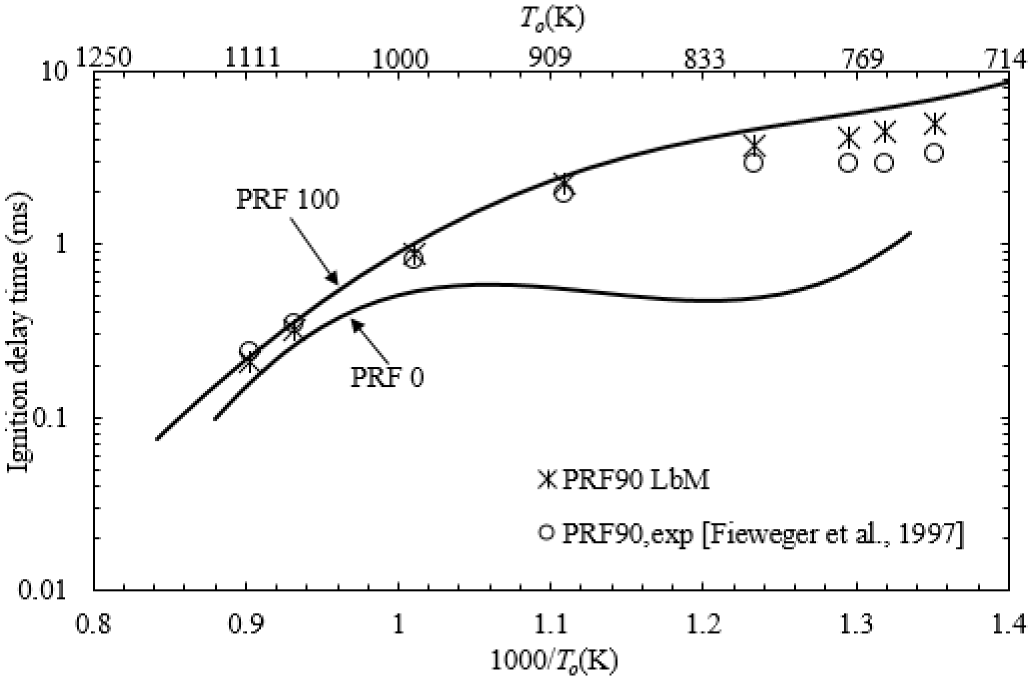

Figure 5.7. Ignition delay time versus reciprocal temperature for stoichiometric pure individual constituents (PRF0 and PRF100) represented by solid lines and their blend, PRF90, represented by circles, measurements made at 4.0 MPa. LbM results are represented by asterisks.

5.2.4 Toluene/*n*-heptane blend.

Experimental delay times for a stoichiometric toluene/*n*-heptane blend with fractional liquid volume ratios of 0.35 of *n*-heptane and 0.65 of toluene were obtained from the shock tube measurements of Herzler et al. [2007]. All mixtures were stoichiometric at a pressure of 3.0 MPa and temperatures between 620 and 1180K. Table 5.3 shows the proportions of constituent fuels in the blend in different fractions, derived from Eqs. (4.11) and (4.13). The blend was designated as T78, indicative of the toluene mole fraction in the fuel.

	Composition		Fuel designation
	toluene	*n*-heptane	
Liquid volume fraction	0.65	0.35	T78
Fuel mole fraction	0.78	0.22	

Table 5.3. Liquid fuel blends designation and constituents proportions.

Similar to the procedure for PRF blends, the LbM predictions are presented along with the measurements. The predictions in Fig. 5.8 agree relatively well with the experimental results at the higher temperatures. However, there is substantial disagreement at the low temperatures, from where the *n*-heptane NTC region starts. The asterisked predicted values become rather closer to the toluene values than to the measured blend values.

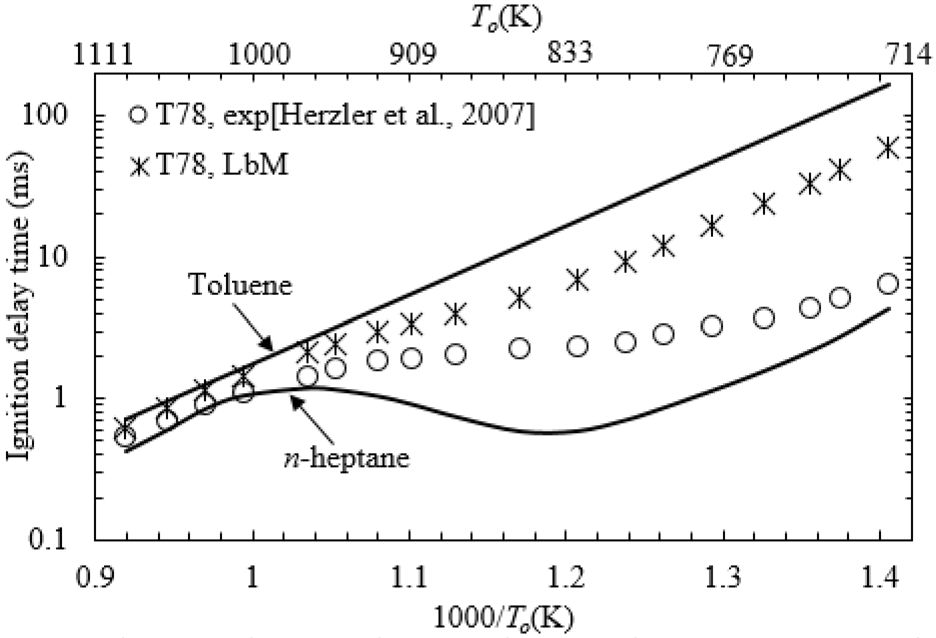

Figure 5.8. Experimental ignition delay time versus reciprocal temperatures for Toluene and *n*-heptane represented by solid curves and their blend, T78, represented by circles. LbM results are represented by asterisks. (Ø=1.0, Pressure 3.0 MPa).

5.2.5 *iso*-octane/*n*-butanol blend.

Figs. 5.9 and 5.10 show both the LbM predictions, the measured ignition delay times of the constituent mixtures, and of their blends for stoichiometric *I50* and *I70*, the compositions of which are shown in Table 4.3. Measurements were at 2.0 MPa for both blends. Results for the constituent fuels and their blends are shown in more detail in Section 4.5.1. Here only the experimental points for blend results are shown for comparison with the LbM predictions. For *I50*, LbM over-predicts the values of τ throughout the temperature range. For *I70*, fairly good predictions occur throughout the temperature range, but with slightly over-prediction at low temperature. In general, predictions were better at the higher temperatures.

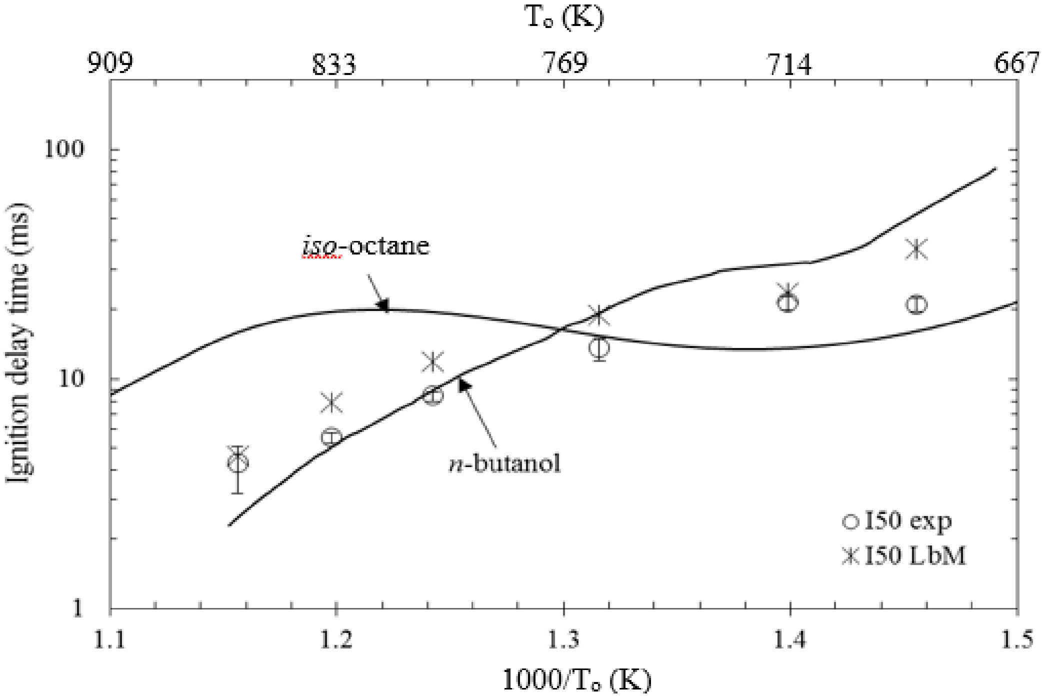

Figure 5.9. Experimental ignition delay time against reciprocal temperatures for *iso*-octane and *n*-butanol represented by solid curves and their blend, *I50*, represented by circles, LbM predictions are represented by asterisks. (Ø=1.0, Pressure 2.0 MPa).

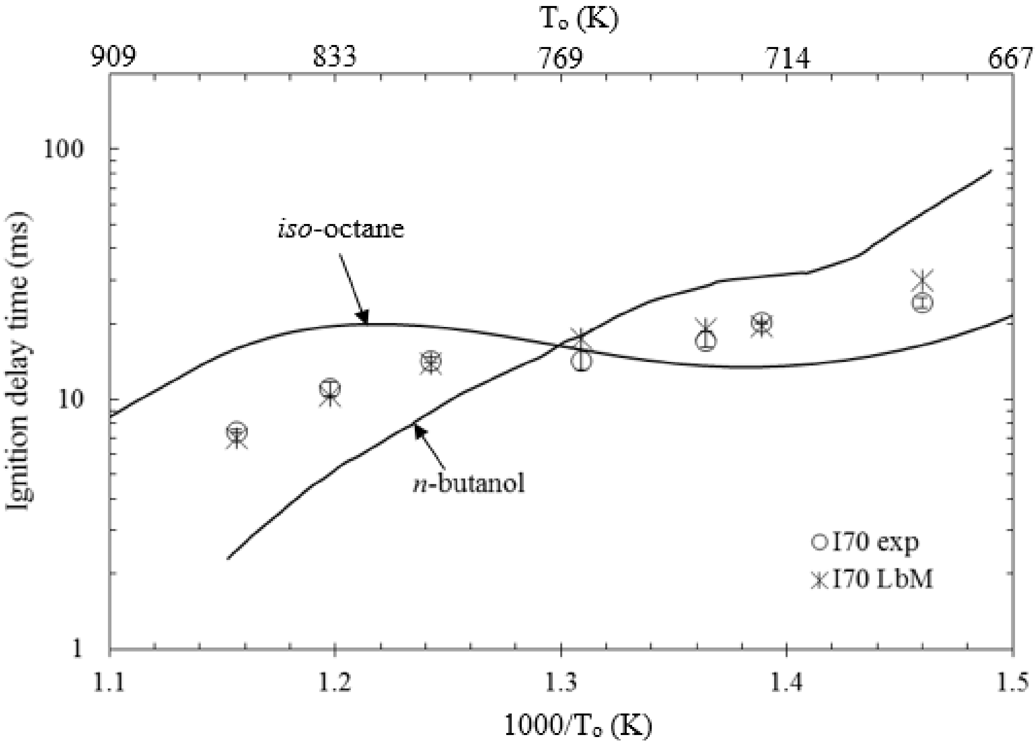

Figure 5.10. Experimental ignition delay time against reciprocal temperatures for *iso*-octane and *n*-butanol represented by solid curves and their blend, *I70*, represented by circles, LbM predictions are represented by asterisks. (Ø=1.0, Pressure 2.0 MPa).

5.2.6 Toluene/*n*-butanol blend.

Figs. 5.11 and 5.12 compare the LbM predictions, the measured ignition delay times of the constituent mixtures, and of the stoichiometric *T50* and *T70* blends, measured in the course of present work at 2.0 MPa. Detailed composition of these blends are shown in Table 4.3, along with their experimental measurements in Section 4.5.2. As with the *iso*-octane/*n*-butanol blends, only experimental points for blends are shown in this case, to allow clear comparison between the experimental results and LbM predictions. The LbM ignition delay times strongly over-predict the blends' measured ignition delay times throughout the temperature range.

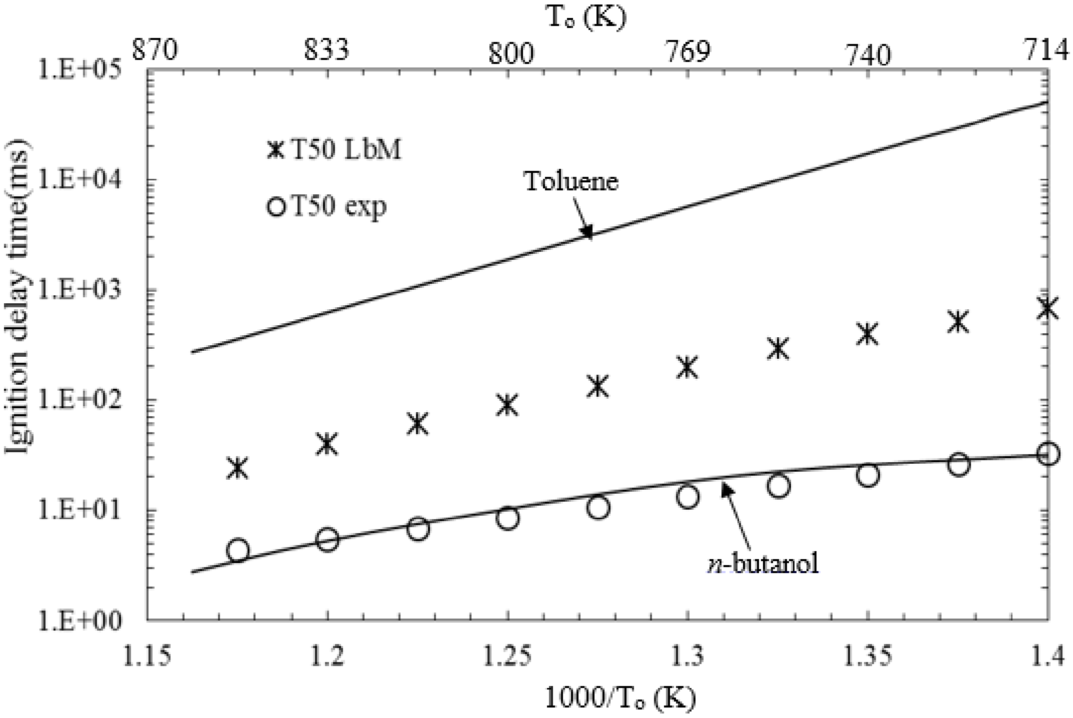

Figure 5.11. Experimental ignition delay time against reciprocal temperatures for Toluene and *n*-butanol represented by solid curves and their blend, *T50*, represented by circles, LbM predictions are represented by asterisks. (∅=1.0, Pressure 2.0 MPa).

A very surprising feature is observed with these blends, in that the experimental values for the blends are so close to the values of *n*-butanol. The reason for this feature was suggested in Section 4.5.2, that, *n*-butanol generates chain branching radicals that overwhelm those created by toluene and thus the *n*-butanol reactions dominate over those of the toluene. This feature makes the LbM blending law fails to predict correctly the τ values.

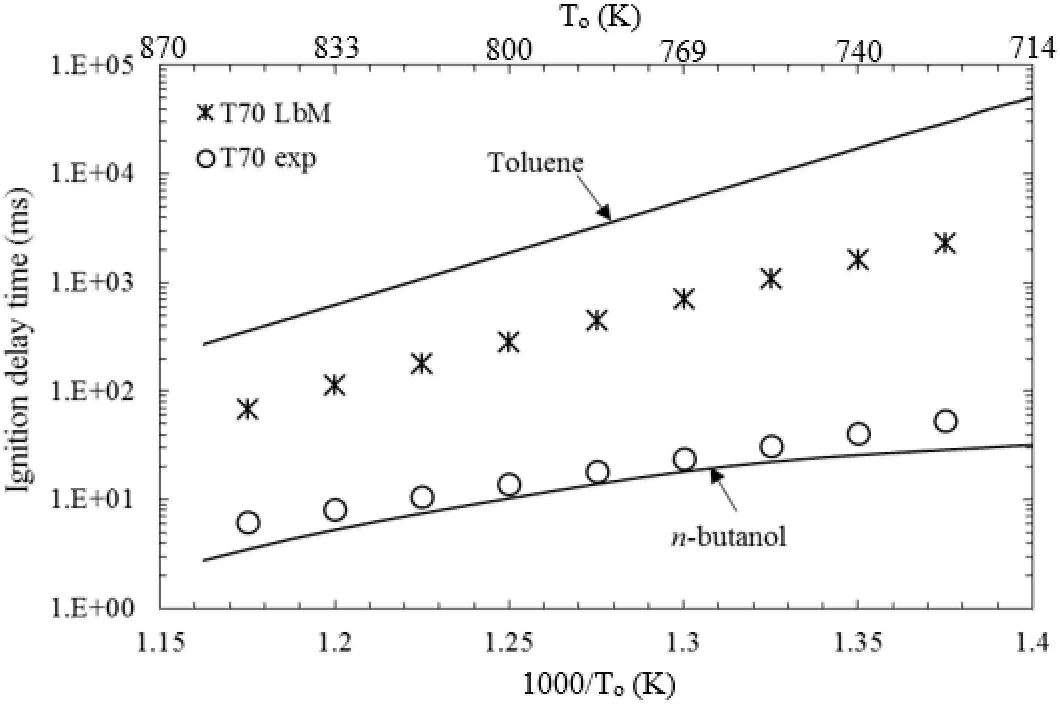

Figure 5.12. Experimental ignition delay time against reciprocal temperatures for Toluene and *n*-butanol represented by solid curves and their blend, *T70*, represented by circles, LbM predictions are represented by asterisks. (Ø=1.0, Pressure 2.0 MPa).

5.2.7 TRF/ethanol and TRF/*n*-butanol blends.

A further analysis of LbM predictions was conducted on the blends of TRF/ethanol and TRF/*n*-butanol. Fuel mole fraction, fuel/air mole fractions of ethanol and *n*-butanol in the TRF/ethanol (E blends) and TRF/*n*-butanol (B blends) were calculated from their corresponding liquid volume fractions using Eq. (4.11). The data are summarised in Tables 4.5 and 4.7 in Chapter 4. The measured ignition delay times for the TRF mixture and the blends were presented in Sections 4.6.3 and 4.6.4 in Chapter 4. Only experimental data points for blends are shown here, in order to feature a clear comparison with LbM predictions.

Figs. 5.13-5.15 show the plots of measured ignition delay times together, with the LbM predicted values for TRF/ethanol. The best predictions occur with E25 in Fig. 5.13, but otherwise the ethanol blend values are over-predicted, particularly at low temperatures.

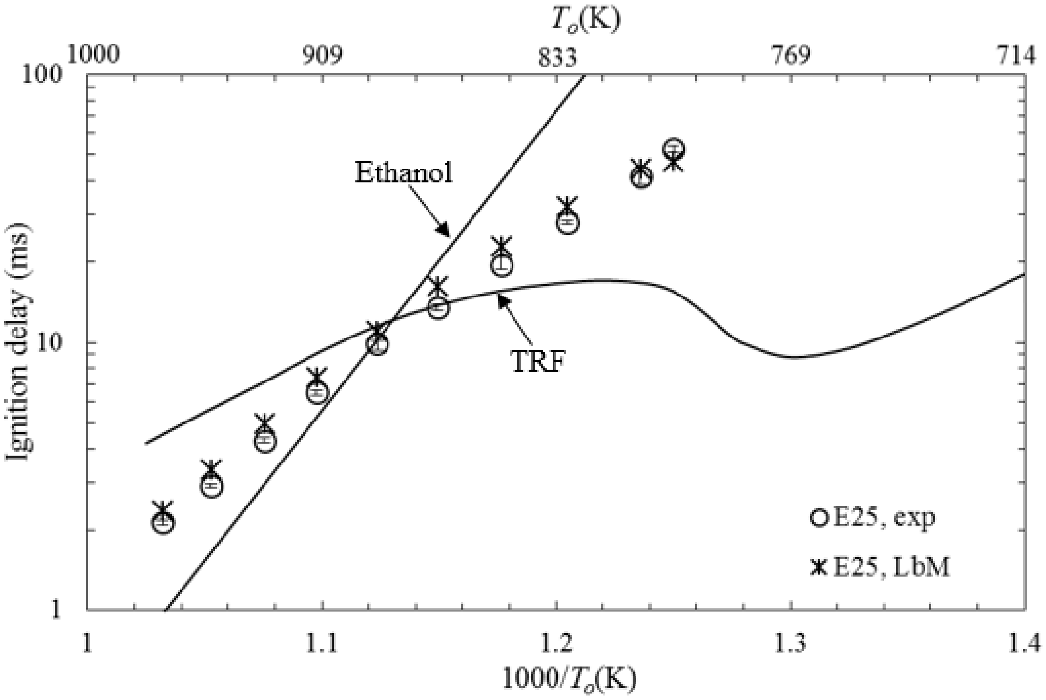

Figure 5.13. Experimental ignition delay time against reciprocal temperatures for TRF and Ethanol represented by solid curves and their blend E25 represented by circles, LbM predictions represented by asterisks. (∅=1.0, Pressure 2.0 MPa).

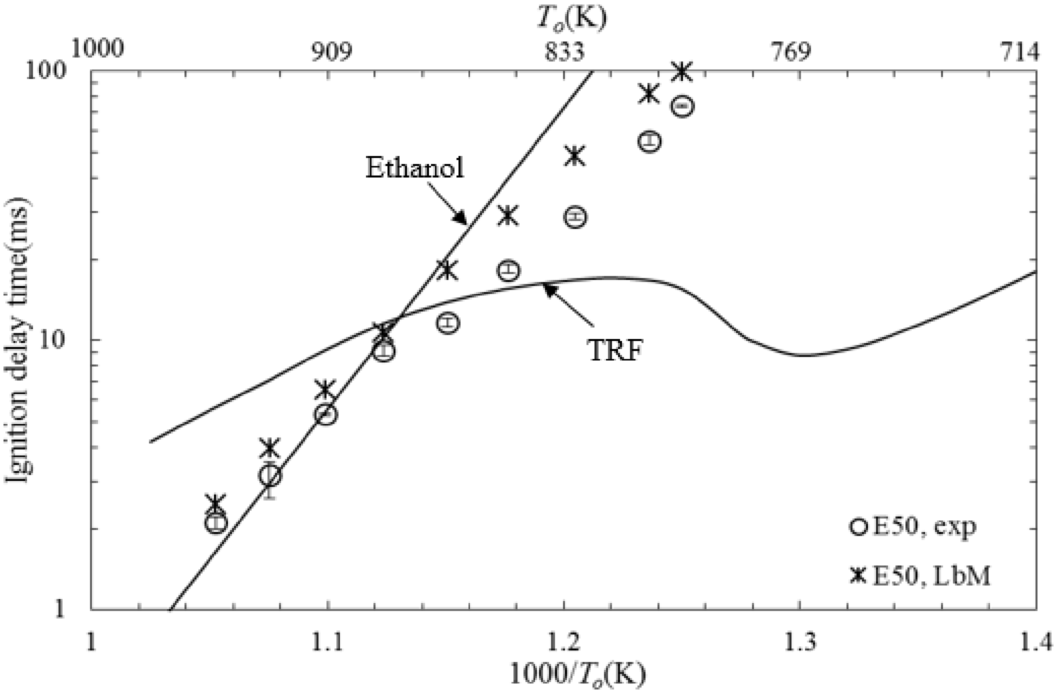

Figure 5.14. Experimental ignition delay time against reciprocal temperatures for TRF and Ethanol represented by solid curves and their blend E50 represented by circles, LbM predictions represented by asterisks. (∅=1.0, Pressure 2.0 MPa).

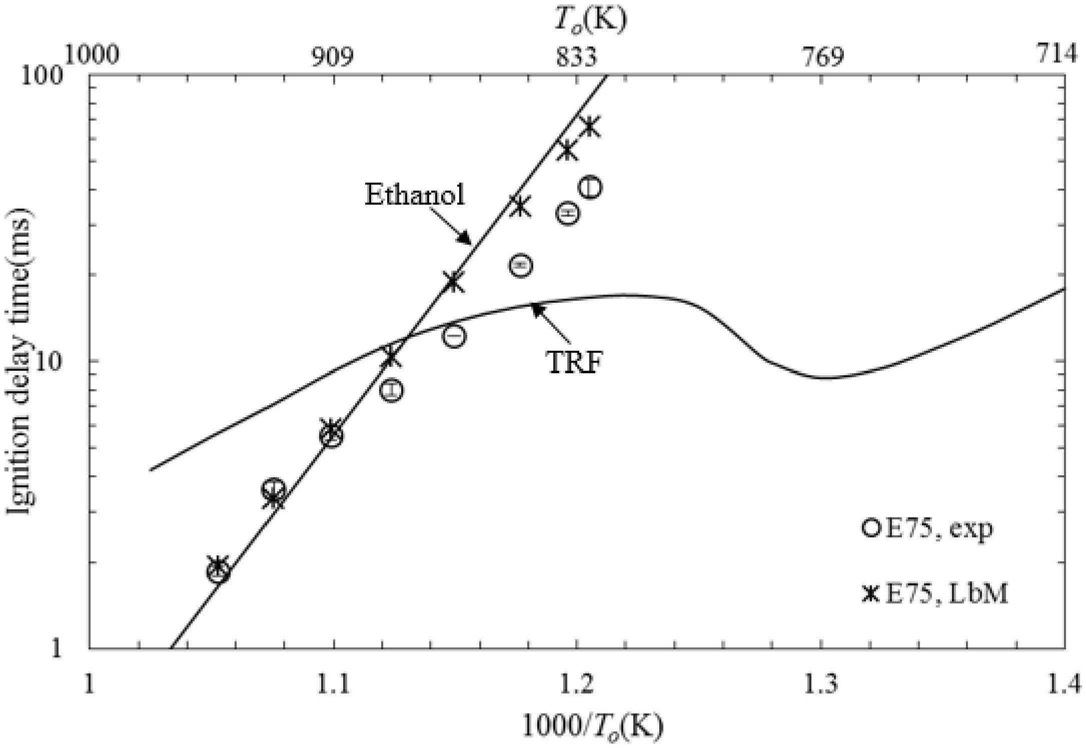

Figure 5.15. Experimental ignition delay time against reciprocal temperatures for TRF and Ethanol represented by solid curves and their blend E75 represented by circles, LbM predictions represented by asterisks. (∅=1.0, Pressure 2.0 MPa).

The TRF/*n*-butanol data extend to lower values of temperatures than those for ethanol and the experimental values indicate some influence of the TRF NTC regime. This is particularly so for B50 in Fig. 5.17. The predicted values show less influence.

It is striking that the τ values for some of the blends are lower than those of the pure constituent fuel. This is particularly evident for B75 blend for temperatures below 800K in Fig. 5.18. At such conditions the LbM blending law fails to predict τ values.

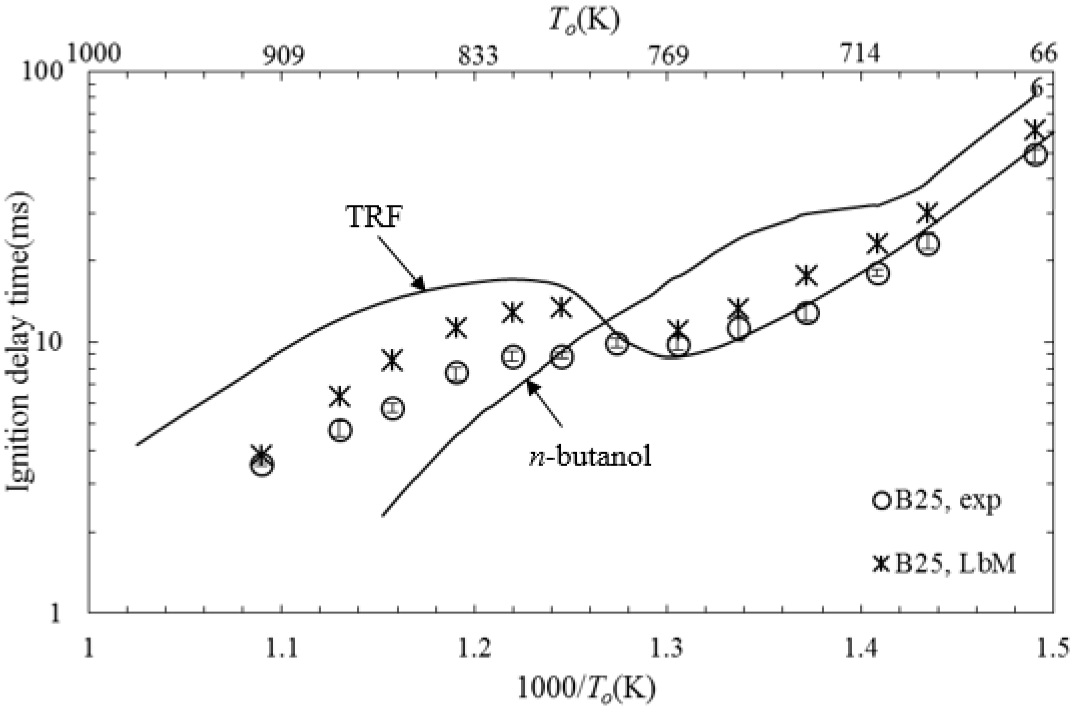

Figure 5.16. Experimental ignition delay time against reciprocal temperatures for TRF and *n*-butanol represented by solid curves and their blend B25 represented by circles, LbM predictions represented by asterisks. (Ø=1.0, Pressure 2.0 MPa).

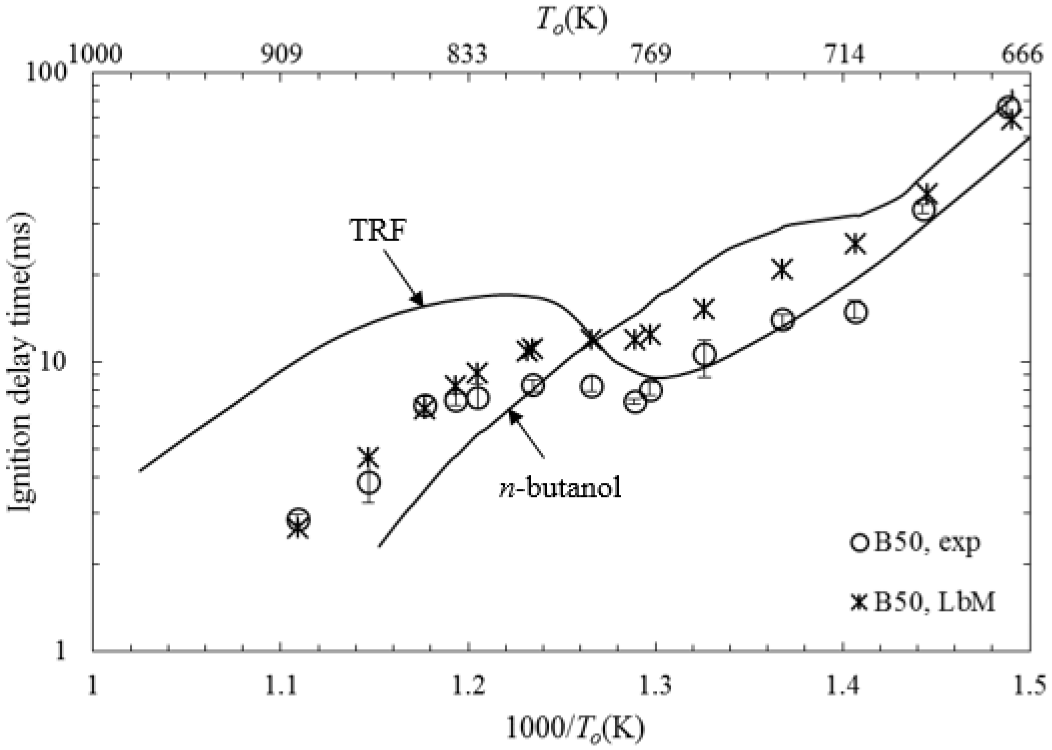

Figure 5.17. Experimental ignition delay time against reciprocal temperatures for TRF and n-butanol represented by solid curves and their blend B50 represented by circles, LbM predictions represented by asterisks. (Ø=1.0, Pressure 2.0 MPa).

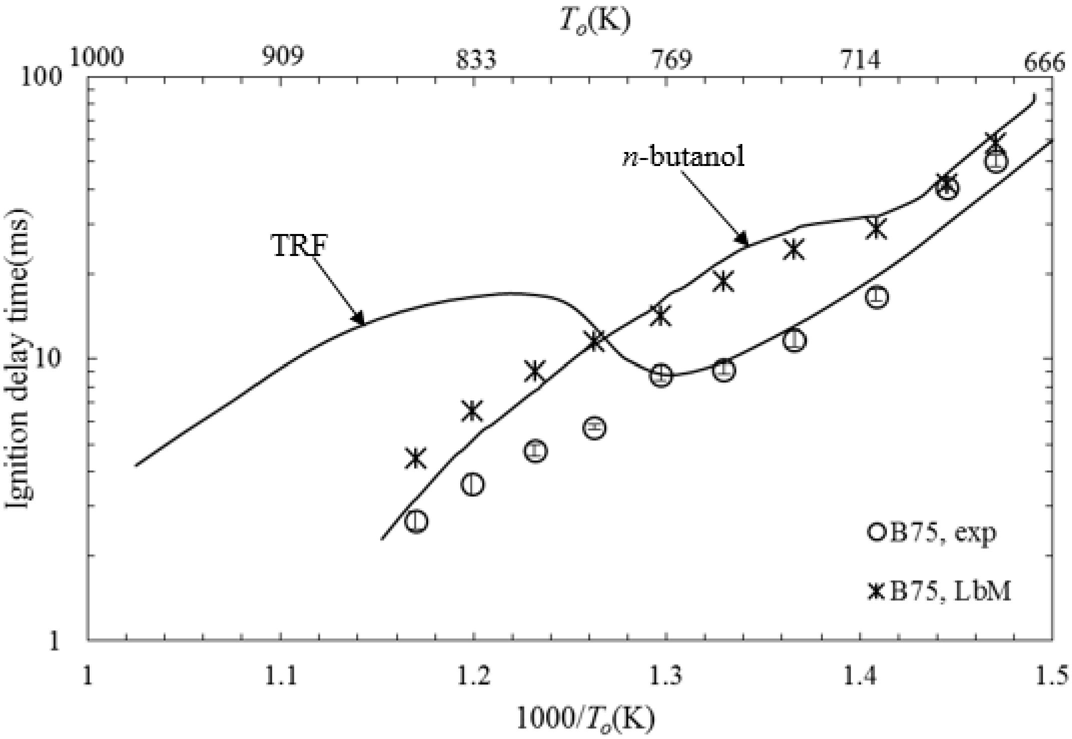

Figure 5.18. Experimental ignition delay time against reciprocal temperatures for TRF and n-butanol represented by solid curves and their blend B75 represented by circles, LbM predictions represented by asterisks. (∅=1.0, Pressure 2.0 MPa).

5.3 Improved blending law for PRF mixture.

A further development was made to improve the LbM blending law empirically for the PRF mixtures. More generally, the results obtained from the above 14 different blends show that the blending linearity of Eq. (5.8) is most closely followed when there is no NTC behaviour. A good example of this is the good predictability of the blending law for CH_4/H_2 blends in Section 5.2.1. The LbM predictions begin to deviate from the experimental values when one, or both, of the components show NTC behaviour. In this section the LbM predicted ignition delay times for PRF mixtures are compared with experimental values. In the PRF mixtures, the presence of *n*–heptane ensures the occurrence of NTC behaviour. The onset of NTC in this case was defined by the corresponding temperature at the inflexion point after the local maximum, τ, of *n*-heptane curve, which is about 870K. For temperatures below 870K, it was found that the experimental ignition delay times of the PRF mixtures from Fieweger et al. [1997] could be related to the octane number (ON), temperature T_o, LbM predicted delay times τ_{LbM} and an exponential factor *m* using the following empirical expression for τ_i.

$$\tau_i = \tau_{LbM}(ON.1000/T_o)^m \text{, for } 1000/T_o > 1.15. \tag{5.11}$$

With τ_i equal to the experimental values, and those of *m* were calculated from;

$$m = \frac{\log(\tau_i/\tau_{LbM})}{\log(ON.1000/T_o)} \tag{5.12}$$

Fig. 5.19 shows values of *m* for different PRF mixtures and temperatures at a pressure of 2.0 MPa. Evaluated in this way, a linear fit curve is fitted through the data points and there suggest a constant value of -0.8 for $1000/T_o$ > 1.19.

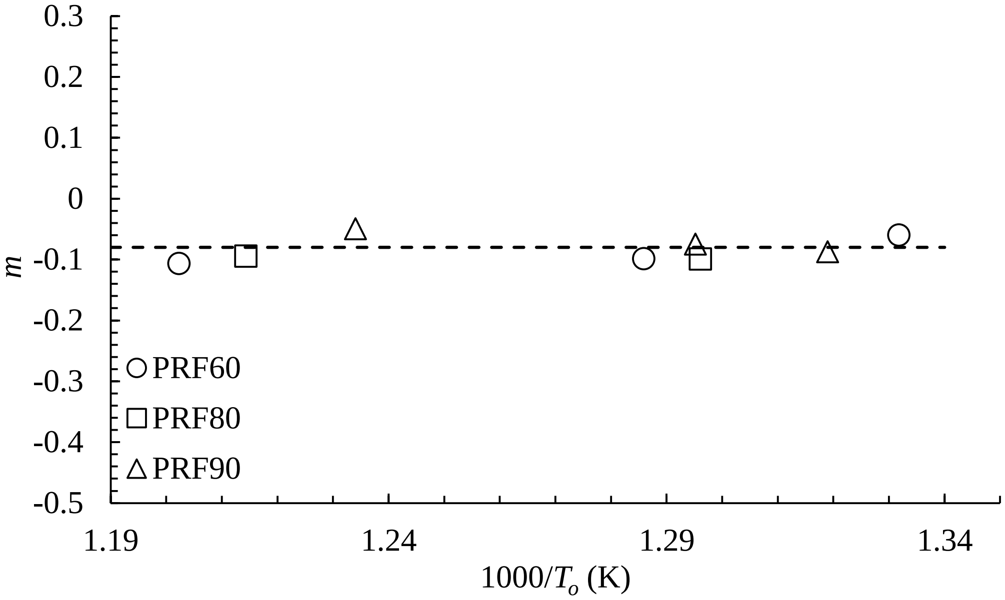

Figure 5.19. Values of m for PRF mixtures at different temperature, Pressure 2.0 MPa. The dotted line is the best fit through the values of *m*.

With this value of *m*, and application of Eq. (5.11) for the temperatures below 870K, the values of τ_i are plotted in Figs. 5.20-5.22, by the square symbols. There is very good agreement between the three PRFs and conditions shown, and the measurements, shown by the circle symbols. However, such a direct procedure was not applicable to the other blends in Section 5.2.

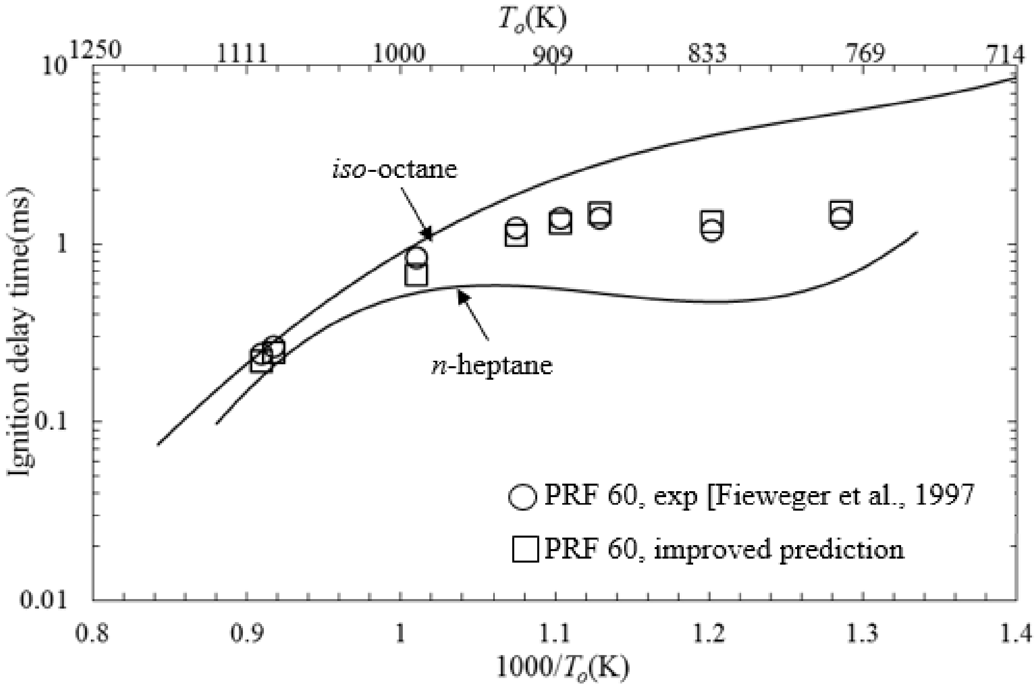

Figure 5.20. Experimental ignition delay time against reciprocal temperatures for *n*-heptane and *iso*-octane represented by solid curves and their blend, PRF60, represented by circles. τ_{LbM} PRF corrected values are shown by square symbols. (Ø=1.0, Pressure 4.0 MPa).

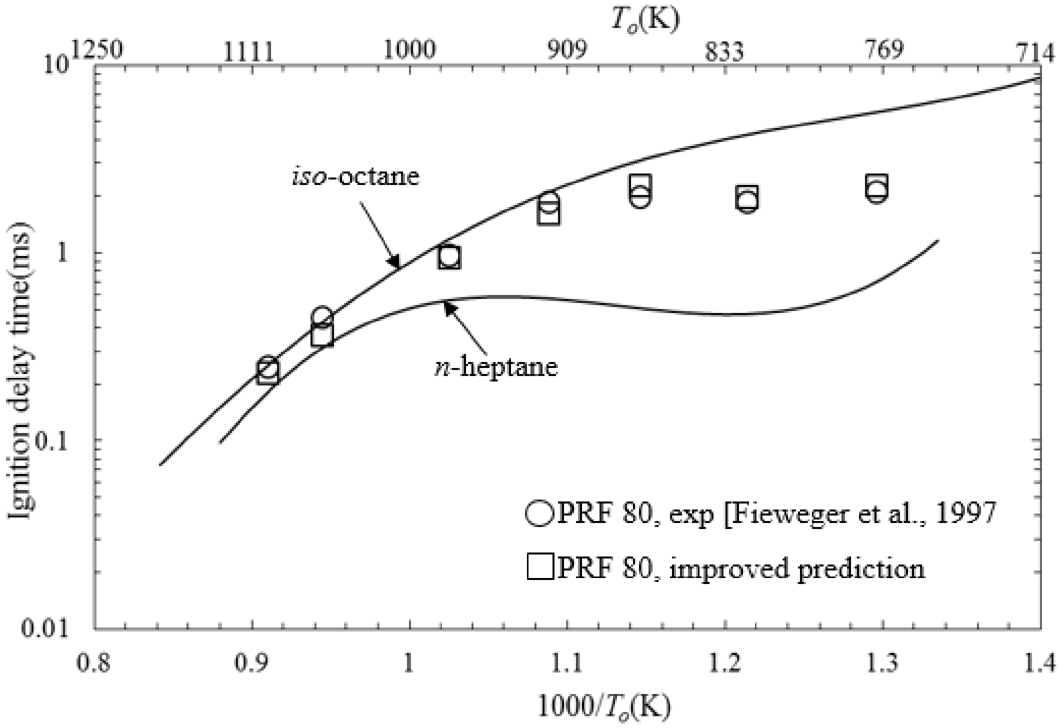

Figure 5.21. Experimental ignition delay time against reciprocal temperatures for *n*-heptane and *iso*-octane represented by solid curves and their blend, PRF80, represented

by circles. τ_{LbM} PRF corrected values are shown by square symbols. (∅=1.0, Pressure 4.0 MPa).

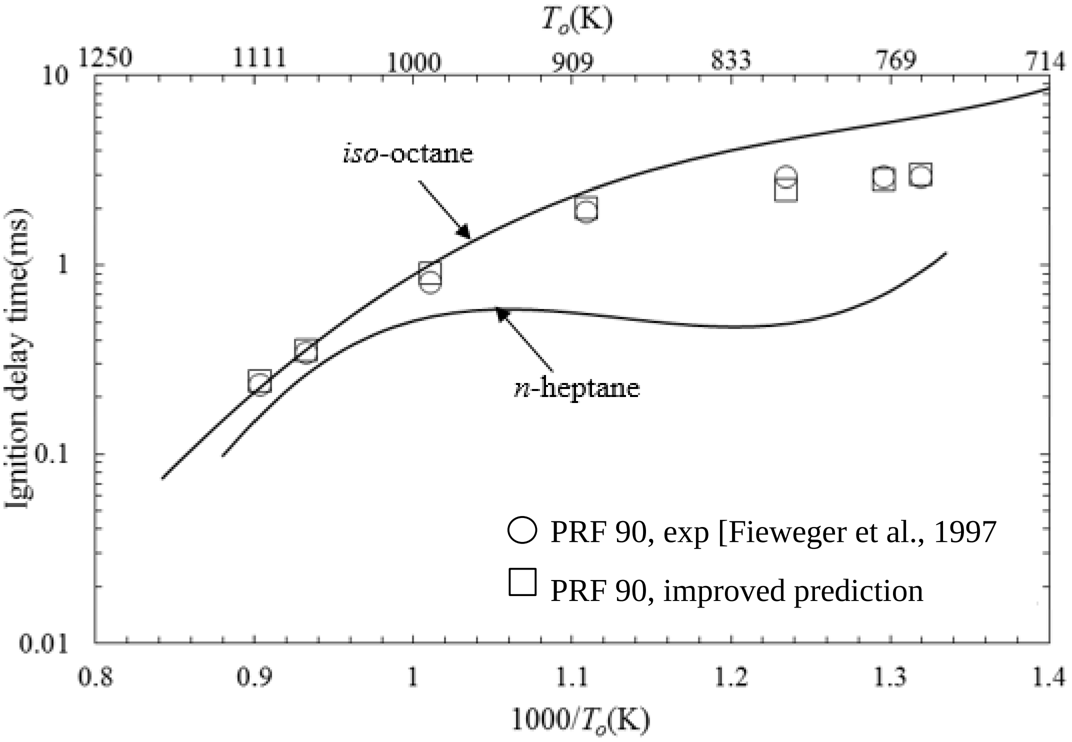

Figure 5.22. Experimental ignition delay time against reciprocal temperatures for *n*-heptane and *iso*-octane represented by solid curves and their blend, PRF90, represented by circles. τ_{LbM}PRF corrected values are shown by square symbols. (∅=1.0, Pressure 4.0 MPa).

5.3 Generalisation of deviations of LbM ignition delay times from experimental measurements.

This Section reports a study of the difference between the LbM predictions and experimental measurements, for all the fuel blends studied in Section 5.2. The aim was to generalise these differences as a function of temperature and fuel concentration. Changes are made to the Arrhenius parameters employed in the LbM method in Eq. (5.7).

The starting point is the predictions of the values of lnA, rather than E/R, on the grounds that concentrations of intermediate radicals and species are likely to centre on changes in collision frequencies, and hence values of A. These cannot be derived by simple mole weighting. Changes in lnA are assumed to vary nonlinearly with fuel concentration and temperature. Hence the methodology is termed as the non-linear by mole (nLbM) method.

Essentially, values of lnA for each fuel/air constituent mixture, obtained from Eq. (5.10), $A = \tau\exp(-E/RT)$, are "tweaked" to obtain a perfect fit to their experimental τ values using their known values of (E/R). These modified values of lnA are identified as lnA_f. The difference between the original measured values of lnA and those of lnA_f are calculated for each constituent mixture B and C. Importantly, the differences are designated as lnA'_B and lnA'_C. These values are regarded as the deviation values from the "true" values of lnA. Thus:

$$lnA_{fB} = lnA_B - lnA'_B, \text{ and} \tag{5.12}$$

$$lnA_{fC} = lnA_C - lnA'_C. \tag{5.13}$$

Similarly, for their blend, D,

$$lnA_{fD} = lnA_D - lnA'_D \tag{5.14}$$

Values of lnA'_D, for blend D are expressed in terms of the mole weightings x_B and x_C of the constituent mixtures by:

$$lnA'_D = x_B lnA'_B + x_C lnA'_C. \tag{5.15}$$

From all the calculated values in this equation for the different mixtures, it was found that the values of the two terms on the right side of the equation were always within 10% of each other. From Eq. (5.15) $lnA'_D$was readily evaluated. The proposed revised values of lnA_D, namely lnA_{fD}, are found from Eqs. (5.8), (5.14) and (5.15).

$$lnA_{fD} = (x_B.lnA_B + x_C.lnA_C) - (x_B.lnA'_B + x_C.lnA'_C) \tag{5.16}$$

Fig. 4.23 shows the deviation parameters $x_{TRF}lnA'_{TRF}$ and $x_{but}lnA'_{but}$ for the TRF/*n*-butanol blend, B25, at different reciprocal temperatures and a pressure 2.0 MPa.

With these revised Arrhenius A, but with the original values (E/R) values for the constituent mixtures the revised ignition delay times, $\tau_{D_{(nLbM)}}$;

$$\begin{aligned} ln\tau_{D_{(nLbM)}} = {} & x_B(lnA_B + (E/RT)_B) + x_C(lnA_C + (E/RT)_C) - (x_B.lnA'_B) \\ & - (x_C.lnA'_C) \end{aligned} \tag{5.17}$$

$$ln\tau_{D_{(nLbM)}} = ln\tau_{D_{(LbM)}} - 2(x_B.lnA'_B) \tag{5.18}$$

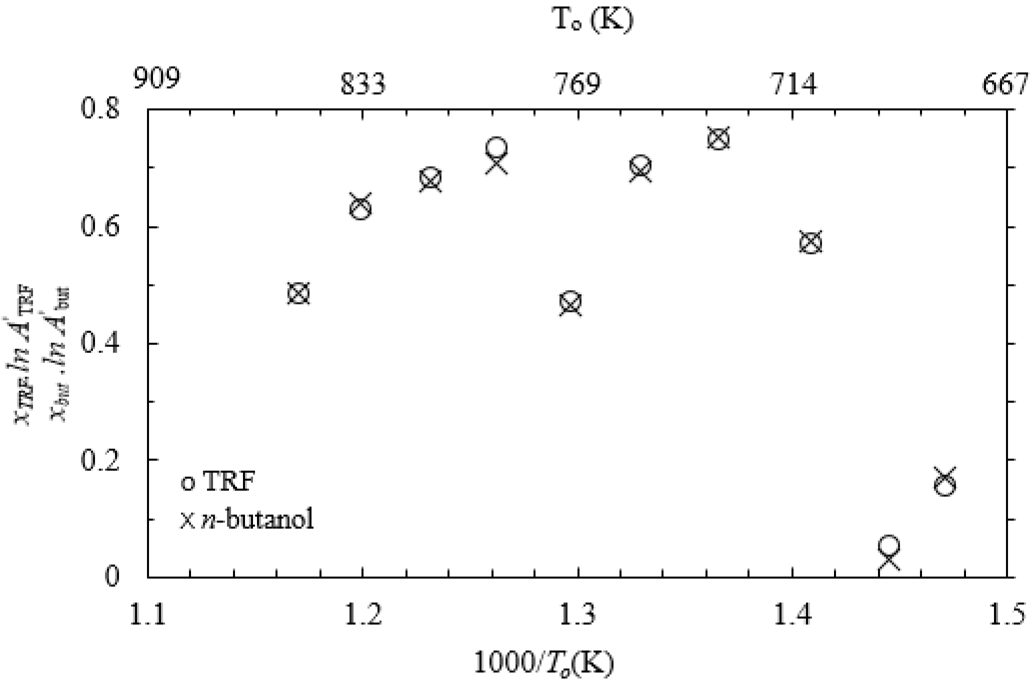

Figure 5.23. Values of $x.lnA'$ for *n*-butanol and TRF obtained from blend B25, at different reciprocal temperatures, pressure 2.0 MPa.

The procedure adopted was to express values of $x_B.lnA'_B$ as a function of reciprocal temperature for different blend compositions. These were then used to re-evaluate the values of τ_D for the blends. Results are highlighted, first for the PRF blends, which are followed by other blends.

5.3.1 Primary Reference Fuel (PRF) blends.

The three PRF blends which were considered in Section 5.2.3 were subjected to this same analysis and the calculated $x_{iso-octane}.lnA'_{iso-octane}$ values are plotted against reciprocal temperature in Fig. 5.24. A fairly general trend in values was obtained for the three PRF mixtures and second order best fit curve was fitted through the data points. The ignition delay times were calculated from Eq. (5.18) with the values of $x_{iso-octane}.lnA'_{iso-octane}$ from the best fit curve in Fig. 5.24. The values of τ are plotted against the reciprocal temperature in Figs. 5.25-5.27, along with the LbM predictions and experimental values. The revised blend values of τ are close to the measured values.

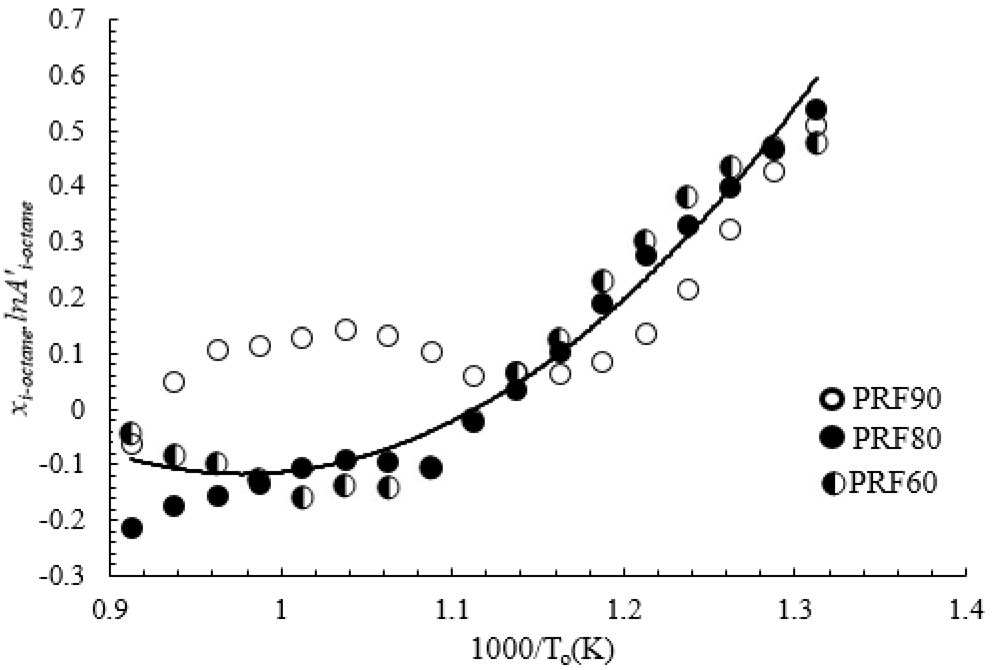

Figure 5.24. Values of the correction factors $x_{iso-octane} . lnA'_{iso-octane}$ for stoichiometric PRF blends, at pressure of 4.0 MPa and different reciprocal temperatures.

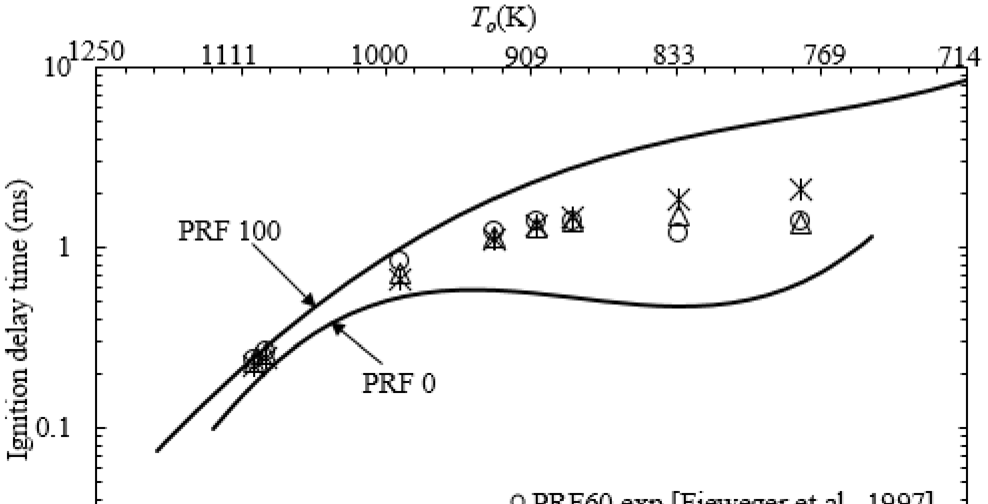

Figure 5.25. Experimental and predicted ignition delay time against reciprocal temperature for PRF0 and PRF100 represented by solid curves. Their blend, PRF60, is represented by circles. Predicted values from LbM and nLbM methods are also shown. (∅=1.0, Pressure 4.0 MPa).

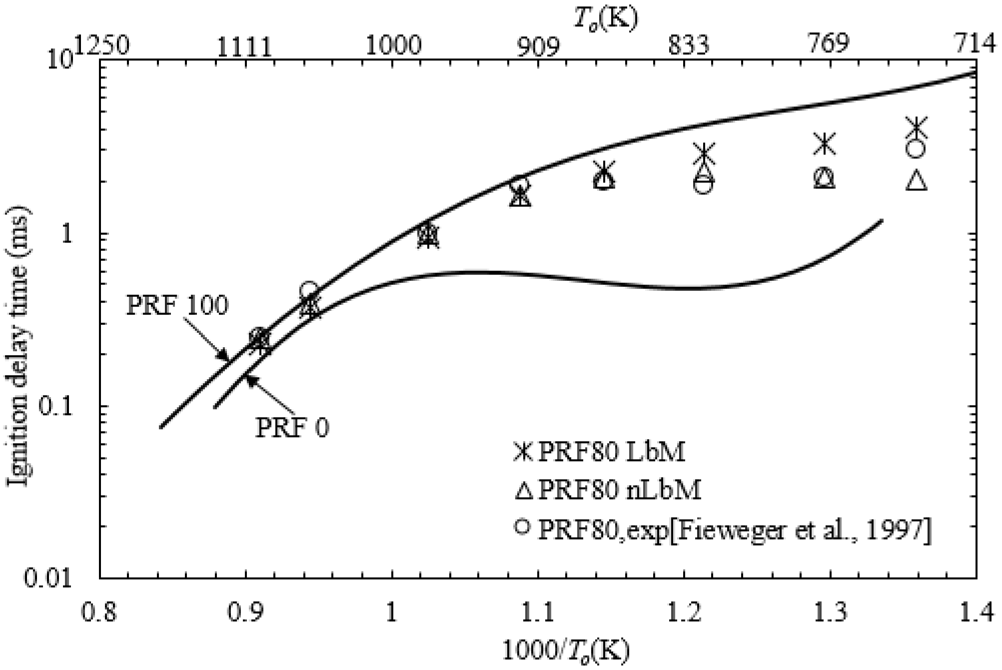

Figure 5.26. Experimental and predicted ignition delay time against reciprocal temperature for PRF0 and PRF100 represented by solid curves. Their blend, PRF80, is represented by circles. Predicted values from LbM and nLbM methods are also shown. (Ø=1.0, Pressure 4.0 MPa).

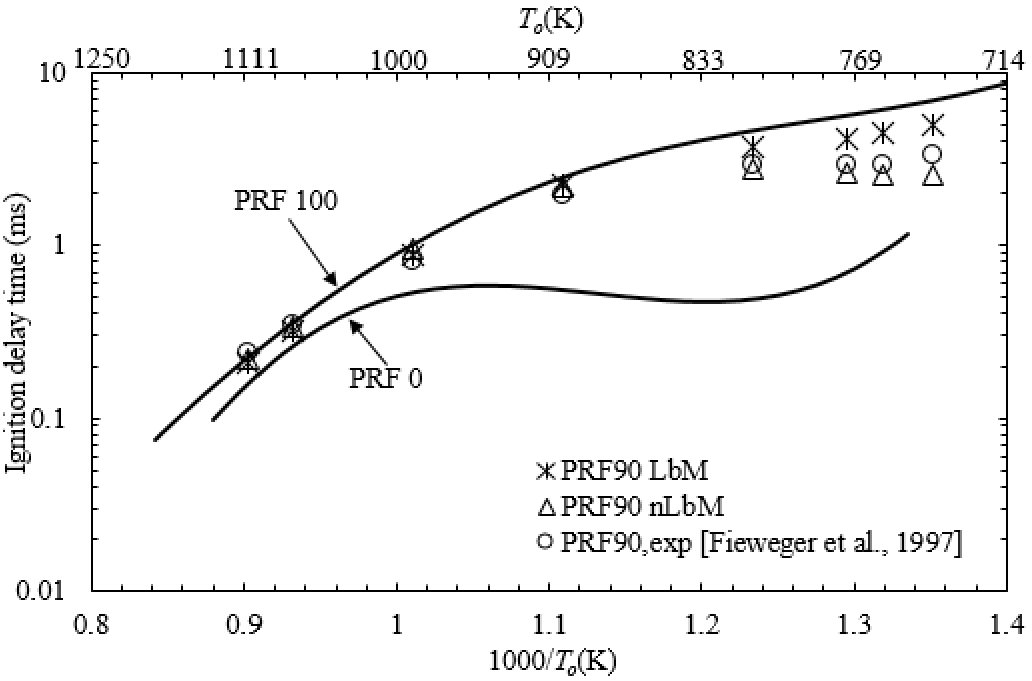

Figure 5.27. Experimental and predicted ignition delay time against reciprocal temperature for PRF0 and PRF100 represented by solid curves. Their blend, PRF90, is represented by circles. Predicted values from LbM and nLbM methods are also shown. (Ø=1.0, Pressure 4.0 MPa).

It is clear from these three figures that the nLbM approach is accurately descriptive. The same approach was adapted for other blends.

5.3.2 Toluene/*n*-heptane blend.

In contrast, for the toluene/n-heptane blend [Herzler et al., 2007], the correction factor $x_{tol}.\ln A'_{tol}$ was found to vary linearly with reciprocal temperature, as shown in Fig. 5.28. The nLbM and experimental results are shown in Fig. 5.29 for the T78 blend, and an excellent agreement between them is observed.

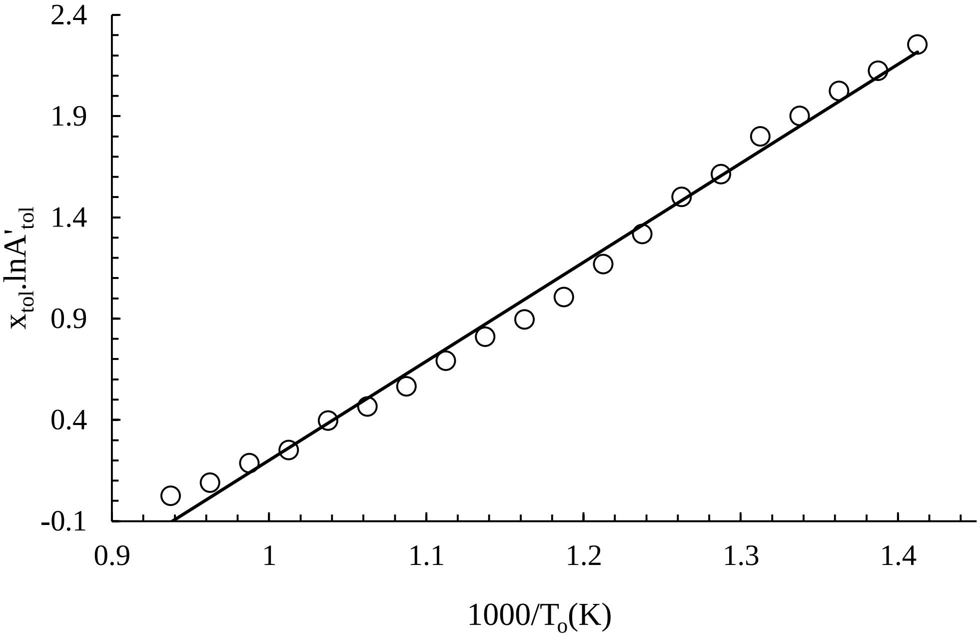

Figure 5.28. Values of correction factor $x_{tol}\,.\,lnA'_{tol}$ for T78 blend, Ø=1.0, at Pressure 3.0 MPa and different reciprocal temperatures.

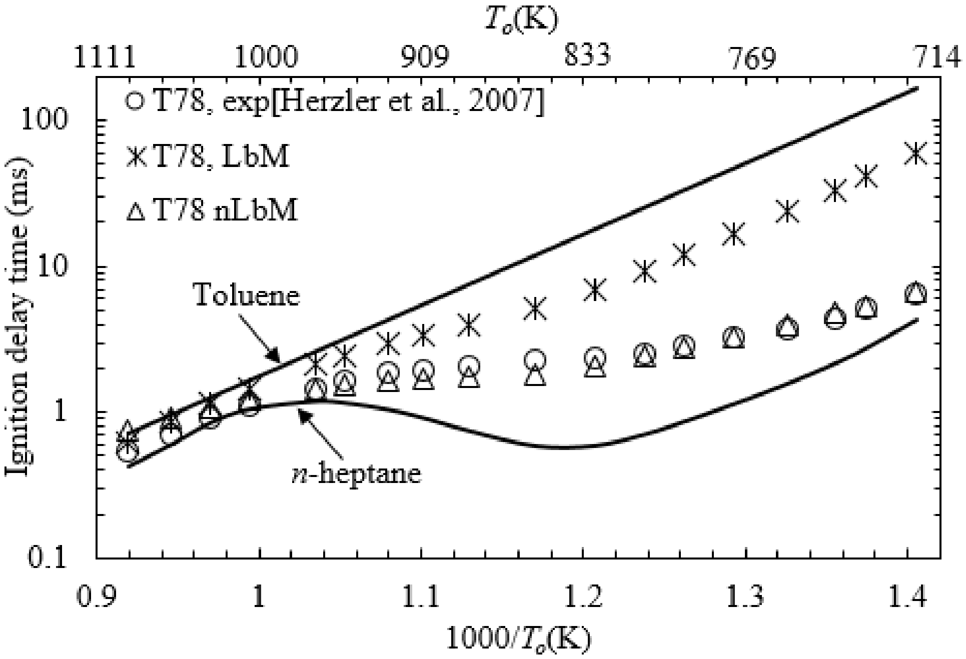

Figure 5.29. Experimental and predicted ignition delay time against reciprocal temperature for Toluene and n-heptane represented by solid curves and their blend, T78, represented by circles, LbM and nLbM results are respectively represented by asterisks and triangles. (∅=1.0, Pressure 3.0 MPa).

5.3.3 Toluene/*n*-butanol blends.

Fig. 5.30 shows the correction factor $x_{but}.\ln A'_{but}$ for T50 and T70 blends at different reciprocal temperatures. A general expression was obtained for this factor as a function of percentage mole fraction of *n*-butanol in the blend and the temperature. This took the form;

$$x_{but}.lnA'_{but} = f_o + f[100x_{but}], \tag{5.19}$$

f_o and f are linear functions with their coefficients given by:

$$f_o = 8.49T^* - 6.66 \tag{5.20}$$

$$f = -0.049T^* + 0.028 \tag{5.21}$$

where T^*= 1000/T_o,

Results from the nLbM methodology using Eq. (5.19) gives excellent agreement with the experimental ignition delay times for T50 and T70, as is shown in Figs. 5.31 and 5.32. It is noteworthy that the ignition delay times for T50 and T70 blends are now accurately predicted as close to those of pure *n*-butanol.

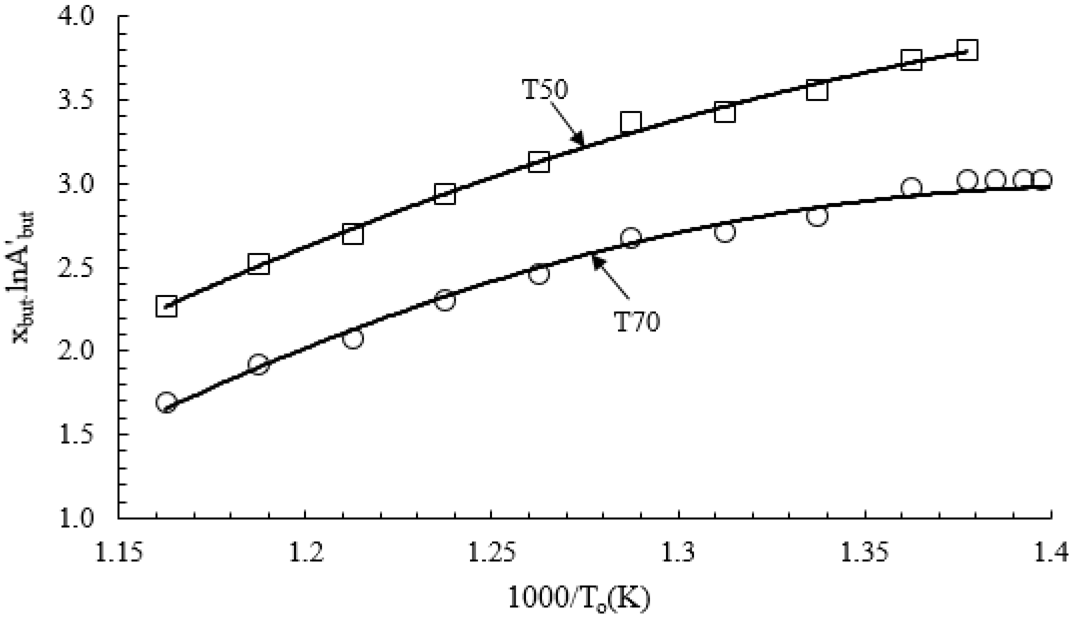

Figure 5.30. Values of $x_{but}\ .lnA'_{but}$ for T50 and T70 blends, at changing temperature.

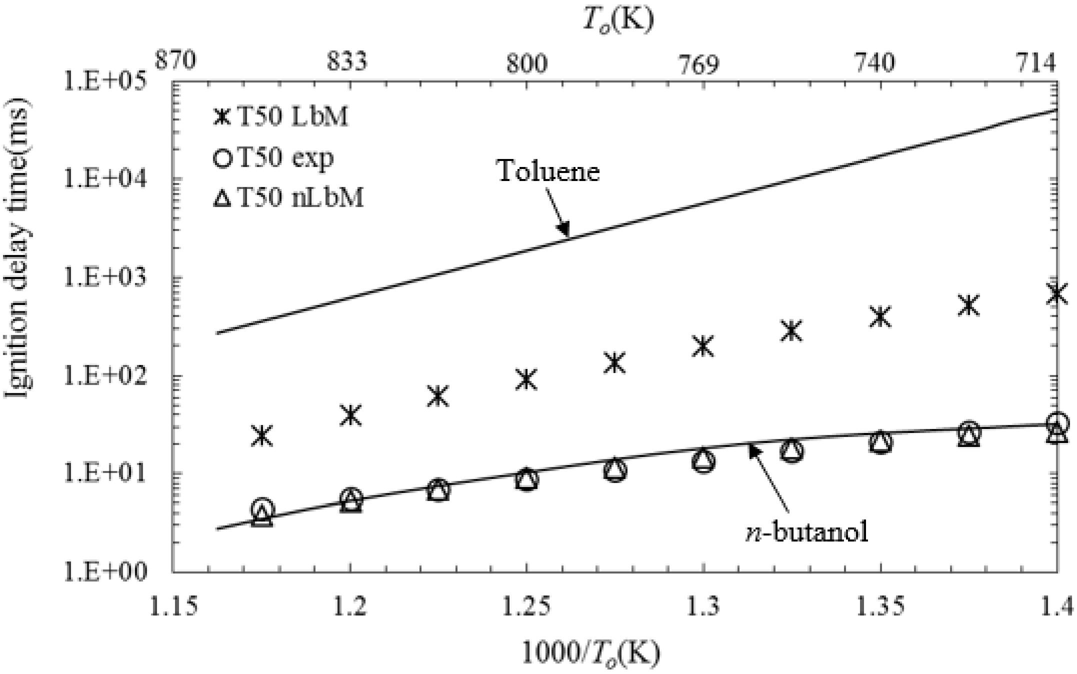

Figure 5.31. Experimental and predicted ignition delay time against reciprocal temperature for Toluene and n-butanol represented by solid curves and their blend, T50, represented by circles, LbM and nLbM results are respectively represented by asterisks and triangles. (Ø=1.0, Pressure 2.0 MPa).

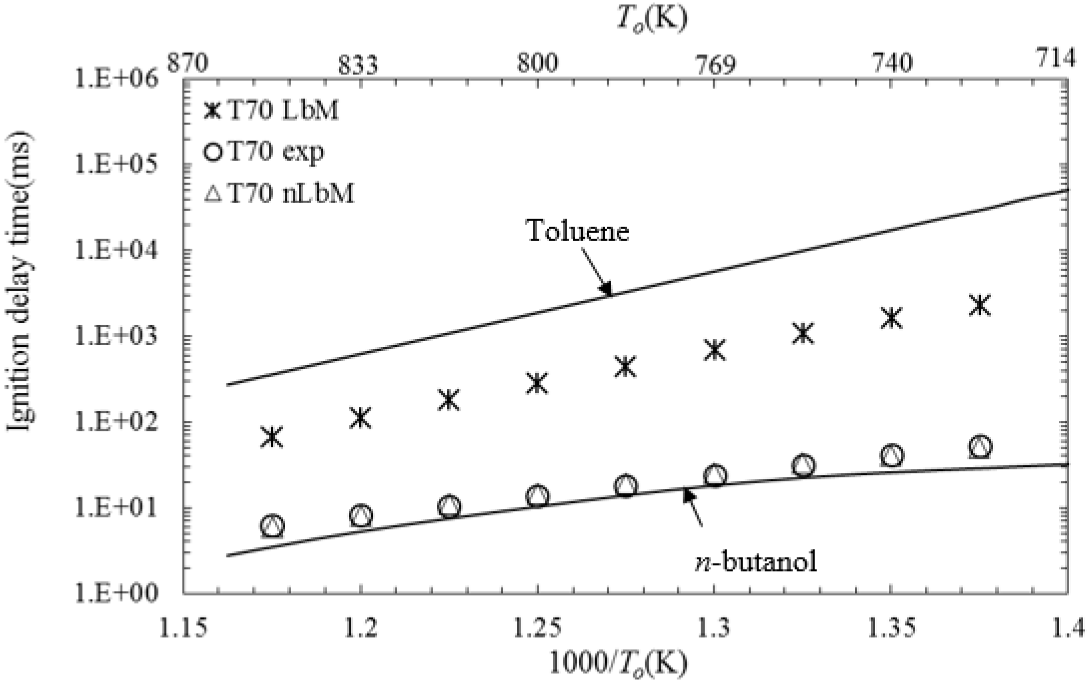

Figure 5.32. Experimental and predicted ignition delay time against reciprocal temperature for Toluene and *n*-butanol represented by solid curves and their blend, T70, represented by circles, LbM and nLbM results are respectively represented by asterisks and triangles. (Ø=1.0, Pressure 2.0 MPa).

5.3.4 *iso*-octane/*n*-butanol blends.

The same technique was used to obtain correction factors for the I50 and I70 blends. In this case, the functions f_o and f necessitated 4th degree polynomials. Different coefficients were obtained for three main regions; the pre-NTC region (T<703K), the NTC region (T=703-815K) and post-NTC region (T>815K) indicated by (i), (ii) and (iii), respectively.

$$\text{(i)}\ f_o = -918.65T^{*4} + 4657.47T^{*3} - 8767.3T^{*2} + 7270.8T^{*} - 2243.9, \qquad (5.22)$$

$$f = 49.03T^{*4} - 268.9T^{*3} + 541.6T^{*2} - 477.2T^{*} + 155.6, \qquad (5.23)$$

$$\text{(ii)}\ f_o = 6376.8T^{*4} - 33746.46T^{*3} + 66871.9T^{*2} - 58805.7T^{*} + 19361.9, \qquad (5.24)$$

$$f = -22.68T^{*4} + 125.4T^{*3} - 258.3T^{*2} + 235.1T^{*} - 79.8, \qquad (5.25)$$

$$\text{(iii)}\ f_o = 6666.8T^{*4} - 38303.16T^{*3} + 82559.7T^{*2} - 79125.49T^{*} + 28450.9, \qquad (5.26)$$

$$f = -1122.1T^{*4} + 6399.7T^{*3} - 13686T^{*2} + 13007.3T^{*} - 4635.5, \qquad (5.27)$$

Again, $x_{but}.\, lnA'_{but} = f_o + f[100x_{but}]$.

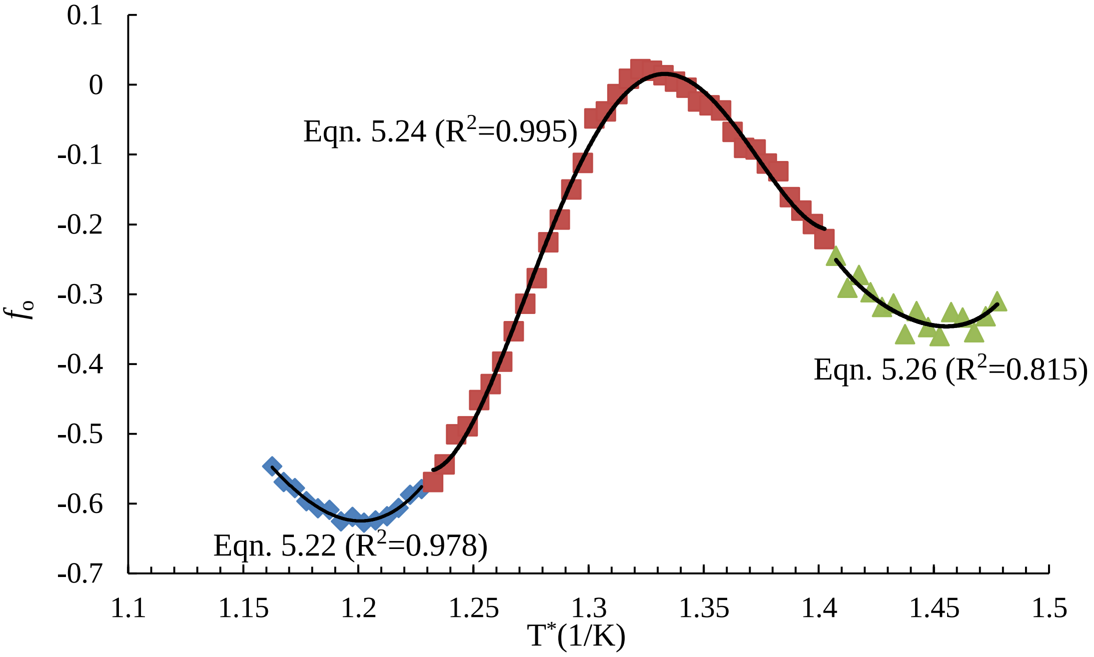

Figure 5.33. Best fit lines for values of f_o at different temperatures, with their R-squared values.

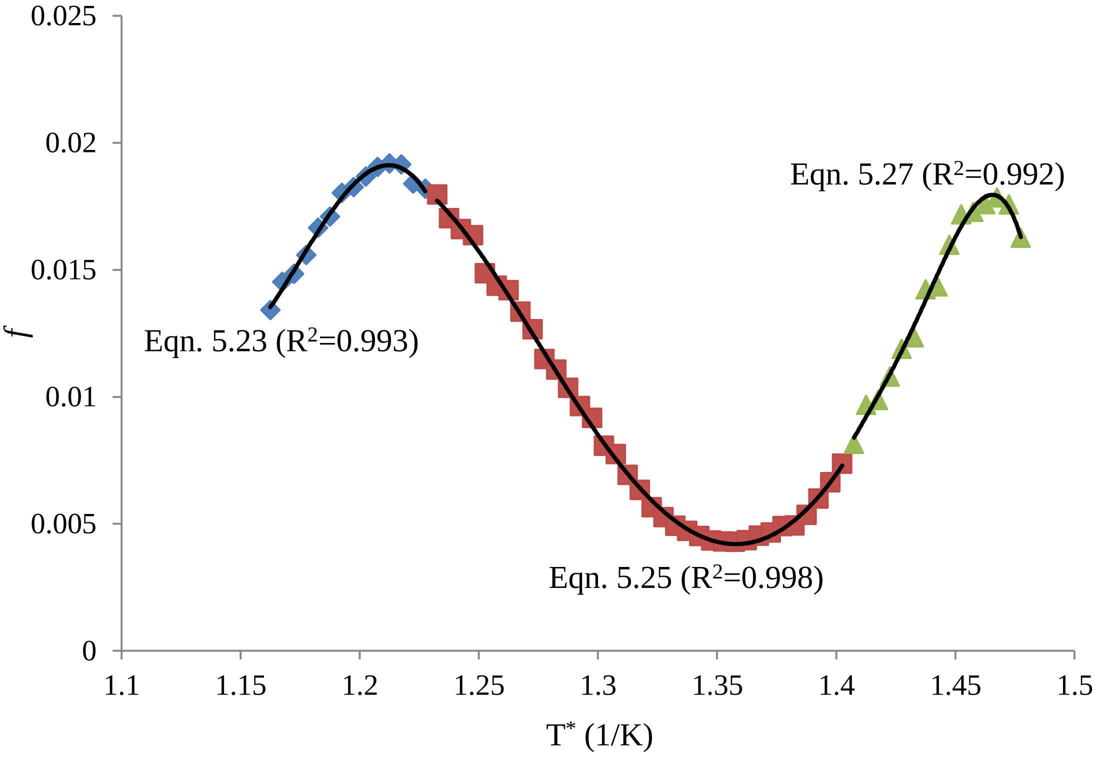

Figure 5.34. Best fit lines for values of f at different temperatures, with their R-squared values.

Ignition delay times were recalculated from Eq. (5.18) with the respective correction factors from Eqs. (5.22-5.27). These are plotted against reciprocal temperature for I50 and I70 blends in Figs. 5.35 and 5.36. Predictions from the nLbM method are compared with experimental values for the two blends, the nLbM predictions for these blends are good, but at the expense of a fourth order curve fit.

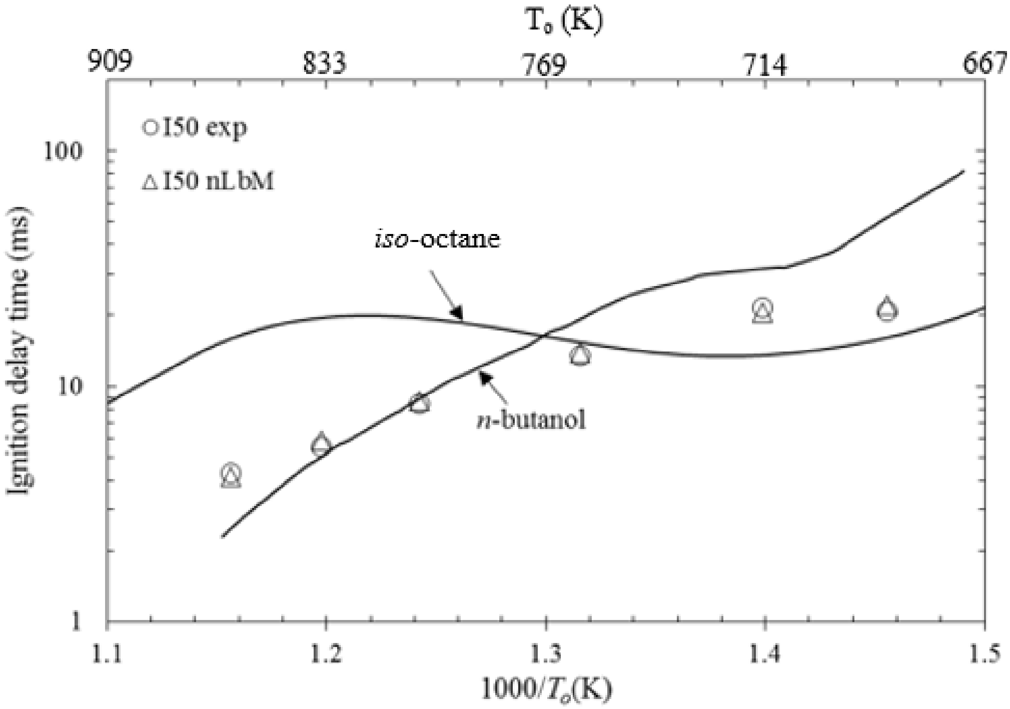

Figure 5.35. Experimental ignition delay times against reciprocal temperatures for *iso*-octane and *n*-butanol represented by solid curves and their blend, I50, represented by circles. nLbM results are represented by triangles. (Ø=1.0, Pressure 2.0 MPa).

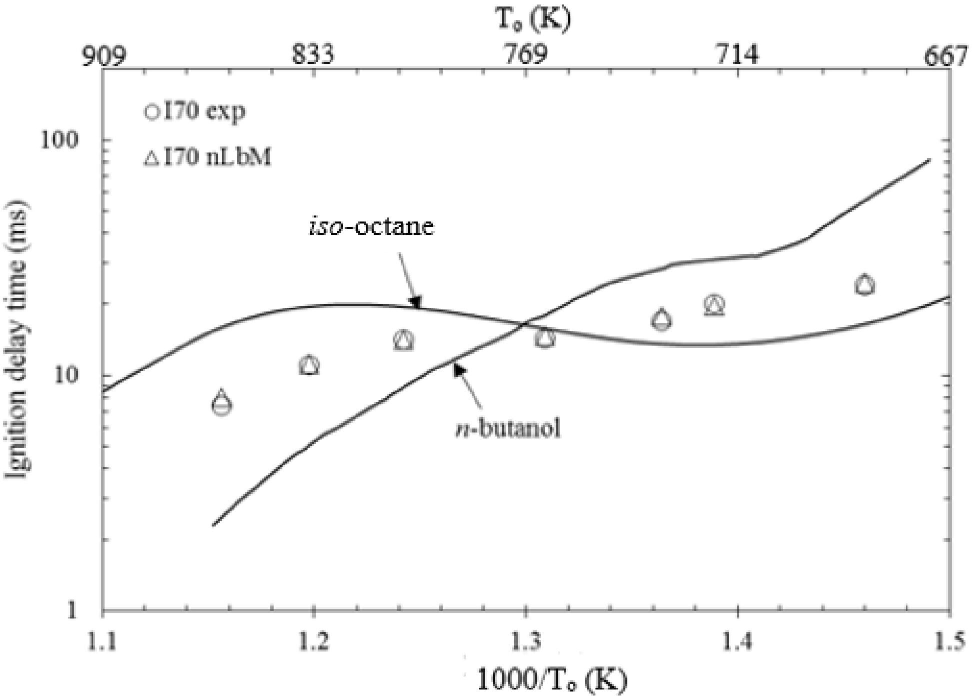

Figure 5.36. Experimental ignition delay times against reciprocal temperatures for *iso*-octane and *n*-butanol represented by solid curves and their blend, I70, represented by circles. nLbM results are represented by triangles. (Ø=1.0, Pressure 2.0 MPa).

5.3.5 TRF/ethanol and TRF/*n*-butanol blends.

The nLbM method was further tested using the experimental results for TRF/Ethanol and TRF/*n*-butanol blends. The relevant correction factors for the different blends are shown in Fig 5.37. The best fit curves for the same liquid volume percentage of ethanol and n-butanol in TRF are also shown in Fig. 5.37. Values of correction factors $x_{TRF}.\,lnA'_{TRF}$ as a function of temperature and percentage of ethanol or *n*-butanol liquid volume in the blend, are expressed by the quadratic equation;

$$x_{TRF}.\,lnA'_{TRF} = -2.04bT^{*2} + 5.07cT^{*} - 2.92d, \qquad (5.28)$$

Where, $b = (ALV\%/25)^{1.83}$, $c = (ALV\%/25)^{1.86}$, $d = (ALV\%/25)^{1.94}$

ALV% = Ethanol or *n*-butanol liquid volume percentage in the blend mixture.

Figs. 5.38-5.43 show the measured and predicted values of ignition delay times for the different blends. The τ values obtained using the correction factor in Eq. (5.28) show fairly good agreement with experimental τ values for all the blends and conditions.

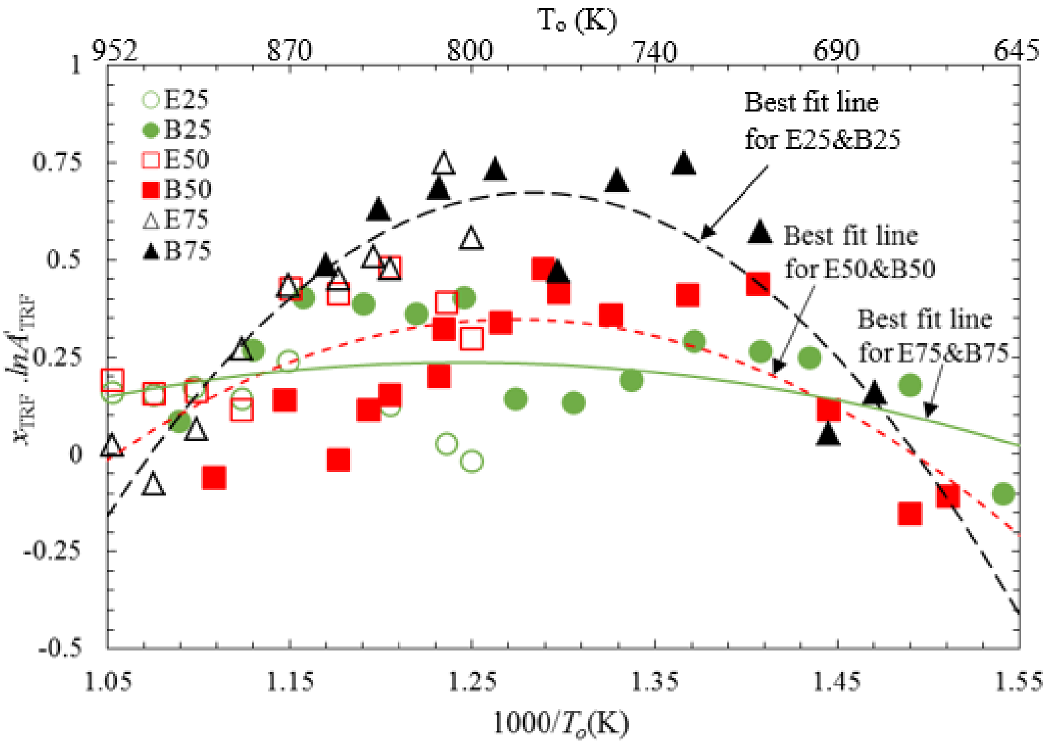

Figure 5.37. Values of $x_{TRF}.\, lnA'_{TRF}$ at 2.0 MPa at different reciprocal temperatures for TRF/ethanol and TRF/*n*-butanol blends. The lines are the best fit curves through the same percentage of liquid volume of ethanol and *n*-butanol in the blends. (∅=1.0, Pressure 2.0 MPa).

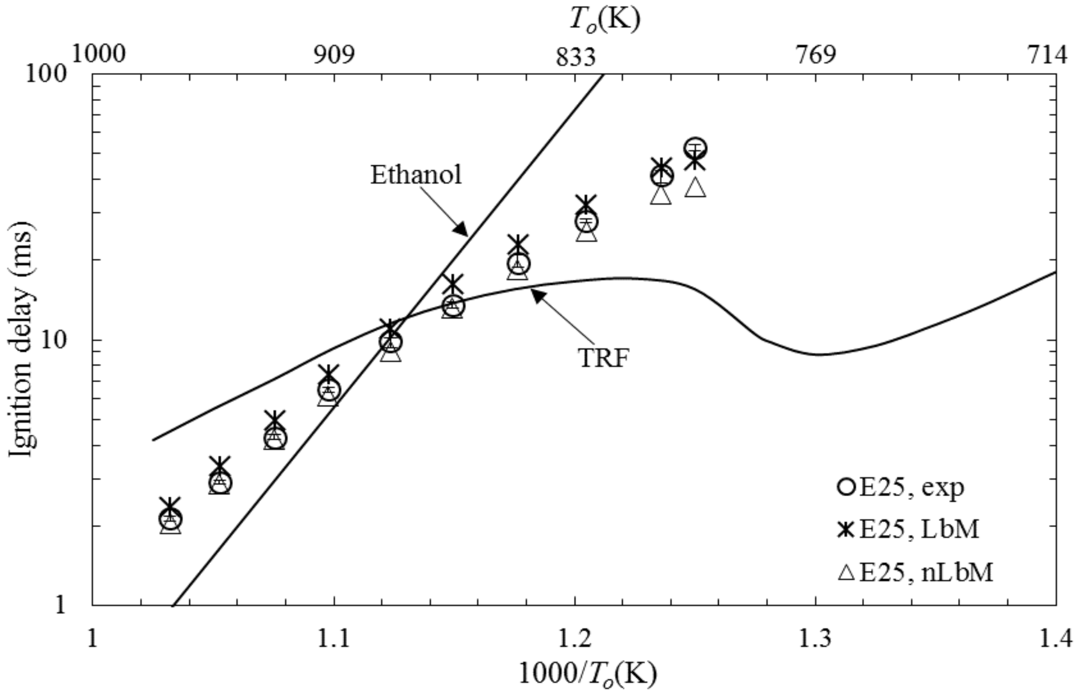

Figure 5.38. Experimental ignition delay time against reciprocal temperatures for TRF and Ethanol represented by solid curves and their blend E25 represented by circles. nLbM

results are represented by triangles and corresponding LbM results by asterisks. (∅=1.0, Pressure 2.0 MPa).

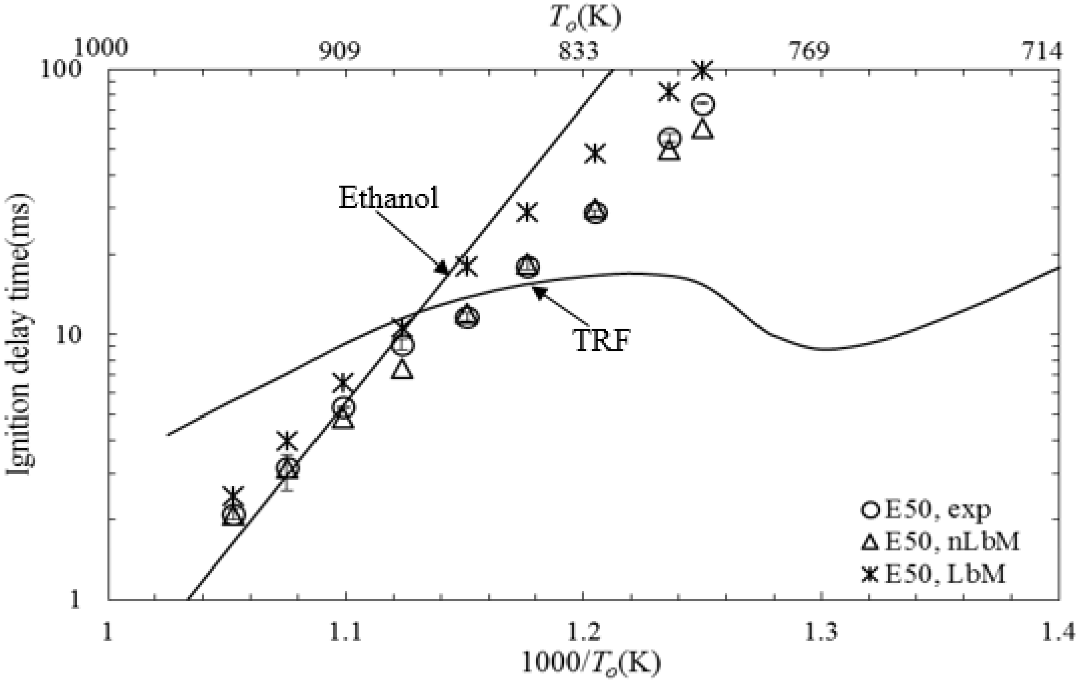

Figure 5.39. Experimental ignition delay time against reciprocal temperatures for TRF and Ethanol represented by solid curves and their blend E50 represented by circles. nLbM results are represented by triangles and corresponding LbM results by asterisks. (∅=1.0, Pressure 2.0 MPa).

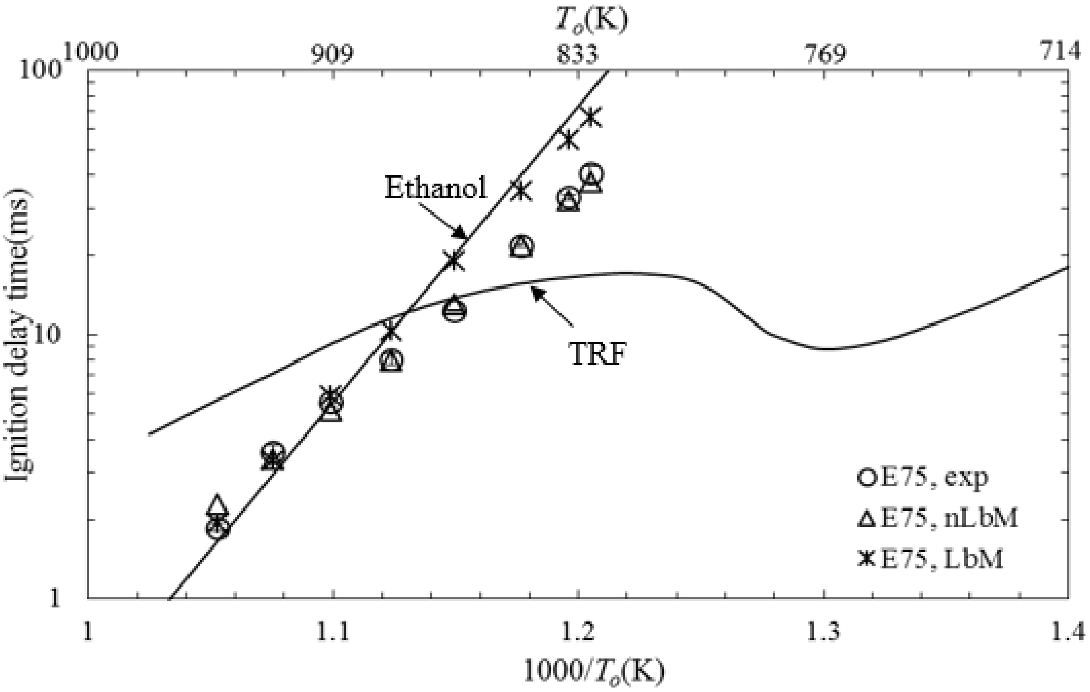

Figure 5.40. Experimental ignition delay time against reciprocal temperatures for TRF and Ethanol represented by solid curves and their blend E75 represented by circles. nLbM

results are represented by triangles and corresponding LbM results by asterisks. (Ø=1.0, Pressure 2.0 MPa).

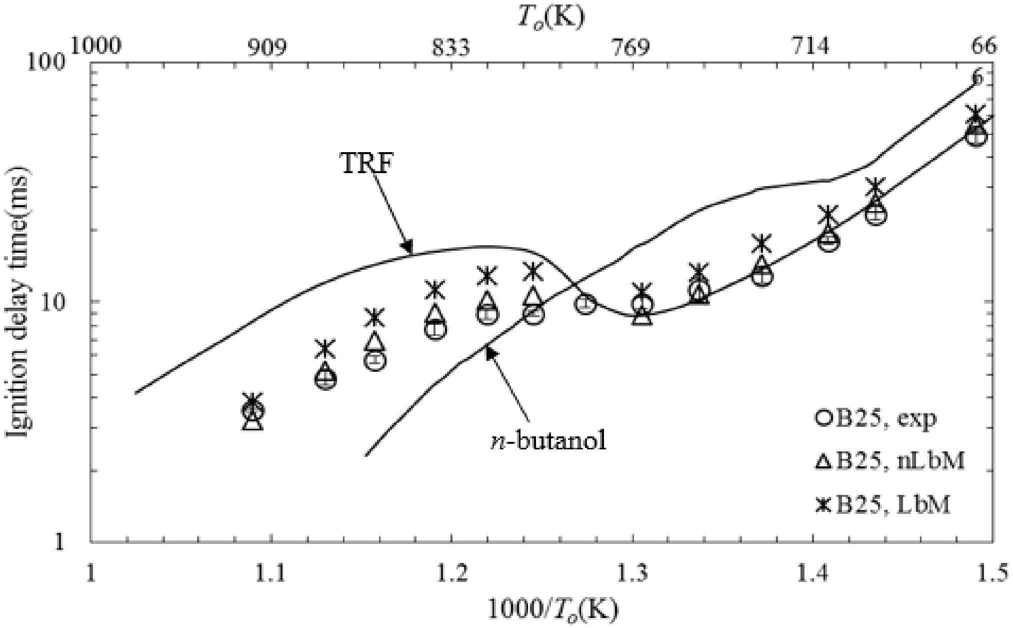

Figure 5.41. Experimental ignition delay time against reciprocal temperatures for TRF and n-butanol represented by solid curves and their blend B25 represented by circles. nLbM results are represented by triangles and corresponding LbM results by asterisks. (Ø=1.0, Pressure 2.0 MPa).

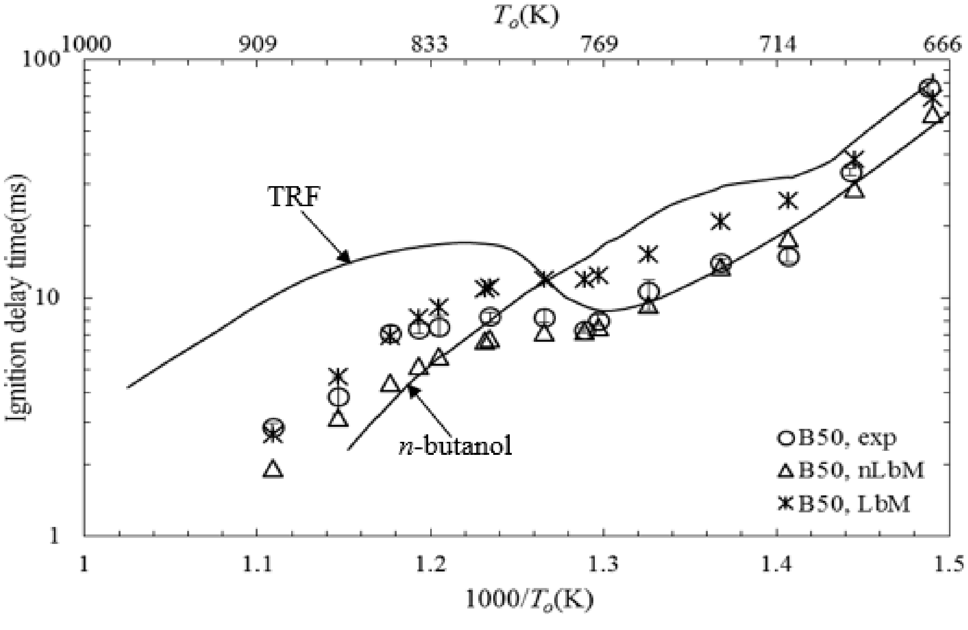

Figure 5.42. Experimental ignition delay time against reciprocal temperatures for TRF and n-butanol represented by solid curves and their blend B50 represented by circles. nLbM results are represented by triangles and corresponding LbM results by asterisks. (Ø=1.0, Pressure 2.0 MPa).

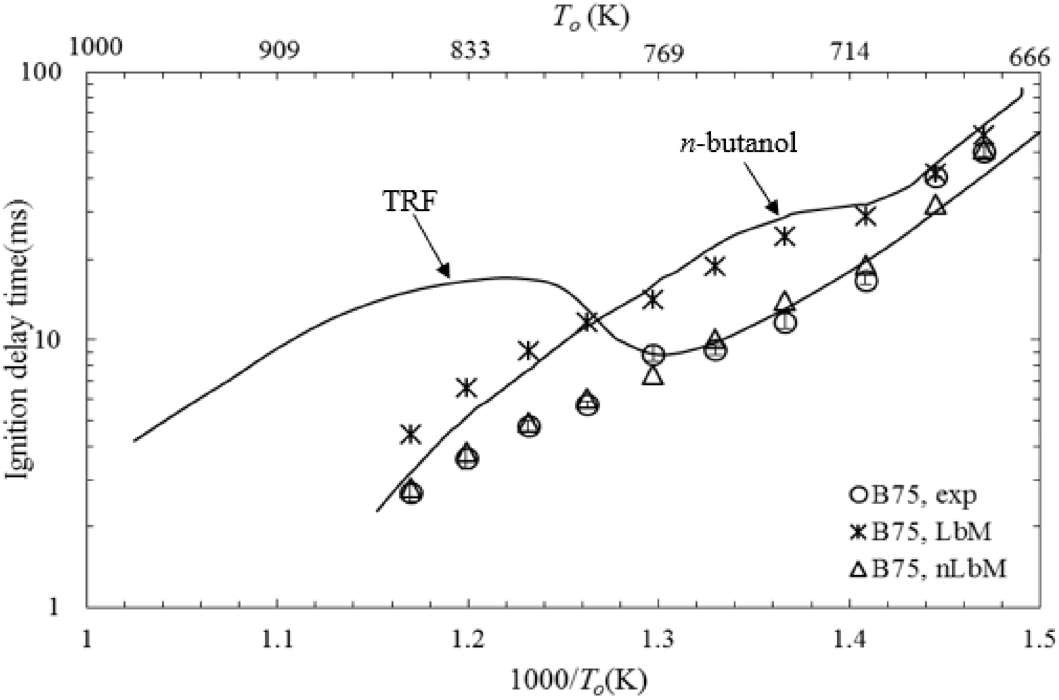

Figure 5.43. Experimental ignition delay time against reciprocal temperatures for TRF and n-butanol represented by solid curves and their blend B75 represented by circles. nLbM results are represented by triangles and corresponding LbM results by asterisks. ($\emptyset$=1.0, Pressure 2.0 MPa).

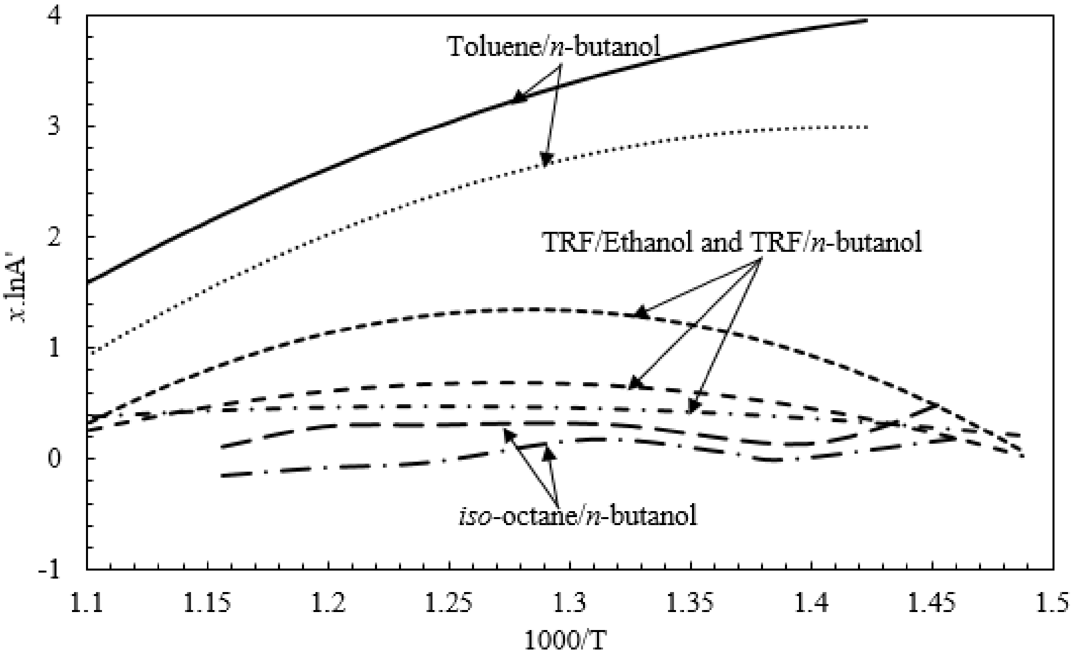

Figure 5.44. Deviations of predicted from measured blend delay times, *x*.lnA', against reciprocal temperatures for different blends.

5.4 Summary.

Limitations in the predictions of τ values of blends using the LbM method necessitated the introduction of a further correction method, which is generalized for different fuel classes. Fig. 5.44 summarises these correction values, x.lnA', for the different blends, at different temperatures. These correction values give an insight into the difference between experimental and predicted τ values, described below.

5.4.1 Toluene/*n*-butanol blends.

The differences for Toluene/*n*-butanol blends are the highest of all the blends tested, and decline with the increase in temperature and amount of *n*-butanol in the blend. The chemistry of the more reactive component in the blend, *n*-butanol in this case, dominates at lower temperatures and blends delay times are closer to those of pure *n*-butanol. This suggests that at lower temperatures, *n*-butanol generates chain branching radicals faster than toluene and these then make toluene more reactive, with consequent shorter delay times. Similar results have been reported by Di Sante [2012], Hartmann et al. [2011] and Vanhove et al. [2006] for toluene/*n*-heptane, with *n*-heptane having a similar effect on toluene like *n*-butanol.

5.4.2 TRF/ethanol and TRF/*n*-butanol blends.

For these blends, at higher and lower temperatures, measured ignition delay times are fairly well predicted using the LbM method, although an over prediction is seen in the temperature range where TRF NTC behaviour is observed. In this intermediate temperature range, as it was the case with toluene/*n*-butanol blends, the more reactive component in the blend tends to dominate the chemistry and generate chain branching radicals at the faster rate than the less reactive component in quantities sufficient enough to initiate auto-ignition reactions. This reduces the delay times to values shorter than those predicted by LbM. This effect increases with the proportion of *n*-butanol (or ethanol) in the blend.

5.4.3 *iso*-octane/*n*-butanol blends.

These blends show relatively better agreement between measured and predicted delay times, throughout the temperature range. However, with the increase of *n*-butanol in the blend the same effect as that observed with the other classes of blends occurs. At the higher temperatures the more reactive *n*-butanol makes *iso*-octane more reactive, while at the lower temperatures the *iso*-octane is more reactive than *n*-butanol.

5.4.4 Conclusion.

It is evident that it is difficult to accurately predict the ignition delay times of blends with components of different reactivities based on the delay times of each component. Chain branching radicals generated during reactions play a big role in determining the overall ignition delay time. At the same temperature, the more reactive component tends to generate these radicals first in quantities which are sufficient to initiate the chain reactions within the blend. This can quickly elevate the temperature of the bulk mixture and promote earlier ignition.

It is further observed that the over prediction of LbM values is more pronounced with the increase in the differences in reactivity of the constituent fuels. Fig. 5.45 shows the relationship between the deviations of predicted delay times from the measured ones, x.lnA', and the differences in τ for the separate components, $\tau_B - \tau_C$. For $(\tau_B - \tau_C)$ > 20 ms, the increased difference in τ values results in larger deviation of predicted from measured delay times, where as there is no substantial change of x.lnA' when values of $(\tau_B - \tau_C)$ are lower.

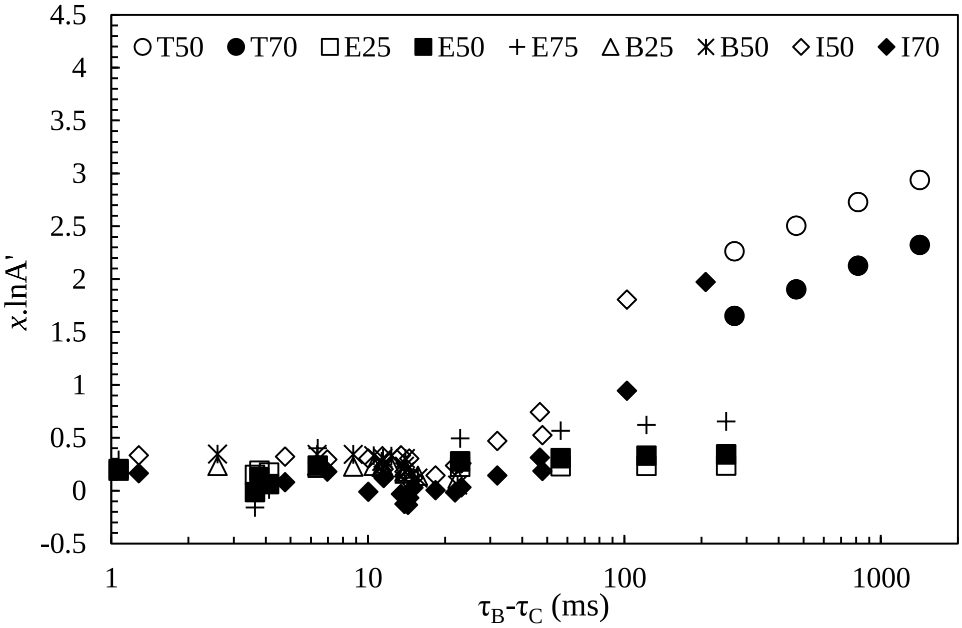

Figure 5.45. Deviations of predicted from measured blend delay times, x.lnA', against the difference in measured delay times of individual components in the blend.

CHAPTER 6: CONCLUSIONS SUMMARY AND FUTURE RESEARCH.

6.1 Introduction.

Alternative fuels provide an opportunity to achieve improved engine performance, less pollution production, and reduce reliance on conventional petroleum based fuels. These new fuels can be synthetically developed by combining the different individual components of hydrocarbons present in conventional fuels, with sometimes addition of bio-alcohols. The motivation behind this work was to broaden our understanding of the combustion behaviours, specifically auto-ignition property, of, first, the individual components that make synthetic fuels and then followed by their blends under different conditions of pressure, temperature and concentration.

The work in this thesis has measured and investigated ignition delay times using RCM mostly at constant pressure of 2.0 MPa and varying temperatures (650K-1000K) (Chapter 4). Leeds RCM was significantly modified before collecting these measurements (Chapter 2), and this has allowed to improve accuracy as well as reach conditions that were not achievable before. Key conclusions from various work that were conducted in this research are summarised in the following section, together with the recommendations for future research.

6.2 Conclusions.

6.2.1 RCM strength and limitations.

In this work, RCMs from UCT (Section 2.2) and Leeds (Section 2.3) were used to measure τ values of the tested fuels. RCM is an attractive machine for accurately measuring long range of τ over other machines, this is due to:

i) Fairly fast compression comparable to those occurs in engines, the current machine has an average piston speed of 12.7m/s.

ii) Unlike shock tubes, RCMs can maintain its end of compression conditions relatively longer circa 100ms compared to circa 10ms for shock tubes.

iii) Ability to isolate other physical effects such as those occur in engines eg. Valve operation, gas mixing and expansion strokes.

The Leeds RCM was substantially modified to meet the requirements of the current study. These modifications were made to achieve the following; (a) Increase end of compression pressure up to 2.0MPa, (b) Increase and control end of compression temperatures between 600K and 1000K, (c) Improve piston rapidity during compression and ensure it is effectively damped without rebound at the end of compression, (d) Improve mixture preparation accuracy between tests by using a separate mixing chamber and (e) Accurate measurement of piston displacement during compression. Chapter 2 has described details of different modifications that were made to achieve the above said requirements successfully, together with the performance characterisation of machine using well researched fuels of *iso*-octane and toluene in Chapter 3. The results were compared with existing literature data and good agreement was found.

The modified RCM however still had the following limitations;

i) The delay times longer than 120 ms could not be accurately measured, significant non-homogeneity within the core gas occurred resulted into poor measurement repeatability and in some cases mixtures could not be ignited.

ii) The machine could only compress the mixture up to a maximum pressure of 2.7 MPa without piston rebound during ignition. This was due to the limited initial piston holding force by the hydraulic oil which restricted the driving force to a certain amount to ensure the driving force is less than the holding force before firing.

iii) Piston displacement measurements restricted to the final 30 mm of compression, this is due to the type of displacement laser head that is used.

iv) Current set up limits the chamber optical access.

6.2.2 Consortium study of τ measurements of *iso*-octane.

The problems with discrepancy of τ values measured in different RCMs has existed for a while. Differences in heat loss and compression times between machines are reported as the main factors for such discrepancy. Since measurements from RCMs are commonly used to validate and generate chemical kinetic mechanisms, it is very important to understand and quantify these discrepancies between machines. An international RCM workshop was held to address, among other things, this issue where it was decided to measure τ values of *iso*-octane at exactly the same conditions using different RCMs. Analysis of the measured τ values from the consortium yielded the following conclusions:

- Heat loss during the delay time was indeed different for different RCMs. Those with large heat loss measured longer delay times than those with small heat loss. Correction for this effect was made using mean pressure and temperature during delay time.
- Compression times for different RCMs was also different. For machines with slower compression times, combustion reactions start to take place during compression and thus measures shorter ignition delay times than those with faster compression. Corrections were made using values of Livengood-Wu integrals at the end of compression, $(LWI)_o$, for different machines, and extrapolation to $(LWI)_o=0$ was made to obtain ideal τ values.
- At higher temperatures, the auto-ignition is very strong which is evident from the generated pressure oscillations and the calculated LWI falls below unity which suggests that auto-ignition is initiated from hot spots at these conditions.
- Final corrected τ values are generally longer than the original measured values with the big difference seen at the intermediate temperature range where NTC occurs.
- This study can be considered and used as a foundational study to quantify the error in delay times caused by non-ideal behaviour of practical RCMs. Additional studies using these RCMs (or more even better) and different fuels at different conditions, is warranted in order to make possible the generation of an empirical relationship between compression time, heat loss and measured delay times to obtain an ideal τ values. This will isolate the facility dependent errors from the reported experimental results and hence making generation and validation of chemical kinetic mechanism simpler and faster.

6.2.3 τ measurements of hydrocarbon blends with alcohol.

The addition of alcohol, particularly ethanol, in hydrocarbon fuels has received much attention for the past years due to their high resistance to auto-ignition and thus would act as the octane booster when blended with conventional gasoline fuels, and reduce the reliance of petroleum based fuels in transports which are known for its high contribution to CO_2 production. Ethanol is currently widely used in the fuel pumps around the world, with as much as 85% by volume in the US [Davis, 2008]. However, as it was well described in Chapter 1, *n*-butanol has number of advantages over ethanol and potentially provides an opportunity to replace the latter.

Chapter 4 has reported the measured τ values of different hydrocarbons when blended with ethanol and *n*-butanol, and the following main conclusions can be drawn:

- When compared with the hydrocarbons which exhibit NTC behaviour, the τ values of both *n*-butanol and ethanol are higher at lower temperatures and lower at higher temperatures. This is vital to understand the change of fuel behaviour when alcohol is added to these hydrocarbons. Generally, this study shows that, at higher temperatures the addition of alcohol makes those hydrocarbons fuels with NTC behaviour less resistant to auto-ignition, while at lower temperatures it makes them more resistant.
- Increased end of compression pressure reduces the ignition delay times for the individual and blend fuels tested in the intermediate temperature range within the NTC region. Less effect is seen for higher and lower temperatures.
- The addition of alcohol affects the NTC behaviour of the hydrocarbons tested. *n*-butanol greatly weakens their NTC strength while ethanol completely eliminates this behaviour.
- Addition of *n*-butanol to toluene, an aromatic, significantly reduces the τ values of toluene for all temperatures studied in this work. There is substantial difference in reactivity between toluene and *n*-butanol, particularly at lower temperatures. This possibly suggests the more reactive *n*-butanol to dominate the reactions and making its blend with toluene significantly more reactive than pure toluene.
- For the first time τ values were measured (Section 4.6.2) for a high octane TRF surrogate (RON=98.5), proposed by [Morgan et al., 2010], as a representative of European standard commercial gasoline (Gron 98 MK1), at stoichiometric conditions and a pressure of 2.0MPa and temperatures 600K-1000K. Similar to other gasoline surrogates, it was found to have two stage ignition and NTC behaviour within the intermediate temperature range (769K-833K). Addition of alcohol (*n*-butanol and ethanol) in this TRF surrogate affected its auto-ignition property differently at different temperatures, in a similar fashion as that explained above.
- Based on the results shown in this work, some blending strategies can be recommended. Suitability of different blends of hydrocarbons and alcohols, for use in engines, depends on the operating conditions of a given engine. In spark ignited (SI) engines, performance is mainly limited by the occurrence of knock in the end gas. The addition of *n*-butanol or ethanol in gasoline will improve its antiknock properties and thus enable operation at higher temperatures and pressures, and consequently improving performance and reducing emissions. Ethanol improves antiknock property substantially more than *n*-

butanol, with higher effects seen for increased volume. However, this advantage can only be realised at lower temperatures. For example, for TRF mixtures increased delay times are obtained at temperatures lower than 740K when blended with *n*-butanol and 860K with ethanol. At higher temperatures these alcohols promote occurrence of auto-ignition and make them less suitable for use in SI engines and favourable for compression ignition (CI) engines. For use in CI engines, addition of either *n*-butanol or ethanol leads to almost the same auto-ignition effect, with their volume percentage in the blend playing no role. This would favour the use of *n*-butanol over ethanol because ethanol has low energy density as well as limited solubility in diesel fuel; hence the amounts of ethanol-diesel mixtures are restricted to small percentages (typically up to 20%). Availability of this data is also relevant to the efficient operation of homogeneous charge compression ignition (HCCI) engines which are purely controlled by the chemical kinetics of the fuel. Measured ignition delay times at different pressures, temperatures and concentrations make it possible to determine, for a particular fuel, the required initial conditions for HCCI engines as well as the point at which fuel should be injected so that it can be fully premixed before ignition occurs and set a compression ratio that will result to auto-ignition at or near top dead centre (TDC).

- Data collected in this work is also relevant to the chemical kinetics modellers. It was shown in Chapter 4 that, using the Leeds RCM, there was no substantial difference between simulations conducted using constant and variable volume approaches. This makes the lack of non-reactive pressure traces less critical. However, for different conditions of pressures and fuels with longer ignition delay times it will be necessary to obtain non-reactive pressure histories to accurately model the RCM experiment.

6.2.4 Auto-ignition blending law.

- A first attempt at an auto-ignition blending law was based on the mole weighting of Arrhenius parameters, namely, the pre-exponential factor A and the activation temperature, E/R. The method was designated as LbM.
- Good agreement between LbM predictions and experimental results was obtained when the individual fuels in the blend did not show NTC behaviour, such as methane/hydrogen blends (Section 4.2.2). This was in good agreement with the previous proposed auto-ignition blending laws by Cheng et al. [1984] and Gersen et al. [2008].
- For blends of fuels in which either one or both of them has NTC behaviour, a good agreement was obtained between LbM and experimental values only at high temperatures

but poor agreement at lower temperatures, where the NTC behaviour occurs. Very significant differences between predictions and experimental results were obtained when the two components had very different reactivities, such as that for toluene/*n*-butanol blends. (Chapter 4.2.6)

- An attempt was made to empirically generalise, with greater complexity, the differences between the LbM predictions and experimental values for the different classes of hydrocarbons. Using the empirical relations, it was possible to obtain good agreement between the predictions (now designated as nLbM) and experiments, but the relationships were different for different fuels.
- Such auto-ignition blending laws provide quick answers to the key auto-ignition problems in the combustion industry without the need to refer to any specific chemical reactions. More tests using this approach are warranted at different conditions to test its validity at these conditions.

6.3 Future research.

- More development of Leeds RCM is required. This includes, increased end of compression pressure of at least 4.0MPa to closely mimic the pressures achieved in the engines, incorporate crevices in the compression piston head together with the system of crevice containment at the end of compression to contain roll up vortices generated during compression and stop the transfer of mass from the core gas to the crevices after compression, full automation of the machine operation to increase efficiency, measurements of piston displacement for the full compression stroke and make access for optical measurements.
- The author finds the significant change of τ values when *n*-butanol was added to toluene very interesting, and it is proposed that similar studies will be conducted but this time using a more commonly commercially used ethanol and determine whether the same effect will hold.
- To fully characterise the individual fuels and the blends tested in this work, more studies are required at different pressures and equivalence ratios.

Appendix

A. Mixing chamber stress analysis.

Stress analysis for the mixing chamber was conducted at the design level to ensure safety is achieved during operation. In all these calculations reference was made from Raymond and Warren., 1975.

Flanges

1. Top and bottom flanges bending stress.

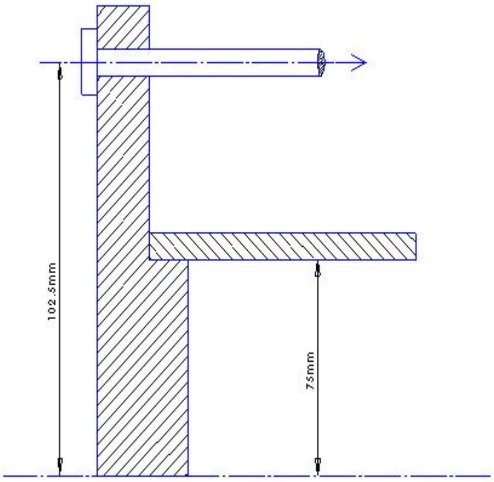

Case 16 [1]

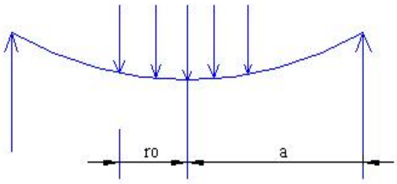

ro = 75mm, a = 102.5mm

Maximum bending moment $M_{max} = \frac{W}{4\pi}[(1+v)ln\frac{a}{r_o}+1]$

$w = q\pi r^2 = 5x10^5 x\pi x(0.075)^2 = 8.8357$ kN

$Poisson's\ ratio, v = 0.3$

$$M_{max} = \frac{8835.7}{4\pi}\left[(1+0.3)\ln\left(\frac{0.1025}{0.075}\right)+1\right] = 988.65N$$

Assumptions: Uniform thickness 20 mm

: Factor of 6 for accidental combustion

$$Bending\ stress, \delta_b = \frac{6M}{t^2}x6 = \frac{36x988.65}{0.02^2} = 88.978MPa$$

Yield strength for Stainless Steel 303 is 240MPa. Therefore there is a safety factor of;

$\frac{240}{88.978} = 2.697$

2. Shear stresses on flanges

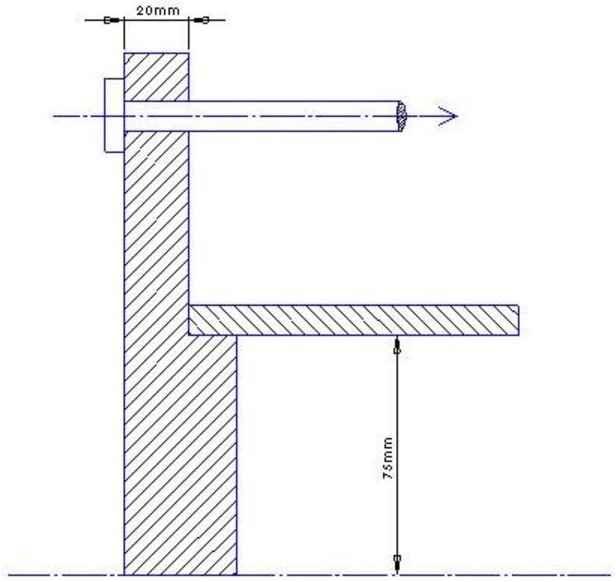

$Shear\ area, A_s = \pi x d x t$

d=0.15m, t=0.02m

$$Shear\ area, A_s = \pi x 0.15 x 0.02 = 9.424x10^{-3}\ m^2$$

Force exerted on the flange due to internal pressure is given as;

$$F = 6xpxA = 6x5x10^5 x\frac{\pi x 0.15^2}{4} = 53.014\ kN$$

$$Shear\ stress, \delta_s = \frac{F}{A_s} = \frac{53.014x10^3}{9.424x10^{-3}} = 5.625\ MPa$$

Compare with yield strength of 240MPa, a safety factor in this case is $\frac{240}{5.625} = 42.6$

Vessel tube

Assumptions: Thin wall pressure vessel

: Factor of 6 for accidental combustion

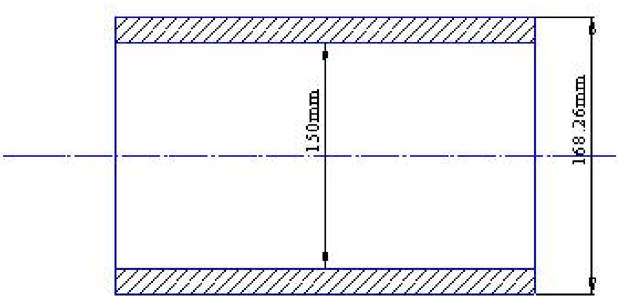

$$Hoop\ stress, \delta_h = 6x\frac{pd}{2t}$$

t = 0.00913m, d = 0.15m

$$Hoop\ stress, \delta_h = 6x\frac{5x10^5x0.15}{2x0.00913} = 24.64\ MPa$$

Yield strength for stainless steel 316L is 170MPa.

Therefore there is a safety factor of $\frac{170}{24.64} = 6.899$

Bolts

Bolts used are M10 class 12.9.

For these bolts the preload is given as 43.85kN (from thread specification catalogue)

This is compared against the force that each bolt will carry, assuming accidental combustion occurs in the mixing chamber.

Total force in the mixing chamber with accidental combustion is 53.014 kN (as calculated above) and there are a total of 8 bolts fastened around the chamber. Therefore each bolt will carry;

$$F_b = \frac{53.014}{8} = 6.626\ kN$$

Therefore a safety factor in the bolts is $\frac{43.85}{6.626} = 6.617$

Flange bending stress due to bolt preload (when no mixture in the mixing chamber)

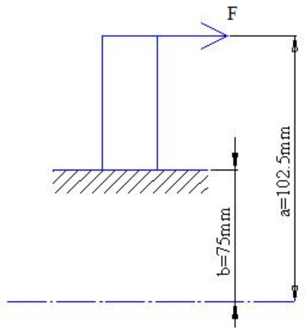

Case 11 [1]

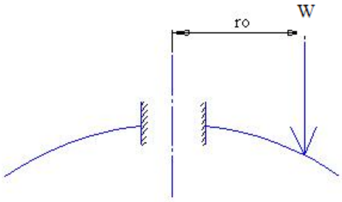

ro = a (If W is at the outer edge)

$$M_{max} = \frac{wa^2}{b} x \frac{C_9}{C_8}$$

$$C_9 = \frac{b}{a}\left\{\frac{1+v}{2}\ln\left(\frac{a}{b}\right) + \frac{1-v}{4}\left[1 - \left(\frac{b}{a}\right)^2\right]\right\}$$

$$C_9 = \frac{0.075}{0.1025}\left\{\frac{1+0.3}{2}\ln\left(\frac{0.1025}{0.075}\right) + \frac{1-0.3}{4}\left[1 - \left(\frac{0.075}{0.1025}\right)^2\right]\right\} = 0.208$$

$$C_8 = \frac{1}{2}\left[1 + v + (1-v)\left(\frac{b}{a}\right)^2\right]$$

$$C_8 = \frac{1}{2}\left[1 + 0.3 + (1-0.3)\left(\frac{0.075}{0.1025}\right)^2\right] = 0.837388$$

Appendix

$$w = \frac{F}{2\pi r} = \frac{43850}{2x\pi x0.1025} = 68.087\ kN/m$$

$$M_{max} = \frac{68087x0.1025^2}{0.075} x \frac{0.208}{0.837388} = 2369N$$

$$Bending\ stress, \delta_b = \frac{6xM_{max}}{t^2} = \frac{6x2369}{0.02^2} = 35.5MPa$$

Therefore a safety factor is $\frac{240}{35.5} = 6.75$

B. Table for stoichiometric coefficient and operating conditions.

Fuel	**Stoichiometric coefficients**	**Operating conditions**		
		P_i(MPa)	T_i(K)	T_c(K)
iso-octane	$C_8H_{18} + 12.5O_2 + 41.05N_2 + 5.95CO_2$	0.0789	304	640
	$C_8H_{18} + 12.5O_2 + 35.1N_2 + 11.9CO_2$	0.792	310	650
		0.766	312	676
		0.771	322	694
	$C_8H_{18} + 12.5O_2 + 47N_2$	0.74	318	713
		0.744	328	731
	$C_8H_{18} + 12.5O_2 + 35.1N_2 + 11.9Ar$	0.708	319	752
		0.712	328	769
	$C_8H_{18} + 12.5O_2 + 16.06N_2 + 30.94Ar$	0.644	306	802
		0.65	321	833
		0.661	353	900
	$C_8H_{18} + 12.5O_2 + 47Ar$	0.589	321	925
		0.591	328	941
Toluene	$C_7H_8 + 9O_2 + 8.14N_2 + 25.7Ar$	0.624	333	916
	$C_7H_8 + 9O_2 + 33.84Ar$	0.571	322	970
		0.572	328	985
		0.574	334	999
		0.575	340	1014
		0.575	347	1031

Table B.1. Stoichiometric coefficients and operating conditions for fuel mixtures studied in this work.

Fuel	**Stoichiometric coefficients**	**Operating conditions**		
		P_i (MPa)	T_i (K)	T_c (K)
n-butanol	$C_4H_{10}O + 6O_2 + 8.28N_2 + 14.28CO_2$	0.86	353	670
	$C_4H_{10}O + 6O_2 + 18.28N_2 + 4.28CO_2$	0.75	323	688
		0.75	333	706
	$C_4H_{10}O + 6O_2 + 22.56N_2$	0.731	323	721
	$C_4H_{10}O + 6O_2 + 16.85N_2 + 5.71Ar$	0.675	314	745
		0.68	331	778
	$C_4H_{10}O + 6O_2 + 10.57N_2 + 11.99Ar$	0.67	353	865
I70	$0.3(C_4H_{10}O) + 0.7(C_8H_{18}) + 10.55O_2 + 25.61N_2 + 14.06CO_2$	0.815	322	652
	$0.3(C_4H_{10}O) + 0.7(C_8H_{18}) + 10.55O_2 + 32.14N_2 + 7.53CO_2$	0.77	324	685
	$0.3(C_4H_{10}O) + 0.7(C_8H_{18}) + 10.55O_2 + 37.16N_2 + 2.51CO_2$	0.764	338	733
	$0.3(C_4H_{10}O) + 0.7(C_8H_{18}) + 10.55O_2 + 18.58N_2 + 21.09Ar$	0.69	325	805
		0.694	340	835
		0.7	355	865
	$0.3(C_4H_{10}O) + 0.7(C_8H_{18}) + 10.55O_2 + 9.54N_2 + 30.13Ar$	0.659	344	895
		0.662	355	918
I50	$0.5(C_4H_{10}O) + 0.5(C_8H_{18}) + 9.25O_2 + 22.45N_2 + 12.33CO_2$	0.816	322	651
	$0.5(C_4H_{10}O) + 0.5(C_8H_{18}) + 9.25O_2 + 28.18N_2 + 6.6CO_2$	0.772	325	687
	$0.5(C_4H_{10}O) + 0.5(C_8H_{18}) + 9.25O_2 + 34.78N_2$	0.75	323	715
		0.76	347	760
	$0.5(C_4H_{10}O) + 0.5(C_8H_{18}) + 9.25O_2 + 16.29N_2 + 18.49Ar$	0.695	326	805
		0.7	341	835
	$0.5(C_4H_{10}O) + 0.5(C_8H_{18}) + 9.25O_2 + 8.36N_2 + 26.42Ar$	0.665	346	895

Table B.2. Stoichiometric coefficients and operating conditions for fuel mixtures studied in this work.

Fuel	**Stoichiometric coefficients**	**Operating conditions**		
		P_i(MPa)	T_i(K)	T_c(K)
T70	$0.3(C_4H_{10}O) + 0.7(C_7H_8) + 8.1O_2 + 30.46N_2$	0.73	323	735
		0.738	337	763
	$0.3(C_4H_{10}O) + 0.7(C_7H_8) + 8.1O_2 + 14.26N_2 + 16.2Ar$	0.671	316	805
		0.66	326	835
	$0.3(C_4H_{10}O) + 0.7(C_7H_8) + 8.1O_2 + 7.32N_2 + 23.13Ar$	0.63	331	895
	$0.3(C_4H_{10}O) + 0.7(C_7H_8) + 8.1O_2 + 30.46Ar$	0.59	328	960
T50	$0.5(C_4H_{10}O) + 0.5(C_7H_8) + 7.5O_2 + 22.85N_2 + 5.35CO_2$	0.74	318	690
		0.746	335	716
	$0.5(C_4H_{10}O) + 0.5(C_7H_8) + 7.5O_2 + 28.2Ar$	0.73	341	765
	$0.5(C_4H_{10}O) + 0.5(C_7H_8) + 7.5O_2 + 13.2N_2 + 15Ar$	0.645	317	810
	$0.5(C_4H_{10}O) + 0.5(C_7H_8) + 7.5O_2 + 6.8N_2 + 21.4Ar$	0.631	336	895
		0.634	346	917
TRF	$0.041(C_8H_{18}) + 0.146(C_7H_{16}) + 0.813(C_7H_8) + 9.44O_2 + 22.02N_2 + 13.48CO_2$	0.822	329	670
		0.83	347	700
	$0.041(C_8H_{18}) + 0.146(C_7H_{16}) + 0.813(C_7H_8) + 9.44O_2 + 35.5N_2$	0.735	323	735
		0.74	335	758
	$0.041(C_8H_{18}) + 0.146(C_7H_{16}) + 0.813(C_7H_8) + 9.44O_2 + 22.02N_2 + 13.48Ar$	0.665	328	815
		0.711	361	870
	$0.041(C_8H_{18}) + 0.146(C_7H_{16}) + 0.813(C_7H_8) + 9.44O_2 + 8.54N_2 + 26.96Ar$	0.631	333	907
		0.637	343	929
	$0.041(C_8H_{18}) + 0.146(C_7H_{16}) + 0.813(C_7H_8) + 9.44O_2 + 35.5Ar$	0.583	323	960
		0.585	343	1008

Table B.3. Stoichiometric coefficients and operating conditions for fuel mixtures studied in this work.

Fuel	**Stoichiometric coefficients**	**Operating conditions**		
		P_i (MPa)	T_i (K)	T_c (K)
E25	$0.0248(C_8H_{18}) + 0.0883(C_7H_{16}) + 0.4903(C_7H_8) + 0.3966(C_2H_6O) + 6.88O_2 + 16.05N_2 + 9.82Ar$	0.698	327	800
		0.7	332	810
		0.704	342	830
		0.714	352	850
		0.718	363	870
	$0.0248(C_8H_{18}) + 0.0883(C_7H_{16}) + 0.4903(C_7H_8) + 0.3966(C_2H_6O) + 6.88O_2 + 6.22N_2 + 19.65Ar$	0.637	329	890
		0.64	339	910
		0.643	348	930
		0.646	357	950
E50	$0.0138(C_8H_{18}) + 0.0493(C_7H_{16}) + 0.2734(C_7H_8) + 0.6635(C_2H_6O) + 5.17O_2 + 12.06N_2 + 7.38Ar$	0.705	330	800
		0.707	335	810
		0.712	346	830
		0.716	356	850
		0.72	366	870
	$0.0138(C_8H_{18}) + 0.0493(C_7H_{16}) + 0.2734(C_7H_8) + 0.6635(C_2H_6O) + 5.17O_2 + 4.68N_2 + 14.76Ar$	0.648	334	890
		0.651	344	910
		0.654	353	930
		0.657	363	950

Table B.4. Stoichiometric coefficients and operating conditions for fuel mixtures studied in this work.

Fuel	**Stoichiometric coefficients**	**Operating conditions**		
		P_i(MPa)	T_i(K)	T_c(K)
E75	$0.0059(C_8H_{18}) + 0.0212(C_7H_{16}) + 0.1175(C_7H_8) + 0.8554(C_2H_6O) + 3.93O_2 + 9.17N_2 + 5.61Ar$	0.715	334	800
		0.716	339	810
	$0.0059(C_8H_{18}) + 0.0212(C_7H_{16}) + 0.1175(C_7H_8) + 0.8554(C_2H_6O) + 3.93O_2 + 5.42N_2 + 9.35Ar$	0.674	325	830
	$0.0059(C_8H_{18}) + 0.0212(C_7H_{16}) + 0.1175(C_7H_8) + 0.8554(C_2H_6O) + 3.93O_2 + 3.55N_2 + 11.22Ar$	0.653	321	850
		0.656	330	870
	$0.0059(C_8H_{18}) + 0.0212(C_7H_{16}) + 0.1175(C_7H_8) + 0.8554(C_2H_6O) + 3.93O_2 + 1.31N_2 + 13.47Ar$	0.627	322	890
		0.63	331	910
		0.633	340	930
		0.636	349	950
B25	$0.0289(C_8H_{18}) + 0.1031(C_7H_{16}) + 0.5725(C_7H_8) + 0.2955(C_4H_{10}O) + 8.42O_2 + 19.64N_2 + 12.02CO_2$	0.832	318	649
		0.84	333	671
		0.845	348	697
	$0.0289(C_8H_{18}) + 0.1031(C_7H_{16}) + 0.5725(C_7H_8) + 0.2955(C_4H_{10}O) + 8.42O_2 + 31.66N_2$	0.745	313	710
		0.75	323	729
	$0.0289(C_8H_{18}) + 0.1031(C_7H_{16}) + 0.5725(C_7H_8) + 0.2955(C_4H_{10}O) + 8.42O_2 + 19.64N_2 + 12.02Ar$	0.705	338	820
		0.71	348	840
	$0.0289(C_8H_{18}) + 0.1031(C_7H_{16}) + 0.5725(C_7H_8) + 0.2955(C_4H_{10}O) + 8.42O_2 + 7.61N_2 + 24.05Ar$	0.639	328	885
		0.643	343	918

Table B.5. Stoichiometric coefficients and operating conditions for fuel mixtures studied in this work.

Fuel	**Stoichiometric coefficients**	**Operating conditions**		
		P_i (MPa)	T_i (K)	T_c (K)
B50	$0.0182(C_8H_{18}) + 0.0648(C_7H_{16}) + 0.3598(C_7H_8) + 0.5572(C_4H_{10}O) + 7.52O_2 + 17.54N_2 + 10.74CO_2$	0.83	328	662
		0.825	333	672
	$0.0182(C_8H_{18}) + 0.0648(C_7H_{16}) + 0.3598(C_7H_8) + 0.5572(C_4H_{10}O) + 7.52O_2 + 28.28N_2$	0.752	316	711
		0.757	327	731
		0.746	338	754
	$0.0182(C_8H_{18}) + 0.0648(C_7H_{16}) + 0.3598(C_7H_8) + 0.5572(C_4H_{10}O) + 7.52O_2 + 17.54N_2 + 10.74Ar_2$	0.705	327	790
	$0.0182(C_8H_{18}) + 0.0648(C_7H_{16}) + 0.3598(C_7H_8) + 0.5572(C_4H_{10}O) + 7.52O_2 + 6.8N_2 + 21.47Ar$	0.624	337	902
B75	$0.0086(C_8H_{18}) + 0.0307(C_7H_{16}) + 0.1702(C_7H_8) + 0.7906(C_4H_{10}O) + 6.72O_2 + 15.67N_2 + 9.6Ar$	0.715	334	800
		0.716	339	810
	$0.0086(C_8H_{18}) + 0.0307(C_7H_{16}) + 0.1702(C_7H_8) + 0.7906(C_4H_{10}O) + 6.72O_2 + 9.28N_2 + 16Ar$	0.674	325	830
	$0.0086(C_8H_{18}) + 0.0307(C_7H_{16}) + 0.1702(C_7H_8) + 0.7906(C_4H_{10}O) + 6.72O_2 + 6.08N_2 + 19.19Ar$	0.653	321	850
		0.656	330	870
	$0.0086(C_8H_{18}) + 0.0307(C_7H_{16}) + 0.1702(C_7H_8) + 0.7906(C_4H_{10}O) + 6.72O_2 + 2.24N_2 + 23.03Ar$	0.627	322	890
		0.63	331	910
		0.633	340	930
		0.636	349	950

Table B.6. Stoichiometric coefficients and operating conditions for fuel mixtures studied in this work.

References

"Generations of biofuels" (n.d). Retrieved from http://energyfromwasteandwood.weebly.com/generations-of-biofuels.html.

Lutz A.E, Kee R.J, Miller J.A, Dwyer H. A, Oppenheim A.K, "Dynamic effects of auto-ignition centres for hydrogen and $C_{1,2}$-hydrocarbon fuels", Symposium (International) on Combustion, 22, 1989, 1683-1693.

Tomlin A.S, Pilling M.J., Turányi T, Merkin J.H, Brindley J, "Mechanism reduction for the oscillatory oxidation of hydrogen: Sensitivity and quasi-steady-state analyses", Combustion and Flame, 91, 1992, 107-130.

Abdullah S. A, Jihad B, Tamour J, Mohammed A, Nehal B, Patrick G, Hassan B, Aamir F, Mani S., (2015), 'Mixed butanols addition to gasoline surrogates: Shock tube ignition delay time measurements and chemical kinetic modelling', *Combustion and Flame*, Volume 162, Issue 10, 3971-3979.

Affleck W. S., Thomas A. (1968), 'An Opposed Piston Rapid Compression Machine for Preflame Reaction Studies'. Proceedings of the Institutions of Mechanical Engineers, 183, 365-387.

Agbro E; Materego M; Lawes M; Tomlin AS, (2015), 'Low temperature ignition properties of n-butanol: key uncertainties and constraints', Proceedings of the European Combustion Meeting.

Ahfaz A, Gokop G, Vijai S.B. S, Khalid A, William L. R, S. Mani S, (2015), 'A computational methodology for formulating gasoline surrogate fuels with accurate physical and chemical kinetic properties', Fuel, Volume 143, 290-300.

References

Aleiferis P.G., Van Romunde Z.R, (2013), ‘An analysis of spray development with iso-octane, n-pentane, gasoline, ethanol and n-butanol from a multi-hole injector under hot fuel conditions’, Fuel, Volume 105, 143-168.

Andrae J.C,G, Brinck T., Kalghatgi G.T., (2008), ‘HCCI experiments with toluene reference fuels modeled by a semi-detailed chemical kinetic model’, Combustion and Flame, Volume 155, Issue 4, 696-712.

Argonne National Laboratory, (2012), ‘International RCM Workshop’, Available from:(http://www.transportation.anl.gov/rcmworkshop/).

Ashraf E, (2015), ‘Investigations on the effects of ethanol–methanol–gasoline blends in a spark-ignition engine: Performance and emissions analysis’, Engineering Science and Technology, an International Journal, 18, 713-719.

Atkinson R.J, Journal of Physical and chemical reference data, volume 1, 1-246, 1989.

Atkinson R.J, Journal of Physical and chemical reference data, volume 2, 1-216, 1994.

Bardwell J., Cyril Hinshelwood, (1951), ‘The Cool Flame of methylethylketone’, Proceedings of the Royal Society of London. Series A, Mathematical and Physical Science, Vol. 205, 1082, 375-390.

Barnard J.A., Bradley J.N., ‘Flame and Combustion-Second Edition’, Chapman and Hall, 1985.

Bates L., Bradley D., Paczko, G., Peters, N, (2015), “Engine Hot Spots: Modes of Auto-ignition and Subsequent Reaction Propagation,” 25th International Colloquium on the Dynamics of Explosions and Reactive systems, Paper 184.

References

Battin-Leclerc F., (2008), ‘Detailed chemical kinetic models for the low-temperature combustion of hydrocarbons with application to gasoline and diesel fuel surrogates’, Progress in Energy and Combustion Science, Volume 34, 4, 440-498.

Beerer, David, McDonnel V, Samuelsen S., Angello L., (2009) ‘Interpretation of Flow Reactor Based Ignition Delay Measurements’, ASME Turbo Expo: Power for Land, Sea, and Air. American Society of Mechanical Engineers, 1011-1026.

Bradley D., Kalghatgi G.T., (2009), ‘Influence of auto-ignition delay time characteristics of different fuels on pressure waves and knock in reciprocating engines’, Combustion and Flame 156, 2307-2318.

Bradley D, ‘‘Hot spots’ and gasoline engine knock’, (1996), Journal of Chemical Society, Faraday Transactions, volume 92, 16, 2959-2964.

Bradley D, Lawes M and Materego M (2015), ‘Interpretation of Auto-ignition Delay Times Measured in Different Rapid Compression Machines’, 25th International Colloquium on the Dynamics of Explosions and Reactive systems, Paper 194.

C.K. Westbrook, W.J. Pitz, M. Mehl, H.J. Curran, “Detailed chemical kinetic reaction mechanisms for primary reference fuels for diesel cetane number and spark-ignition octane number”, Proceedings of the Combustion Institute, Volume 33, 2011, 185-192.

Cancino L.R, Fikri M., Oliveira A.A.M., Schulz C., (2009), ‘Autoignition of gasoline surrogate mixtures at intermediate temperatures and high pressures: Experimental and numerical approaches’, Proceedings of the Combustion Institute, Volume 32, Issue 1, 501-508.

Cheng, R. K. & Oppenheim, A. K. (1984). ‘Autoignition in methane-hydrogen mixtures’. Combustion and Flame, 58, 125-139.

References

Chong-Wen Zhou, John M. Simmie, Henry J. Curran, Rate constants for hydrogen-abstraction by from n-butanol, Combustion and Flame, 158, 2011, 726-731.

Clarkson J, Griffiths J.F., Macnamara J.P., Whitaker B.J., (2001), ‘Temperature fields during the development of combustion in a rapid compression machine’, Combustion and Flame, 125:1162–1175.

Cox A., Griffiths J.F, Mohamed C, Curran H.J, Pitz W.J, Westbrook C.K, (1996), ‘Extents of alkane combustion during rapid compression leading to single-and two-stage ignition’, Symposium (International) on Combustion, Volume 26, Issue 2, 2685-2692.

Davidson D.F, Haylett D.R, Hanson R.K, “Development of an aerosol shock tube for kinetic studies of low-vapor-pressure fuels”, Combustion and Flame, Volume 155, 2008, Pages 108-117.

Darcy D., Nakamura H., Tobin C.J., Mehl M., Metcalfe W.K., Pitz W.J., Westbrook C.K., Curran H.J., (2014), ‘A high-pressure rapid compression machine study of n-propylbenzene ignition’, Combustion and Flame, Volume 161, Issue 1, 65-74.

Das A.K, Uddi M, Sung C, (2012), “Two-line thermometry and H_2O measurement for reactive mixtures in rapid compression machine near 7.6 μm’, Combustion and Flame, Volume 159, Issue 12, 3493-3501.

Davidson D.F., Gauthier B.M, Hanson R.K., (2005), ‘Shock tube ignition measurements of iso-octane/air and toluene/air at high pressures’, Proceedings of the Combustion Institute, Volume 30(1):1175-1182.

Desgroux P, Minetti R, Sochet LR. (1996), ‘Temperature distribution induced by preignition reactions in a rapid compression machine’, Combustion Science and Technology,113–114:193–203.

Desgroux P., Gasnot L., Sochet L.R, (1995),’ Instantaneous temperature measurement in a rapid-compression machine using laser Rayleigh scattering’, Applied Physics B, 61:69-72.

Di Sante R., (2012), ‘Measurements of the auto-ignition of n-heptane/toluene mixtures using a rapid compression machine’, Combustion and Flame, 159, 1, 55-63.

Dibbern, A., Crisafulli, J., Hagopia, M., McDougle, S., Saulsberry H., Regor L, (2009), ‘Implications of Dynamic Pressure Transducer Mounting Variations on Measurements in Pyrotechnic Test Apparatus’, NASA technical reports server (NTRS).

Diehl J.W., Finkbeiner J.W., Disanzo F.P, (1993), ‘Determination of benzene, toluene, ethylbenzene and xylenes in gasolines by gas chromatography/deuterium isotope dilution fourier transform infrared spectroscopy’, Analytical Chemistry, 65(18), 2493-2496.

Donovan M.T., He X., Zigler B.T., Palmer T.R., Wooldridge M.S., Atreya A., (2004), ‘Demonstration of a free-piston rapid compression facility for the study of high temperature combustion phenomena’, Combustion and Flame, Volume 137, Issue 3, 351-365.

Ezevard G, (2011), ‘An innovative rapid compression machine in theory and practise’, PhD thesis, University of Cape Town.

Falconer J.W., Hoare D.E., Savaya Z., (1983), ‘Peroxides in cool flame of iso-butene’, Combustion and Flame, Volume 52, 257-267.

Fieweger K., Blumenthal R., Adomeit G., D. B., (1997), ‘Self-ignition of S.I. engine model fuels: A shock tube investigation at high pressure’, Combustion and Flame, 109, 599-619.

Fomin N.A, 110 years of experiments on shock tubes, Journal of Engineering Physics and Thermophysics, 2010, Volume 83, 6, 1118.

Franck J., Griffiths J.F., Nimmo W., (1988), 'The control of spontaneous ignition under rapid compression', Symposium (International) on Combustion, Volume 21, Issue 1, 447-454.

Bansal G, Mascarenhas A, Chen J.H, "Direct numerical simulations of autoignition in stratified dimethyl-ether (DME)/air turbulent mixtures", Combustion and Flame, 162, 2015, 688-702.

Gabriel da Silva, Joseph W. Bozzelli, Long Liang and John T. Farrell, "Ethanol Oxidation: Kinetics of the α-Hydroxyethyl Radical + O_2 Reaction", J. Phys. Chem. A, 2009, 113 (31), 8923–8933.

Gallagher S.M, Curran H.J, Metcalfe W.K, Healy D., Simmie J.M, Bourque G., (2008), 'A rapid compression machine study of the oxidation of propane in the negative temperature coefficient regime', Combustion and Flame, Volume 153, 316-333.

Gauthier B.M, Davidson D.F, Hanson R.K, (2004), 'Shock tube determination of ignition delay times in full-blend and surrogate fuel mixtures', Combustion and Flame, Volume 139, Issue 4, 300-311.

Georgios K, Daniel S, Diep V, Robert L. R, Akua A, Heejung J, Kent C. J, Thomas D. D, (2015), 'The impact of ethanol and iso-butanol blends on gaseous and particulate emissions from two passenger cars equipped with spray-guided and wall-guided direct injection SI (spark ignition) engines', Energy, Volume 82, 168-179.

Gersen S, Mokhov A.V., Darmeveil J.H, Levinsky H.B., (2010), 'Ignition properties of n-butane and iso-butane in a rapid compression machine', Combustion and Flame, Volume 157, Issue 2, 240-245.

Gersen, S., Anikin, N. B., Mokhov, A. V. & Levinsky, H. B. (2008), 'Ignition properties of methane/hydrogen mixtures in a rapid compression machine', International Journal of Hydrogen Energy, 33, 1957-1964.

Goldsborough S.S. (2012), ‘1st International RCM Workshop: Meeting Report’, Argonne National Laboratory.

Goldsborough, S. S. (2009), ‘A chemical kinetically based ignition delay correlation for iso-octane covering a wide range of conditions including the NTC region’, Combustion and Flame, 156, 1248-1262.

Goutham K., Kumar K., Sung, C.-J., Mehl, M. & Pitz, W. J. (2012), ‘Experimental and surrogate modelling study of gasoline ignition in a rapid compression machine’, Combustion and Flame, 159, 3066-3078.

Goutham K., Kumar, K., Sung, C.-J., Mehl, M. & Pitz, W. J. (2013), ‘Autoignition of gasoline and its surrogates in a rapid compression machine’, Proceedings of the Combustion Institute, 34, 345-352.

Greg H., Tracy B., Carol B., Roger O., John L., Rosanne B., Toni T., Joanna L., Jacqueline J., (2006), ‘Alternative Jet fuels’, Chevron’s Fuels Technical Review.

Griffiths J. F, MacNamara J. P, Mohamed C., Whitaker B.J, Pan J., Sheppard C.G.W., (2001), ‘Temperature fields during the development of autoignition in a rapid compression machine’, Faraday Discuss ,119:287–303.

Griffiths J.F, Halford-Maw P.A., Rose D.J., (1993), ‘Fundamental features of hydrocarbon autoignition in a rapid compression machine’, Combustion and Flame, Volume 95, Issue 3, 291-306.

Griffiths J.F, Jiao Q, Schreiber M., Meyer J, Knoche K.F., (1992), ‘Development of thermokinetic models for autoignition in a CFD code: experimental validation and application of the results to rapid compression studies’, Proceedings of Combustion Institute, 24, 1809–1815.

References

Griffiths J.F, MacNamara J.P, Shepperd C.G.W., Turton D.A, Whitaker B.J., (2002), 'The relationship of knock during controlled autoignition to temperature inhomogeneities and fuel reactivity', Fuel, 81:2219–25.

Griffiths J.F., Halford-Maw P.A., Mohamed C., (1997), 'Spontaneous ignition delays as a diagnostic of the propensity of alkanes to cause engine knock', Combustion and Flame, Volume 111, Issue 4, 327-337.

Griffiths J.F., Jiao Q., Schreiber A., Meyer J., Knoche K.F., Kardylewski W., (1993), 'Experimental and Numerical Studies of Ditertiary ButylPeroxide Combustion at High Pressures in a Rapid Compression Machine', Combustion and flame, 93: 303-315.

Grogan K.P., Goldsborough S.S, Ihme M., (2015), 'Ignition regimes in rapid compression machines', Combustion and Flame 162, 3071-3080.

Gu, X.J., Emerson D.R., Bradley D., (2003), 'Modes of reaction front propagation from hot spots', Combustion and Flame, 133, 63-74.

Curran H.J, Gaffuri P., Pitz W.J, Westbrook C.K, "A comprehensive modelling study of iso-octane oxidation", Combustion and Flame, Volume 129, 2002, 253-280.

Halstead M. P., Kirsch L. J., Quinn, C. P., (1977), 'The autoignition of hydrocarbon fuels at high temperatures and pressures—Fitting of a mathematical model', Combustion and Flame, 30, 45-60.

Hanson, R.K., Davidson D.F, (2014), 'Recent advances in laser absorption and shock tube methods for studies of combustion chemistry', Progress in Energy and Combustion Science, 44, 103-114.

Hartmann M., Gushterova I., Fikri M, Schulz C., Schießl R., Maas U., (2011), 'Auto-ignition of toluene-doped n-heptane and iso-octane/air mixtures: High-pressure shock-tube experiments and kinetics modelling', Combustion and Flame, Volume 158, Issue 1, 172-178.

He, X., Donovan, M. T., Zigler, B. T., Palmer, T. R., Walton, S. M., Wooldridge, M. S., Atreya, A. (2005), 'An experimental and modelling study of iso-octane ignition delay times under homogeneous charge compression ignition conditions', Combustion and Flame, 142, 266-275.

Herzler J, Fikri M, Hitzbleck K, Starke R., Schulz C., Roth P, Kalghatgi G.T., (2007), 'Shock-tube study of the autoignition of n-heptane/toluene/air mixtures at intermediate temperatures and high pressures', Combustion and Flame (149)25-31.

Heufer K.A., Bugler J, Curran H.J., (2013), 'A comparison of longer alkane and alcohol ignition including new experimental results for n-pentanol and n-hexanol', Proceedings of the Combustion Institute, Volume 34, Issue 1, 511-518.

Huang J., Hill P.G., Bushe W.K., Munshi S.R., (2004), 'Shock tube study of methane ignition under engine relevant conditions: experiments and modelling', Combustion and Flame, Volume 136, 25-42.

Ihara T., Tanaka T., Wakai K., (2009), 'Effects of Octane number on autoignition and knocking phenomena in a stratified mixture', Combustion, Explosion and Shock waves, Volume 45, 428-434.

Ivo S, Deanna P. C, Joseph T. H., Sheng Y, Davidson D.F, Ronald K. H, (2012), 'Shock tube measurements of ignition delay times for the butanol isomers', Combustion and Flame, Volume 159, Issue 2, 516-527.

Emdee J.L, Brezinsky K, Glassman I, "A kinetic model for the oxidation of toluene near 1200 K", J. Phys. Chem., 1992, 96 (5), pp 2151–2161.

References

Jaeho C, Woosung S, Wonwook J, Dongyoung J, Cha-Lee M, Simsoo P, (2015), 'Impact of intermediate ethanol blends on particulate matter emission from a spark ignition direct injection (SIDI) engine', Applied Energy, Available August 2015.

Jones D.T., Woods D.R., (1986), 'Acetone–butanol fermentation revisited', Microbiological Reviews, 50:484–524.

Jörg A, Sannakaisa V, 'Corrosion of martensitic stainless steel in ethanol-containing gasoline: Influence of contamination by chloride, H2O and acetic acid', Corrosion Science, 2015, Volume 98, 318-326.

Kahandawala S.S., Suhk S., (2011), 'A shock tube study of igniton delay in the combustion of ethylene', Combustion and Flame, Volume 158, 1019-1031.

Kalghatgi, G., Head, R., Chang, J., Viollet, Y., Babiker, H., Amer A., (2014). 'An Alternative Method Based on Toluene/n-Heptane Surrogate Fuels for Rating the Anti-Knock Quality of Practical Gasolines', SAE International Journal of Fuels and Lubricants, 7(3):663-672.

Cancino L.R, Fikri, M, Oliveira A.A.M, C. Schulz C, Autoignition of gasoline surrogate mixtures at intermediate temperatures and high pressures: Experimental and numerical approaches, Proceedings of the Combustion Institute, Volume 32, 2009, 501-508.

Lee D, Hochgreb S., (1998), 'Rapid compression machine: heat transfer and suppression of corner vortex', Combustion and Flame 114:531–545.

Lee, S., Bae, C., Prucka, R., Fernandes, G., (2005), 'Quantification of Thermal Shock in a Piezoelectric Pressure Transducer', SAE Technical Paper 2005-01-2092.

Lenhert D. B., Miller D.L., Cernansky N.P., Owens K.G., (2009), 'The oxidation of a gasoline surrogate in the negative temperature coefficient region', Combustion and Flame, Volume 156, Issue 3, 549-564.

Li S., Campos A., Davidson D. F., Hanson, R. K. (2014), ‘Shock tube measurements of branched alkane ignition delay times’, Fuel, 118, 398-405.

Livengood J.C., Wu P.C., (1955), ‘Correlation of autoignition phenomena in internal combustion engines and rapid compression machines’, Symposium (International) on Combustion, 5:347-356.

Lutz A.E., Kee, R.J., Mille, J.A., Dwyer, H.A, Oppenheim, A.K., (1988) Symposium (International) on Combustion, 22:1683–1693.

Ribaucour M, Minetti R, Sochet L.R, Curran H.J, Pitz W.J, Westbrook C.K, Ignition of isomers of pentane: An experimental and kinetic modeling study, Proceedings of the Combustion Institute, Volume 28, Issue 2, 2000, 1671-1678.

Mansfield A.B, Wooldridge M.S., Di H., He X, (2015), ‘Low-temperature ignition behavior of iso-octane’, Fuel, Volume 139, 79-86.

Campbell M.F, Wang S, Goldenstein C.S, Spearrin R.M, Tulgestke A.M, Zaczek L.T, Davidson D.F, Hanson R.K, “Constrained reaction volume shock tube study of n-heptane oxidation: Ignition delay times and time-histories of multiple species and temperature”, Proceedings of the Combustion Institute, Volume 35, 2015, 231-239.

Mehl M., Chen J.Y., Pitz W.J, Sarathy S.M., Westbrook C.K., (2011), ‘An Approach for Formulating Surrogates for Gasoline with Application toward a Reduced Surrogate Mechanism for CFD Engine Modeling’, Energy and Fuels, 25 (11), 5215-5223.

Meyer J.W, Oppenheim A.K., (1971), ‘On the shock-induced ignition of explosive gases’, Symposium (International) on Combustion, 13:1153–1164.

Minetti R., Ribaucour, M., Carlier, M., Fittschen, C., Sochet L.R., (1994), ‘Experimental and modelling study of oxidation and auto-ignition of butane at high pressure’, Combustion and Flame, Volume 96, 3:201-211.

Mittal G, Raju M.P., Bhari A., (2011), ‘Numerical assessment of the novel concept of crevice containment in a rapid compression machine’, Combustion and Flame, 158, 2420-2427.

Mittal G., Bhari A., (2013), ‘A rapid compression machine with crevice containment’. Combustion and Flame, 160:2975-2981.

Mittal G., Burke S.M., Davies V.A, Parajuli B., Metcalfe W.K, Curran H.J, (2014), ‘Autoignition of ethanol in a rapid compression machine’, Combustion and Flame, Volume 161, 1164-1171.

Mittal G., Chaos M., Sung C, Dryer F.L., (2008), ‘Dimethyl ether autoignition in a rapid compression machine: Experiments and chemical kinetic modelling', Fuel Processing Technology, Volume 89, 1244-1254.

Mittal G., Gupta S., (2012), ‘Computational assessment of an approach for implementing crevice containment in rapid compression machines’, Fuel, 102, 536-544.

Mittal G., Raju M.P, Sung C. (2012), ‘Vortex formation in a rapid compression machine: Influence of physical and operating parameters’, Fuel, 94, 409-417.

Mittal G., Raju M.P., Sung C.J, (2008), Computational fluid dynamics modelling of hydrogen ignition in a rapid compression machine, Combustion and flame, 155, 417-428.

Mittal G., Sung C., (2007), ‘A Rapid Compression Machine for chemical kinetic studies at elevated pressures and temperatures’, Combustion Science and Technology, Volume 179, 497-530.

Mittal G., Sung C., (2007), ‘Autoignition of toluene and benzene at elevated pressures in a rapid compression machine’, Combustion and Flame, 150, 355-368.

Mittal G., Sung C.J., (2006), ‘Aerodynamics inside a rapid compression machine’, Combustion and Flame, 145:160–80.

Mittal, G., Chomier, M., (2014), ‘Effect of crevice mass transfer in a rapid compression machine, Combustion and Flame, 161:398-404.

Mohamed, C., (1998), ‘Suppression of reaction during rapid compression and its effect on ignition delay’, Combustion and Flame, Volume 112, Issue 3, 438-444.

Morgan N., Smallbone A., Bhave A., Kraft M., Cracknell R., Kalghatgi G., (2010), ‘Mapping surrogate gasoline compositions into RON/MON space’, Combustion and Flame, Volume 157, Issue 6, 1122-1131.

Nazim Z. M, T. Nejat V, (2008), ‘“Green” path from fossil-based to hydrogen economy: An overview of carbon-neutral technologies’, Volume 33, Issue 23, 6804-6839.

Ndaba B., Chiyanzu I., Marx S., (2015), ‘n-butanol derived from biochemical and chemical routes: A review’, Biotechnology Reports, Volume 8, 1-9.

Dagaut P, Pengloana G, Ristoria A, “Oxidation, ignition and combustion of toluene: Experimental and detailed chemical kinetic modelling”, Phys. Chem. Chem. Phys., 2002,4, 1846-1854.

Payman W. and Titman H., (1935), ‘Explosion waves and shock waves. Part III: The initiation of detonation in mixtures of ethylene and oxygen and of carbon monoxide and oxygen’, Proceedings of the Royal Society of London., A152, 418–455.

Payman W., (1928) ,’The detonation-wave in gaseous mixtures and the pre-detonation period, Proceedings of the Royal Society of London, A120, 90–109.

Payman W., Shepherd W.C.F, (1946), ‘Explosion waves and shock waves. Part VI: The disturbance produced by bursting diaphragms with compressed air’, Proceedings of the Royal society of London, A186, 243–321.

Payman W., Shepherd W.C.F., (1937), ‘Explosion waves and shock waves. Part IV: Quasi-detonation in mixtures of methane and air, Proceedings of the Royal Society of London., A158, 348–367.

Payman W., Woodhead D.W, (1931), ‘Explosion waves and shock waves. Part I: The wave-speed camera and its application to the photography of bullets in flight’, Proceedings of the Royal Society of London, A132, 200–213.

Payman W., Woodhead D.W, Titman H, (1935), ‘Explosion waves and shock waves. Part II: The shock wave and explosion products sent out by blasting detonators’, Proceedings of the Royal society of London, A148, 604–622.

PCB Piezotronic, (2015), ‘Introduction to Dynamic Pressure Sensor’, Available from: https://www.pcb.com/TechSupport/Tech_Pres.aspx.

Pepiot-Desjardins P., Pitsch H., (2008), ‘An efficient error-propagation-based reduction method for large chemical kinetic mechanisms’, Combustion and Flame, Volume 154, 1–2, 67-81.

Petersen E. L., Kalitan D.M, Barrett A.B., Reehal S.C, Mertens J.D, Beerer D.J., Richard L. Hack, R.L, McDonell, V.G, (2007), ‘New syngas/air ignition data at lower temperature and elevated pressure and comparison to current kinetics models’, Combustion and Flame, Volume 149, 1–2, 244-247.

Pfahl U., Fieweger K., Adomeit G., (1996), ‘Self-ignition of diesel-relevant hydrocarbon-air mixtures under engine conditions’, Symposium (International) on Combustion, Volume 26, Issue 1, 781-789.

Qin, Z., Yang, H. & Gardiner JR, W. C. (2001), ‘Measurement and modelling of shock-tube ignition delay for propene’, Combustion and Flame, 124, 246-254.

Quinn M.K., Kontis, K., “Pressure-Sensitive Paint Measurements of Transient Shock Phenomena”. Sensors, 2013, 13, 4404-4427.

R. Sivaramakrishnan, R.S. Tranter, K. Brezinsky, A high pressure model for the oxidation of toluene, Proceedings of the Combustion Institute, 30, 2005, 1165-1173.

Randolph, A., (1990), ‘Methods of Processing Cylinder-Pressure Transducer Signals to Maximize Data Accuracy’, SAE Technical Paper 900170.

Randolph, A., 1990, ‘Cylinder-Pressure-Transducer Mounting Techniques to Maximize Data Accuracy’, SAE Technical Paper, 900171.

Raymond J Roark, Warren C. Young, (1975), Formulas for Stress and Strain-Fifth edition, McGraw-Hill, p.338, 366.

Roubaud A., Minetti R., Sochet L.R., (2000), ‘Oxidation and combustion of low alkylbenzenes at high pressure: comparative reactivity and auto-ignition’, Combustion and Flame, 121, 3, 535-541.

Szwaja S, Naber J.D, “Combustion of *n*-butanol in a spark-ignition IC engine”, Fuel, 89, 2010, 1573-1582.

Sarathy S.M., Vranckx S, Yasunaga K, Mehl M., Oßwald P., Metcalfe W.K, Westbrook C.K., Pitz W.J., Kohse-Höinghaus K., Fernandes R.X, Curran H.J, (2012), ‘A comprehensive chemical kinetic combustion model for the four butanol isomers’, Combustion and Flame, Volume 159, Issue 6, 2028-2055.

Schiel-Bengelsdorf B., Montoya J., Linder S., Dürre P., (2013), 'Butanol fermentation'. Environmental Technology, 34:1691–710.

Shahir V.K, JawaharC.P., Suresh P.R, (2015), 'Comparative study of diesel and biodiesel on CI engine with emphasis to emissions—A review', Renewable and Sustainable Energy Reviews, Volume 45, 686-697.

Sharpe G.J, Lawes M., Sheppard C.G.W, Griffiths J.F, Bradley D., (2009), 'Collaborative Research in Energy with South Africa: Fundamental Characterisation of Auto-ignition and flame propagation of synthetic fuels', Research Grant Proposal, University of Leeds.

Shen H.S, Matthew A. Oehlschlaeger, (2009), 'The autoignition of C_8H_{10} aromatics at moderate temperatures and elevated pressures', Combustion and Flame, 156, 5, 1053-1062.

Sileghem, L., Wallner, T. & Verhelst, S. 2015. "A quasi-dimensional model for SI engines fueled with gasoline–alcohol blends: Knock modelling". Fuel, 140, 217-226.

Simmie J.M, (2003), 'Detailed chemical kinetic models for the combustion of hydrocarbon fuels, Progress in Energy and Combustion Science', Volume 29, 6, 599-634.

Spotts M.F., Mechanical Design Analysis, Prentice Hall, Inc, 1964.

Standard test method for motor octane number of spark-ignition engine fuel, ASTM D2700-08.

Standard test method for research octane number of spark-ignition engine fuel, ASTM D2699-08.

Turns S.R, 'Introduction to Combustion', Third edition, 2012, pp.9.

Sung C., Curran H.J., (2014), 'Using Rapid Compression Machines for Chemical Kinetics Studies', Progress in Energy and Combustion Science, 44, 1-18.

T. Turanyi, A. Tomlin, 'Analysis of Kinetic Reaction Mechanisms', Springer, 2015.

Tanaka S., Ayala F., Keck J.C., (2003), 'A reduced chemical kinetic model for HCCI combustion of primary reference fuels in a rapid compression machine', Combustion and flame, Volume 133, 467-481.

Tashiro, Yukihiro, Yoshida, Tsuyoshi, Noguchi, Takuya, Sonomoto, Kenji, Recent advances and future prospects for increased butanol production by acetone-butanol-ethanol fermentation, Eng. Life Sci., volume 13, 5, 1618-2863.

Thomas N.A, Michael R.G, (1984), 'Determination of hydrocarbons types in petroleum liquids by supercritical fluid chromatography with flame ionization detection', Analytical Chemistry, 56, 1767-1769.

University of Illinois, (2014), 'Advanced Fuels Research', Available from (http://tonghun.mechse.illinois.edu/Research/fuels.html).

US, Energy Information Administration, International Energy Outlook 2012 with Projections to 2035.

US, Energy Information Administration, International Energy Outlook 2013 with Projections to 2040.

US, Energy Information Administration, International Energy Outlook 2014 with Projections to 2040.

US, Energy Information Administration, International Energy Outlook 2010.

Vancoillie J, Demuynck J., Sileghem L., Van De Ginste M., Verhelst S., Brabant L., Hoorebeke L, (2013), 'The potential of methanol as a fuel for flex-fuel and dedicated spark-ignition engines', Applied Energy, Volume 102, 140-149.

Vanhove G., Petit G., Minetti R., (2006), 'Experimental study of the kinetic interactions in the low-temperature autoignition of hydrocarbon binary mixtures and a surrogate fuel', Combustion and Flame, Volume 145, Issue 3, 521-532.

Vieille P., (1899), 'Sur les discontinuites produites par la de′tente brusque de gas comprimes', Comptes Rendus de l'Academie des Sciences de Paris, 129, 1228–1230.

Vranckx S., Lee C., Chakravarty H.K., Fernandes R.X., (2013), 'A rapid compression machine study of the low temperature combustion of cyclohexane at elevated pressures', Proceedings of the Combustion Institute, Volume 34, 377-384.

W.J. Pitz, R. Seiser, J.W Bozzelli et al., Chemical kinetic characterisation of combustion of toluene; Proceeding of second joint meeting of the US sections of the combustion institute, 2001.

Weiqi J., Peng Z., Tanjin H., Zhi W., Ling T., He X., Law C.K, (2015), 'Intermediate species measurement during iso-butanol auto-ignition', Combustion and Flame, Volume 162, Issue 10, 3541-3553.

Westbrook C.K, Curran H.J, Pitz W.J., Griffiths J.F., Mohamed C., Wo S.K, (1998), 'The effects of pressure, temperature, and concentration on the reactivity of alkanes: Experiments and modelling in a rapid compression machine', Symposium (International) on Combustion, Volume 27, Issue 1, 371-378.

World Coal Institute, 2005.

Wurmel J, Simmie J.M., (2005), ‘CFD studies of a twin-piston rapid compression machine’, Combustion and Flame,141:417–30.

Würmel J., (2004), ‘Detailed chemical kinetics combined with a computational fluid dynamics study of a twin piston rapid compression machine’, PhD Thesis, Galway: National University of Ireland.

Würmel J., Silke E.J, Curran H.J, Ó Conaire M.S., Simmie J.M, (2007), ‘The effect of diluent gases on ignition delay times in the shock tube and in the rapid compression machine’, Combustion and Flame, Volume 151, Issues 1–2, 289-302.

Xiaolei G, Zuohua H, Jian C, Jing G, Xuesong W, Chia-Fon L, (2012), ‘Emission characteristics of a spark-ignition engine fuelled with gasoline-n-butanol blends in combination with EGR’, Fuel, Volume 93, 611-617.

Xudong Z, Yang W, Shuaiqing X, Yongsheng Z, (2013), ‘Study of knock in a high compression ratio spark-ignition methanol engine by multi-dimensional simulation’, Energy, Volume 50,150-159.

Yates A., Bell A., Swarts A., (2010). “Insights relating to the autoignition characteristics of alcohol fuels”. Fuel, 89, 83-93.

Yu J, Jinle L, Weihong J, Yunliu Y, Sheng Y, (2014),’Current status and prospects of industrial bio-production of n-butanol in China’, Biotechnology Advances.

Z.M. Djurisic, A.V. Joshi, H.Wang: Second joint Meeting in US sections of the combustion Institute, paper 238, 2001.

Zhang C, Wu H., (2015) ‘Combustion characteristics and performance of a methanol fuelled homogenous charge compression ignition (HCCI) engine’, Journal of the Energy Institute, 1-8.

Zhu, Y., Li, S., Davidson, D. F. & Hanson, R. K. (2015). “Ignition delay times of conventional and alternative fuels behind reflected shock waves”. Proceedings of the Combustion Institute, 35, 241-248.